nature portfolio

Peer Review File

TiO2-facet-dependent reconstruction of Pt nanoparticles during CO oxidation

Corresponding Author: Professor Kwangjin An

This file contains all reviewer reports in order by version, followed by all author rebuttals in order by version.

Version 0:

Reviewer comments:

Reviewer #1

(Remarks to the Author)
TiO2-facet-dependent reconstruction of Pt nanoparticles during CO oxidation

In this study, Jihun Kim, Yunkyung Kim et al. synthesized morphology-controlled Pt/TiO2 catalysts with Pt nanoparticles (NPs), supported on anatase TiO2, exposing either (001) or (101) facets. The investigation of facet-dependent metal-support interactions (MSI) combined experimental characterization with theoretical modelling. Results showed that the TiO2 (001) facet stabilizes Pt NPs with low nuclearity, enhances Pt–TiO2 interactions, and preserves Pt morphology during CO oxidation, leading to higher catalytic activity. In contrast, the (101) facet favoured high-nuclearity Pt NPs with weaker MSI. The study highlights that the exposed support facet drives the structural reconstruction of supported metal NPs, tailoring their geometric and electronic properties, which significantly impacts catalytic performance. Although the work is interesting, there are several critical questions:
1. The study uses Pt clusters, but the impact of CO coverage on Pt nanoparticles during CO oxidation reactions is not addressed in detail. Previous research (ACS Catal. 2024, 14, 3504-3513) highlights the influence of CO adsorption on Pt structure and reactivity. How was CO coverage considered in the simulations, and how might it affect the catalytic behavior of Pt during CO oxidation? The authors should consider this point under the reaction conditions.
2. Recent studies (Science 2024, 386(6724), 915-920) indicate that Pt nanoparticles can also be encapsulated at TiO2(011). How do the metal-support interactions (MSI) differ on TiO2(011) compared to TiO2(001) and TiO2(101)? How was MSI accounted for in your model, and what impact does it have on the stability and catalytic performance of Pt nanoparticles?
3. The methodology for the Graph Neural Network (GNN) model is not fully described. The authors should provide details on the architecture, hyperparameters, and training process of the GNN model, as well as performance metrics (e.g., RMSE, MAE) for the training, validation, and test sets. This would help in evaluating the model's accuracy and reliability.
4.The reaction mechanism lacks transition state calculations and microkinetic simulations. These are essential for understanding the activation barriers and rate-determining steps of the catalytic reaction. The authors should include these calculations and provide the overall reaction rate to give a more complete picture of the catalytic process?
5. CO adsorption appears to induce reconstruction and surface roughening of Pt nanoparticles. How does CO influence the morphological changes of Pt nanoparticles, particularly under different CO concentrations and on distinct TiO2 facets? What role does facet-dependent CO-induced restructuring play in the catalytic process, especially during CO oxidation?
6. How do the interface interactions between Pt nanoparticles and TiO2 change under different CO/O2 ratios? How do these changes affect the reactivity and selectivity of the catalytic reaction, particularly under O2-rich or CO-rich conditions?
7. The differences in Pt binding strength on TiO2 (001) and (101) facets were discussed, but further clarification is needed. How do these differences in binding influence the morphological stability and catalytic performance of Pt nanoparticles? How does stronger Pt binding on TiO2 (001) contribute to enhanced catalytic activity?
8. How do the redox properties of TiO2 (001) and (101) facets differ, and how do these differences impact the activation of reactive oxygen species and lattice oxygen in the MvK pathway? How do these factors contribute to the superior catalytic performance of Pt/TiO2 (001) compared to Pt/TiO2 (101)?

Reviewer #2

(Remarks to the Author)

Kim et al. performed a comprehensive study to investigate the TiO2-facet sensitivity of Pt NP shapes during CO oxidation. A couple of advanced characterization and methods and theoretical simulations were applied to show the PTS exhibits significantly higher activity for CO oxidation than PTR owing to the facile generation of oxygen vacancies at TiO2(001) facets, which is beneficial for MvK reaction mechanism. This work is well performed in experimental and theoretical techniques, however, some critical information is missing. Thus, I cannot recommend the publication of this manuscript in the present form.
(1) The authors used same Pt201 faceted NP as the model to perform the GNN-MD simulations on TiO2(001) and TiO2(101). A larger MSD of PTS than MSD of PTR is observed and used to explain the larger reconstruction of Pt NPs on TiO2(001). However, the theoretical models are not consistent with the experimental observations that the fresh Pt NPs on TiO2(001) adopts hemispherical morphology (Fig. 1b) and Pt NPs on TiO2(101) adopts faceted morphology (Fig. 1d). Moreover, this model is not similar as the morphology of spent catalyst as shown in Fig. 2j. Thus, the GNN-MD simulation in this work is meaningless.
(2) The experiments showed the faceting process occurs during the CO oxidation. Please elucidate the reconstruction mechanism of Pt NP during CO oxidation.
(3) Moreover, the authors give the DFT results of the reaction pathway using Pt28 nanorod as the model, but do not pinpoint the reconstruction beneficial or detrimental to the MvK mechanism.
(4) The -ICOHP values are used to explain the weak MSI interaction and facile depletion of lattice oxygen atom at TiO2(001). However, it contradicts to the calculated stronger Pt binding on TiO2(001) (-0.78 eV) than on TiO2(101) (-0.68 eV). Please explain this inconsistency.
(5) TOC looks like giving a strategy to enhance the catalytic activity and prevent sintering of Pt NP. But it is not discussed in the paper and does not fit the topic.

Reviewer #3

(Remarks to the Author)
In this study, Kim et.al reported TiO2-facet dependent reconstruction of Pt NPS and reactivity for CO oxidation. The authors claimed a TiO2-facet and CO driven reconstruction and dynamics of Pt NPs that determines their CO oxidation reactivity. However, upon reviewing their data, I did not find sufficient and direct evidence to support the dynamic restructuring of Pt under reaction conditions, and the correlation between the reshaping of Pt NPs and their reactivity remains vague. Notably, a significant sintering of PTS was observed after the reaction (Figure S13), which must be carefully considered before the authors can validate their conclusions. Therefore, I cannot recommend the publication of this work in its current form, unless the authors provide systematic experimental evidence to substantiate their claims. For further details, please refer to my specific comments below.
1. The reshaping of the Pt NPs lacks sufficient/direct evidence. The STEM images of fresh samples exhibit insufficient resolution, which did not show their authentic shape and lattice structure. Notably, the high-resolution images of fresh Pt NPs in Figure S2d exhibit a cuboctahedral shape that is highly similar to that of the spent sample. This significantly undermining the validity of the authors' conclusions regarding Pt reshaping. Atomic-resolution STEM images of both Pt NPs before and after reaction should be provided with the same quality. In situ TEM experiment is also encouraged to show direct evidence of the reconstruction of Pt NPs.
2. In Figure S13, the size of Pt NPs on PTR shows a significant increase from 1.8nm to 3.2nm after reaction likely due to sintering. However, a critical inconsistency emerges when comparing this data to the spent Pt NPs presented in Figure 2. The Pt NP selected for analysis in Figure 2 are substantially smaller than the 3.2 nm average size reported in Figure S13. This seems to be arbitrary and raises concerns about the representativeness of the data used to support claims about post-reaction shape changes. The authors should show more individual Pt NPs of different sizes to validate the change of shape after reaction statistically.
3. A critical oversight in the current analysis is the failure to consider the size difference of PTS and PTR when interpreting their shape evolution and reactivity. The sintering of PTR can be a major reason for its low reactivity rather than the reshaping. A more careful investigation is needed before the authors draw their conclusion
4. The DRIFTS data of PTS and PTR (Figure 3a-b) show very minor difference, which is not sufficient to substantiate the authors' claim of a significant disparity in Pt shape between the two samples. Additionally, the sintering of PTR could be another reason for the increase of terrace sites, which should be considered.
5. The EXAFS data of PTR before and after reaction in Figure 2a also show very minor difference, whereas the TEM data in Figure S13 show an obvious sintering of PTR after reaction. The authors should explain this discrepancy.
6. The parameters of EXAFS fitting should be carefully checked. For example, the σ2 for Pt–O bond in the Spent PTS, CO-rich (CO/O2=5) is too high. And the uncertainty in curve fitting is also important to present.
7. The size difference of PTR and PTS after reaction should be also considered for their DFT calculation.
8. Many earlier studies have been documented regarding the TiO2-facet dependency and MSI effect (Chin. J. Catal, 2019, 40, 1534-1539; J. Catal, 2021, 398, 109-122; Chin. J. Catal, 2025, 70,378-387), where TiO2 (001) support itself is also essential for the catalytic performance (Prog. Nat. Sci.: Mater. Int., 2021, 31, 1-13). Therefore, the role of TiO2(001) support, such as enriched oxygen vacancies, should be also considered for their high reactivity, other than the reshaping of Pt NPs.

Version 1:

Reviewer comments:

Reviewer #1

(Remarks to the Author)
While the authors have addressed several of my previous concerns, several critical technical issues remain that require further clarification.
Specifically, the methodology used to determine CO coverage on the Pt surface needs to be clearly defined, as it is unclear if the "abundant" CO model utilized is physically accurate under realistic conditions. This high CO loading also raises questions regarding cluster stability; the authors should investigate whether such high adsorbate density causes cluster "lifting" or structural instability.
Furthermore, the observed lack of full encapsulation on the anatase surfaces may be attributed to the absence of oxygen vacancies in the model, which are generally considered a fundamental driver of the SMSI.
Regarding the kinetic results, the reported activation barrier of 3.37 eV for Pt28/TIO2 is exceptionally high and deviates significantly from values typically found in the literature; therefore, this result must be carefully re-verified.
Finally, to ensure the validity of the theoretical framework, a formal comparison between the calculated reaction rates and measured experimental rates should be provided.

Reviewer #2

(Remarks to the Author)
The authors have thoroughly addressed my technical questions. However, I remain somewhat concerned about the novelty of the work in the context of a high-profile journal such as Nature Communications. It is well established that the Pt–TiO_2(001) interface exhibits stronger metal–support interactions compared to Pt–TiO_2(101), and the lower oxygen vacancy (V_o) formation energy and correspondingly higher catalytic activity on the (001) facet are therefore somewhat expected. I would encourage the authors to more clearly articulate the distinctive scientific advance or conceptual novelty of their findings to better align with the high standards of Nature Communications.

Reviewer #3

(Remarks to the Author)
I truly appreciate the authors' efforts in providing supplementary experimental results. Nevertheless, upon reviewing the additional data, I still consider it insufficient to support their claim regarding "TiO2-facet-dependent reconstruction of Pt nanoparticles during CO oxidation". The morphology of Pt nanoparticles (NPs) is predominantly dictated by the TiO2 support, attributed to wetting/dewetting effects that are well-documented in the literature. During CO oxidation reactions, only surface roughening of Pt NPs is observed and similar CO-induced surface roughening phenomena have been extensively reported by in situ TEM/STM. Critically, no evidence is provided in the manuscript to illustrate how these subtle structural changes modulate catalytic reactivity. Alternatively, it is more plausible that the enhanced CO oxidation reactivity stems from the initial structure of Pt NPs on different TiO2 support, rather than their reconstruction during the reaction. Notably, the enriched oxygen vacancies (Ov) on TiO2(001) may play a more pivotal role than Pt NP morphology that is inadequately addressed in the current manuscript. Overall, this work lacks significant scientific advances and may not meet the rigorous standards of Nature Communications. Therefore, I regret that I cannot recommend the publication of this manuscript in its present form.
Some specific comments for the authors to consider:
1. The initial structure of Pt NPs is determined by the TiO2 facet due to wetting/dewetting, but the reconstruction during reaction is quite subtle. The author should provide more compelling evidence to clarify how such subtle surface roughening modulates catalytic reactivity, other than their initial structure.
2.I strongly suspect that the enriched Ov on TiO2(001) may play a more crucial role than the morphology of Pt NPs. These Ov species can facilitate O_2 activation through the MVK mechanism and thus enhance the CO oxidation reactivity. To distinguish the respective contributions of Pt NP shape and Ov on TiO2 support, the authors are advised to compare the reactivity of Pt clusters deposited on different TiO2 facets.
3.The authors should note that the enriched Ov on TiO2(001) (reducibility of the support) results in stronger MSI interaction and consequently the shape of Pt NPs, rather than vice versa. Earlier studies have shown the electron transfer from the defects of support can influence the shape of support metal particles.
4.Other than the reshaping of Pt NPs, the reconstruction of TiO2 at Pt-TiO2 interface and the stability of Pt NPs should be also considered.

Version 2:

Reviewer comments:

Reviewer #1

(Remarks to the Author)
The authors have revised the paper accordingly and the paper looks more convincing. I recommend the paper for publication.

Reviewer #2

(Remarks to the Author)

The authors have substantially improved the manuscript. Current version meets the criteria of Nature Communications.

Reviewer #3

(Remarks to the Author)
I appreciate the authors' efforts in providing a detailed response to my previous comments. But upon careful review of the revised manuscript, I still have substantial concerns regarding the novelty of this work, particularly for the high-profile journal like Nature Communications.
The current results can only support a TiO2-facet dependent reactivity derived from either the initial morphology of Pt NPs or metal-support interaction. Such effects have already been widely reported in the existing literature. Direct experimental evidence is still missing to explicitly identify the structural reconstruction of Pt/TiO2 during CO oxidation, which represents the core claim of this work. Given limited novelty and the lack of sufficient in situ structural characterization, I cannot support the publication of this manuscript.
Some specific comments for the authors to consider:
1. It is unclear what the reconstruction of Pt NPs refers to, beyond their initial morphology and surface roughening. Noted that both catalysts undergo surface roughening but display different reactivity, the authors should explicitly clarify the structural changes of Pt NPs during CO oxidation and their respective contributions to catalytic performance.
2. The enhanced reactivity after the first catalytic cycle may stem from the initial reduction of Pt NPs or the Pt-TiO2 interface, which could generate abundant Ov. Direct experimental evidence is required to verify the intrinsic structural evolution of Pt NPs after the first run, to exclude simple surface reduction.
3.The additional data on Pt/Al2O3 are not comparable or supportive, due to marked differences in particle size, morphology and metal–support interactions.

Version 3:

Reviewer comments:

Reviewer #3

(Remarks to the Author)
After careful evaluation, I still find insufficient evidence to support their core claim of "TiO2-facet-dependent reconstruction of Pt nanoparticles during CO oxidation"in the title. The authors only demonstrate facet-dependent initial morphological features of the catalyst before reaction, arising from wetting/dewetting effects that have been well documented in existing literature. The authors also claim "a dynamic structural evolution of Pt-TiO2 during reaction", but they only provided indirect evidence, inferring CO-induced surface roughening by DRIFTS and Pt facilitated reduction of TiO2 support by TPR, which are also well known in literature. Simply combining these known observations cannot establish sufficient novelty for this work.
Given the absence of direct evidence (e.g., in situ ETEM characterization) demonstrating how Pt reconstructs during the CO reaction and how such structural changes correlate with CO catalytic reactivity (rather than simple surface reduction), I remain skeptical about the novelty of this work.

Reviewer #4

(Remarks to the Author)
In the submission the authors show that the support facet governs the initial morphology, reaction-induced restructuring behaviour of supported Pt nanoparticles on TiO2 during CO oxidation, which are not unexpected. But a paper with solid experimental results to demonstrate them is of importance and interest in the community. and deserves the publication in Nature Communications. Below are two minor issues needed to be clarified before the publication:
1. Based on the adopted reaction pressures, the "AP-XPS" should be "NAP-XPS".
2. Figure 3 a and d: The y axis unite is normalized intensity. Why and how are the signals normalized? These are important for reproducibility.

Response to the reviewers' comments

The followings are the responses to the reviewers' comments for the manuscript *NCOMMS-25-68798*

Reviewer #1

General comment 1: *Overall comment:* In this study, Jihun Kim, Yunkyung Kim et al. synthesized morphology-controlled Pt/TiO_2 catalysts with Pt nanoparticles (NPs), supported on anatase TiO_2, exposing either (001) or (101) facets. The investigation of facet-dependent metal-support interactions (MSI) combined experimental characterization with theoretical modelling. Results showed that the TiO_2 (001) facet stabilizes Pt NPs with low nuclearity, enhances Pt–TiO_2 interactions, and preserves Pt morphology during CO oxidation, leading to higher catalytic activity. In contrast, the (101) facet favoured high-nuclearity Pt NPs with weaker MSI. The study highlights that the exposed support facet drives the structural reconstruction of supported metal NPs, tailoring their geometric and electronic properties, which significantly impacts catalytic performance. Although the work is interesting, there are several critical questions:

Response: We thank the reviewer for the constructive and detailed assessment of our work. The comments were highly valuable in helping us refine the logical structure of the manuscript and strengthen our central message. In response, we have revised the manuscript to improve both methodological rigor and internal consistency.

In the revision, we strengthened the theoretical and structural framework in three ways. First, we incorporated transition-state calculations and microkinetic analysis to place the facet-dependent trends on a quantitative kinetic basis. Second, we refined the nanoparticle (NP)-structure description by introducing global energetic optimization and quantitative wetting descriptors, which improves the consistency between the structural models and the experimentally observed morphologies. Third, we explicitly evaluated how CO-rich conditions perturb Pt NP structure in a facet-dependent manner, and we integrated these results into the discussion of metal–support interactions (MSIs) and oxygen activation.

Together, these revisions provide a clearer and more coherent mechanistic picture of TiO_2-facet-dependent Pt catalysis, while preserving the original experimental conclusions. We believe that the revised manuscript now offers a more robust and quantitatively grounded

interpretation of how support facets govern Pt structure, redox behavior, and catalytic performance. Detailed responses to each specific comment are provided below.

Comment 1: The study uses Pt clusters, but the impact of CO coverage on Pt nanoparticles during CO oxidation reactions is not addressed in detail. Previous research (*ACS Catal.* 2024, 14, 3504-3513) highlights the influence of CO adsorption on Pt structure and reactivity. How was CO coverage considered in the simulations, and how it might affect the catalytic behavior of Pt during CO oxidation? The authors should consider this point under the reaction conditions.

Response: We thank the reviewer for raising an important point regarding the role of CO coverage on Pt nanoparticles (NPs) under CO oxidation conditions. Recent studies reported in *ACS Catalysis* have demonstrated that CO adsorption can influence Pt catalysis through two primary effects: suppression of O_2 activation on Pt surfaces and CO-induced structural reconstruction of Pt NPs.

In the present study, the influence of CO coverage on Pt reactivity was considered with explicit attention to the structural characteristics of rod-shaped Pt NPs. Unlike compact Pt clusters, rod-like geometries expose an extended and highly heterogeneous ensemble of adsorption sites, including terraces, edges, and end-cap regions, each exhibiting distinct CO binding strengths. As a result, defining a single, uniform CO coverage on such NPs is inherently nontrivial, as increasing CO loading does not correspond to homogeneous site blocking but rather to preferential occupation of undercoordinated Pt sites that are most relevant for O_2 adsorption and activation. A rigorous treatment of CO coverage effects on rod-shaped NPs would therefore require systematic sampling of site-specific adsorption motifs, lateral CO–CO interactions, and the accompanying structural reorganization of the NP.

Under CO-rich conditions, these effects collectively act to suppress direct O_2 activation on Pt surfaces, thereby shifting the dominant oxidation pathway toward lattice oxygen participation through the Mars van Krevelen (MvK) mechanism. Accordingly, the present work focuses on facet-dependent oxygen supply and activation from the TiO_2 support, which governs the observed reactivity trends under reaction-relevant conditions.

Nevertheless, to qualitatively assess the impact of CO-induced restructuring under reaction-relevant conditions, additional GNN-based molecular dynamics (MD) simulations were performed for CO-covered Pt NPs. Importantly, the initial Pt/TiO_2 structures used for these

simulations were not arbitrary clusters, but facet-dependent Pt_{201} morphologies obtained from a genetic algorithm (GA) global optimization, which will be discussed in the Comment 1 from Reviewer 2. This procedure allows the Pt NP morphology to naturally emerge on each TiO_2 facet under a well-defined energetic framework, providing physically realistic metal-support contact geometries that are consistent with experimental wetting trends.

Action taken: By introducing CO adsorption on these GA-optimized Pt/TiO_2 structures, the simulations explicitly probe CO-induced restructuring of Pt NPs starting from facet-appropriate morphologies, enabling a meaningful comparison of facet-dependent structural responses under comparable CO-rich conditions.

To explicitly assess the impact of CO-induced structural reconstruction under reaction-relevant conditions, we performed additional GNN-based MD simulations for CO-covered Pt_{201} NPs supported on $TiO_2(001)$ and $TiO_2(101)$. In these simulations, CO molecules were initially adsorbed on the top sites of surface-exposed Pt atoms to represent a CO-rich environment (Supplementary Figs. 28a, b). For $Pt_{201}/TiO_2(001)$, 101 CO molecules were adsorbed on 137 surface Pt atoms, corresponding to a surface coverage of 73.7%. For $Pt_{201}/TiO_2(101)$, 106 CO molecules were adsorbed on 139 surface Pt atoms, corresponding to a surface coverage of 76.3%. Thus, both systems were examined under closely matched CO-rich conditions, ensuring that coverage does not act as a confounding variable in comparing facet-dependent behavior.

The CO-covered systems were equilibrated at 523 K for 100 ps (Supplementary Figs. 28c, d). Thermal equilibration was confirmed by the convergence of total energy and temperature. As shown in Supplementary Figs. 29a, b, both Pt_{201}/TiO_2 systems exhibit stable thermal equilibration, with the total energy and temperature converging rapidly within the initial stage of the simulation and remaining stable throughout the trajectory. These simulations explicitly account for CO adsorption and allow evaluation of the structural response of Pt NPs under CO-rich conditions. Detailed facet-dependent structural responses are discussed separately below in Comment 5.

In summary, the effect of CO coverage was explicitly considered by performing additional MD simulations on CO-covered Pt NPs under comparable CO-rich conditions. These results address the reviewer's concern by demonstrating how CO coverage was treated in the simulations and how CO adsorption influences the structural state of Pt NPs under reaction-relevant conditions.

The corresponding figures and analyses have been added to the revised manuscript, along with Supplementary Figs. 28 and 29, with additional related discussion addressed in the response to Comment 5.

The following paragraph has been added to the *Computational insights into facet-dependent Pt reconstructions on TiO_2* section on Page 10: *"To further elucidate experimentally observed CO-induced reconstruction behaviour, additional CO-covered GNN-based MD simulations were performed on $Pt_{201}/TiO_2(001)$ and $Pt_{201}/TiO_2(101)$ (Supplementary Note 7). Under high CO coverage (~0.75 ML) and reaction-relevant thermal conditions (523 K), CO adsorption perturbed the coordination environment of surface Pt atoms in a facet-dependent manner, as evidenced by the broadening of coordination-number distributions (Figs. 4e, f) and Pt–Pt RDFs (Supplementary Fig. 29), particularly on the (101) facet (Supplementary Table 6), supporting experimental observations of CO-induced Pt roughening."*

In addition, details of the GNN-based MD methodology employed to reproduce CO-induced reconstruction were added in Supplementary Note 7.

*"**Supplementary Note 7. CO-induced Reconstruction Simulations** CO-induced structural reconstruction of Pt NPs was investigated using explicit CO adsorption followed by structural relaxation and molecular dynamics (MD) simulations. For each optimized Pt_{201}/TiO_2 structure, surface Pt atoms were first identified based on a combined coordination and geometric criterion. Pt–Pt coordination numbers were evaluated using a cutoff distance of 3.0 Å, while interactions with the TiO_2 support (Ti and O atoms) were identified using a cutoff distance of 3.5 Å. Pt atoms with reduced Pt coordination were classified as surface atoms when they were either located at the metal–support interface, positioned far from the cluster center, or exhibited very low Pt coordination. In addition, Pt atoms located near the top of the NP were also considered surface atoms if their coordination number was below a threshold. This procedure enabled robust identification of catalytically accessible surface Pt sites across different NP morphologies.*

CO molecules were adsorbed on the identified surface Pt atoms using a site-by-site construction protocol. For each surface Pt atom, a CO molecule was placed along an outward direction defined relative to the NP geometry, with a fixed Pt–C distance of 1.85 Å and a C–O bond length of 1.15 Å. To avoid unphysical steric overlap, newly added CO molecules were excluded if the distance between any CO atom and existing atoms was smaller than 1.8 Å.

When overlap was detected, the corresponding adsorption site was skipped. As a result, the final CO coverage was determined self-consistently by geometric accessibility rather than by imposing a predefined coverage value.

The CO-covered structures were subsequently relaxed using the limited-memory Broyden–Fletcher–Goldfarb–Shanno (LBFGS) algorithm to remove residual forces arising from the initial CO placement. Structural optimization was performed until the maximum atomic force fell below 0.05 eV $Å^{-1}$. The relaxed CO-covered configurations were then used as initial structures for finite-temperature MD simulations.

MD simulations were carried out in the canonical (NVT) ensemble using a Langevin thermostat. A time step of 1.0 fs was employed, and the system temperature was maintained at 523 K. A friction coefficient of 0.001 was used to ensure stable temperature control while allowing sufficient atomic mobility. Each simulation was propagated for 100,000 MD steps, corresponding to a total simulation time of 100 ps. Atomic trajectories and thermodynamic quantities were recorded at regular intervals throughout the simulation. These simulations enabled direct observation of CO-induced structural rearrangements of Pt NPs under CO-rich conditions."

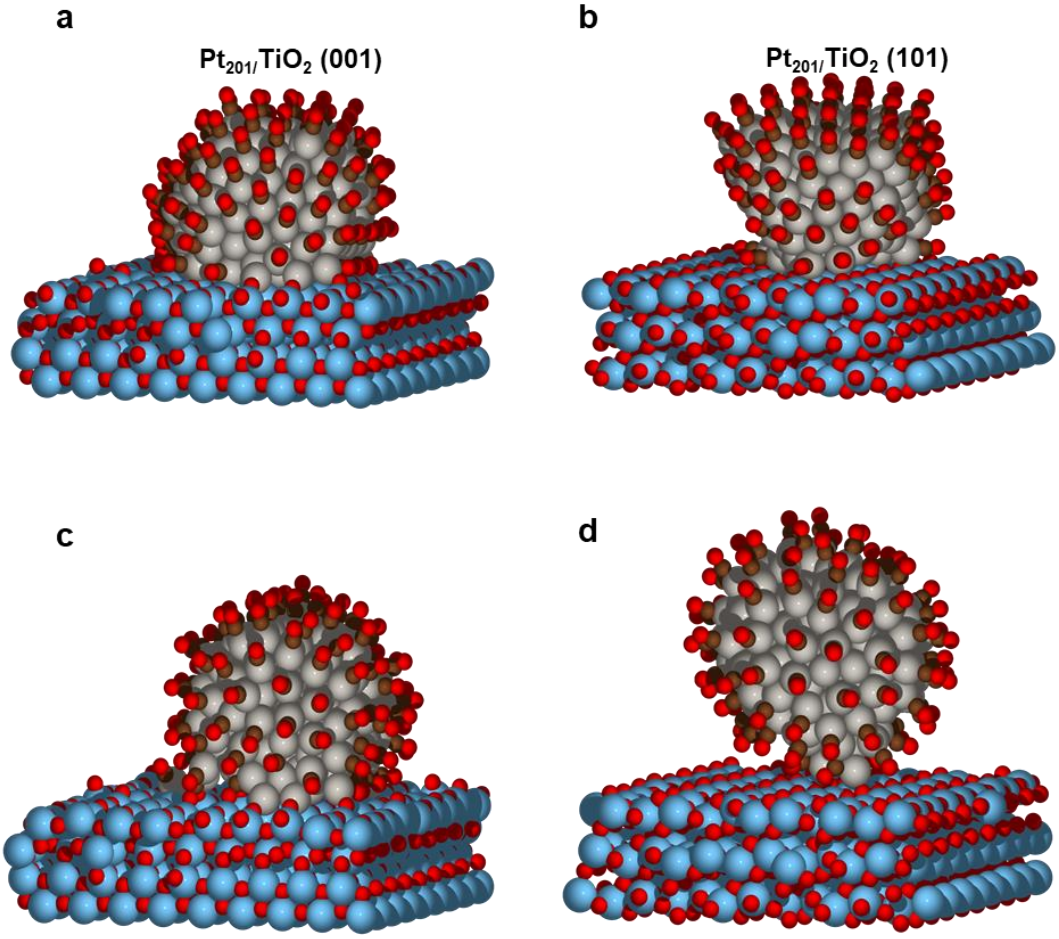

Supplementary Figure 28. CO-induced reconstruction of Pt_{201} NPs on TiO_2 facets. Initial configurations of CO-saturated Pt_{201} NPs supported on (a) TiO_2(001) and (b) TiO_2(101), with CO molecules adsorbed at the available Pt top sites. Corresponding structures after GNN–MD simulations at 523 K for 100 ps under CO-rich conditions are shown for (c) Pt_{201}/TiO_2(001) and (d) Pt_{201}/TiO_2(101).

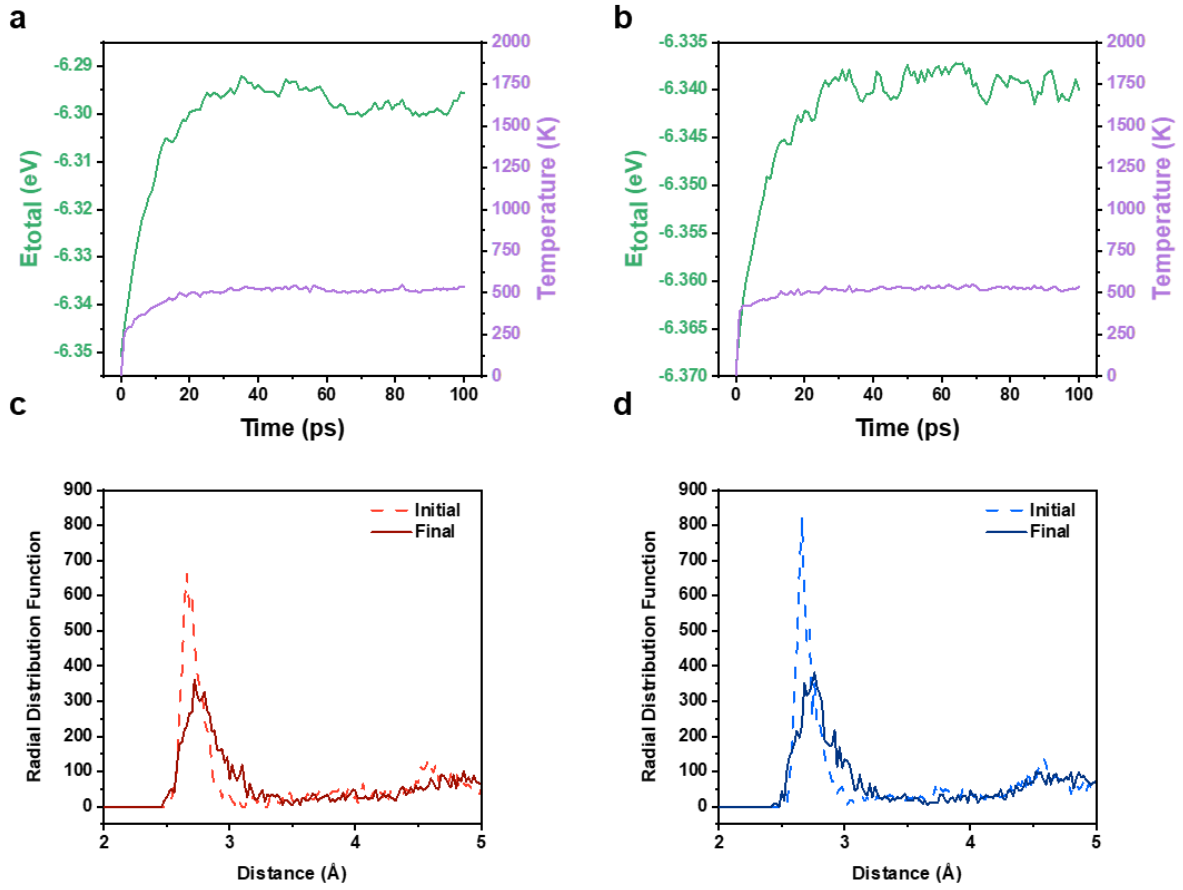

Supplementary Figure 29. Thermal convergence and CO-induced structural evolution of Pt_{201} NPs on TiO_2 facets revealed by GNN–MD simulations. Time evolution of total energy and temperature for (a) $Pt_{201}/TiO_2(001)$ and (b) $Pt_{201}/TiO_2(101)$ during GNN–MD simulations at 523 K, confirming thermal equilibration under CO-rich conditions. Radial distribution functions of Pt atoms before and after simulation are shown for (c) $Pt_{201}/TiO_2(001)$ and (d) $Pt_{201}/TiO_2(101)$.

Comment 2: Recent studies (*Science* 2024, 386(6724), 915-920) indicate that Pt nanoparticles can also be encapsulated at TiO_2(011). How do the metal-support interactions (MSIs) differ on TiO_2(011) compared to TiO_2(001) and TiO_2(101)? How was MSI accounted for in your model, and what impact does it have on the stability and catalytic performance of Pt nanoparticles?

Response: We thank the reviewer for highlighting recent reports on strong metal-support interaction behavior of Pt NPs on TiO_2(011), which raise an important question regarding how MSIs differ among TiO_2 facets and how such differences are reflected in our modeling framework. In particular, the reviewer's comment motivates a direct comparison between the extreme interaction regime reported for rutile TiO_2(011) and the anatase TiO_2(001) and TiO_2(101) systems investigated in this work.

Following the methodology reported in *Science* (2024, 386, 915-920), we constructed a rutile TiO_2(011) surface model containing 12.5% oxygen vacancies, with vacancies distributed near the surface region. A Pt_{201} NP was generated and placed on the rutile TiO_2(011) surface in its most stable adsorption configuration prior to MD simulations, following the same protocol in our initial manuscript for Pt_{201}/anatse TiO_2 models. Using the same simulation framework (PFP v4.0.0 implemented in Matlantis), we reproduced the reported simulation conditions of 1500 K, 0.8 ns and extended the analysis to anatase TiO_2(001) and TiO_2(101) surfaces using an identical Pt_{201} NP model (Figs. R1a, c). This approach enabled a direct and consistent comparison of MSI across different TiO_2 facets. Energy and temperature convergence plot for all three models are illustrated in Figs. R1b, d, e.

Under these conditions, the Pt/rutile TiO_2(011) system exhibited pronounced SMSI behavior (Fig. R1e), characterized by extensive wetting of the Pt NP, a substantial increase in Pt–Ti coordination, upward migration of support atoms toward the metal particle, and significant flattening of the Pt morphology. These structural signatures are fully consistent with the encapsulation behavior reported in *Science* (2024, 386, 915-920) and confirm that our simulation framework reliably captures extreme MSI regimes on rutile TiO_2(011).

In contrast, neither anatase TiO_2 surface exhibited full encapsulation behavior. However, clear facet-dependent differences were observed between TiO_2(001) and TiO_2(101). On TiO_2(001), moderate MSI developed, as evidenced by the formation of additional Pt–Ti bonds, partial upward displacement of lattice oxygen, and a net downward movement of the Pt NP toward the support. These features indicate enhanced metal–support contact without overgrowth or

encapsulation. By comparison, the $Pt_{201}/TiO_2(101)$ system showed minimal changes in Pt–Ti coordination and Pt–O separation, and the Pt NP largely retained its initial morphology, reflecting substantially weaker MSI.

Importantly, MSI was not introduced as an empirical parameter in our model, but emerged naturally from the explicit atomistic description of Pt–Ti–O interactions within both the density functional theory (DFT) and GNN-MD simulation-based frameworks. In the DFT calculations, MSI was quantified through adhesion energy analysis (Table R1), revealing stronger Pt binding on $TiO_2(001)$ than on $TiO_2(101)$. In addition, ICOHP analysis showed weaker Pt–O bonding on $TiO_2(001)$, which facilitates lattice oxygen activation. Consistently, GNN-based MD simulations at experimentally relevant temperatures (573 K) demonstrated higher atomic mobility and enhanced interfacial restructuring on $TiO_2(001)$.

These facet-dependent differences in MSI have direct implications for both the structural stability and the catalytic behavior of Pt NPs. Extremely strong interactions, as observed on rutile $TiO_2(011)$, lead to encapsulation and extensive morphological flattening, which can limit the accessibility of Pt surface sites. In contrast, the moderate interaction regime observed on anatase $TiO_2(001)$ stabilizes the Pt NP against detachment or large-scale restructuring while maintaining accessible metal–support contact regions. The weaker interaction on $TiO_2(101)$ results in a more rigid Pt morphology with limited metal–support coupling. This comparison confirms that the Pt/TiO_2 systems investigated in this work are structurally distinct from the extreme interaction regime reported for rutile $TiO_2(011)$, and that facet-dependent MSIs can be consistently assessed within the scope of the present models.

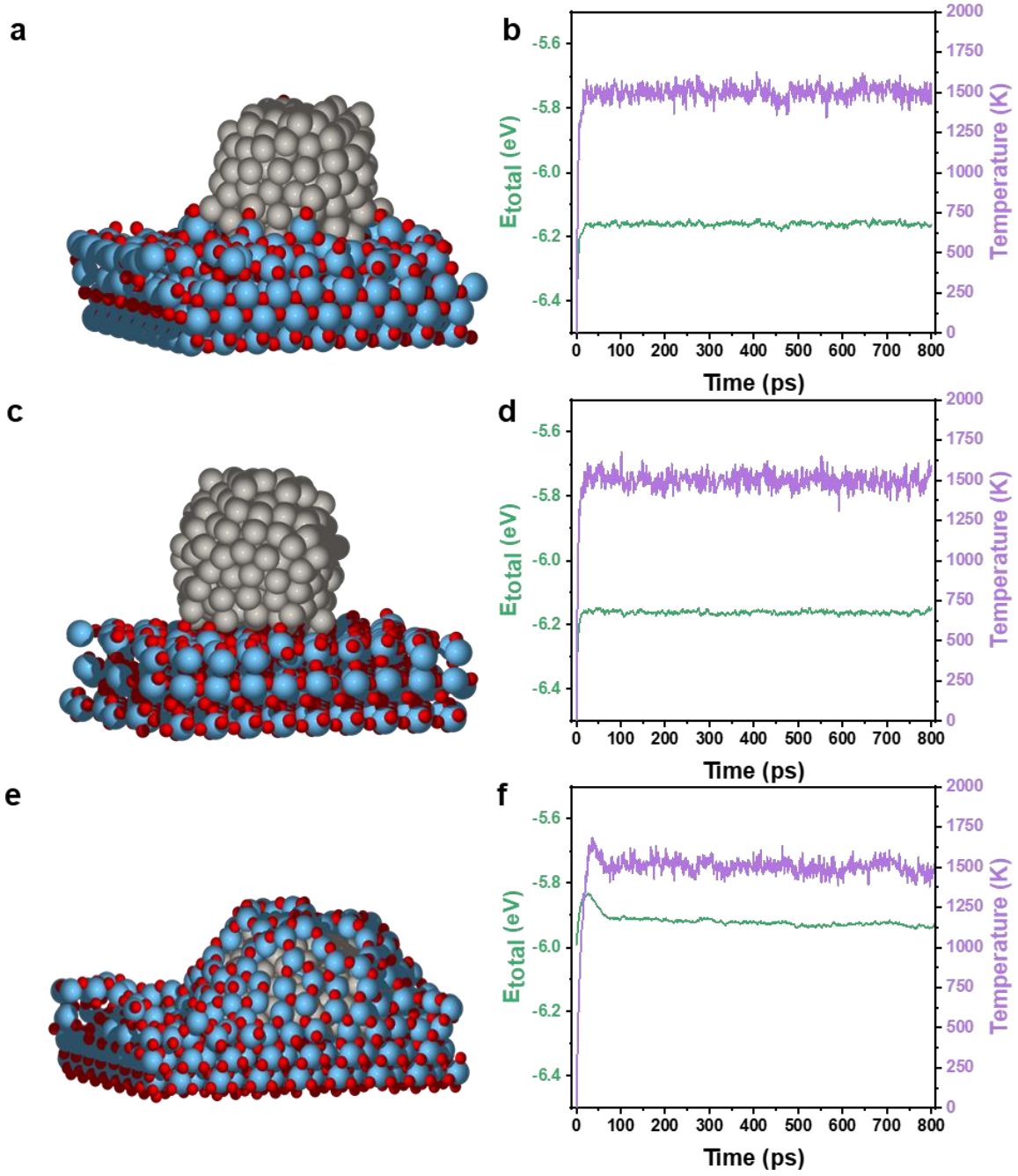

Figure R1. Thermal convergence and facet-dependent structural evolution of Pt_{201} NPs on TiO_2 revealed by GNN–MD simulations. Final snapshots after the simulations at 1500 K for 0.8 ns for (a) $Pt_{201}/TiO_2(001)$, (c) $Pt_{201}/TiO_2(101)$, and (e) Pt_{201}/rutile $TiO_2(011)$ with time evolution of total energy and temperature confirming stable thermal equilibration during simulations for (b) $Pt_{201}/TiO_2(001)$, (d) $Pt_{201}/TiO_2(101)$, and (f) Pt_{201}/rutile $TiO_2(011)$.

Table R1. Quantitative structural descriptors extracted from GNN–MD simulations after 0.8 ns at 1500 K for Pt_{201} NPs supported on different TiO_2 facets.

	ΔPt–Ti bonds	*ΔO average z (Å)*	*ΔPt–O separation (Å)*	*ΔPt height (Å)*
Pt/anatase TiO_2(001)	+11	+0.23	−2.22	+0.39
Pt/anatase TiO_2(101)	−1	+0.07	+0.05	+1.73
Pt/rutile TiO_2(011)	+440	0.71	−7.33	−2.10

Reported values correspond to changes(Δ) relative to the corresponding initial configurations prior to MD simulations. Specifically, changes in number of Pt–Ti bonds (ΔPt–Ti bonds), the changes in the average vertical displacement of surface oxygen atoms (ΔO average z (Å)), the changes in the mean Pt–O separation (ΔPt–O separation (Å)), and the changes in the overall height of the Pt NP with respect to the initial structure (ΔPt height (Å)).

Action taken: These additional simulations and analyses have been incorporated into the revised manuscript. The following paragraph has been added to the *Computational insights into facet-dependent Pt reconstructions on TiO_2* section on Page 10: *"Additional GNN-MD simulations at 1500 K for 0.8 ns were conducted to probe structural evolution under extreme thermal conditions (Supplementary Table 3). Although pronounced Pt flattening on TiO_2(001) was observed, unphysical slab distortion also occurred, indicating that these conditions are unsuitable for equilibrium structure prediction (Supplementary Fig. 24)."*

Insights gained from this additional analysis have been integrated into the main text to strengthen the discussion of facet-dependent MSIs in anatase TiO_2, without explicitly including the rutile TiO_2(011) system (Supplementary Fig. 24 and Supplementary Table 3).

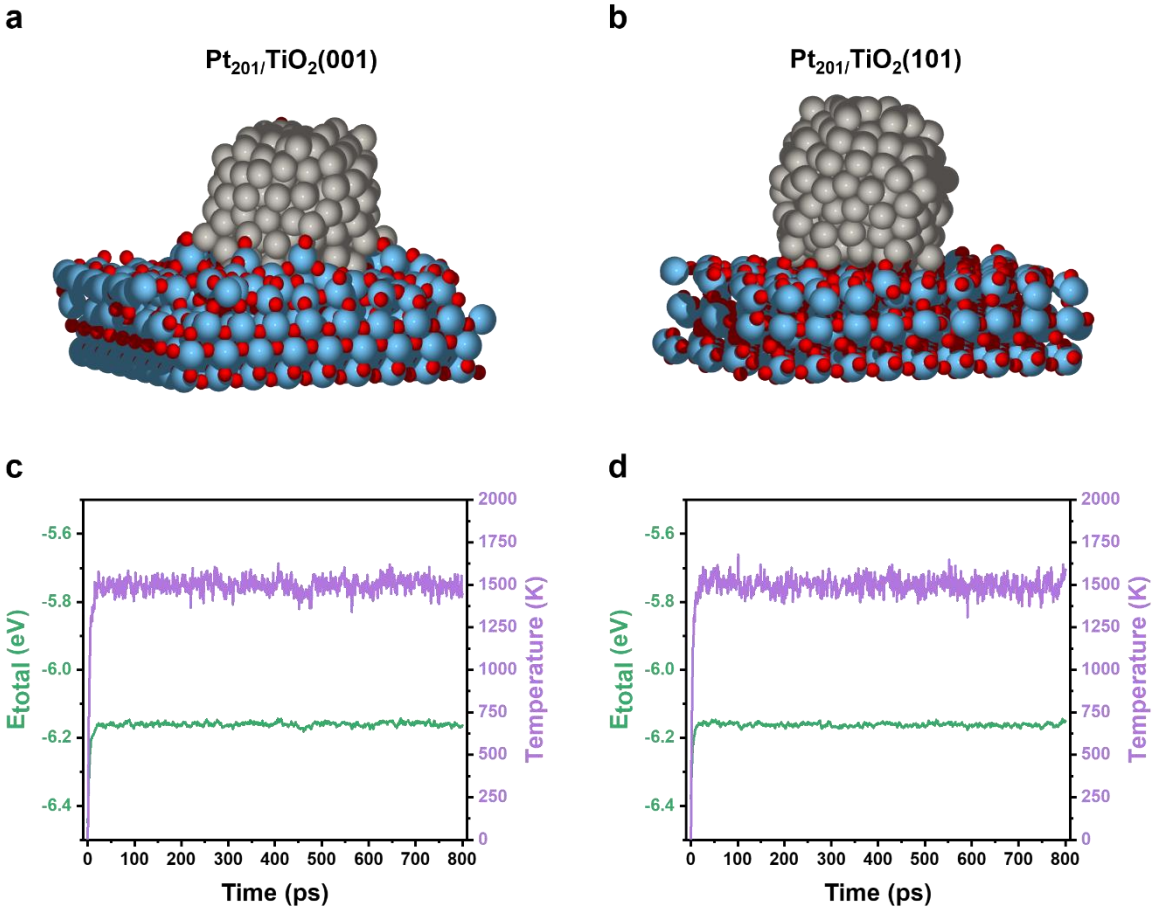

Supplementary Figure 24. Thermal convergence and facet-dependent structural evolution of Pt_{201} NPs on TiO_2 revealed by GNN–MD simulations under extreme conditions. Final snapshots after the simulations at 1500 K for 0.8 ns for (a) $Pt_{201}/TiO_2(001)$ and (b) $Pt_{201}/TiO_2(101)$, with time evolution of total energy and temperature confirming stable thermal equilibration during simulations for (c) $Pt_{201}/TiO_2(001)$ and (d) $Pt_{201}/TiO_2(101)$.

Supplementary Table 3. Quantitative structural descriptors extracted from GNN–MD simulations after 0.8 ns at 1500 K for Pt_{201} NPs supported on different TiO_2 facets.

	ΔPt–Ti bonds	ΔO average z (Å)	ΔPt–O separation (Å)	ΔPt height (Å)
Pt/anatase TiO_2(001)	+11	+0.23	−2.22	+0.39
Pt/anatase TiO_2(101)	−1	+0.07	+0.05	+1.73

Reported values correspond to changes (Δ) relative to the corresponding initial configurations prior to MD simulations. Specifically, changes in number of Pt–Ti bonds (ΔPt–Ti bonds), the changes in the average vertical displacement of surface oxygen atoms (ΔO average z (Å)), the changes in the mean Pt–O separation (ΔPt–O separation (Å)), and the changes in the overall height of the Pt NP with respect to the initial structure (ΔPt height (Å))

Comment 3: The methodology for the Graph Neural Network (GNN) model is not fully described. The authors should provide details on the architecture, hyperparameters, and training process of the GNN model, as well as performance metrics (e.g., RMSE, MAE) for the training, validation, and test sets. This would help in evaluating the model's accuracy and reliability.

Response: We thank the reviewer for pointing out that the description of the graph neural network (GNN) model was insufficient in the original manuscript. In response, we have expanded the methodological description of the GNN-based MD simulations and added quantitative information on model accuracy and validation.

The detailed description about our GNN model is provided below. In this study, we employed the Preferred Potential (PFP, version 4.0.0), a pre-trained universal neural network potential developed by Preferred Networks and implemented in the Matlantis platform, for large-scale MD simulations of Pt_{201} clusters on TiO_2 surfaces. PFP is based on the TeaNet (Tensor-embedded Atom Network) architecture, which incorporates tensor-based message passing to preserve rotational and reflectional symmetries and employs a variable cutoff scheme suitable for surface and cluster environments. The model was trained on an extensive dataset of DFT calculations, including bulk crystals, surface slab models, atomic clusters, adsorption configurations, and high-temperature disordered structures. As a pre-trained potential, the model architecture and training hyperparameters are defined by the developer and were not modified in the present study.

Details of the training hyperparameters, including learning rate schedules, batch sizes, and the number of training epochs, are not publicly disclosed due to the proprietary nature of the model. However, the reliability of PFP has been extensively validated in prior benchmark studies (*Comput. Mater. Sci.* 2022, 207, 111280, *Nat. Commun.* 2022, 13, 2991). According to the literature, PFP achieves mean absolute errors on the order of 5–14 $meV \cdot atom^{-1}$ for energies and 0.065–0.13 $eV \cdot atom^{-1}$ for forces across adsorption structures and high-temperature disordered configurations relevant to MD simulations. These benchmark metrics indicate that PFP reproduces DFT-level energies and forces with sufficient accuracy for structural and dynamical analyses.

In addition to these published benchmarks, we further assessed the applicability of PFP to the Pt/TiO_2 system investigated in this study by directly comparing PFP predictions with DFT

calculations for selected quantities, as shown in Supplementary Fig. 50. First, we evaluated the formation energies of Pt clusters with varying sizes (ranging from approximately 5 to 55 atoms) against DFT values. The parity plot demonstrates excellent agreement between PFP and DFT, with an MAE of 0.043 $eV \cdot atom^{-1}$ for Pt formation energies across the entire size range (Supplementary Fig. 50a). This low error confirms that PFP accurately captures the energetics of Pt clusters relevant to our Pt_{201} NP simulations. Second, we compared PFP-calculated adsorption energies for key adsorbates in our CO oxidation mechanism (CO, O_2, and O) on Pt/TiO_2 catalyst surfaces with DFT reference values, obtaining an MAE of approximately 0.22 eV (Supplementary Fig. 50b). This level of accuracy is sufficient for screening catalytic properties and identifying trends in reaction energetics across different TiO_2 facet configurations. Furthermore, we evaluated the accuracy of force predictions during structure optimization by comparing the maximum force at each optimization iteration between PFP and DFT calculations (Supplementary Fig. 50c), confirming reliable convergence behavior during geometry optimizations. These validation results demonstrate that PFP provides adequate accuracy for capturing the facet-dependent structural dynamics of Pt NPs on TiO_2 surfaces investigated in this work.

Overall, these validation results demonstrate that, within the scope of the quantities examined, PFP reliably reproduces DFT trends for Pt cluster energetics, adsorption energies, and force convergence, thereby justifying its application in the present Pt/TiO_2 simulations.

Action taken: These descriptions and validation of GNN model results have been added to Supplementary Note 12 and Supplementary Fig. 50.

*"**Supplementary Note 12. Graph neural network potential and validation** Large-scale molecular dynamics (MD) simulations in this study were performed using a graph neural network (GNN) interatomic potential, the Preferred Potential (PFP, version 4.0.0), as implemented in the Matlantis platform. PFP is a pre-trained, universal neural network potential developed by Preferred Networks and is designed to reproduce density functional theory (DFT)-level energies and forces across a wide range of chemical environments, including bulk materials, surfaces, cluster, and disordered structures.*

As a proprietary pre-trained model, detailed architectural parameters and training hyperparameters are defined by the developer and were not modified in this study. The performance of PFP has been benchmarked in previous reports, showing mean absolute errors

(MAEs) of approximately 5–14 meV per atom for total energies and 0.065–0.13 eV·Å^{-1} for atomic forces, indicating DFT-level accuracy suitable for MD simulations.

To further validate the applicability of PFP to the Pt/TiO$_2$ systems studied here, we directly compared PFP predictions with DFT reference calculations for representative properties (Supplementary Fig. 50). First, the formation energies of Pt clusters spanning a wide size range (approximately 5–55 atoms) were evaluated. The resulting parity plot demonstrates excellent agreement between PFP and DFT, with a mean absolute error of 0.043 eV per atom across the entire size range (Supplementary Fig. 50a). Second, adsorption energies of key species involved in the CO oxidation reaction (CO, O$_2$, and O) on Pt/TiO$_2$ catalyst surfaces were compared between PFP and DFT calculations. An MAE of approximately 0.22 eV was obtained for adsorption energies (Supplementary Fig. 50b), which is sufficient for identifying facet-dependent trends in adsorption energetics and reaction pathways. Third, force convergence during structural relaxation closely matches DFT results, confirming the reliability of PFP for geometry optimization and MD simulations (Supplementary Fig. 50c).

Overall, these validation results demonstrate that PFP reliably reproduces DFT trends for Pt cluster energetics, adsorption energies, and force predictions within the scope relevant to this work. This level of accuracy justifies the use of PFP for capturing facet-dependent structural dynamics and CO-induced reconstruction phenomena of Pt NPs supported on TiO$_2$ surfaces."

Accordingly, the relevant references (24 and 25) about previous works about GNN models discussed in this work have been added to the revised Supplementary Information files.

24. Hojo, H. et al. Lattice-Plane-Dependent Distribution of Ce^{3+} at Pt and CeO_2 Interfaces for Pt/CeO_2 Catalysts. *ACS Nano* **18**, 4775-4782 (2024).
25. Li, S.D. et al. Unusual Facet-Dependent Sintering in Pd-TiO_2 Catalysts Revealed by Theory and Experiment. *ACS Catal.* **14**, 1608-1619 (2024).

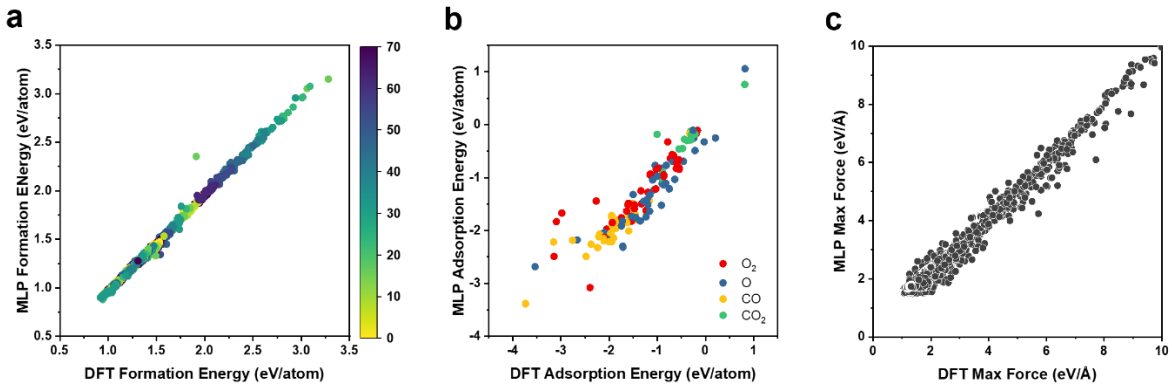

Supplementary Figure 50. Validation of the PFP GNN potential through comparison with DFT calculations. (a) Parity plot of Pt cluster formation energies predicted by PFP and DFT (b) Comparison of adsorption energies for key CO oxidation intermediates on Pt/TiO_2 surfaces calculated by PFP and DFT (c) Parity comparison of maximum atomic forces during structure optimization between PFP and DFT.

Comment 4: The reaction mechanism lacks transition state calculations and microkinetic simulations. These are essential for understanding the activation barriers and rate-determining steps of the catalytic reaction. The authors should include these calculations and provide the overall reaction rate to give a more complete picture of the catalytic process.

Response: We thank the reviewer for this valuable suggestion. We agree that reaction energies alone are insufficient to identify activation barriers, rate-determining processes, and overall catalytic performance. A kinetic description that explicitly accounts for transition states and the competition between elementary steps is required to provide a more complete mechanistic picture.

In particular, for reducible oxide supports such as TiO_2, the MvK mechanism involves coupled surface reactions and lattice oxygen redox steps, whose relative rates and surface coverages cannot be reliably inferred from static energetics alone. Therefore, a microkinetic framework that directly solves the coupled rate equations is more appropriate than heuristic approaches that assume a single rate-determining step.

To address this point, we adopted an ODE-based microkinetic modeling approach that allows the steady-state surface coverages and overall reaction rates to naturally emerge from the competition between adsorption, surface reactions, and lattice oxygen regeneration. This enables a physically rigorous comparison of the two Pt/TiO_2 facets at the rate level, without imposing a priori assumptions on the controlling step.

Action taken: We have revised the manuscript to explicitly state that transition state energies were calculated using the *Nudged Elastic Band method* for all elementary steps except those involving the adsorption of newly supplied gas-phase reactants. The calculated transition state energies and the corresponding kinetic energy diagram have been added in Fig. 6a and discussed in the revised *Results* section.

Microkinetic analysis was performed using the MKMCXX code. MKMCXX is an ordinary-differential-equation-based microkinetic solver developed by the group of Ivo Filot at Eindhoven University of Technology and has been previously applied to CO oxidation on metal/oxide catalysts, including Au/TiO_2 systems (*J. Catal.* 2020, 392, 39-47), as well as in recent *ACS Catalysis* studies referenced by Reviewer 1 in Comment 1.

In this approach, all elementary steps involved in the MvK CO oxidation mechanism are explicitly described by coupled rate equations. These equations were solved by time integration

until steady-state surface coverages and reaction rates were obtained. This framework avoids heuristic assumptions such as predefining a rate-determining step and instead allows the steady-state kinetics to emerge naturally from the competition between adsorption, surface reactions, and lattice oxygen redox processes.

Gas-surface adsorption and desorption steps were modeled using the Hertz-Knudsen formalism, while surface reaction steps were described by Arrhenius-type rate expressions using activation free energies derived from DFT calculations. All thermodynamic quantities were treated consistently in terms of Gibbs free energies, ensuring that the DFT-derived energetics were directly translated into kinetic parameters.

The microkinetic model is based on a MvK-type mechanism involving lattice oxygen participation and oxygen vacancy formation on the TiO_2 support.

Surface states

S0: *
(Initial stoichiometric surface with an empty active site)

S1: CO*
(CO adsorbed on metallic Pt site)

S2: O_v*
(Oxygen vacancy formed after CO oxidation)

S3: O_2*O_v
(O_2 adsorbed at an oxygen vacancy)

S4: O*
(Activated oxygen species after O_2 dissociation)

S5: CO* + O*
(Co-adsorbed CO and activated oxygen)

Elementary reaction steps

R1: $CO(g) + S0 \rightleftharpoons S1$

(CO adsorption and desorption on Pt)

R2: S1 → S2 + CO_2(g)
(CO oxidation by lattice oxygen and CO formation, vacancy generation)

R3: O_2(g) + S2 ⇌ S3

(O_2 adsorption at oxygen vacancy)

R4: S3 ⇌ S4

(O_2 dissociation and formation of activated oxygen)

R5: CO(g) + S4 ⇌ S5

(CO adsorption adjacent to activated oxygen)

R6: S5 → S2 + CO_2(g)
(CO oxidation by activated oxygen and regeneration of vacancy)

This reaction network closes the catalytic cycle by coupling CO oxidation with vacancy formation and re-oxidation of the oxide support.

The microkinetic modeling results provide mechanistic insight into the facet-dependent CO oxidation activity of Pt/TiO_2 catalysts. As shown in Supplementary Fig. 31a, the surface coverages of key intermediates exhibit markedly different temperature-dependent behaviors on Pt/TiO_2(001) and Pt/TiO_2(101). On Pt/TiO_2(001), the dominant surface species undergo a clear transition with increasing temperature, indicating an earlier depletion of strongly bound intermediates and the emergence of reaction-relevant vacant sites. In contrast, Pt/TiO_2(101) maintains a relatively stable surface coverage profile over the entire temperature range, suggesting limited surface turnover and restricted access to active reaction pathways.

These distinct coverage evolutions directly translate into the facet-dependent reaction rates predicted by the microkinetic model. As shown in Supplementary Fig. 31b, the CO_2 turnover frequency on Pt/TiO_2(001) increases sharply above approximately 550 K, whereas Pt/TiO_2(101) remains orders of magnitude less active across the same temperature range. This divergence cannot be attributed solely to the differences in adsorption energetics, but rather reflects fundamentally different kinetic regimes governed by the availability of reactive lattice oxygen and the efficiency of surface regeneration steps.

The sharp increase in activity on Pt/TiO_2(001) coincides with the temperature range in which lattice oxygen participation becomes kinetically accessible, consistent with a MvK-type mechanism. In this regime, facile lattice oxygen activation and replenishment enable sustained CO oxidation without excessive surface poisoning. By contrast, the limited activity of Pt/TiO_2(101) indicates that lattice oxygen activation remains kinetically hindered, leading to persistent surface blockage and suppressed reaction rates even at elevated temperatures.

Importantly, the microkinetic predictions closely mirror the experimentally observed trends in apparent activation energies, thereby providing a quantitative link between atomistic energetics and macroscopic reactivity. The agreement between microkinetic modeling and experiment supports the conclusion that the superior CO oxidation performance of Pt/TiO_2(001) originates from its ability to more readily access lattice oxygen–mediated reaction pathways, rather than from differences in CO adsorption strength alone.

Action taken: The revised version of reaction energy profile, including transition state calculations are now provided in Fig. 6a, and the corresponding discussion have been added to the *Reaction mechanism and the origin of superior catalytic activity* section on Pages 11–12: *"DFT calculations were employed to elucidate the influence of reconstructed Pt structures at the Pt–TiO_2 interfaces on the catalytic activity. A complete reaction energy diagram was derived for the optimised Pt_{28}/TiO_2(001) and (101) models following the MvK pathway (Fig. 5a). The energetics of the rate-determining step—the reaction between adsorbed CO and a lattice O atom—exhibit strong facet dependence. On Pt_{28}/TiO_2(001), the activation barrier is 1.58 eV, whereas on Pt_{28}/TiO_2(101), it rises to 3.37 eV. These values closely mirror the experimentally observed E_a, with Pt_{28}/TiO_2(001) achieving higher CO oxidation rates due to more facile lattice oxygen activation. This interpretation is further supported by microkinetic modeling results, which quantitatively reproduce the facet-dependent reactivity trends (Supplementary Fig. 31 and Supplementary Note 8)."*

A brief description of microkinetic analysis has been added in the Supplementary Note 8 and Supplementary Fig. 31.

*"**Supplementary Note 8. Microkinetic Simulations** Microkinetic analysis was performed using the MKMCXX code, an ordinary-differential-equation-based microkinetic solver developed by the group of Ivo Filot at Eindhoven University of Technology, which has been previously applied to CO oxidation on metal and reducible oxide catalysts.[12, 13]*

Within this framework, the elementary steps involved in the Mars van Krevelen CO oxidation mechanism were described by a set of coupled rate equations and solved by time integration until steady-state surface coverages and reaction rates were obtained. Surface states and elementary reaction steps are illustrated below.

[Surface states]

*S0: **

(Initial stoichiometric surface with an empty active site)

*S1: CO**

(CO adsorbed on metallic Pt site)

*S2: O_v**

(Oxygen vacancy formed after CO oxidation)

*S3: O_2*O_v*

(O_2 adsorbed at an oxygen vacancy)

*S4: O**

(Activated oxygen species after O_2 dissociation)

S5: CO + O**

(Co-adsorbed CO and activated oxygen)

[Elementary reaction steps]

R1: CO(g) + S0 $\rightleftharpoons$ S1

(CO adsorption and desorption on Pt)

R2: S1 $\rightarrow$ S2 + CO_2(g)

(CO oxidation by lattice oxygen and CO formation, vacancy generation)

R3: O_2(g) + S2 $\rightleftharpoons$ S3

(O_2 adsorption at oxygen vacancy)

R4: S3 $\rightleftharpoons$ S4

(O_2 dissociation and formation of activated oxygen)

R5: CO(g) + S4 ⇌ S5

(CO adsorption adjacent to activated oxygen)

R6: S5 → S2 + CO_2(g)

(CO oxidation by activated oxygen and regeneration of vacancy)

This approach enables a self-consistent description of steady-state kinetics without explicitly assuming a predefined rate-determining step, allowing the relative contributions of adsorption, surface reactions, and lattice oxygen redox processes to be evaluated within a unified kinetic framework.

Gas–surface adsorption and desorption steps were modeled using the Hertz–Knudsen formalism, while surface reaction steps were described by Arrhenius-type rate expressions with activation free energies derived from density functional theory calculations. All thermodynamic quantities were consistently treated in terms of Gibbs free energies, ensuring direct correspondence between DFT-derived energetics and kinetic parameters."

Accordingly, following references (12 and 13) used to establish the microkinetic modeling framework has been added to the revised Supporting Information files.

12. Chang, M.-W. et al. Dynamics of gold clusters on ceria during CO oxidation. *J. Catal.* **392**, 39-47 (2020).
13. Chen, C. et al. Reactant-induced dynamic stabilization of highly dispersed Pt catalysts on ceria dictating the reactivity of CO oxidation. *ACS Catal.* **14**, 3504-3513 (2024).

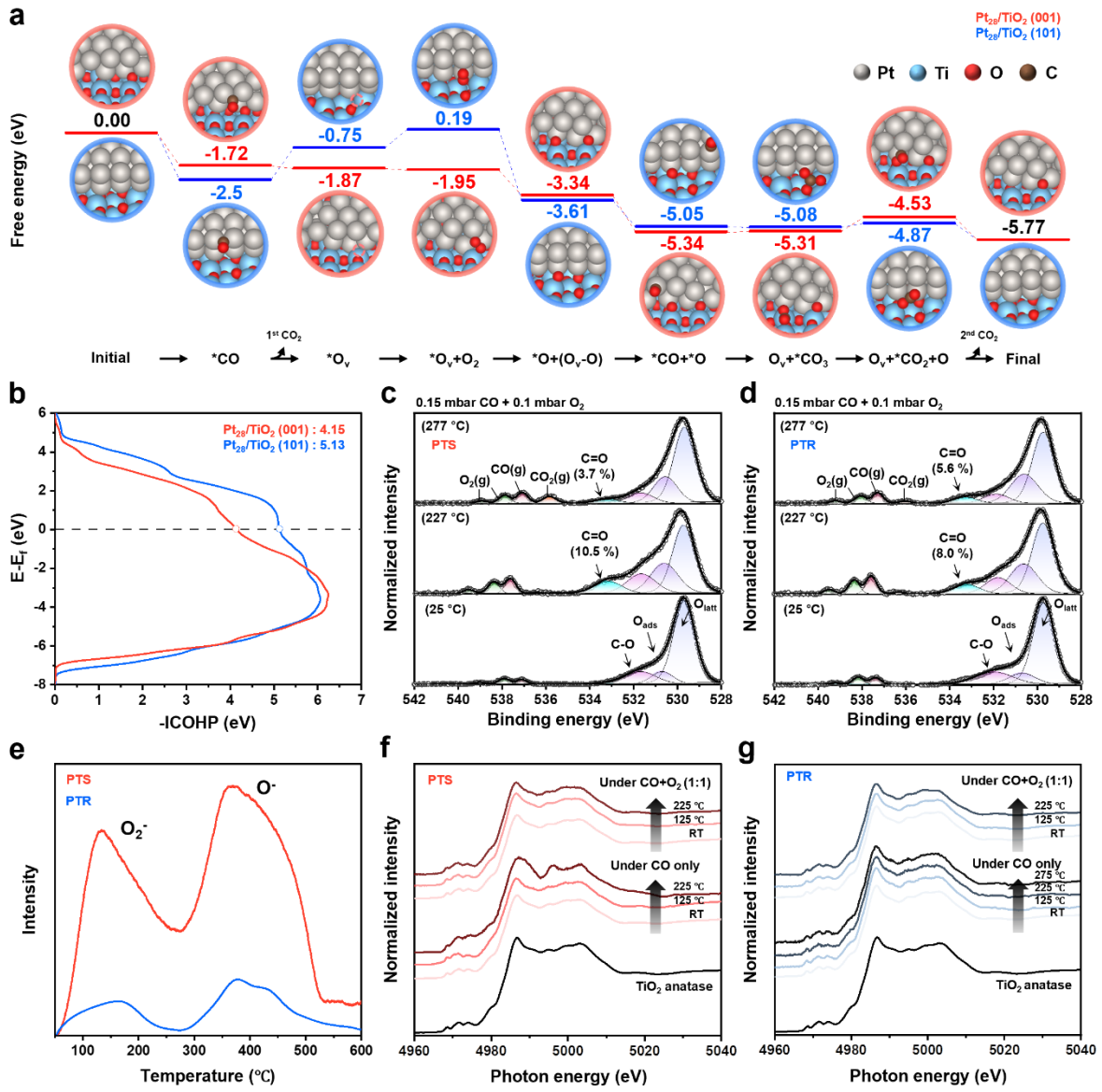

Figure 6. Synergistic effects of Pt morphology and TiO_2 facets on CO oxidation activity. (a) DFT-calculated reaction energy profiles for CO oxidation via the MvK mechanism on $Pt_{28}/TiO_2(001)$ and (101). (b) ICOHP analysis of oxygen vacancy formation on Pt_{28}/TiO_2 models. (c, d) Normalised *in situ* O 1*s* AP-XPS spectra ($h\nu$ = 650 eV) for (c) PTS and (d) PTR catalysts under CO oxidation conditions (0.15 mbar of CO, 0.1 mbar of O_2) at 25, 227, and 277 °C. (e) Reaction-order analysis of CO oxidation on post-reaction Pt/TiO_2 catalysts with respect to CO and O_2 partial pressures. Reaction rates were measured in the kinetically relevant regime (<5% CO conversion) at 80 °C for PTS and 160 °C for PTR, corresponding to their respective light-off temperatures. (f, g) Ti *K*-edge *in situ* XANES spectra of (f) PTS and (g) PTR under CO-reducing (middle panels: 5% CO/He) and CO + O_2 co-feed (upper panels: 5% CO + 5% O_2/He) conditions.

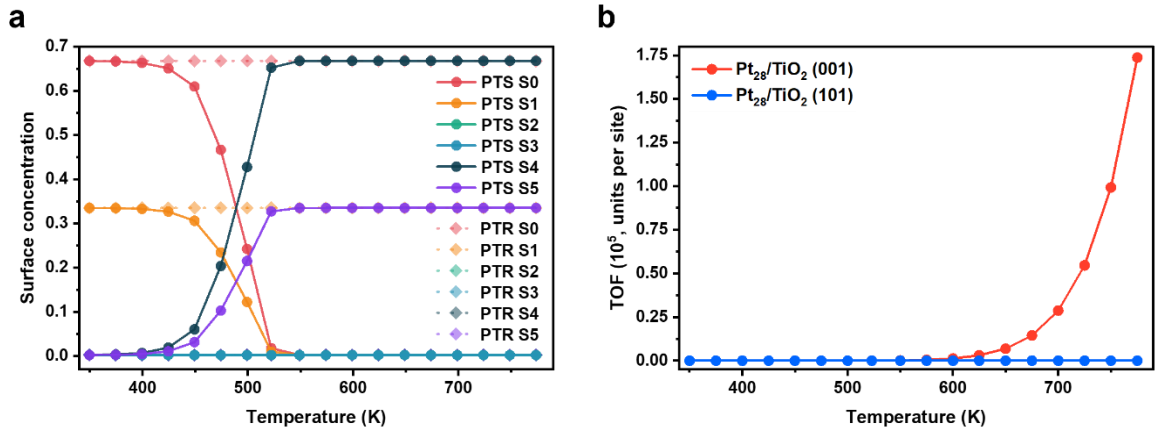

Supplementary Figure 31. Microkinetic modeling results for CO oxidation on Pt_{28}/TiO_2 catalysts. (a) Temperature-dependent surface coverages of reaction intermediates predicted for Pt_{28}/TiO_2(001) (PTS) and Pt_{28}/TiO_2(101) (PTR). (b) Corresponding CO_2 turnover frequencies (TOFs), highlighting the markedly enhanced activity of Pt_{28}/TiO_2(001) at elevated temperatures.

Comment 5: CO adsorption appears to induce reconstruction and surface roughening of Pt nanoparticles. How does CO influence the morphological changes of Pt nanoparticles, particularly under different CO concentrations and on distinct TiO_2 facets? What role does facet-dependent CO-induced restructuring play in the catalytic process, especially during CO oxidation?

Response: We thank the reviewer for the question regarding CO-induced reconstruction and surface roughening of Pt NPs, as well as the roles of CO concentration and TiO_2 facet dependence during CO oxidation. Here, we focus on how CO adsorption modifies the local structure of Pt NPs and how this response differs between TiO_2 facets.

Using the CO-covered MD simulations described above in Comment 1, we analyzed the structural response of Pt NPs to CO adsorption on TiO_2(001) and TiO_2(101) (Supplementary Fig. 28). GNN-based MD simulations performed at 523 K for 100 ps show that CO adsorption induces local rearrangements of surface Pt atoms on both facets, while the overall NP morphology remains largely preserved. The convergence of total energy and temperature during the simulations (Supplementary Fig. 29a, b) confirms that the observed structural changes arise from thermally equilibrated dynamics under CO-rich conditions.

The structural evolution of the Pt NPs was quantified using Pt–Pt radial distribution functions (RDFs) (Supplementary Fig. 29c, d) and coordination number (CN) distributions before and after the simulations (Fig. 4e, f). CO adsorption leads to surface roughening and a redistribution of Pt coordination environments on both facets, manifested as a broadening of the first-neighbor Pt–Pt RDF peak and a widening of the CN distributions. While the mean Pt–Pt coordination numbers remain nearly unchanged, the CN distributions broaden after annealing, indicating an increased heterogeneity of surface coordination environments. The corresponding mean values and standard deviations of the CNs before and after CO adsorption are summarized in Supplementary Table 6.

Notably, the extent of coordination redistribution differs between the two facets. Pt_{201} supported on TiO_2(101) exhibits a more pronounced broadening of coordination environments after CO adsorption, whereas Pt_{201} on TiO_2(001) shows a comparatively constrained redistribution under comparable CO coverage (73.7% for Pt_{201}/TiO_2(001), and 76.3% for Pt_{201}/TiO_2(101)). These results indicate that CO adsorption acts as a structural perturbation that reshapes the local coordination environments of Pt NPs under CO-rich conditions, with the magnitude of this

response modulated by facet-dependent MSIs.

Importantly, these facet-dependent changes in coordination heterogeneity provide a structural framework for interpreting the experimental CO-DRIFTS results. CO-DRIFTS is inherently sensitive to the coordination environment of surface Pt atoms, with distinct vibrational features corresponding to CO adsorption on undercoordinated and well-coordinated Pt sites. The redistribution of Pt coordination environments predicted by the simulations is therefore consistent with the experimentally observed evolution of coordination-sensitive CO adsorption bands during CO oxidation.

Overall, by explicitly analyzing how CO adsorption perturbs the local coordination environments of Pt NPs and how this perturbation differs between TiO_2 facets, the present results directly address the reviewer's question regarding the role of CO concentration and facet-dependent CO-induced restructuring. These findings clarify that CO adsorption does not simply block active sites, but dynamically modifies the distribution of Pt surface coordination environments in a facet-dependent manner, providing important structural context for understanding the catalytic behavior observed under CO oxidation conditions.

Action taken: These results and discussions have been incorporated into the revised manuscript, and corresponding data are now presented in Fig, 4e, f and Supplementary Figs. 28 and 29, and Supplementary Table 6. The following paragraph has been added to the *Computational insights into facet-dependent Pt reconstructions on TiO_2* section on Page 10: *"To further elucidate experimentally observed CO-induced reconstruction behaviour, additional CO-covered GNN-based MD simulations were performed on $Pt_{201}/TiO_2(001)$ and $Pt_{201}/TiO_2(101)$ (Supplementary Note 7). Under high CO coverage (~0.75 ML) and reaction-relevant thermal conditions (523 K), CO adsorption perturbed the coordination environment of surface Pt atoms in a facet-dependent manner, as evidenced by the broadening of coordination-number distributions (Figs. 4e, f) and Pt–Pt RDFs (Supplementary Fig. 29), particularly on the (101) facet (Supplementary Table 6), supporting experimental observations of CO-induced Pt roughening."*

* Supplementary Figs. 28 and 29 are presented in the response to Comment 1.

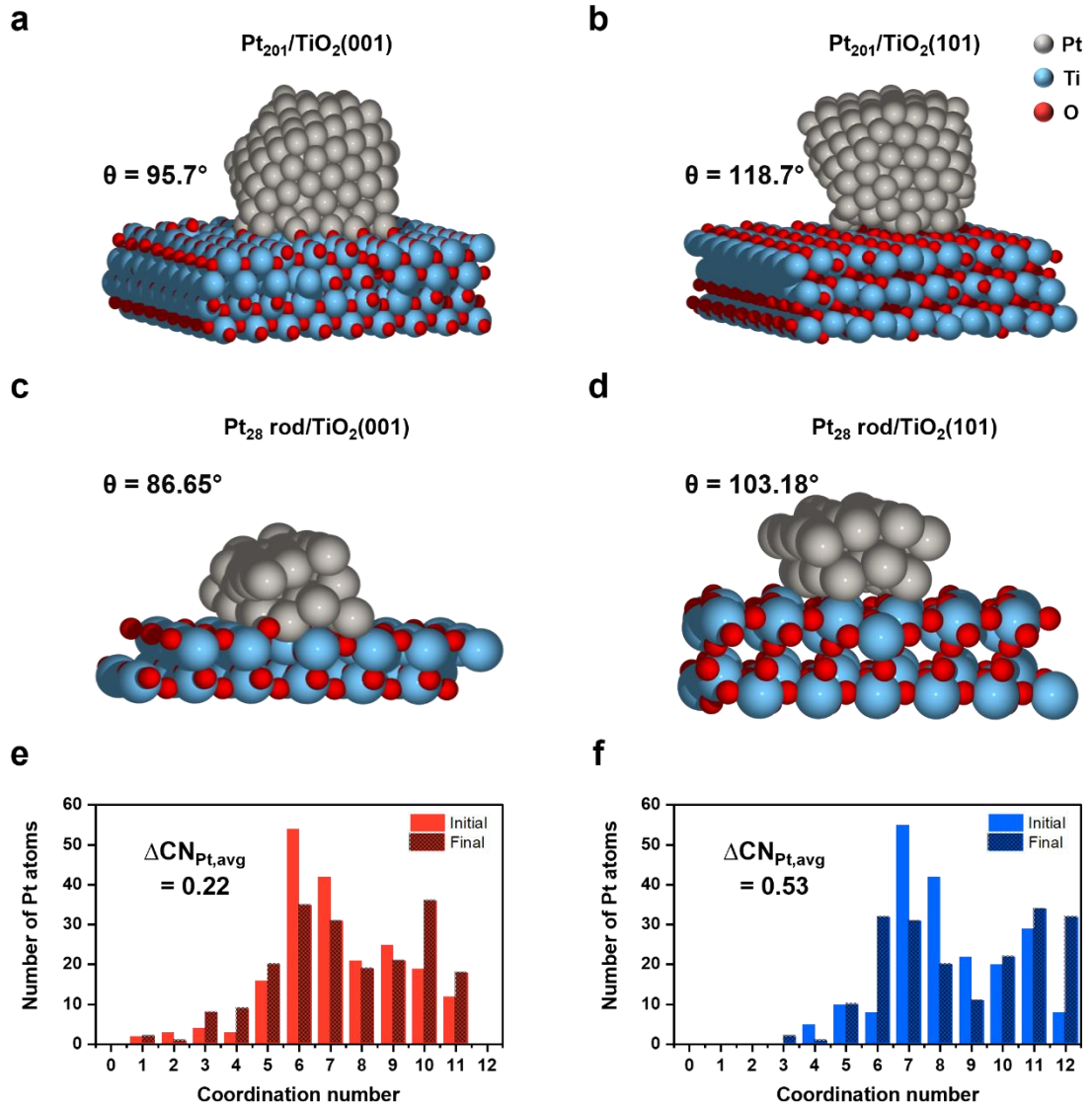

Figure 4. Computational insights into Pt/TiO_2 catalyst morphology with facet-controlled TiO_2 supports. (a, b) Snapshots of Pt_{201} clusters supported on (a) TiO_2(001) and (b) TiO_2(101) after genetic algorithm (GA)-based optimisation. (c, d) DFT-optimised structures of Pt_{28} rod models on (c) TiO_2(001) and (d) TiO_2(101). The values indicated in panels (a–d) correspond to the effective contact angles (θ) of the Pt clusters on TiO_2 surfaces, extracted from the optimised geometries. (e, f) Pt coordination-number (CN) distributions before and after CO-covered GNN-based molecular dynamics simulations at 523 K for 100 ps for GA-optimised (e) Pt_{201}/TiO_2(001) and (f) Pt_{201}/TiO_2(101), indicating facet-dependent CO-induced structural changes (initial: before MD simulation; final: after MD simulation).

Supplementary Table 6. Pt–Pt CN statistics for CO-covered Pt_{201} NPs before and after GNN–MD simulations at 523 K, 100ps.

System	Mean CN	Std. dev.
Initial $Pt_{201}/TiO_2(001)$	8.19	2.04
Final $Pt_{201}/TiO_2(001)$	8.41	2.41
Initial $Pt_{201}/TiO_2(101)$	8.35	1.96

Comment 6: How do the interface interactions between Pt nanoparticles and TiO_2 change under different CO/O_2 ratios? How do these changes affect the reactivity and selectivity of the catalytic reaction, particularly under O_2-rich or CO-rich conditions?

Response: We thank the reviewer for this insightful question regarding how Pt–TiO_2 interface interactions evolve under different CO/O_2 ratios and how these changes influence catalytic behavior.

Since the reaction investigated in this study is CO oxidation and CO_2 is the sole reaction product, we address this question primarily from the perspectives of catalytic activity and reaction mechanism. To more precisely probe the intrinsic catalytic behavior of the Pt–TiO_2 interface, reaction-order analysis of CO oxidation was conducted using post-reaction Pt/TiO_2 catalysts, which preserve the reshaped Pt structures identified by STEM and DRIFTS analyses (Figs. 2 and 3, and Supplementary Figs. 12 and 13).

As shown in Fig. 6e, both catalysts exhibit near-zero reaction orders with respect to CO (n_{CO} = 0.07 for PTS and 0.09 for PTR), whereas the reaction orders with respect to O_2 are substantially higher, particularly for PTR (n_{O2} = 0.20 for PTS and 0.41 for PTR). The negligible CO dependence indicates that the Pt surface is saturated with CO under the examined conditions. In contrast, the fractional dependence on O_2 suggests that the overall reaction rate is governed by lattice oxygen replenishment rather than by O_2 dissociation on Pt sites, in agreement with previous reports (*J. Am. Chem. Soc.* 2017, 139, 14150-14165).

Such kinetic behavior is characteristic of a MvK-type mechanism, in which lattice oxygen

directly participates in CO oxidation. Within this framework, the higher O_2 reaction order observed for PTR implies slower reoxidation kinetics, indicating less efficient oxygen transfer across the Pt–TiO_2 interface. In contrast, PTS exhibits a weaker O_2 dependence, consistent with a more facile oxygen supply from the TiO_2 support, likely enabled by the reconstructed interfacial geometry. This interpretation is well aligned with prior studies on reverse oxygen spillover, in which oxygen migrates from oxide supports to interfacial metal atoms, as well as with mechanistic models proposed for Pt/TiO_2 systems, where oxygen transfer from TiO_2 to interfacial Pt sites on metallic Pt clusters governs the overall reaction rate (*ACS Catal*. 2017, 7, 6493-6513, *J. Am. Chem. Soc.* 2017, 139, 14150-14165).

Taken together, these results indicate that under varying CO/O_2 conditions, both catalysts fundamentally follow an MvK-type mechanism, as evidenced by their similar reaction-order trends. However, the extent of interfacial interaction—particularly oxygen migration to interfacial Pt sites and the resulting atomic-scale fluxional behavior during CO oxidation—differs markedly depending on the exposed TiO_2 facet.

Furthermore, DFT-predicted lower O_v formation energies and a higher O_v abundance on the TiO_2(001) facet, corroborated by O 1*s* XPS analyses (Supplementary Figs. 32 and 35 and Supplementary Note 11), indicate that the (001) facet intrinsically possesses more redox-active properties. When combined with the facet-dependent interfacial geometry revealed by computational simulations (Fig. 4), these findings demonstrate that the synergistic interplay between the intrinsically redox-active TiO_2(001) facet and the reconstructed Pt–TiO_2 interface directly leads to enhanced catalytic activity, by enabling more efficient lattice-oxygen participation under both O_2-rich and CO-rich conditions.

Action taken: In the revised manuscript, We have performed reaction-order analyses of CO oxidation using post-reaction Pt/TiO_2 catalysts, and the corresponding results have been added to the *Reaction mechanism and the origin of superior catalytic activity* section and are presented in Fig. 6e, with the relevant discussion included on Page 13: *"To evaluate the intrinsic catalytic behaviour of the reshaped Pt structures, reaction-order analysis of CO oxidation was performed using post-reaction Pt/TiO_2 catalysts prepared at 240 °C for 2 h. (See Methods) As shown in Fig. 6e, both catalysts exhibit near-zero reaction orders with respect to CO (n_{CO} = 0.07 for PTS and 0.09 for PTR), indicating CO-saturated surfaces. In contrast, the reaction orders with respect to O_2 are substantially larger (n_{O2} = 0.20 for PTS and 0.41 for PTR), and this fractional O_2 dependence suggests that lattice oxygen replenishment governs*

the overall rate, in accordance with a MvK-type mechanism.[68] Within this framework, the higher O_2 dependence of PTR reflects slower reoxidation kinetics and less efficient oxygen transfer across the Pt–TiO_2(101) interface, whereas the weaker O_2 dependence of PTS indicates a more facile supply of lattice oxygen from TiO_2(001) to interfacial Pt sites enabled by the reconstructed interface geometry. This interpretation is consistent with reports of reverse oxygen spillover, in which lattice oxygen migrates from oxide supports to interfacial metal atoms,[14] and aligns with mechanistic studies identifying oxygen transfer to interfacial Pt sites as rate-limiting in Pt/TiO_2 systems.[68] These kinetic trends, together with structural observations and DFT-predicted energetics of O_v formation and oxygen replenishment, highlight the central role of facet-dependent interfacial restructuring in determining catalytic activity."

We also have added the results of O 1*s* XPS measurements acquired under UHV conditions to the *Reaction mechanism and the origin of superior catalytic activity* section to explicitly evaluate the intrinsic O_v characteristics of TiO_2 facets, while the existing O_2-TPD and EPR results are summarized. These data are now presented in Supplementary Fig. 35, and the following paragraph has been revised on Page 13: "*Beyond the theoretical and kinetic insights into facet-dependent Pt reconstruction and catalytic activity, the intrinsic redox properties of TiO_2 facets were examined, focusing on O_v abundance and reactive oxygen species relevant to interfacial redox behaviour (Supplementary Note 11). O 1s XPS analyses under UHV conditions (Supplementary Figs. 35a,b) show that pristine TiO_2(001) and PTS exhibit O_{ads}/O_{latt} ratios—as a descriptor of O_v abundance—that are 1.76 and 1.95 times higher, respectively, than those of their TiO_2(101) counterparts. Consistently, O_2-TPD and EPR analyses (Supplementary Figs. 36 and 37 and Supplementary Note 11) reveal a higher population of reactive oxygen species on the (001) facet, which is further enhanced at the Pt–TiO_2(001) interface, consistent with its intrinsically higher O_v abundance.*"

To further clarify the role of O_v and to emphasize the synergistic interplay between the redox-active TiO_2(001) support and the reconstructed Pt interface in determining the enhanced catalytic activity, we have expanded the corresponding discussion on Page 14: *"Overall, these spectroscopic results indicate that the TiO_2(001) facet provides more efficient oxygen reservoir at the Pt–TiO_2 interface under reaction conditions, owing to its higher intrinsic O_v abundance and more reactive oxygen species. Consistently, O 1s XPS analyses under reaction environments (Supplementary Figs. 35c, d and Supplementary Note 11) show that PTS exhibits a pronounced decrease in the O_{ads}/O_{lat} ratio with increasing temperature (from 0.56 to 0.38),*

whereas PTR shows only a marginal change. This behaviour suggests that oxygen species associated with O_v sites on TiO_2(001) are more efficiently consumed and replenished at the Pt–TiO_2(001) interface, facilitating oxygen transfer to interfacial Pt sites and thereby supporting the enhanced catalytic activity observed for PTS."

* Fig. 6e is provided in the response to Comment 4.

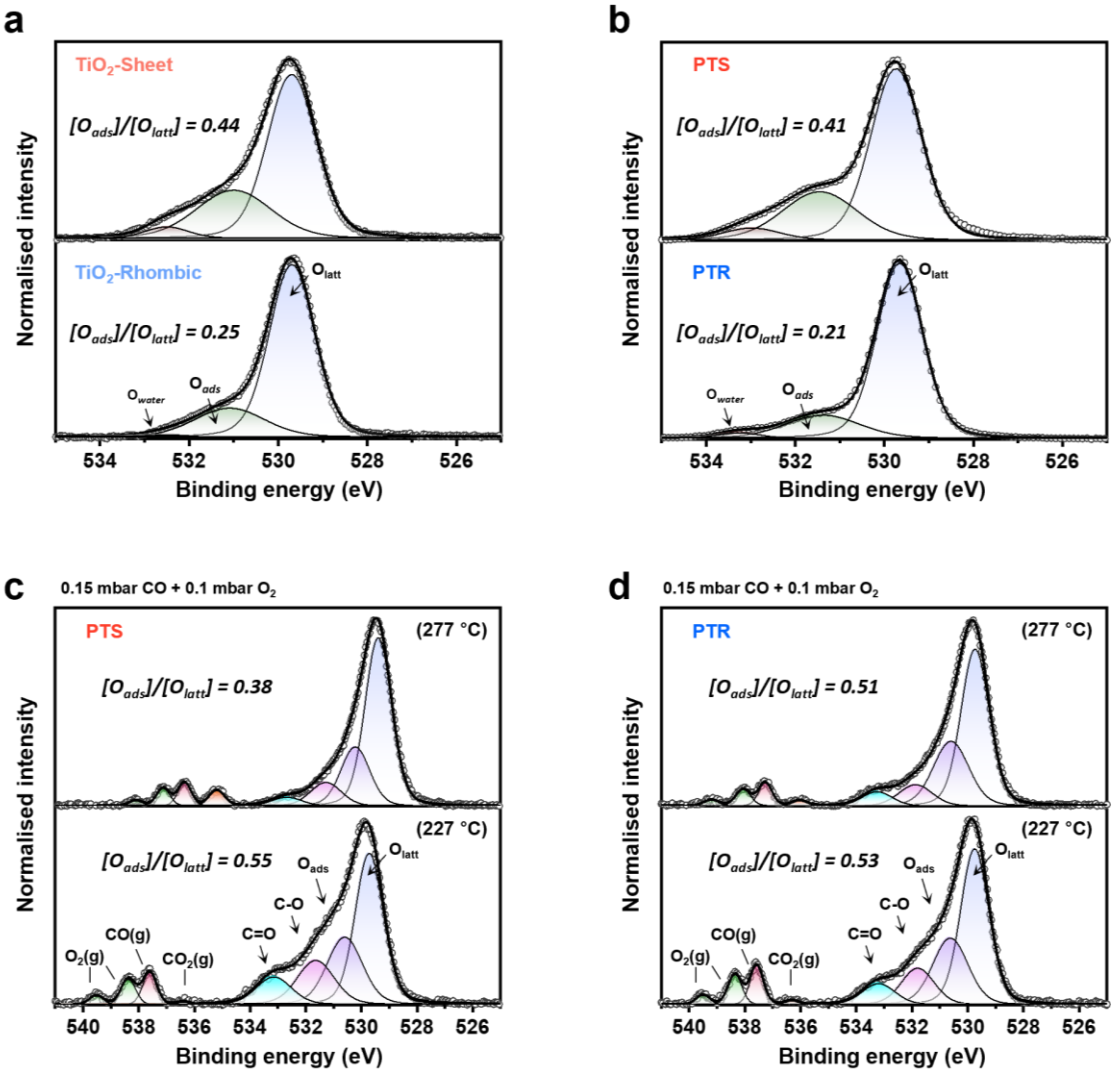

Supplementary Figure 35. Normalised O 1*s* XPS spectra of (a) pristine TiO_2 and (b) Pt/TiO_2 catalysts measured under UHV conditions, and of (c) PTS and (d) PTR catalysts measured under CO oxidation conditions (0.15 mbar CO and 0.1 mbar O_2) at 227 and 277 °C.

Comment 7: The differences in Pt binding strength on TiO_2(001) and (101) facets were discussed, but further clarification is needed. How do these differences in binding influence the morphological stability and catalytic performance of Pt nanoparticles? How does stronger Pt binding on TiO_2(001) contribute to enhanced catalytic activity?

Response: The reviewer raises an important question regarding how the facet-dependent differences in Pt binding strength on TiO_2(001) and TiO_2(101) influence both the morphological stability and the catalytic performance of Pt NPs. In CO oxidation over Pt/TiO_2 under conditions where the MvK mechanism is operative, catalytic activity is governed not only by the intrinsic properties of Pt sites, but also by how efficiently lattice oxygen can be supplied from the oxide support and replenished through redox cycling at the metal-support perimeter.

In our system, stronger Pt binding on TiO_2(001), as evidenced by a smaller contact of 86.65° on TiO_2(001) and 103.18° on TiO_2(101) and higher adhesion energy, stabilizes a wetted Pt morphology with an enlarged and robust metal–support contact area. Consistently, the geometric contact area estimated from the morphology analysis is larger for Pt_{28}/TiO_2(001) (103.2 $Å^2$) than for Pt_{28}/TiO_2(101) (70.4 $Å^2$), indicating substantially enhanced wetting and metal-support contact on the (001) facet. This enhanced wetting improves morphological stability by anchoring the NP more strongly to the support and increases the length and stability of the metal–support perimeter. Because lattice oxygen transfer and vacancy-mediated redox cycling are most likely to occur at or near this perimeter, a larger and more stable perimeter directly promotes sustained MvK turnover under reaction conditions, consistent with recent reports (*Nat. Commun.* 2024, 15, 8293) highlighting the critical role of metal–oxide perimeter sites in CO oxidation on reducible oxides. In contrast, weaker Pt binding on TiO_2(101) leads to a less wetted morphology with a reduced effective perimeter, limiting the extent of support-mediated oxygen participation.

At the same time, stronger global MSI does not imply stronger local oxide bonding at the perimeter. Our site-resolved ICOHP analysis shows that the metal–oxygen bonds associated with oxygen vacancy formation at the Pt/TiO_2(001) perimeter exhibit reduced integrated bonding strength compared to those on TiO_2(101). Lower -ICOHP values indicate increased antibonding occupation and weaker local metal–oxygen bonding, which facilitates oxygen vacancy formation and lattice oxygen participation in the MvK pathway. This apparent coexistence of strong Pt adhesion and weakened local metal–oxygen bonding is physically

reasonable, as MSI can redistribute charge density and orbital hybridization at specific perimeter oxygen sites, stabilizing Pt anchoring while simultaneously lowering the energetic cost of oxygen removal, as has been previously demonstrated (*J. Am. Chem. Soc.* 2013, 135, 906-909) for metal–oxide interfaces where oxide reducibility is strongly modified by interfacial electronic interactions.

Taken together, stronger Pt binding on TiO_2(001) enhances morphological stability by maintaining a wetted NP with an extended and stable perimeter, while simultaneously promoting lattice oxygen activation through locally weakened metal–oxygen bonding at that perimeter. This coupled effect provides a chemically grounded explanation for the superior CO oxidation activity observed on Pt/TiO_2(001) compared to Pt/TiO_2(101).

Action taken: In the revised manuscript, we expanded the *Results and Discussion* section to explicitly clarify how facet-dependent Pt binding strength governs NP wetting, perimeter stability, and lattice oxygen reactivity, and corresponding data are presented in Supplementary Table 5 and Supplementary Fig. 26.

The following paragraph have also added to the *Reaction mechanism and the origin of superior catalytic activity* section on Page 10: *"Quantitative analysis confirms that the DFT-level adhesion energy is more favorable on TiO_2(001) (−0.86 eV per Pt atom) than on TiO_2(101) (−0.80 eV), in line with stronger MSI on the high-energy (001) facet along with the normalised Pt binding energy shown in Supplementary Table 5. The effective contact angle similarly reflects enhanced wetting, with θ = 86.7° on TiO_2(001) versus 103.2° on TiO_2(101) (Supplementary Fig. 26)."*

Also, we further revised the discussion of ICOHP to emphasize its site-specific relevance to metal–oxygen bond weakening and oxygen vacancy formation at the metal–support perimeter, thereby resolving the apparent discrepancy between stronger Pt binding and enhanced oxide reducibility on TiO_2(001). The following paragraph has been added on Page 12: *"The summed -ICOHP values for the target oxygen, accounting for both Pt–O and Ti–O bonds, are lower on TiO_2(001) (4.15) than on TiO_2(101) (5.13), indicating weaker oxygen bonding at the Pt_{28}/TiO_2(001) interface (Fig. 6b). This weakening is further supported by the broader and flatter geometry of the Pt_{28} cluster on TiO_2(001), which increases perimeter contact and yields a larger population of oxygen atoms directly coordinated to Pt. Such interfacial motifs are preferentially involved in lattice oxygen activation during redox catalysis, consistent with*

previous studies highlighting the role of metal–support interfacial sites. In the present system, this beneficial configuration arises naturally from facet-induced reconstruction on TiO_2(001), which expands the metal-support interface and weakens specific oxygen bonds."

Supplementary Table 5. Surface energies of TiO_2(001) and (101) facets and the corresponding normalised Pt binding energies (per Pt atom) in the DFT-optimized Pt_{28} rod on TiO_2 models.

	Pt_{28}/TiO_2(001)	Pt_{28}/TiO_2(101)
Surface energy [eV·Å^{-2}]	0.084	0.067
Normalized Pt binding E [eV·atom^{-1}]	−0.78	−0.68
Normalized Adhesion E [eV·atom^{-1}]	−0.86	−0.80
Interfacial area of Pt–TiO_2 [Å^2]	103.2	70.4
Surface area normalised Adhesion E [eV·Å^{-2}]	−0.233	−0.316

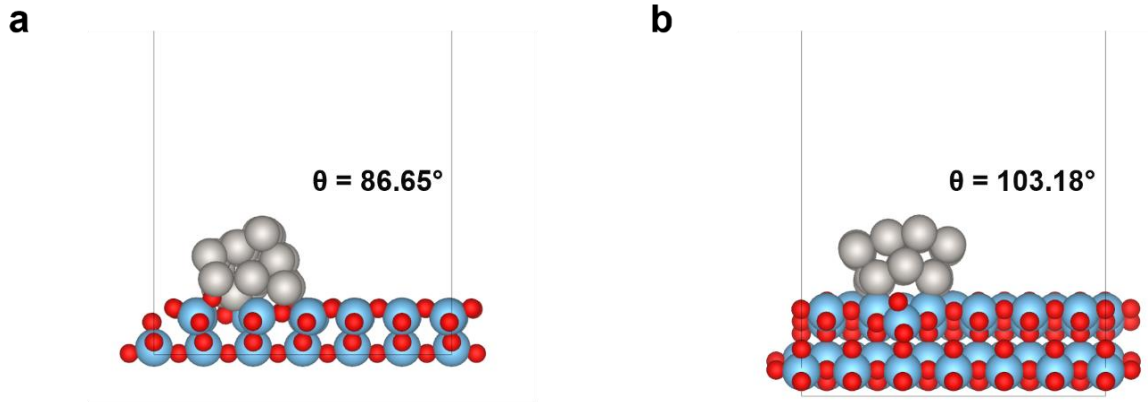

Supplementary Figure 26. Side-view representations of DFT-optimized models: (a) Pt_{28} rod on TiO_2(001) facet and (b) Pt_{28} rod on TiO_2(101) facet.

Comment 8: How do the redox properties of TiO_2(001) and (101) facets differ, and how do these differences impact the activation of reactive oxygen species and lattice oxygen in the MvK pathway? How do these factors contribute to the superior catalytic performance of Pt/TiO_2(001) compared to Pt/TiO_2(101)?

Response: We sincerely thank the reviewer for this insightful question regarding the facet-dependent redox properties of TiO_2 and their impact on reactive oxygen activation and lattice oxygen participation in the MvK pathway. This point is central to distinguishing the contribution of the TiO_2 support from metal-induced effects.

Action taken: To directly address this comment, we systematically evaluated the redox properties of anatase TiO_2(001) and TiO_2(101) facets by calculating oxygen vacancy formation energies at multiple representative surface oxygen sites. The calculated vacancy formation energies are now summarized in Supplementary Fig. 32. Across all examined sites, TiO_2(001) consistently exhibits significantly lower oxygen vacancy formation energies than TiO_2(101), indicating a higher intrinsic reducibility of the (001) facet. This trend persists across multiple oxygen coordination environments, demonstrating that the enhanced reducibility of TiO_2(001) is a robust facet property rather than a site-specific anomaly.

Lower oxygen vacancy formation energies directly facilitate lattice oxygen participation in the MvK pathway by lowering the energetic barrier for oxygen removal and enabling faster vacancy generation under reaction conditions. In addition, facile vacancy formation promotes molecular O_2 activation during vacancy healing, as reduced oxide surfaces can more readily transfer electrons to O_2 to form reactive oxygen species, thereby sustaining rapid redox cycling.

These computational findings are consistent with experimental Raman spectroscopy results (Supplementary Figs. 3c, d), which reveal clear differences in oxygen coordination environments between TiO_2(001) and TiO_2(101). The Raman features associated with Ti–O bonding and lattice distortion indicate a higher population of undercoordinated or distorted oxygen species on TiO_2(001), in line with its lower vacancy formation energies and enhanced redox flexibility.

Importantly, the intrinsic facet-dependent redox properties of TiO_2 are also reflected in catalytic measurements performed on TiO_2 supports in the absence of Pt. As shown in Supplementary Fig. 4c, TiO_2(001) exhibits a higher CO oxidation conversion than TiO_2(101) even without metal loading. This observation confirms that the enhanced reactivity of Pt/TiO_2(001) does not

arise solely from metal-induced effects, but is rooted in the inherently higher redox activity of the TiO_2(001) support itself.

Taken together, these results demonstrate that anatase TiO_2(001) possesses intrinsically more favorable redox properties than TiO_2(101), as reflected by its lower oxygen vacancy formation energies, enhanced ability to activate reactive oxygen species, and more efficient lattice oxygen participation in the MvK pathway. However, these intrinsic properties alone are not sufficient to fully account for the observed catalytic performance.

The catalytic enhancement emerges most effectively when the redox-active TiO_2(001) facet is coupled with Pt NPs through a SMSI. The Pt–TiO_2 interface provides the necessary reaction perimeter where lattice oxygen from the support can directly participate in CO oxidation and where vacancies can be rapidly regenerated through O_2 activation. In this sense, TiO_2(001) defines the redox propensity of the system, while Pt NPs and their interfacial contact with the support enable efficient utilization of this redox potential under reaction conditions.

Therefore, the superior performance of Pt/TiO_2(001) arises from a synergistic interplay between the intrinsically higher reducibility of the TiO_2(001) facet and the strong Pt–TiO_2 interaction, which together promote sustained lattice oxygen turnover and high catalytic activity.

Action taken: To address the reviewer's comment, two clarifying statements regarding the intrinsic facet effects of TiO_2 have been added to the revised manuscript on page 12.

First, the intrinsic reducibility of different TiO_2 facets is explicitly discussed by referencing the previously reported oxygen vacancy formation energy calculations.

"This facet-intrinsic difference in reducibility is further supported by calculated O_v formation energies across multiple surface sites (Supplementary Fig. 32), confirming the greater intrinsic oxygen mobility of (001) facet."

Second, we clarify that enhanced adhesion on specific facets increases the metal–support contact sites and weakens specific interfacial bonds, thereby conferring a kinetic advantage during the reaction.

"In the present system, this beneficial configuration arises naturally from facet-induced reconstruction on TiO_2(001), which expands the metal-support interface and weakens specific oxygen bonds."

Reviewer #2

General comments: Kim et al. performed a comprehensive study to investigate the TiO_2-facet sensitivity of Pt NP shapes during CO oxidation. A couple of advanced characterization and methods and theoretical simulations were applied to show the PTS exhibits significantly higher activity for CO oxidation than PTR owing to the facile generation of oxygen vacancies at TiO2(001) facets, which is beneficial for MvK reaction mechanism. This work is well performed in experimental and theoretical techniques, however, some critical information is missing. Thus, I cannot recommend the publication of this manuscript in the present form.

Response: We thank Reviewer #2 for the constructive and thoughtful assessment of our work. We appreciate the reviewer's concerns regarding the consistency between theoretical models and experimental observations, as well as the mechanistic interpretation of reconstruction and metal-support interaction effects.

In response, we substantially revised the manuscript to clarify the scope and role of each computational approach and to improve consistency with experimental evidence. In particular, we refined our modeling strategy by clearly separating equilibrium morphology determination from reaction-driven structural dynamics, and by strengthening the connection between reconstructed structures and catalytic function. These revisions improve the physical interpretation of the theoretical results and place them in closer alignment with the experimental observations.

We believe that these changes significantly enhance the clarity, rigor, and overall quality of the manuscript. Detailed responses to the reviewer's specific comments are provided below.

Comment 1: The authors used same Pt_{201} faceted NP as the model to perform the GNN–MD simulations on TiO_2(001) and TiO_2(101). A larger MSD of PTS than MSD of PTR is observed and used to explain the larger reconstruction of Pt NPs on TiO_2(001). However, the theoretical models are not consistent with the experimental observations that the fresh Pt NPs on TiO_2(001) adopts hemispherical morphology (Fig. 1b) and Pt NPs on TiO_2(101) adopts faceted morphology (Fig. 1d). Moreover, this model is not similar as the morphology of spent catalyst as shown in Fig. 2j. Thus, the GNN–MD simulation in this work is meaningless.

Response: We thank the reviewer for raising this important concern regarding the apparent inconsistency between the theoretical models and experimentally observed Pt NP morphologies on TiO_2(001) and TiO_2(101). We agree that the original GNN–MD simulations, which

employed an identical Pt_{201} cluster on both facets, were not intended to reproduce equilibrium NP morphologies observed for fresh or spent catalysts.

This limitation arises from the intrinsic nature of MD, which probes short-time atomic mobility rather than global energetic minimization. While MD is well suited to assess facet-dependent reconstruction tendencies, it is not an appropriate tool for determining equilibrium morphology, which is governed by long-time thermodynamics.

Based on this recognition, we revised our computational strategy by clearly separating equilibrium morphology determination from reconstruction kinetics. Facet-dependent equilibrium morphologies are now obtained using a genetic algorithm-based global optimization approach, while GNN–MD simulations are retained to probe relative atomic mobility and roughening tendencies near the metal-support contact region.

This conceptual separation resolves the reviewer's concern and allows each computational method to be applied within a physically appropriate scope, thereby improving consistency between experiment and theory.

Action taken: In the original manuscript, GNN-based MD simulations were performed at 523 K to probe the structural response of Pt_{201} NPs on $TiO_2(001)$ and $TiO_2(101)$. Under these conditions, the overall Pt NP morphology remained largely preserved on both facets, and only subtle differences in atomic mobility were observed. While these simulations were useful for comparing relative reconstruction tendencies under identical thermal conditions, we acknowledge that they did not reproduce the experimentally observed hemispherical morphology on $TiO_2(001)$ or the more faceted morphology on $TiO_2(101)$.

Following the concern raised by Reviewer 1, we explicitly tested whether more aggressive MD conditions could bridge this gap. Additional GNN–MD simulations were therefore performed at an elevated temperature of 1500 K for approximately 0.8 ns (Supplementary Fig. 24). Under these harsh conditions, the Pt NP on $TiO_2(001)$ indeed evolved toward a geometry that was visibly closer to the support and qualitatively more similar to the experimentally observed hemispherical morphology (Supplementary Fig. 24a). However, this apparent improvement was accompanied by substantial and simultaneous structural changes in the TiO_2 support itself. As a result, the final morphology reflected a convolution of accelerated Pt mobility and support deformation, making it difficult to isolate intrinsic facet-dependent effects in a physically meaningful and comparable manner between $TiO_2(001)$ and $TiO_2(101)$ (Supplementary Figs.

24c, d). Based on this observation, we concluded that MD simulations, even when performed under extreme conditions, are not an appropriate tool for determining equilibrium Pt NP morphologies on TiO_2 facets.

To address this limitation, we revised our computational strategy and explicitly separated the problem of equilibrium morphology determination from that of reconstruction dynamics. The equilibrium morphology of Pt NPs on different TiO_2 facets was determined using a genetic-algorithm-based global optimization approach, in which the Pt_{201} morphology emerges from global energetic minimization on each facet without imposing a predefined initial shape. Using this approach, Pt_{201} on $TiO_2(001)$ relaxed into a strongly wetted, hemispherical-like geometry, whereas Pt_{201} on $TiO_2(101)$ retained weakly wetted and faceted morphology, in direct agreement with experimental observations. Top view (Supplementary Figs. 21a, b) and side view (Supplementary Figs. 21c, d) of these different morphologies are shown along with the evolution of total energies during the genetic algorithm optimization (Supplementary Figs. 21e, f). Consistent with the stronger interaction with the TiO_2 surface, $Pt_{28}/TiO_2(001)$ showed pronounced Pt–O and Pt–Ti bonds in radial distribution functions (Supplementary Fig. 22).

To quantitatively compare these facet-dependent morphologies, we introduced voxel-based contact area and contact angle descriptors. The contact area was evaluated from the projected footprint of the Pt NP on the TiO_2 surface using a voxelized representation of the Pt–support contact region, and the contact angle θ was estimated using a spherical-cap approximation,

$$\cos\theta = \frac{R^2 - h^2}{R^2 + h^2}$$

where h is the height of the Pt NP measured from the support surface reference plane, and R is the effective footprint radius of the Pt NP at the metal–support interface.

For the GA-optimized Pt_{201} models, this analysis confirms stronger wetting on $TiO_2(001)$ than on $TiO_2(101)$, as quantified by effective contact angles of 95.74° and 118.66°, respectively. These quantitative descriptors provide a physically transparent measure of facet-dependent wetting behavior that is directly consistent with the experimentally observed hemispherical morphology on $TiO_2(001)$ and the more faceted morphology on $TiO_2(101)$.

Importantly, establishing such morphology descriptors at the NP scale enables a direct connection to reaction-scale DFT models, which necessarily employ reduced structural

representations. To test whether the facet-dependent wetting trends identified at the NP level persist at the reaction-model scale, we evaluated the same contact angle descriptor for our DFT Pt_{28} rod models on $TiO_2(001)$ and $TiO_2(101)$.

Using an identical geometric definition adapted to the rod geometry, the DFT models yield contact angles of 86.65° on $TiO_2(001)$ and 103.18° on $TiO_2(101)$, reproducing the same facet-dependent wetting trend observed for the GA-optimized Pt_{201} NPs. While the absolute values differ due to the distinct geometry and length scale of the rod models, the consistent ordering across models confirms that the facet-dependent wetting behavior is robust and transferable.

Finally, the role of GNN–MD simulations was redefined in the revised manuscript. Rather than being used to generate equilibrium morphologies, GNN–MD is now employed to probe relative facet-dependent reconstruction and roughening tendencies under identical initial geometries and simulation protocols. The main-text morphology discussion and figures have been replaced by GA-derived structures and quantitative wetting descriptors (Supplementary Note 5 and Supplementary Figure 21, 22), while the MD-based analyses are relocated and explicitly framed as kinetic indicators rather than morphology predictors (Supplementary Note 6 Supplementary Figure 24). This revision directly resolves the reviewer's concern and ensures consistency between theoretical models and experimental observations.

Accordingly, following paragraph has been added the *Computational insights into facet-dependent Pt reconstructions on TiO_2* section on Page 9: *"To simulate experimentally relevant (~1.8 nm) Pt NPs, we optimised Pt_{201} on anatase TiO_2 facets using genetic algorithm (GA) optimisation to identify facet-specific equilibrium morphologies (Supplementary Note 5). The GA-optimised results revealed a pronounced facet dependence: on anatase $TiO_2(001)$, the Pt_{201} cluster spread into a strongly wetted, hemispherical-like morphology, while on $TiO_2(101)$ it adopted a more compact, faceted shape (Supplementary Fig. 21). We introduced geometric descriptors to quantitatively evaluate the facet-dependent differences in Pt–TiO_2 adhesion. The $Pt_{201}/TiO_2(001)$ showed pronounced Pt–O and Pt–Ti bonds in radial distribution functions (RDFs) compared to $Pt_{201}/TiO_2(101)$ (Supplementary Fig. 22). We further computed the interfacial contact area and an effective contact angle (θ) based on a spherical-cap approximation using the Young-Dupré relation to quantify NP wetting behaviour.[59] The results show a markedly stronger wetting behaviour of Pt on $TiO_2(001)$ than on $TiO_2(101)$: the effective contact angle is reduced to ~95.7° on $TiO_2(001)$ (Fig. 4a), compared to ~118.7° on $TiO_2(101)$ (Fig. 4b), indicating enhanced lateral spreading of the NP on the higher-energy (001) surface.*

These trends are consistent with experimentally observed particle shapes and quantify facet-dependent MSI strength.

We also performed GNN-based molecular dynamics (MD) simulations at 523 K using identical initial Pt_{201} Wulff-construction-based clusters supported on $TiO_2(001)$ and $TiO_2(101)$ (Supplementary Note 6), to assess the dynamic accessibility of these morphologies under thermal excitation relevant to experimental synthesis. The Pt cluster on $TiO_2(001)$ exhibited significantly greater atomic mobility and interfacial disorder than on $TiO_2(101)$, as reflected by a larger mean squared displacement (MSD) and broader Pt–Pt RDF (FWHM = 0.304 Å on (001) vs. 0.160 Å on (101) (Supplementary Fig. 23)). These results indicate that Pt on $TiO_2(001)$ is more fluxional and susceptible to thermal restructuring."

In addition, relevant discussions are provided in Supplementary Note 5 and 6:

*"**Supplementary Note 5. Genetic Algorithm-Based Structure Search for Pt_{201}/TiO_2** A genetic algorithm (GA) was employed to identify the most stable configurations of Pt_{201} clusters supported on TiO_2 surfaces. The GA search was performed using the Atomic Simulation Environment (ASE), in which candidate structures were generated, evolved, and evaluated through iterative cycles combined with local structural relaxation using the LBFGS algorithm. Initial Pt_{201} cluster candidates were randomly generated above the TiO_2 surface within a predefined three-dimensional region, allowing unbiased sampling of cluster positions and orientations while avoiding unphysical overlap with the support. Minimum interatomic distance constraints based on covalent radii were applied during candidate generation to ensure physically reasonable Pt–Pt, Pt–O, and Pt–Ti separations.*

To mimic bulk-like behavior of the oxide support, the bottom two atomic layers of the TiO_2 slab were fixed throughout the GA search and subsequent structural relaxation, while all Pt atoms and surface TiO_2 atoms were fully relaxed. The GA was executed with a population size of 20 over 20 generations. New candidate structures were generated using cut-and-splice crossover operations combined with stochastic mutation operations, including mirror and rattle moves, applied with a probability of 0.3. Each candidate structure was locally optimized using the LBFGS algorithm with a force convergence criterion of 0.05 $eV \cdot Å^{-1}$ and a maximum of 200 optimization steps. The relaxed total energy was used as the fitness score for selection and population update. During the GA evolution, slightly relaxed distance criteria were adopted for Pt–Pt pairs to allow sufficient structural flexibility of the Pt cluster while maintaining

chemically reasonable bonding environments.

The fitness of each candidate was evaluated based on its total energy after relaxation, and lower-energy structures were preferentially retained in the population for subsequent generations. The GA search was continued until no further improvement in the lowest-energy structures was observed. The final optimized structures reported in this work correspond to the lowest-energy configurations obtained from the GA search for each TiO_2 facet.

The GA workflow was designed to ensure robust convergence of the structure search rather than to impose specific structural motifs. Distance constraints and generation limits were introduced solely to prevent unphysical configurations and numerical instabilities during candidate generation. Importantly, all reported Pt_{201}/TiO_2 structures were fully optimized without constraints on Pt atoms, ensuring that the final geometries reflect intrinsic energetic preferences rather than algorithm-induced bias."

*"**Supplementary Note 6. Construction of Pt_{201}/TiO_2 Models for GNN-MD Simulations** Pt_{201} NPs were generated using an ASE-based Wulff construction and placed on TiO_2 slab models constructed with facet-dependent supercells. For anatase $TiO_2(001)$ and $TiO_2(101)$, stoichiometric slabs were used without introducing oxygen vacancies, and Pt_{201} was positioned above the surface following the same placement protocol prior to relaxation. For each slab model, the Pt_{201} NP was first translated such that its geometric center in the xy plane coincided with the center of the slab surface, while the lowest Pt atom was aligned above the topmost surface layer. The initial vertical separation between the NP and the slab was determined based on the sum of the covalent radii of the surface TiO_2 atoms and the lowest-coordinated Pt atoms, followed by a small additional downward displacement to ensure interfacial contact without unphysical overlap.*

To sample different interfacial registries, the Pt_{201} NP was rotated around the surface normal (z axis) in increments of 15°, corresponding to a total of 24 distinct rotational configurations spanning a full 360° rotation. For each rotational orientation, the NP–slab composite structure was generated using the same placement protocol and subsequently subjected to structural relaxation. The total energies of the relaxed configurations were compared, and the lowest-energy structure among the rotational ensemble was selected as the most stable initial configuration for subsequent GNN–MD simulations. All initial structures were subsequently relaxed and used as starting configurations for GNN–MD simulations under identical

thermostat and ensemble settings"

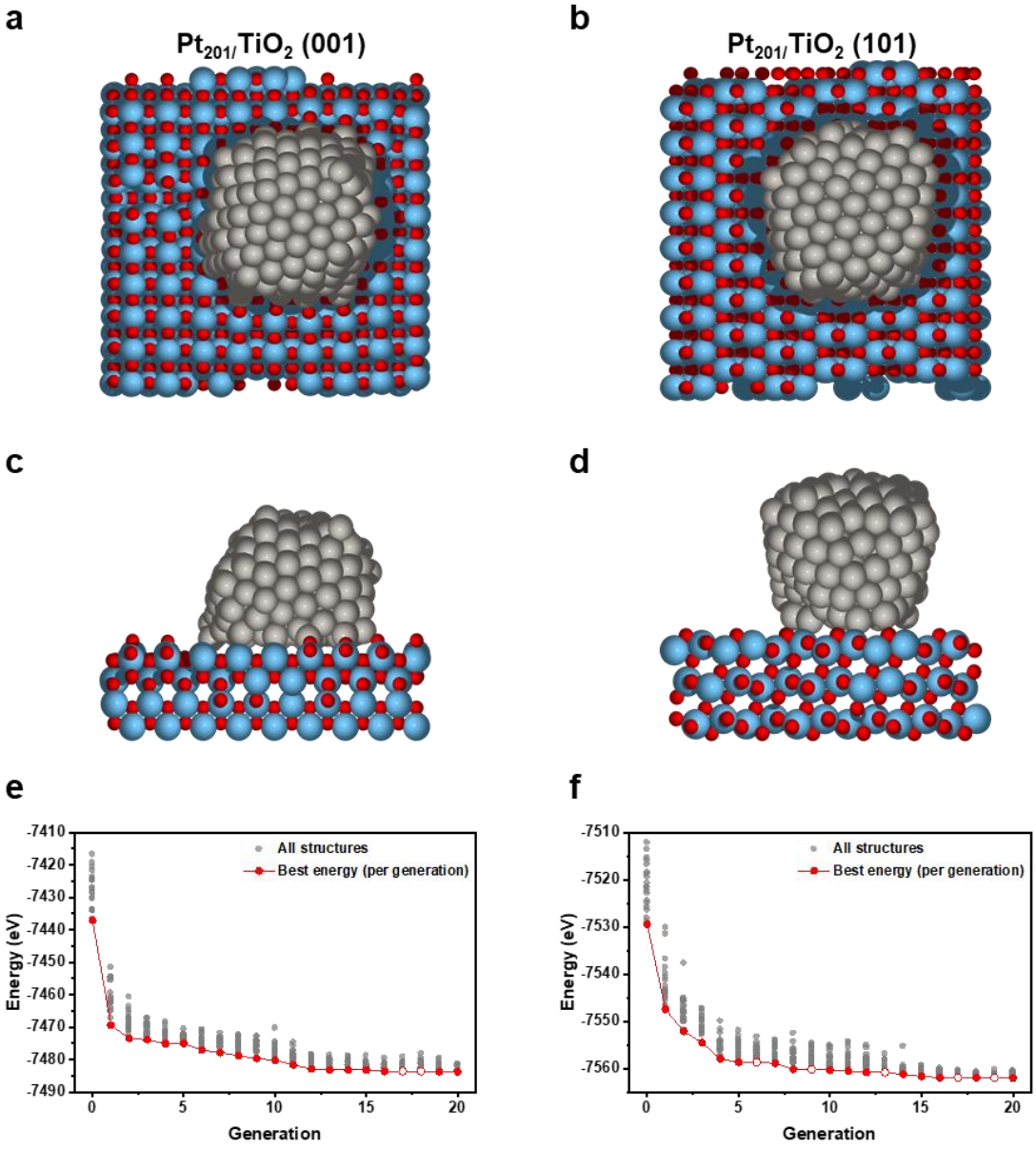

Supplementary Figure 21. Facet-dependent equilibrium morphology of Pt_{201} NPs on TiO_2 obtained by GA optimization. Top views of the lowest-energy Pt_{201} NP configurations supported on (a) $TiO_2(001)$ and (b) $TiO_2(101)$, and the corresponding side views shown in (c) and (d), illustrating facet-dependent wetting and metal–support contact geometry. The evolution of total energies during the genetic algorithm optimization is shown for (e) $Pt_{201}/TiO_2(001)$ and (f) $Pt_{201}/TiO_2(101)$. Grey dots represent the energies of all candidate structures sampled in each generation, while the red line denotes the lowest-energy structure per generation. Filled red circles indicate generations where a new global minimum energy was identified, whereas open red circles indicate generations in which the global minimum remained unchanged.

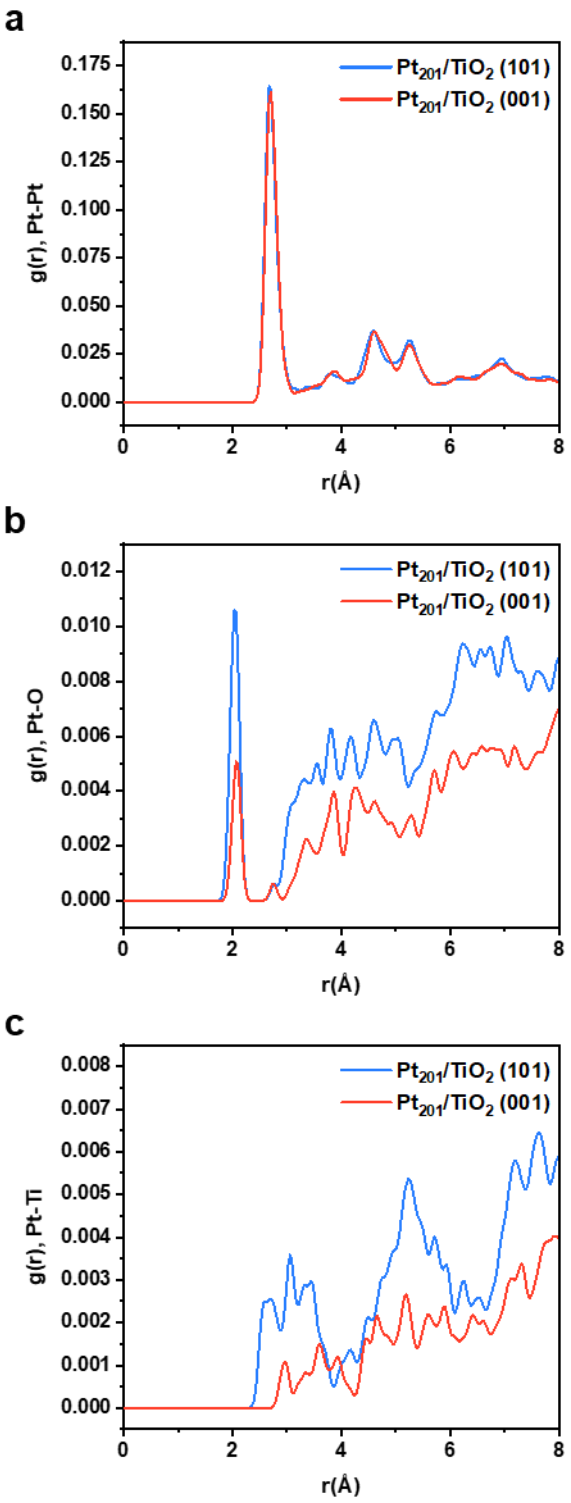

Supplementary Figure 22. Radial distribution functions $g(r)$ for (a) Pt–Pt, (b) Pt–O, and (c) Pt–Ti atomic species obtained from genetic algorithm optimization of Pt_{201}/TiO_2 species. Red: $Pt_{201}/TiO_2(001)$ and Blue: $Pt_{201}/TiO_2(001)$.

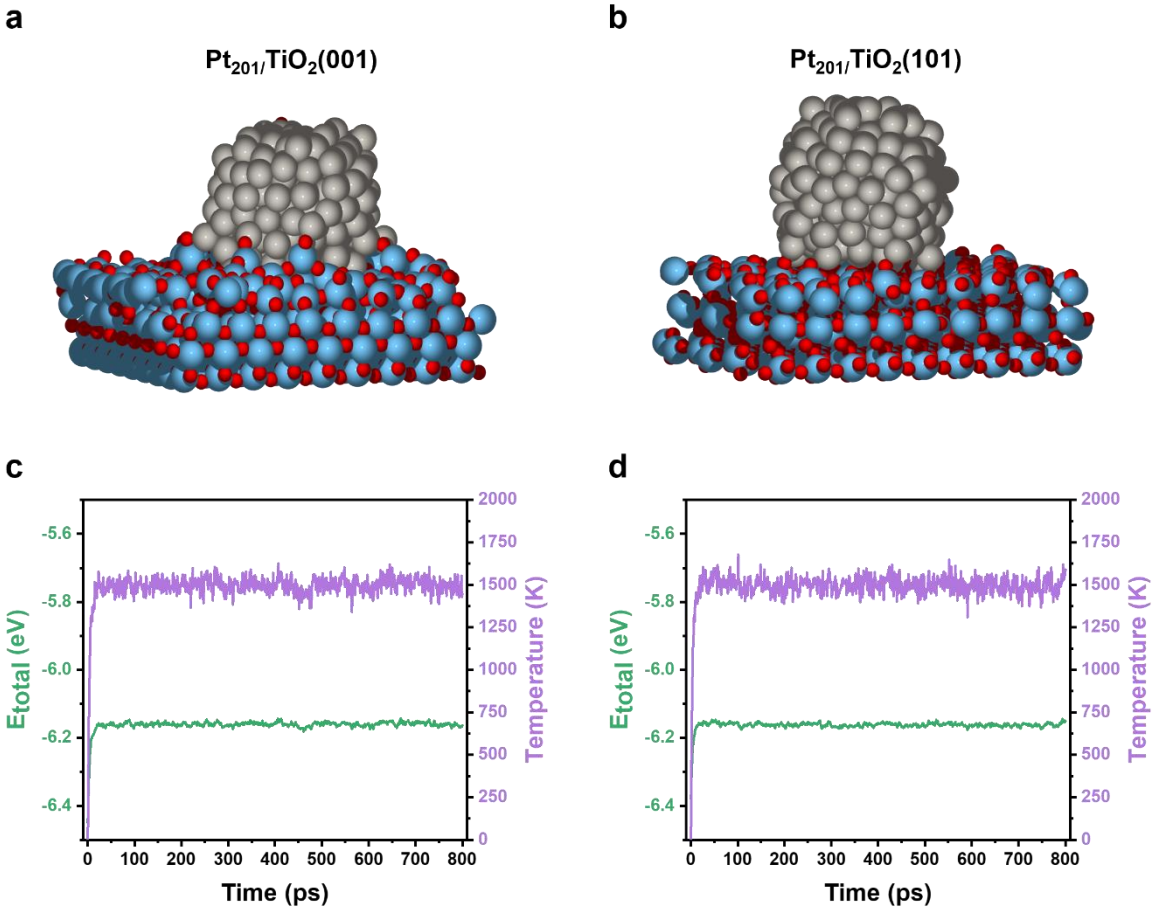

Supplementary Figure 24. Thermal convergence and facet-dependent structural evolution of Pt_{201} NPs on TiO_2 revealed by GNN–MD simulations under extreme conditions. Final snapshots after the simulations at 1500 K for 0.8 ns for (a) $Pt_{201}/TiO_2(001)$ and (b) $Pt_{201}/TiO_2(101)$, with time evolution of total energy and temperature confirming stable thermal equilibration during simulations for (c) $Pt_{201}/TiO_2(001)$ and (d) $Pt_{201}/TiO_2(101)$.

Accordingly, the following reference 59 was added to the revised manuscript.

59. Wang, T. et al. Nature of metal-support interaction for metal catalysts on oxide supports. *Science* **386**, 915-920 (2024).

Comment 2: The experiments showed the faceting process occurs during the CO oxidation. Please elucidate the reconstruction mechanism of Pt NP during CO oxidation.

Response: We sincerely thank the reviewer for this insightful comment regarding the reconstruction and faceting mechanism of Pt NPs during CO oxidation. We fully agree that understanding the atomic-scale origin of Pt NP reconstruction is essential for correctly interpreting the experimentally observed faceting behavior.

CO-induced reconstruction of Pt NPs under CO oxidation conditions has been extensively investigated in prior experimental and theoretical studies (*ACS Catal*. 2020, 10, 5, 3183-3193, *J. Am. Chem. Soc*. 2017, 139, 12, 4551-4558). These works have established that reconstruction is not a simple re-faceting process, but a dynamic, coverage- and reaction-driven phenomenon arising from the interplay between strong Pt–CO bonding, surface stress, and metal–support redox chemistry.

In particular, combined DFT-based Wulff constructions and *in situ* STEM studies (*J. Am. Chem. Soc*. 2017, 139, 12, 4551-4558) have demonstrated that under near-saturation CO coverage, flat low-index Pt facets such as {100} become thermodynamically destabilized and undergo roughening toward stepped or high-index vicinal facets, while close-packed {111} facets remain comparatively stable. Under CO saturation, additional Pt atomic layers can transiently form on {100}-like regions, supplied by Pt atoms migrating from subsurface or adjacent terrace sites, indicating that reconstruction proceeds through atom-by-atom rearrangement rather than abrupt phase transformation.

Importantly, these studies emphasize that Pt under CO oxidation conditions does not undergo a single well-defined phase transition. Instead, the surface oscillates between competing chemical states associated with CO adsorption, oxygen removal, and reoxidation. This so-called frustrated phase transition generates local strain and electronic instability, which the system relieves through atomic-scale roughening, step formation, and coordination redistribution. As a result, the experimentally observed faceting during CO oxidation reflects the cumulative outcome of repeated, fluctuating surface rearrangements driven by coverage and reaction dynamics, rather than equilibrium crystal reshaping alone.

On reducible oxide supports, this behavior is further amplified at the metal–support perimeter, where lattice oxygen extraction and replenishment continuously perturb Pt–O and Pt–support bonding configurations. Operando and theoretical studies on Pt/CeO_2 systems (*ACS Catal*.

2024, 14, 5, 3504-3513, *J. Mater. Chem. A* 2021, 9, 24579-24590) have shown that CO oxidation proceeds through dynamic restructuring localized at the metal–oxide interface, where redox cycling induces repeated weakening and reformation of metal-oxygen bonds, further promoting surface roughening and mobility. Instead, our objective is to clarify how this well-known reconstruction pathway manifests differently on TiO_2(001) and TiO_2(101), and how facet-dependent redox properties of the support govern the extent and outcome of Pt surface restructuring during CO oxidation.

Based on this established mechanistic understanding, the present work does not aim to re-derive the general CO-induced reconstruction mechanism itself. Instead, our objective is to clarify how this well-known reconstruction pathway manifests differently on TiO_2(001) and TiO_2(101), and how facet-dependent redox chemistry and MSIs govern the extent and outcome of Pt surface restructuring during CO oxidation. To support this facet-dependent viewpoint, we additionally performed explicit CO-adsorbed GNN–MD simulations on Pt_{201}/TiO_2(001) and Pt_{201}/TiO_2(101) (Supplementary Fig. 28) and directly compared the resulting coordination-level roughening responses under closely matched CO-rich conditions.

To support the above discussion and explicitly address the reviewer's question, we incorporated additional CO-covered GNN-based MD simulations using the GA-optimized Pt_{201}/TiO_2(001) and Pt_{201}/TiO_2(101) structures established in Reviewer 2, Comment 1. CO molecules were adsorbed on surface-exposed Pt top sites to represent a CO-rich environment under reaction-relevant conditions. For Pt_{201}/TiO_2(101), 106 CO molecules were adsorbed on 139 surface Pt atoms (76.3% coverage), while for Pt_{201}/TiO_2(001), 101 CO molecules were adsorbed on 137 surface Pt atoms (73.7% coverage), ensuring closely matched CO coverages and eliminating coverage as a confounding variable.

The CO-covered systems were equilibrated by GNN–MD at 523 K for 100 ps, and thermal equilibration was verified by the convergence of both total energy and temperature throughout the trajectories (Supplementary Figs. 29a, b). We then quantified CO-induced roughening and reconstruction signatures using Pt–Pt radial distribution functions (RDFs) and Pt–Pt CN distributions before and after the simulations (Supplementary Figs. 29c, d and Figs. 4e, f). In both facets, CO adsorption broadened the first-neighbor Pt-Pt RDF peak and widened the CN distribution, indicating that redistributes local Pt coordination environments, consistent with the mechanistic picture established in prior operando/DFT studies of CO-saturated Pt surfaces where roughening proceeds via atom-by-atom rearrangement and coordination rebalancing

under strong Pt–CO bonding.

Importantly, the magnitude of coordination redistribution was facet dependent under the same CO-rich conditions. For $Pt_{201}/TiO_2(001)$, the Pt CN distribution changed from mean CN = 8.19 with standard deviation 2.04 (initial) to mean CN = 8.41 with standard deviation 2.41 (final). For $Pt_{201}/TiO_2(101)$, the redistribution was more pronounced, shifting from mean CN = 8.35 with standard deviation 1.96 (initial) to mean CN = 8.88 with standard deviation 2.47 (final) (Supplementary Table 6). Thus, both facets undergo CO-induced coordination broadening, but $Pt_{201}/TiO_2(101)$ exhibits a larger broadening and a larger net shift of the mean coordination under comparable CO coverages. This provides a quantitative basis for stating that CO adsorption acts as a structural perturbation that reshapes Pt surface coordination, and that the extent of this perturbation is modulated by facet-dependent metal-support interactions.

Action taken: These results and analyses have been incorporated into the revised *Results and Discussion* section and Supplementary Note 7, together with the corresponding Figs. 4e, f and Supplementary Figs. 28 and 29, and Supplementary Table 6.

The following paragraph has been added to the *Computational insights into facet-dependent Pt reconstructions on TiO_2* section on Page 10: *"To further elucidate experimentally observed CO-induced reconstruction behaviour, additional CO-covered GNN-based MD simulations were performed on $Pt_{201}/TiO_2(001)$ and $Pt_{201}/TiO_2(101)$ (Supplementary Note 7). Under high CO coverage (~0.75 ML) and reaction -relevant thermal conditions (523 K), CO adsorption perturbed the coordination environment of surface Pt atoms in a facet-dependent manner, as evidenced by the broadening of coordination-number distributions (Figs. 4e, f) and Pt–Pt RDFs (Supplementary Fig. 29), particularly on the (101) facet (Supplementary Table 6), supporting experimental observations of CO-induced Pt roughening."*

Relevant discussion is provided in Supplementary Note 7:

*"**Supplementary Note 7. CO-induced Reconstruction Simulations** CO-induced structural reconstruction of Pt NPs was investigated using explicit CO adsorption followed by structural relaxation and molecular dynamics (MD) simulations. For each optimized Pt_{201}/TiO_2 structure, surface Pt atoms were first identified based on a combined coordination and geometric criterion. Pt–Pt coordination numbers were evaluated using a cutoff distance of 3.0 Å, while interactions with the TiO_2 support (Ti and O atoms) were identified using a cutoff distance of 3.5 Å. Pt atoms with reduced Pt coordination were classified as surface atoms when they were*

either located at the metal–support interface, positioned far from the cluster center, or exhibited very low Pt coordination. In addition, Pt atoms located near the top of the NP were also considered surface atoms if their coordination number was below a threshold. This procedure enabled robust identification of catalytically accessible surface Pt sites across different NP morphologies.

CO molecules were adsorbed on the identified surface Pt atoms using a site-by-site construction protocol. For each surface Pt atom, a CO molecule was placed along an outward direction defined relative to the NP geometry, with a fixed Pt–C distance of 1.85 Å and a C–O bond length of 1.15 Å. To avoid unphysical steric overlap, newly added CO molecules were excluded if the distance between any CO atom and existing atoms was smaller than 1.8 Å. When overlap was detected, the corresponding adsorption site was skipped. As a result, the final CO coverage was determined self-consistently by geometric accessibility rather than by imposing a predefined coverage value.

The CO-covered structures were subsequently relaxed using the limited-memory Broyden–Fletcher–Goldfarb–Shanno (LBFGS) algorithm to remove residual forces arising from the initial CO placement. Structural optimization was performed until the maximum atomic force fell below 0.05 $eV \cdot Å^{-1}$. The relaxed CO-covered configurations were then used as initial structures for finite-temperature MD simulations.

MD simulations were carried out in the canonical (NVT) ensemble using a Langevin thermostat. A time step of 1.0 fs was employed, and the system temperature was maintained at 523 K. A friction coefficient of 0.001 was used to ensure stable temperature control while allowing sufficient atomic mobility. Each simulation was propagated for 100,000 MD steps, corresponding to a total simulation time of 100 ps. Atomic trajectories and thermodynamic quantities were recorded at regular intervals throughout the simulation. These simulations enabled direct observation of CO-induced structural rearrangements of Pt NPs under CO-rich conditions."

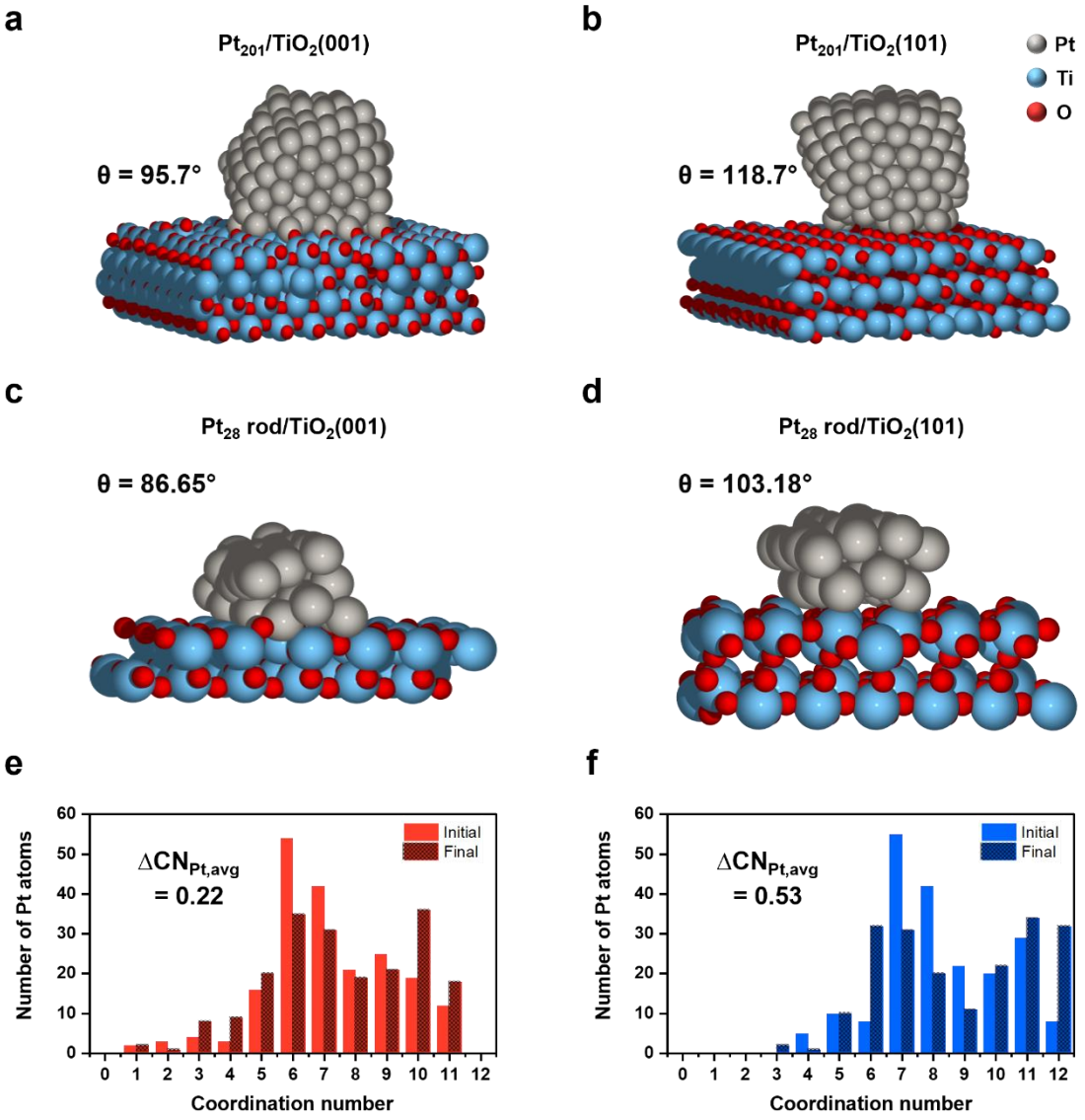

Figure 4. Computational insights into Pt/TiO_2 catalyst morphology with facet-controlled TiO_2 supports. (a, b) Snapshots of Pt_{201} clusters supported on (a) TiO_2(001) and (b) TiO_2(101) after genetic algorithm (GA)-based optimisation. (c, d) DFT-optimised structures of Pt_{28} rod models on (c) TiO_2(001) and (d) TiO_2(101). The values indicated in panels (a–d) correspond to the effective contact angles (θ) of the Pt clusters on TiO_2 surfaces, extracted from the optimised geometries. (e, f) Pt coordination-number (CN) distributions before and after CO-covered GNN-based molecular dynamics simulations at 523 K for 100 ps for GA-optimised (e) Pt_{201}/TiO_2(001) and (f) Pt_{201}/TiO_2(101), indicating facet-dependent CO-induced structural changes (initial: before MD simulation; final: after MD simulation).

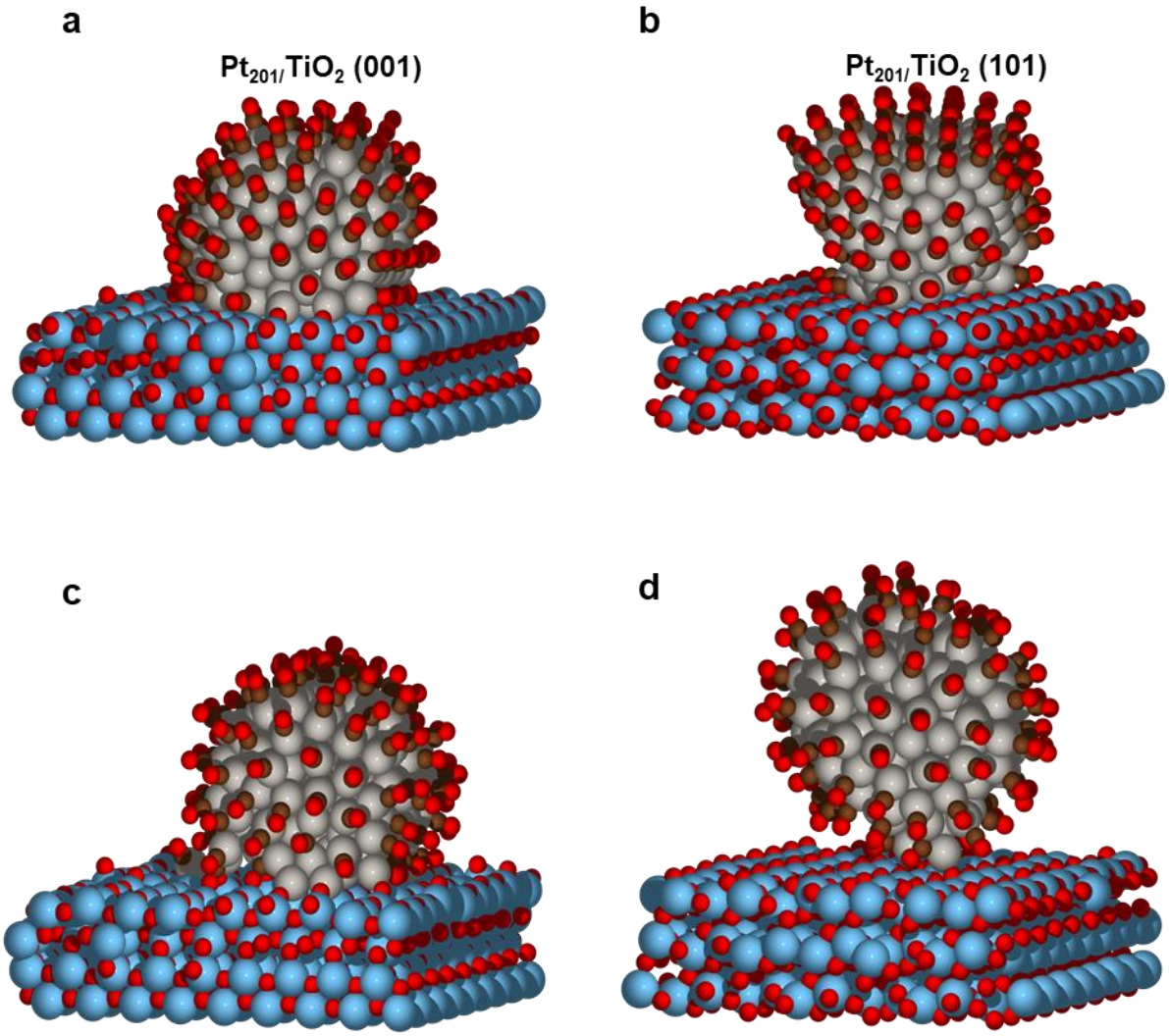

Supplementary Figure 28. CO-induced reconstruction of Pt_{201} NPs on TiO_2 facets. Initial configurations of CO-saturated Pt_{201} NPs supported on (a) TiO_2(001) and (b) TiO_2(101), with CO molecules adsorbed at the available Pt top sites. Corresponding structures after GNN–MD simulations at 523 K for 100 ps under CO-rich conditions are shown for (c) Pt_{201}/TiO_2(001) and (d) Pt_{201}/TiO_2(101).

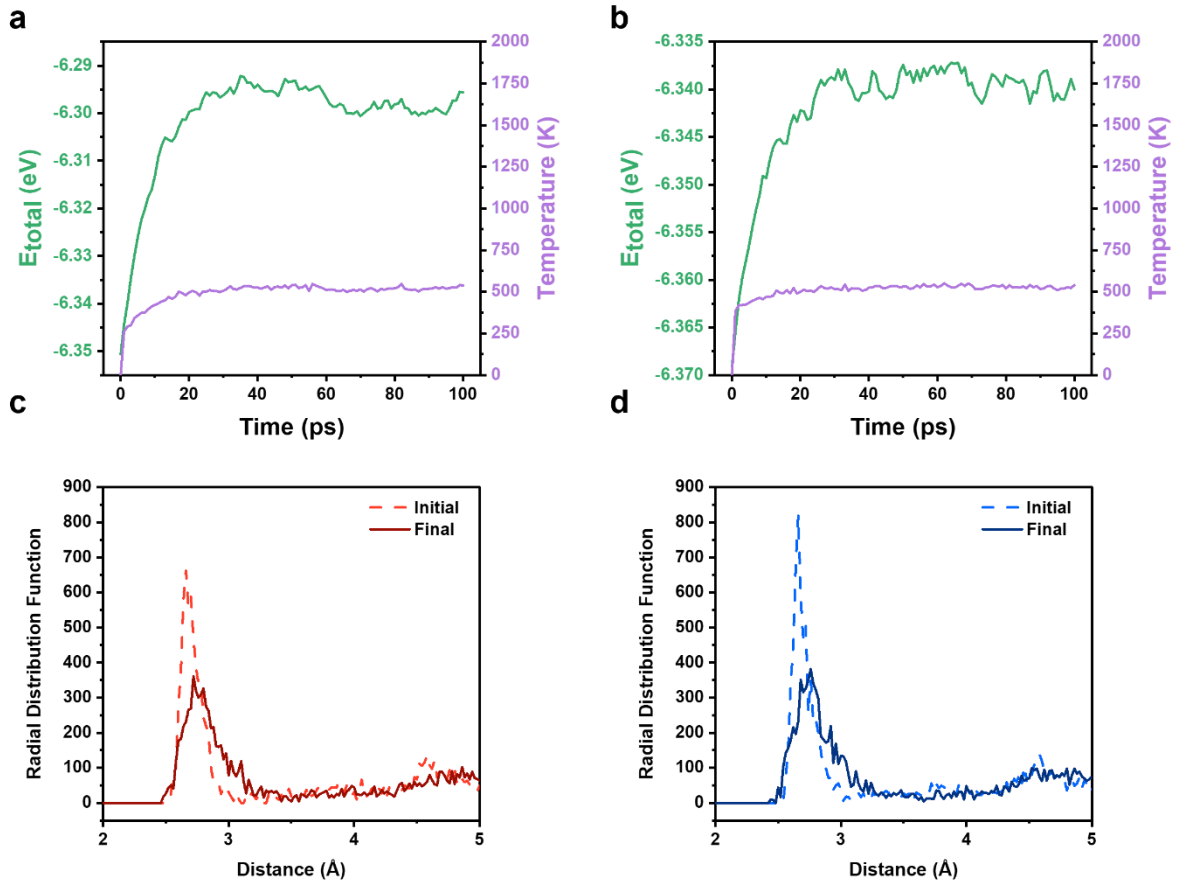

Supplementary Figure 29. Thermal convergence and CO-induced structural evolution of Pt_{201} NPs on TiO_2 facets revealed by GNN–MD simulations. Time evolution of total energy and temperature for (a) $Pt_{201}/TiO_2(001)$ and (b) $Pt_{201}/TiO_2(101)$ during GNN–MD simulations at 523 K, confirming thermal equilibration under CO-rich conditions. Radial distribution functions of Pt atoms before and after simulation are shown for (c) $Pt_{201}/TiO_2(001)$ and (d) $Pt_{201}/TiO_2(101)$.

Supplementary Table 6. Pt–Pt CN statistics for CO-covered Pt_{201} NPs before and after GNN–MD simulations at 523 K, 100ps.

System	Mean CN	Std. dev.
Initial $Pt_{201}/TiO_2(001)$	8.19	2.04
Final $Pt_{201}/TiO_2(001)$	8.41	2.41
Initial $Pt_{201}/TiO_2(101)$	8.35	1.96

Comment 3: Moreover, the authors give the DFT results of the reaction pathway using Pt_{28} nanorod as the model, but do not pinpoint the reconstruction beneficial or detrimental to the MvK mechanism.

Response: We thank the reviewer for this comment. We agree that, in the original manuscript, the DFT reaction pathways obtained using the Pt_{28} nanorod models were mainly presented as facet-dependent MvK energetics, without clearly explaining which aspects of Pt NP reconstruction are relevant to the MvK mechanism.

Previous experimental and theoretical studies (*ACS Catal*. 2017, 7, 10, 6493-6513) have established that, for CO oxidation on reducible oxides, the key structural factor governing the MvK pathway is not the global shape of the metal NP itself, but the structure and bonding environment of oxygen atoms located at the metal–oxide perimeter, where lattice oxygen removal and vacancy healing occur. In these studies, reconstruction is understood as a process that modifies the metal–support contact geometry and, consequently, the population and reactivity of perimeter oxygen sites, rather than as an isolated morphological phenomenon.

In the revised manuscript, we clarify that our Pt_{28} nanorod DFT models were constructed to reflect the reconstructed contact geometries inferred from both experimental observations and GA-optimized NP morphologies. This allows the DFT reaction pathways to explicitly capture how reconstruction alters the metal–support contact region that is directly involved in the MvK cycle. We further show that reconstruction on $TiO_2(001)$ leads to a more developed metal–support contact, which increases the number of perimeter oxygen motifs and modifies their local bonding environment, consistent with prior reports (*J. Am. Chem. Soc.* 2013, 135, 2, 906-909 3) that oxygen vacancy formation is energetically favored at metal–oxide interfaces.

By making this connection explicit, the revised manuscript now explains why the reconstructed geometries represented by the Pt_{28} models are beneficial for the MvK mechanism on $TiO_2(001)$, rather than presenting the reaction energetics in isolation.

In the revised manuscript, we strengthened the link between reconstruction and the MvK pathway by explicitly connecting reconstruction-derived structural descriptors to the DFT reaction models.

First, we clarified that the Pt_{28} nanorod models were designed to represent the facet-dependent wetting geometries observed experimentally and obtained from GA optimization of Pt_{201} NPs, rather than being generic cluster models. To quantify reconstruction in a way that is directly

transferable between NP-scale and DFT-scale models, we introduced voxel-based contact area and contact angle descriptors.

For the GA-optimized Pt_{201} structures, Pt on $TiO_2(001)$ exhibits a smaller contact angle (95.74°) and a larger contact area (391.1 $Å^2$) than on $TiO_2(101)$ (118.66° and 257.5 $Å^2$), indicating stronger wetting and an expanded metal–support contact region. Importantly, the Pt_{28} nanorod models preserve the same trend, with smaller contact angles (86.65° vs 103.18°) and larger contact areas (103.2 $Å^2$ vs 70.4 $Å^2$) on $TiO_2(001)$ compared to $TiO_2(101)$. This consistency ensures that the DFT reaction pathways are evaluated on structures that realistically reflect the reconstructed contact geometry.

Second, we revised the discussion of the MvK mechanism to explain how this expanded contact region impacts lattice oxygen participation. Prior work (*Nat. Commun.* 2024, 15, 8293) has shown that oxygen atoms located at the metal–oxide perimeter can be removed at significantly lower energetic cost than oxygen atoms on the bare oxide surface, and that these sites dominate oxidation chemistry on supported metals. We now explicitly state that reconstruction is beneficial when it increases the density of such perimeter oxygen motifs, which is the case for the more strongly wetted $Pt/TiO_2(001)$ system.

Third, we added electronic structure analysis to support this geometric interpretation. The work function of $Pt_{28}/TiO_2(001)$ (5.56 eV) is substantially lower than that of $Pt_{28}/TiO_2(101)$ (6.61 eV), and the interfacial charge redistribution along the surface normal is significantly larger for $Pt_{28}/TiO_2(001)$ shown in Supplementary Fig. 27. These trends are consistent with recent reports (*Nat. Catal.* 2025, 8, 1038-1050) linking moderate MSI, enhanced wetting, and high oxidation activity on reducible oxides, having work function close to Pt metal (5.12–5.93eV) and further electron transfer among Pt and TiO_2. We use these results to corroborate that reconstruction on $TiO_2(001)$ leads to stronger electronic coupling at the metal-support interface, which facilitates oxygen vacancy formation and healing in the MvK cycle.

Action taken: A brief description of this analysis has been added in the manuscript, along with Supplementary Figs. 26 and 27 and Supplementary Table 5.

The following paragraph has been added to the *Computational insights into facet-dependent Pt reconstructions on TiO_2* section on Page 10: *"Relaxation of an identical hexagonal Pt_{28} rod (Supplementary Fig. 25) on each facet reproduced the facet-dependent reconstruction trend: Pt_{28} on $TiO_2(001)$ flattens considerably (Fig. 4c), while Pt_{28} on $TiO_2(101)$ remains close to its*

initial shape (Fig. 4d), with different Pt CNs (Supplementary Table 4). Quantitative analysis confirms that the DFT-level adhesion energy is more favourable on TiO_2(001) (−0.86 eV per Pt atom) than on TiO_2(101) (−0.80 eV), in line with stronger MSI on the high-energy (001) facet along with the normalised Pt binding energy shown in Supplementary Table 5. The effective contact angle similarly reflects enhanced wetting, with θ = 86.7° on TiO_2(001) versus 103.2° on TiO_2(101) (Supplementary Fig. 26). This trend is consistent with the Pt_{201} GA models (95.7° and 118.7°, respectively). Additionally, in line with previous Pt–oxide studies,[65] the TiO_2(001) support shows a work function (5.56 eV) close to that of Pt, resulting in limited interfacial charge redistribution and moderate MSI (Supplementary Fig. 27)."

Accordingly, the reference 65 have been added to the revised manuscript.

65. Jiang, C. et al. Predictive model for the discovery of sinter-resistant supports for metallic nanoparticle catalysts by interpretable machine learning. *Nat. Catal.*, 1-13 (2025).

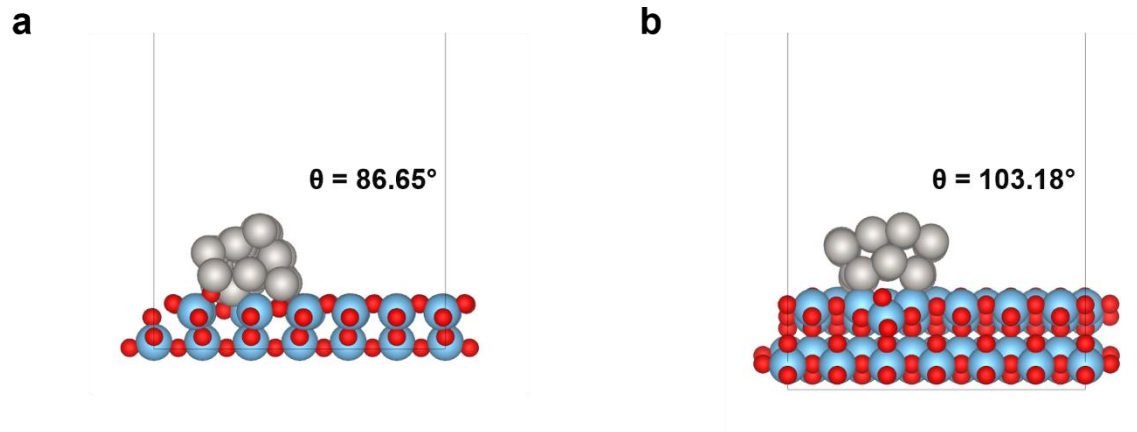

Supplementary Figure 26. Side-view representations of DFT-optimized models: (a) Pt_{28} rod on TiO_2(001) facet and (b) Pt_{28} rod on TiO_2(101) facet.

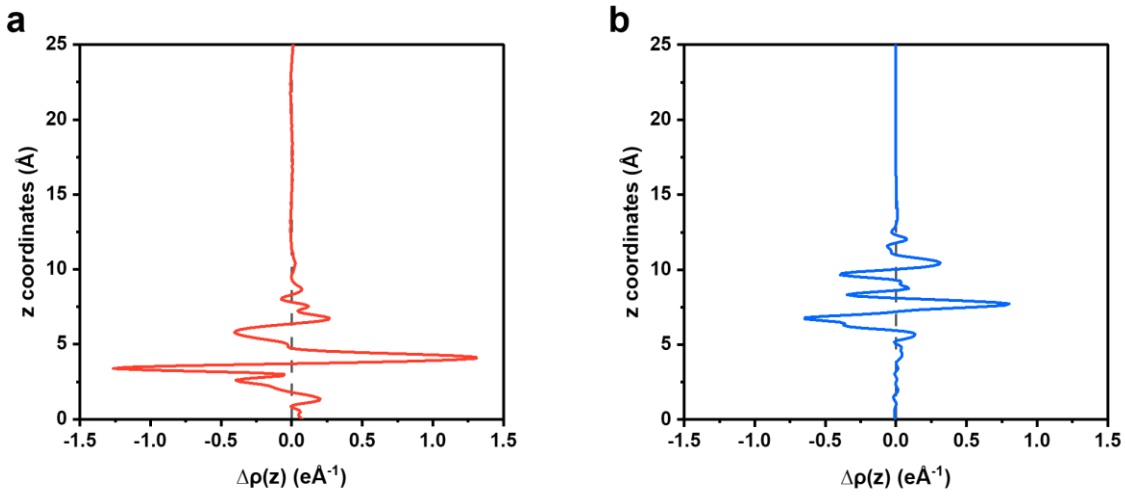

Supplementary Figure 27. One-dimensional planar-averaged charge density along the z-direction for (a) Pt_{28}/TiO_2(001) and (b) Pt_{28}/TiO_2(101).

Supplementary Table 5. Surface energies of TiO_2(001) and (101) facets and the corresponding normalised Pt binding energies (per Pt atom) in the DFT-optimized Pt_{28} rod on TiO_2 models.

	$Pt_{28}/TiO_2(001)$	$Pt_{28}/TiO_2(101)$
Surface energy [eV·Å^{-2}]	0.084	0.067
Normalized Pt binding E [eV·atom^{-1}]	−0.78	−0.68
Normalized Adhesion E [eV·atom^{-1}]	−0.86	−0.80
Interfacial area of Pt–TiO_2 [Å^2]	103.2	70.4
Surface area normalised Adhesion E [eV·Å^{-2}]	−0.233	−0.316

Comment 4: The -ICOHP values are used to explain the weak MSI interaction and facile depletion of lattice oxygen atom at $TiO_2(001)$. However, it contradicts to the calculated stronger Pt binding on $TiO_2(001)$ (−0.78 eV) than on $TiO_2(101)$ (−0.68 eV). Please explain this inconsistency.

Response: We thank the reviewer for pointing out the apparent inconsistency between the stronger Pt binding on $TiO_2(001)$ and the smaller -ICOHP values used to rationalize facile lattice oxygen depletion. We agree that, without clarification, these results may appear contradictory.

However, this apparent inconsistency arises from conflating two quantities that probe different physical aspects of the MSI. The Pt binding energy quantifies the global adhesion strength of the Pt particle to the support, reflecting the cumulative stabilization from all Pt–O and Pt–Ti interactions across the entire metal–support contact region. In contrast, the -ICOHP values discussed in the manuscript were intentionally evaluated for specific lattice oxygen sites relevant to oxygen vacancy formation, and therefore represent a local descriptor of the covalent bonding that must be broken to remove that particular oxygen atom.

As a result, stronger overall Pt adhesion can coexist with locally weakened Ti–O bonding at vacancy-prone perimeter oxygen sites. Enhanced Pt-O coordination at the metal–support perimeter can redistribute bonding such that the removable oxygen becomes less strongly anchored by Ti–O covalency, thereby lowering the energetic cost of lattice oxygen depletion, even when the overall Pt–support interaction is stronger.

Thus, the Pt binding energies and -ICOHP values are not contradictory, but complementary, describing global adhesion and local vacancy-site bonding, respectively.

To explicitly resolve this point, we revised the manuscript to clearly distinguish between global metal–support adhesion and local bonding descriptors associated with lattice oxygen removal (Supplementary Table 5).

First, we expanded the adhesion analysis using the Pt_{28} rod models to show that Pt exhibits stronger overall binding on $TiO_2(001)$ than on $TiO_2(101)$. The total adhesion energy is −24.08 eV for $Pt_{28}/TiO_2(001)$ compared to −22.26 eV for $Pt_{28}/TiO_2(101)$, corresponding to a more negative adhesion energy per Pt atom on $TiO_2(001)$ (−0.86 eV vs −0.80 eV). This stronger adhesion is primarily driven by the significantly larger metal-support contact area on $TiO_2(001)$ (103.2 $Å^2$) relative to $TiO_2(101)$ (70.4 $Å^2$), indicating enhanced wetting on the (001) facet.

Second, we clarified that the -ICOHP analysis targets specific perimeter oxygen motifs associated with the most stable oxygen vacancy configurations, rather than averaging over the entire interface. For these sites, we now explicitly report the summed -ICOHP values of the bonds broken upon vacancy formation and show that, despite stronger global adhesion on TiO_2(001), the local bonding framework at these oxygen sites is weaker overall due to reduced Ti−O covalent stabilization and increased Pt coordination. This bonding redistribution is consistent with established interpretations of COHP analysis, in which lower -ICOHP values correspond to increased antibonding occupation and weaker net bonding, facilitating oxygen vacancy formation.

Finally, we added a normalisation of the adhesion energy by contact area, showing that while TiO_2(101) exhibits a more negative adhesion energy density (−0.316 eV·Å^{-2}) than TiO_2(001) (−0.233 eV·Å^{-2}), the larger interfacial footprint on TiO_2(001) leads to stronger total adhesion and a higher density of perimeter oxygen motifs. These revisions clarify that stronger Pt binding and facile lattice oxygen depletion are not mutually exclusive, but arise from different scales of bonding at the reconstructed metal-support interface.

Action taken: Discussions of this analysis have been added in the manuscript, along with the Supplementary Table 5.

The following paragraph have added to the *Computational insights into facet-dependent Pt reconstructions on TiO_2* section on Page 10*: "Quantitative analysis confirms that the DFT-level adhesion energy is more favourable on TiO_2(001) (−0.86 eV per Pt atom) than on TiO_2(101) (−0.80 eV), in line with stronger MSI on the high-energy (001) facet along with the normalised Pt binding energy shown in Supplementary Table 5."*

The following paragraph have also added to the *Reaction mechanism and the origin of superior catalytic activity* section on Page 12: *"The summed -ICOHP values for the target oxygen, accounting for both Pt–O and Ti–O bonds, are lower on TiO_2(001) (4.15) than on TiO_2(101) (5.13), indicating weaker oxygen bonding at the Pt_{28}/TiO_2(001) interface (Fig. 6b). This weakening is further supported by the broader and flatter geometry of the Pt_{28} cluster on TiO_2(001), which increases perimeter contact and yields a larger population of oxygen atoms directly coordinated to Pt. Such interfacial motifs are preferentially involved in lattice oxygen activation during redox catalysis, consistent with previous studies highlighting the role of metal–support interfacial sites. In the present system, this beneficial configuration arises*

naturally from facet-induced reconstruction on TiO_2(001), which expands the metal-support interface and weakens specific oxygen bonds."

Supplementary Table 5 is included in the response to Comments 3.

Comment 5: TOC looks like giving a strategy to enhance the catalytic activity and prevent sintering of Pt NP. But it is not discussed in the paper and does not fit the topic.

Response and Action taken: We thank the reviewer for this helpful comment regarding the Table of Contents (TOC) graphic. As correctly noted, the primary aim of this study is to elucidate the facet-dependent reconstruction of Pt NPs and its synergistic impact on catalytic activity, emphasizing that both geometric factors and intrinsic redox properties should be considered in facet-driven MSI studies.

Although differences in catalytic activity and sintering resistance are observed among the Pt/TiO_2 catalysts, these results are presented to clarify the underlying reconstruction behavior rather than to propose a prescriptive strategy for enhancing activity or preventing Pt sintering. Given that the facet-dependent morphological evolution of Pt during CO oxidation is already comprehensively illustrated in Fig. 5, and since a TOC graphic is not mandatory under the current journal guidelines, we have removed the TOC graphic in the revised manuscripts.

We appreciate the reviewer's suggestion, which helped us prevent potential confusion and better align the presentation with the core focus of this work.

Reviewer #3

General comments: In this study, Kim et.al reported TiO_2-facet dependent reconstruction of Pt NPS and reactivity for CO oxidation. The authors claimed a TiO_2-facet and CO driven reconstruction and dynamics of Pt NPs that determines their CO oxidation reactivity. However, upon reviewing their data, I did not find sufficient and direct evidence to support the dynamic restructuring of Pt under reaction conditions, and the correlation between the reshaping of Pt NPs and their reactivity remains vague. Notably, a significant sintering of PTR was observed after the reaction (Figure S13), which must be carefully considered before the authors can validate their conclusions. Therefore, I cannot recommend the publication of this work in its current form, unless the authors provide systematic experimental evidence to substantiate their claims. For further details, please refer to my specific comments below.

Response: We sincerely thank the reviewer for the careful and constructive evaluation of our manuscript. In response to this important concern, we have substantially strengthened both the experimental and theoretical analyses and expanded the corresponding discussions throughout the revised manuscript. Detailed point-by-point responses to the specific comments are provided below. We believe that these additions significantly improve the clarity, rigor, and robustness of our conclusions.

We fully acknowledge the reviewer's concern regarding the pronounced sintering observed for the spent PTR catalyst and its potential impact on the interpretation of post-reaction structural analyses. We agree that, particularly for PTR, thermally driven sintering could confound the assessment of intrinsic facet-dependent reconstruction effects if not carefully controlled. Accordingly, we have re-evaluated this issue in depth and revised both the experimental protocol and the corresponding interpretations in the manuscript.

In the original submission, the spent catalysts were prepared at relatively high final reaction temperatures (300 °C for 2 h at CO/O_2 = 0.2 and 1, 350 °C for 2 h at CO/O_2 = 3, and 400 °C for 2 h at CO/O_2 = 5). These temperatures were chosen to maintain consistency with the catalytic activity measurements shown in Fig. 1e and Supplementary Fig. 4, where both PTS and PTR had already reached complete CO conversion under highly diluted catalyst-bed conditions. Because these temperatures were well above the catalytic ignition temperature (~240 °C) identified by *in situ* DRIFTS (Fig. 3), we initially considered them sufficient to ensure representative exposure of the catalysts to reaction conditions prior to structural

characterization.

However, as correctly pointed out by the reviewer, these activity measurements were conducted using a highly diluted catalyst bed, which inherently requires higher temperatures to reach full CO conversion. Consequently, the temperatures used for preparing the spent catalysts were harsher than necessary to probe CO-induced Pt reconstruction alone and could additionally promote thermally driven sintering, particularly for PTR. Consistent with this concern, the spent PTR catalyst exhibited substantial particle growth, with the average Pt size increasing from 1.83 nm to 3.18 nm (Supplementary Fig. 13 in the original manuscript; Supplementary Fig. 15 in the revised version).

We therefore fully accept the reviewer's point that, under the original conditions, sintering effects cannot be excluded from the analysis of the spent PTR catalyst. To eliminate this ambiguity and to isolate the intrinsic reconstruction behavior, we redesigned the post-reaction treatment protocol and repeated the structural analyses under milder, kinetically relevant conditions.

Specifically, we prepared the spent catalysts at a final reaction temperature of 240 °C, corresponding to the catalytic ignition temperature at which complete CO conversion is achieved for both PTS and PTR, as established by *in situ* DRIFTS measurements (Fig. 3). We further confirmed that undiluted catalysts reach 100% CO conversion within the same temperature range (Supplementary Figs. 44a,b). After holding the catalysts at 240 °C for 2 h under CO/O_2 = 1, both PTS and PTR exhibited no statistically significant sintering, as evidenced by their post-reaction Pt size distributions (Supplementary Figs. 12 and 13). Under these conditions, the observed Pt morphologies therefore reflect the intrinsic facet-dependent influence of the TiO_2 support combined with CO-adsorbate-induced reconstruction during reaction, without contributions from thermally driven sintering.

The same protocol (240 °C for 2 h) was also applied for the spent catalyst analysis under CO/O_2 = 0.2 to eliminate any effects arising solely from differences in final reaction temperature. For CO/O_2 = 5, the catalyst was treated at 350 °C for 2 h, corresponding to the temperature at which the undiluted PTR catalyst reaches its maximum achievable CO conversion (~40%), as shown in Supplementary Fig. 44c. Although this temperature is lower than that used in the original manuscript, it still lies within a regime where sintering may occur; therefore, we explicitly acknowledge this possibility and carefully qualify the interpretation of the corresponding

STEM and EXAFS results in the revised manuscript.

In the revised manuscript, we have re-evaluated all post-reaction characterizations under conditions where sintering does not interfere with structural interpretation, and we have updated all corresponding results accordingly. These include newly acquired XRD, Raman, Pt size distributions, STEM images, post-reaction CO-DRIFTS spectra, and EXAFS data obtained under the revised treatment conditions.

Specifically, XRD and Raman analyses (Supplementary Fig. 3) showed no discernible differences from the original data, confirming the structural stability of the TiO_2 supports. The post-reaction Pt size distributions (Supplementary Figs. 12 and 13) revealed no significant particle growth for either PTS or PTR under CO/O_2 = 0.2 and 1. Under CO/O_2 = 5, mild sintering was observed for PTR—consistent with the original findings—and this has been explicitly noted in the revised manuscript. STEM images of the spent catalysts (Figs. 2h, j and Supplementary Figs. 12 and 13) consistently reproduced the facet-dependent morphological features reported in the original manuscript: PTS retained the parallel Pt– TiO_2(004) alignment, whereas PTR maintained its stepped interface with TiO_2(101) (Supplementary Figs. 10 and 11).

All EXAFS datasets were newly acquired (Figs. 2a–g and Supplementary Figs. 7–9), and the corresponding curve-fitting results are summarized in Supplementary Table 2. The revised FT- and WT-EXAFS spectra again show that Pt–O coordination is dominant for PTS, while Pt–Pt coordination is more pronounced in PTR. These trends are consistent for both fresh and spent catalysts, indicating that the extracted coordination numbers reflect intrinsic structural differences, not sintering. The overall magnitude of CN changes is somewhat reduced due to the lower treatment temperature, as expected. Under CO-rich conditions (CO/O_2 = 5), where mild sintering of PTR was observed, we clearly state in the revised manuscript that the increase in Pt–Pt CN arises from particle growth.

Post-reaction CO-DRIFTS spectra (Figs. 3a, d) exhibited qualitatively similar trends as before but with smaller spectral shifts, consistent with the absence of sintering-induced increases in terrace-site CO adsorption (see also response to Comment 4). Second *in situ* DRIFTS measurements on the spent catalysts (Supplementary Fig. 30) also confirmed the previously observed facet-dependent behavior. Notably, the CO–Pt_int band, which was observed for PTR under the harsher 300 °C conditions, was no longer detected at 240 °C, suggesting that these partially oxidized interfacial Pt species are no longer stabilized under mild conditions. This

comparison further supports the conclusion that PTR intrinsically exhibits weaker interfacial interactions with TiO_2 than PTS during the reaction.

Overall, the reviewer's comment led us to systematically re-examine the post-reaction treatment protocol and to perform comprehensive remeasurements under well-controlled, non-sintering conditions. The updated STEM, DRIFTS, and EXAFS results are fully consistent with each other and reaffirm the conclusions of the original manuscript, now free from potential artifacts caused by thermally induced sintering. We are grateful to the reviewer for raising this important point, which has significantly improved the scientific clarity and robustness of our study.

Action taken: In the revised manuscript, the reaction conditions applied prior to post-reaction structural analyses have been explicitly stated in the main text to ensure that thermally induced sintering does not influence the results. The following sentence has been added on Page 6: *"To exclude thermally induced sintering effects on post-reaction structural analyses, both catalysts were treated at 240 °C for 2 h under identical reaction conditions (CO/O_2 = 1) prior to analysis. The rationale for this condition is discussed in Supplementary Note 2."*

An extended discussion of the rationale for selecting these conditions, together with Supplementary Fig. 44, is now provided in Supplementary Note 2, with additional related discussion addressed in the response to Comment 4.

*"**Supplementary Note 2. Rationale for Post-Reaction Treatment Conditions** To prepare spent catalysts for post-reaction structural analysis, the final reaction temperatures were initially set to 300 °C for 2 h under CO/O_2 = 0.2 and 1, 350 °C for 2 h under CO/O_2 = 3, and 400 °C for 2 h under CO/O_2 = 5. These temperatures correspond to reaction conditions well above those required to achieve complete CO conversion in the reactivity comparison experiments (Fig. 1e and Supplementary Fig. 4), where both PTS and PTR had already surpassed 100% CO conversion. The use of such harsher temperatures was intended to ensure sufficient exposure of the catalysts to reaction environments prior to structural characterization.*

STEM analysis of the spent catalysts treated under these conditions revealed that the overall facet-dependent Pt morphology was preserved across different reaction atmospheres (Supplementary Figs. 14 and 15). However, a pronounced increase in Pt particle size was observed for PTR, with the average Pt size increasing from 1.83 nm to 3.18 nm, whereas PTS remained largely resistant to particle growth under the same conditions. This observation

indicates that, in addition to CO-induced Pt reconstruction (which is discussed based on in situ DRIFTS measurements in the main text), thermally driven sintering occurred for PTR under the high-temperature treatment conditions.

We attribute this sintering behavior of PTR to the use of a highly diluted catalyst bed during the reactivity tests, which inherently required higher reaction temperatures to reach complete CO conversion. As a result, the temperatures employed for preparing the spent catalysts were harsher than necessary to induce Pt NP reconstruction alone and could also promote thermally driven sintering, particularly for PTR, as evidenced by the significant increase in average Pt particle size under all measured conditions (Supplementary Fig. 15). Consequently, for samples treated under these conditions, size-related effects cannot be excluded from the interpretation of the corresponding DRIFTS and EXAFS structural analyses.

To eliminate thermally induced sintering effects while preserving CO-adsorbate-driven reconstruction, the final reaction temperature for preparing spent catalysts was therefore lowered to 240 °C. This temperature was selected based on in situ DRIFTS results showing that complete catalytic ignition occurs for both PTS and PTR at approximately 240 °C (Figs. 3 and 5). We further confirmed that undiluted catalysts reach 100% CO conversion within the same temperature range (Supplementary Figs. 44a, b). After holding the samples at 240 °C for 2 h under $CO/O_2 = 1$, both PTS and PTR exhibited no significant sintering in their post-reaction Pt size distributions (Supplementary Figs. 12 and 13). Under these conditions, the observed Pt morphology reflects the intrinsic facet-dependent influence of the TiO_2 support together with reconstruction induced by adsorbed CO during reaction, allowing post-reaction structural analyses to be interpreted without contributions from sintering.

For spent catalyst analysis under $CO/O_2 = 0.2$, the same treatment condition (240 °C for 2 h) was applied to eliminate any influence arising solely from differences in the final reaction temperature. For $CO/O_2 = 5$, the catalyst was treated at 350 °C for 2 h, corresponding to the temperature at which the undiluted PTR catalyst reached its maximum achievable CO conversion (~40%), as shown in Supplementary Fig. 44c. Although this treatment temperature is lower than that used initially, it still lies within a regime where sintering may occur; therefore, this possibility is explicitly considered when interpreting the corresponding STEM and EXAFS results."

All newly acquired post-reaction characterization results under the revised treatment conditions

are now presented in the revised manuscript and Supplementary Information, including Figs. 2 and 3, Supplementary Figs. 3 and 7–15, Supplementary Fig. 30, and Supplementary Table 2. The original post-reaction Pt size distributions have been relocated to Supplementary Figs. 14 and 15, while the second *in situ* DRIFTS data from the original manuscript are now included as Supplementary Fig. 30. All experimental conditions are clearly specified in the corresponding figure captions, and instances of TEM-observed sintering are explicitly noted in both the main text and figure captions. As the revised datasets reproduce the same overall trends as the original results, only minor revisions were made to the associated *Results and Discussion* sections.

In addition to these data updates, several further modifications were made to improve the overall logical flow of the manuscript and to facilitate clearer comparison with the original version. In the ex situ STEM analyses (Fig. 2), the images were replaced with higher-resolution data, and the figure layout was refined to enhance visual clarity, particularly in the side-view projections. Additional representative STEM images are also provided in Supplementary Figs. 12 and 13.

For the DRIFTS results (Fig. 3), the following revised paragraph was repositioned on Page 8 to improve narrative continuity and flow: *"These spectral changes are accompanied by suppression of the 1850 cm^{-1} CO–Pt_{bridge} feature, as clearly resolved in the enlarged DRIFTS spectra (Supplementary Fig. 16), together with enhanced CO–$Pt_{step/edge}$ and CO_2 (g) signals, which is indicative of CO-induced surface roughening prior to catalytic ignition.*[58] *Notably, these spectral changes occur more rapidly on PTS than on PTR, suggesting a facet-dependent difference in the restructuring behaviour."*

In addition, to strengthen the combined discussion of EXAFS and STEM results obtained under various CO/O_2 conditions and to demonstrate that Pt morphology evolution is governed by both TiO_2 facets and adsorbates, the following paragraph has been added on Page 7: *"Further STEM analyses of spent catalysts under various CO/O_2 conditions, including harsher thermal treatments (Supplementary Figs. 12–15 and Supplementary Note 2), show that facet-dependent Pt NP morphologies are largely preserved. Under O_2-rich conditions, PTS exhibits more dispersed metallic features, including partial redispersion into single atoms, whereas PTR remains largely intact and shows comparable redispersion only under harsher O_2-rich conditions. In contrast, under CO-rich conditions, PTS remains sintering-resistant despite increased Pt–Pt CNs indicative of structural ordering, whereas PTR undergoes pronounced*

sintering, which becomes severe under harsher thermal treatments due to its weak interfacial contact with TiO_2. The corresponding increase in Pt–Pt CNs for PTR thus reflects particle growth driven by sintering. These observations indicate that Pt NP evolution under different CO/O_2 environments is governed by the interplay between adsorbate-induced restructuring—particularly by strongly adsorbed CO[52, 53]—and facet-dependent redox behaviour at the Pt–TiO_2 interface."

Furthermore, to reinforce the discussion of facet-dependent Pt restructuring based on additional spectroscopic evidence, the following paragraph has been added on Page 11: *"In the second in situ DRIFTS measurements (Supplementary Figs. 30a,b), the CO–Pt_{int} feature was observed exclusively for the spent PTS catalyst and was absent for spent PTR, although CO-induced surface roughening features were present for both catalysts. By contrast, when the spent catalysts were prepared under harsher conditions (300 °C for 2 h), CO–Pt_{int} features also emerged for PTR (Supplementary Figs. 30c,d). These results indicate that PTR intrinsically exhibits weaker Pt–TiO_2 interactions, requiring higher energy for CO adsorbed at perimeter Pt sites to activate interfacial oxygen species. Consequently, Pt fluxional behaviour at the Pt/TiO_2 interface differs between the two facets during CO oxidation, leading to facet-dependent Pt restructuring."*

Following references (1–2) were added to the revised Supplementary information files.

1. Boubnov, A. et al. Oscillatory CO oxidation over Pt/Al_2O_3 catalysts studied by in situ XAS and DRIFTS. *Top. Catal.* **56**, 333-338 (2013).
2. DeRita, L. et al. Catalyst Architecture for Stable Single Atom Dispersion Enables Site-Specific Spectroscopic and Reactivity Measurements of CO Adsorbed to Pt Atoms, Oxidized Pt Clusters, and Metallic Pt Clusters on TiO_2. *J. Am. Chem. Soc.* **139**, 14150-14165 (2017).

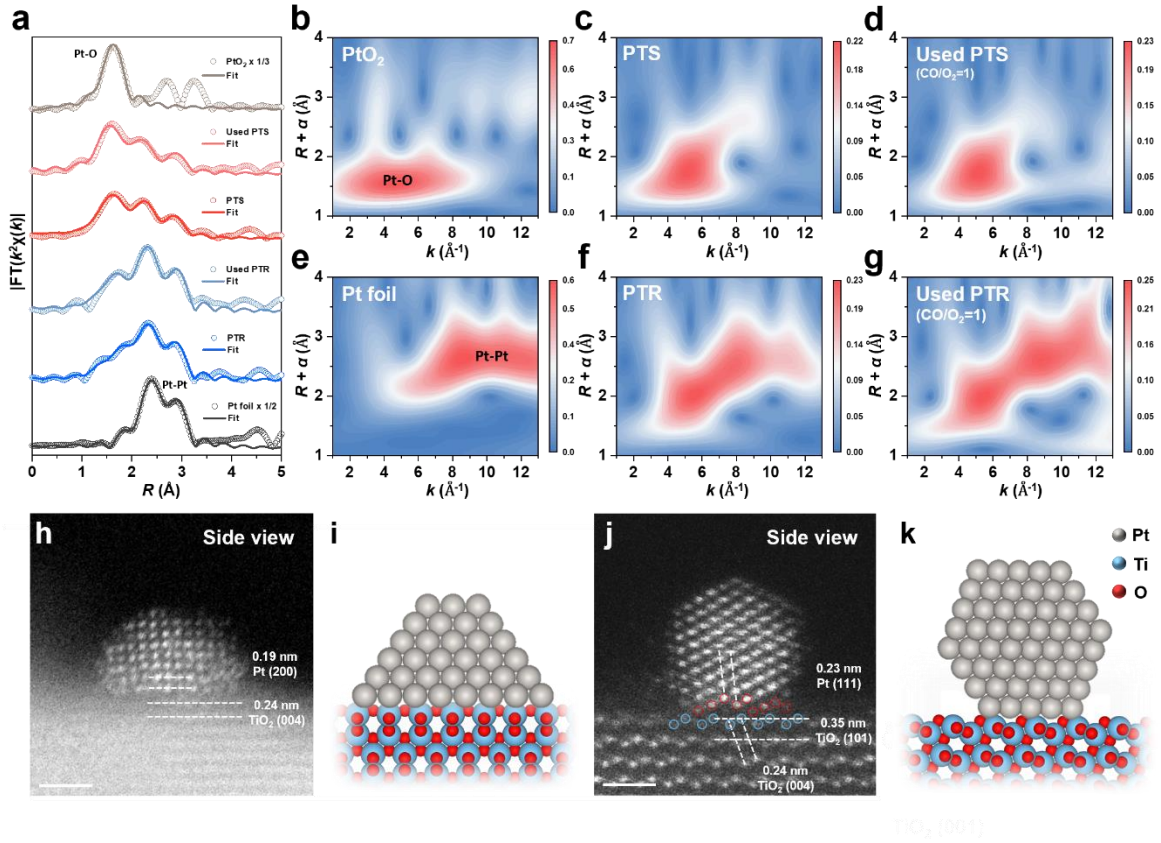

Figure 2. *Ex situ* EXAFS and STEM analyses illustrating evolution of Pt morphology of fresh and spent Pt/TiO_2 catalysts before and after CO oxidation. (a) Fourier transform k^2-weighted $\chi(k)$ EXAFS spectra at the Pt L_3-edge with fitting for fresh and spent Pt/TiO_2 catalysts (CO/O_2 = 1), compared to Pt foil and PtO_2 references. (b-g) Corresponding WT-EXAFS contour maps for (c) fresh and (d) spent Pt/TiO_2 catalysts, alongside (b) PtO_2 and (e) Pt foil references. (h, j) HAADF-STEM images (The scale bar is 1 nm) of spent Pt/TiO_2 catalysts: (h) PTS showing a side view of TiO_2(004) plane, and (j) PTR showing a side view of TiO_2(101) plane. The positions of Pt and Ti atoms in (j) are indicated by red and blue circles, respectively. (i, k) Structural model depicting reconstructed Pt NPs on (i) PTS and (k) PTR after CO oxidation.

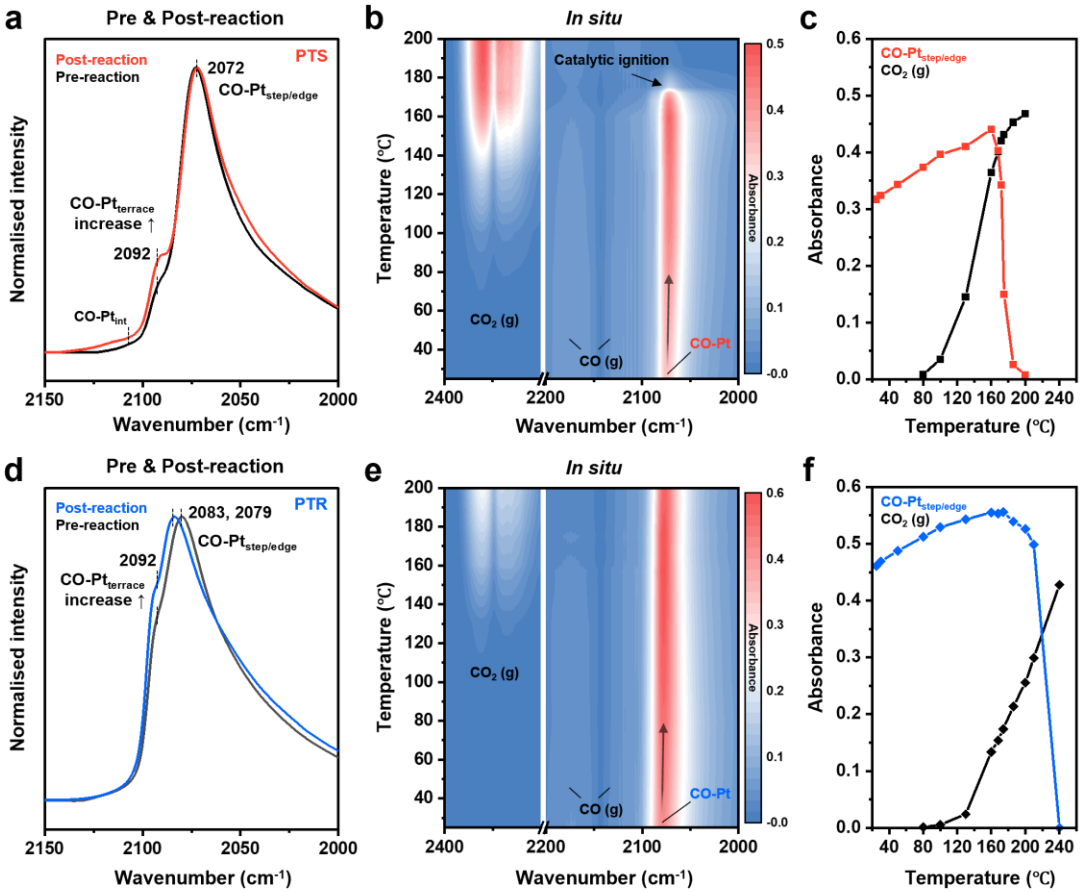

Figure 3. *In situ* DRIFTS spectra of Pt/TiO$_2$ catalysts during CO oxidation. (a, d) Normalised CO-DRIFTS spectra recorded pre- and post-CO oxidation at 25 °C. (b, e) Contour maps of *in situ* DRIFTS spectra acquired under CO oxidation. (c, f) Intensity plots tracking CO adsorbed on Pt$_{step/edge}$ sites and gas-phase CO$_2$ evolution.

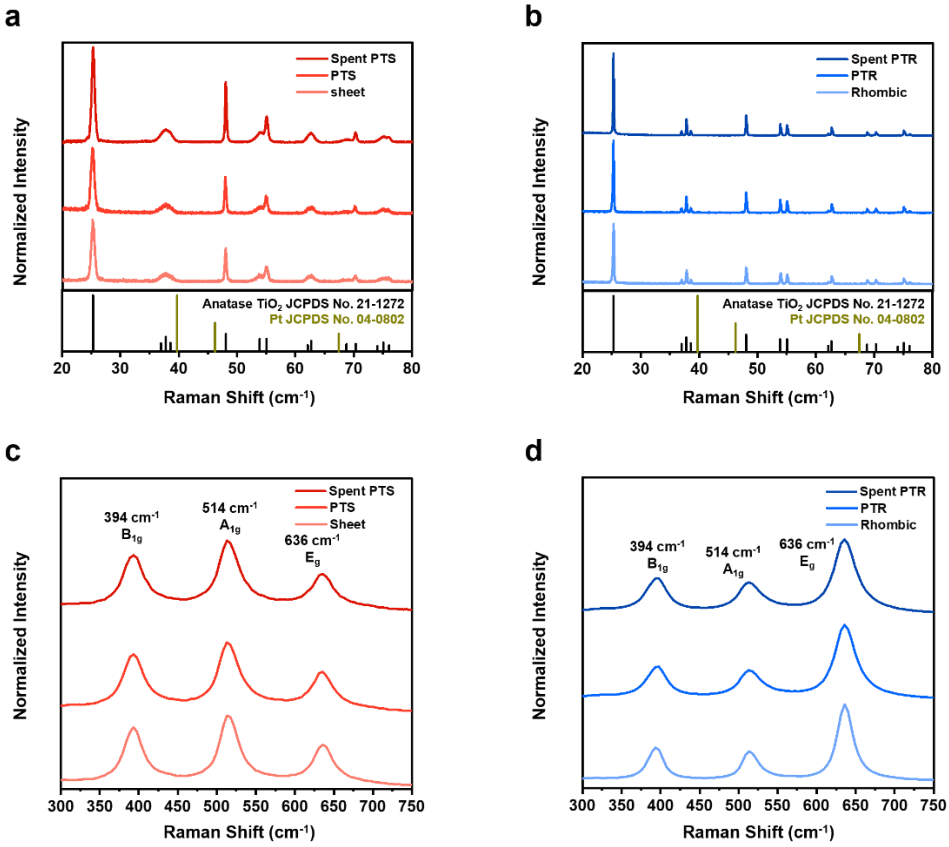

Supplementary Figure 3. (a–b) XRD patterns and (c–d) Raman spectra of TiO_2 supports and Pt/TiO_2 catalysts before and after CO oxidation. (a, c) Sheet-shaped TiO_2 with predominantly exposed (001) facets, fresh PTS, and spent PTS; (b, d) Rhombic TiO_2 with predominantly exposed (101) facets, fresh PTR, and spent PTR. Spent catalysts were prepared by treating the samples at 240 °C for 2 h (CO/O_2 = 1).

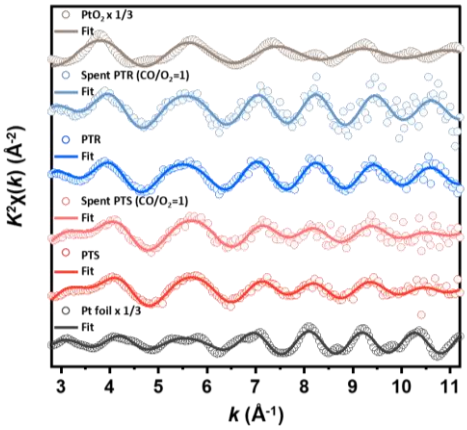

Supplementary Figure 7. Pt L_3-edge EXAFS k^2-weighted χ(k) spectra of fresh and spent Pt/TiO_2 catalysts, compared with Pt foil and PtO_2 reference samples. Spent catalysts (CO/O_2 = 1) were prepared by treating the samples at 240 °C for 2 h.

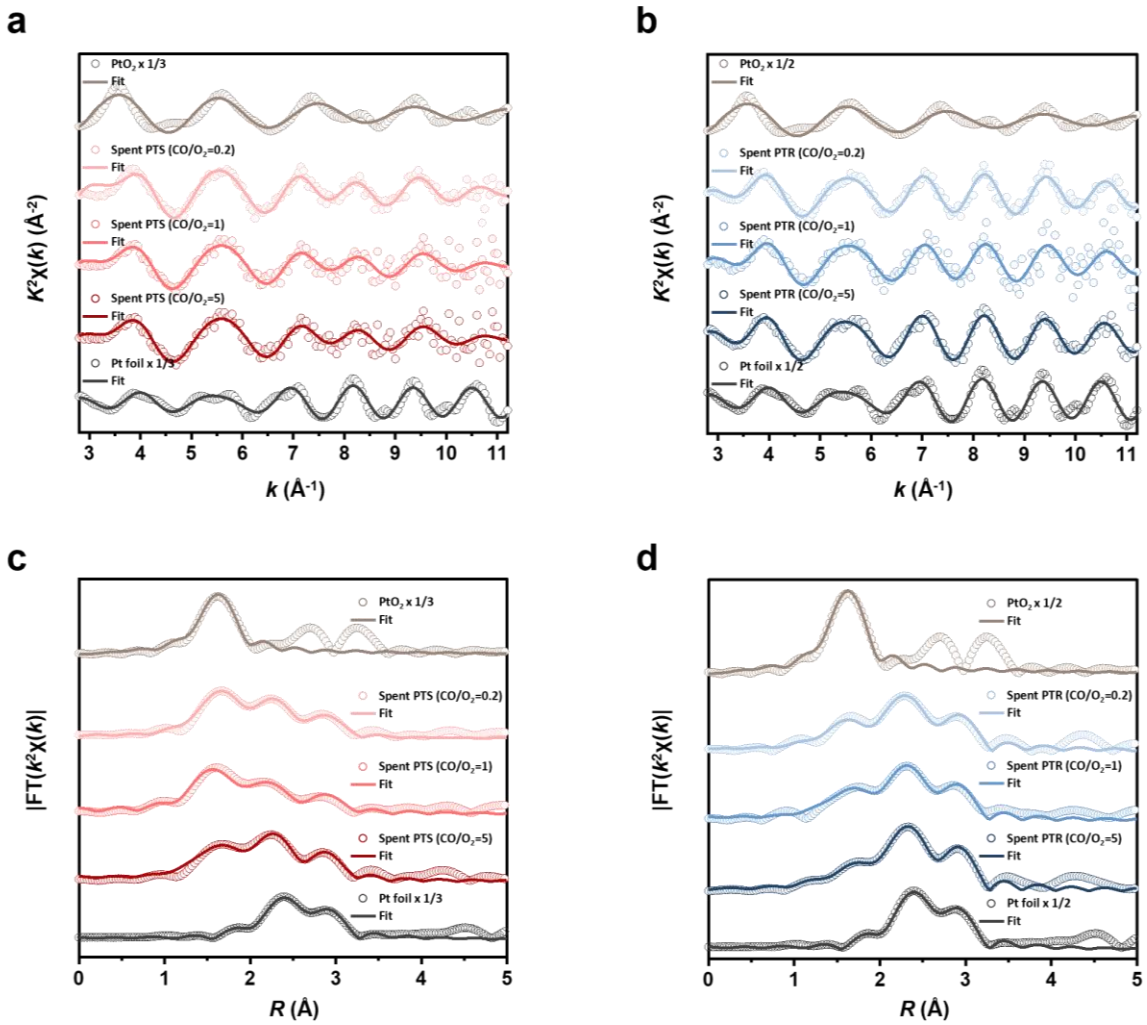

Supplementary Figure 8. (a, b) k^2-weighted $\chi(k)$ functions of Pt L_3-edge EXAFS spectra for spent Pt/TiO_2 catalysts after CO oxidation under different CO/O_2 ratios (0.2, 1, and 5). (c, d) Corresponding FT-EXAFS spectra and fitting results, showing the local coordination environment of Pt after catalytic reaction. Spent catalysts were prepared by treating the samples at 240 °C for 2 h (CO/O_2 = 0.2 and 1) and 350 °C for 2 h (CO/O_2 = 5). Further details regarding the temperature selection criteria are provided in Supplementary Note 2.

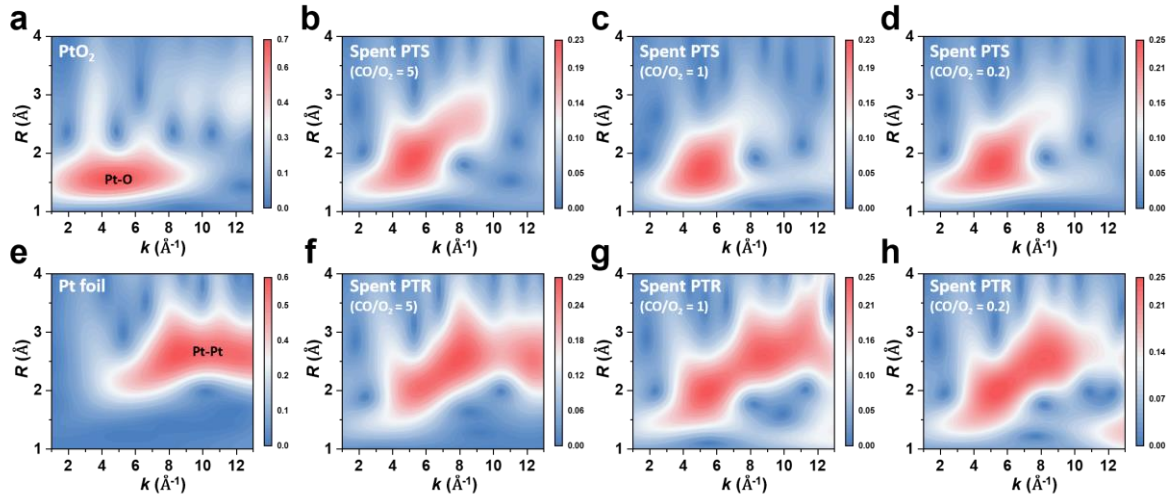

Supplementary Figure 9. WT contour maps of $k^2\chi(k)$ functions from Pt L_3-edge EXAFS for spent Pt/TiO_2 catalysts after CO oxidation under various CO/O_2 ratios, compared with reference materials: (a) PtO_2, (b–d) spent PTS at CO/O_2 = 5, 1, and 0.2, respectively, (e) Pt foil, and (f–h) spent PTR at CO/O_2 = 5, 1, and 0.2, respectively. Spent catalysts were prepared by treating the samples at 240 °C for 2 h (CO/O_2 = 0.2 and 1) and 350 °C for 2 h (CO/O_2 = 5). Further details regarding the temperature selection criteria are provided in Supplementary Note 2. These maps visualize changes in Pt coordination and bonding environments induced by different reaction conditions.

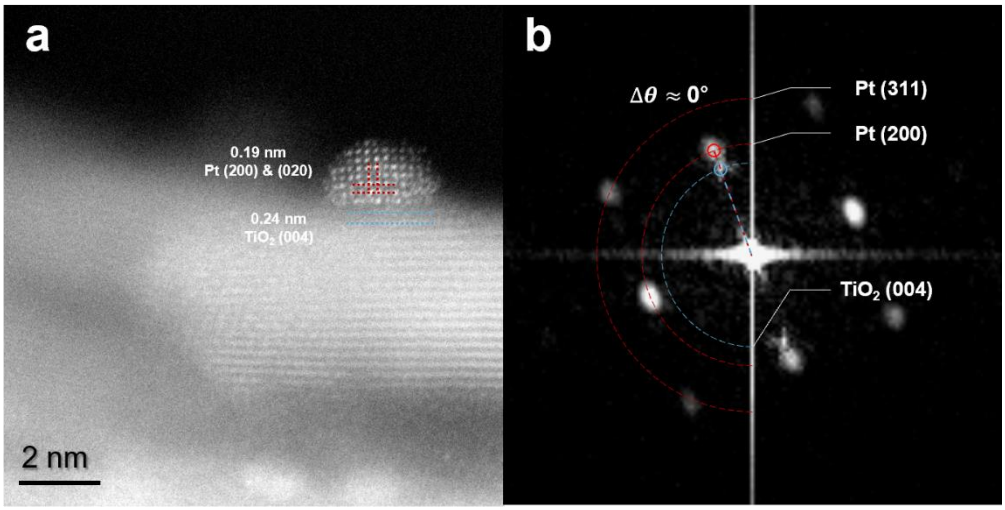

Supplementary Figure 10. (a) HAADF-STEM image of the spent PTS catalyst after CO oxidation. (b) Corresponding fast Fourier transform (FFT) pattern image, indicating lattice alignment and potential epitaxial relationship between Pt and the TiO_2(001) facet. Spent catalysts were prepared by treating the samples at 240 °C for 2 h (CO/O_2 = 1)

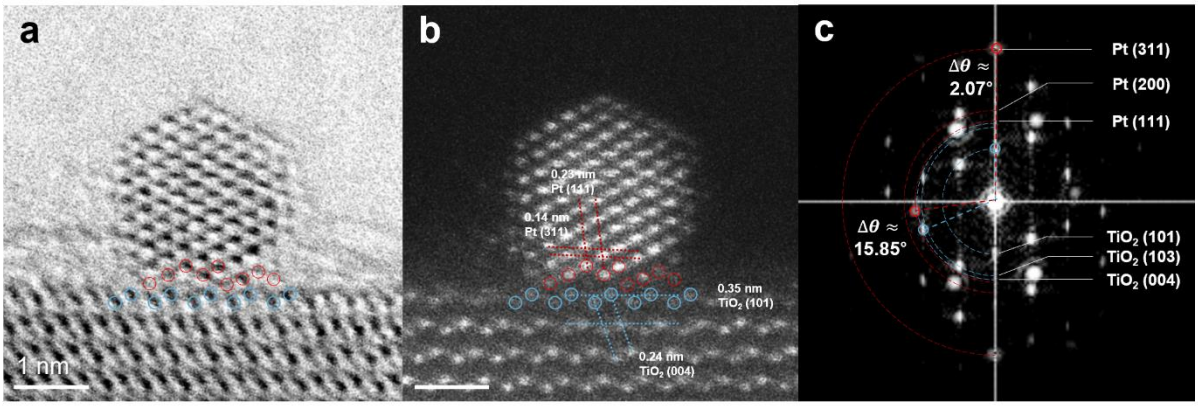

Supplementary Figure 11. (a) Bright-field and (b) dark-field STEM images of the spent PTR catalyst after CO oxidation. (c) Corresponding FFT pattern of image (b). The positions of Pt and Ti atoms in (b) are indicated by red and blue circles, respectively, based on contrast differences observed in (a), highlighting the lattice mismatches and interface step structures between Pt and the TiO_2(101) facet. Spent catalysts were prepared by treating the samples at 240 °C for 2 h (CO/O_2 = 1)

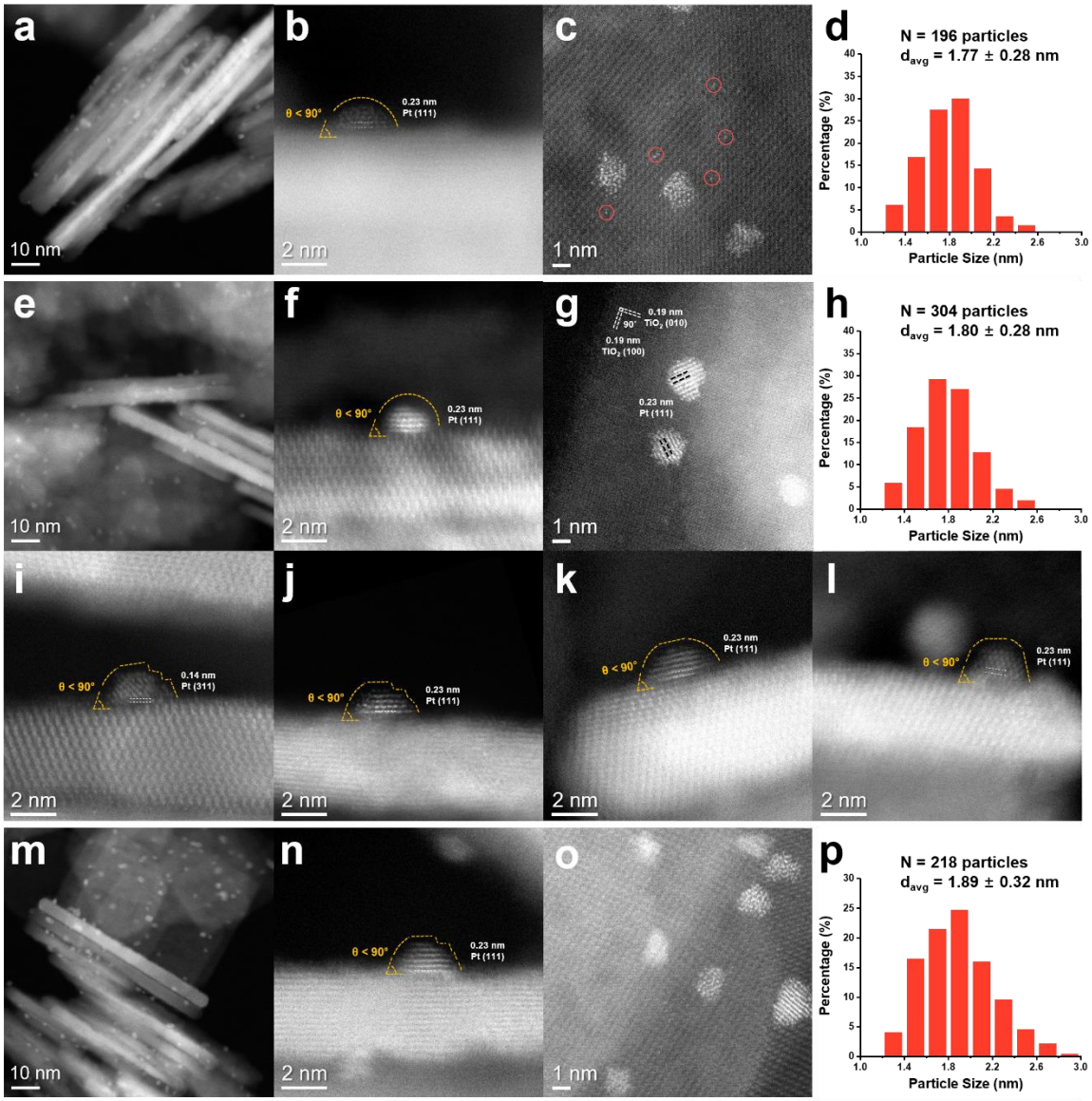

Supplementary Figure 12. HAADF−STEM images and corresponding Pt particle size distributions of the spent PTS catalyst after CO oxidation under varying CO/O_2 ratios: (a–d) CO/O_2 = 0.2, (e–l) CO/O_2 = 1, and (m–p) CO/O_2 = 5. Each set shows representative NP morphology and size histogram, indicating facet-dependent reconstruction behavior of Pt on TiO_2(001). For CO/O_2 = 0.2 and 1, the catalysts were treated at 240 °C for 2 h to prevent thermally induced sintering while ensuring that the CO-adsorbate-induced reconstruction process is fully reflected. For CO/O_2 = 5, the spent catalyst was treated at 350 °C for 2 h, corresponding to the maximum-conversion temperature of the undiluted PTR catalyst. No significant sintering of the spent PTS catalyst was observed across all conditions. Further details regarding the temperature selection criteria are provided in Supplementary Note 2.

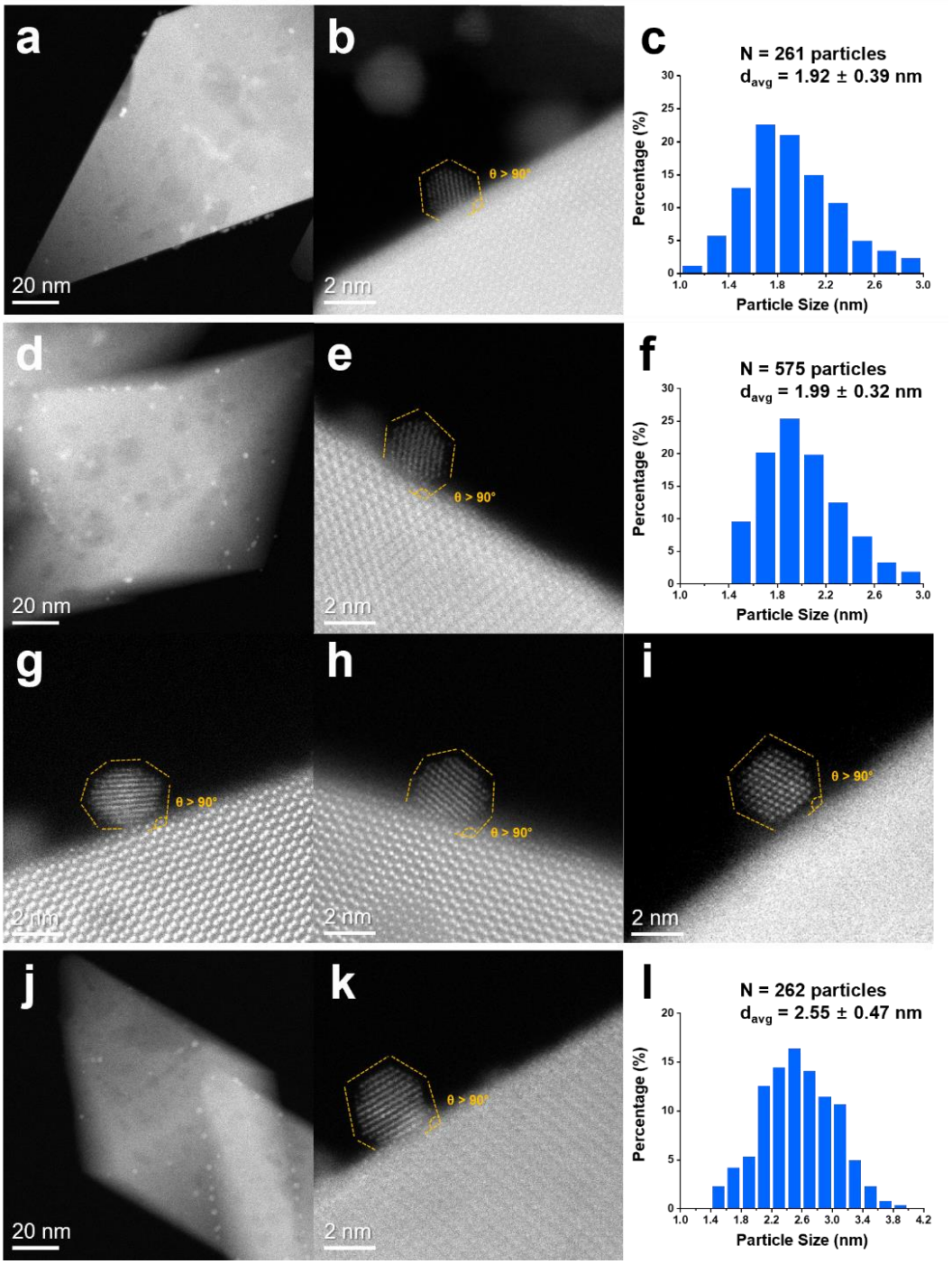

Supplementary Figure 13. HAADF−STEM images and corresponding Pt particle size distributions of the spent PTR catalyst after CO oxidation under various CO/O_2 ratios: (a–c) CO/O_2 = 0.2, (d–i) CO/O_2 = 1, and (j–l) CO/O_2 = 5. Each set shows representative NP morphology and size histogram, indicating facet-dependent reconstruction behavior of Pt on TiO_2(101). For CO/O_2 = 0.2 and 1, the catalysts were treated at 240 °C for 2 h to prevent thermally induced sintering while ensuring that the CO-adsorbate-induced reconstruction process is fully reflected. For CO/O_2 = 5, the spent catalyst was treated at 350 °C for 2 h, corresponding to the maximum-conversion temperature of the undiluted PTR catalyst; slight sintering was observed under this condition. Further details regarding the temperature selection criteria are provided in Supplementary Note 2.

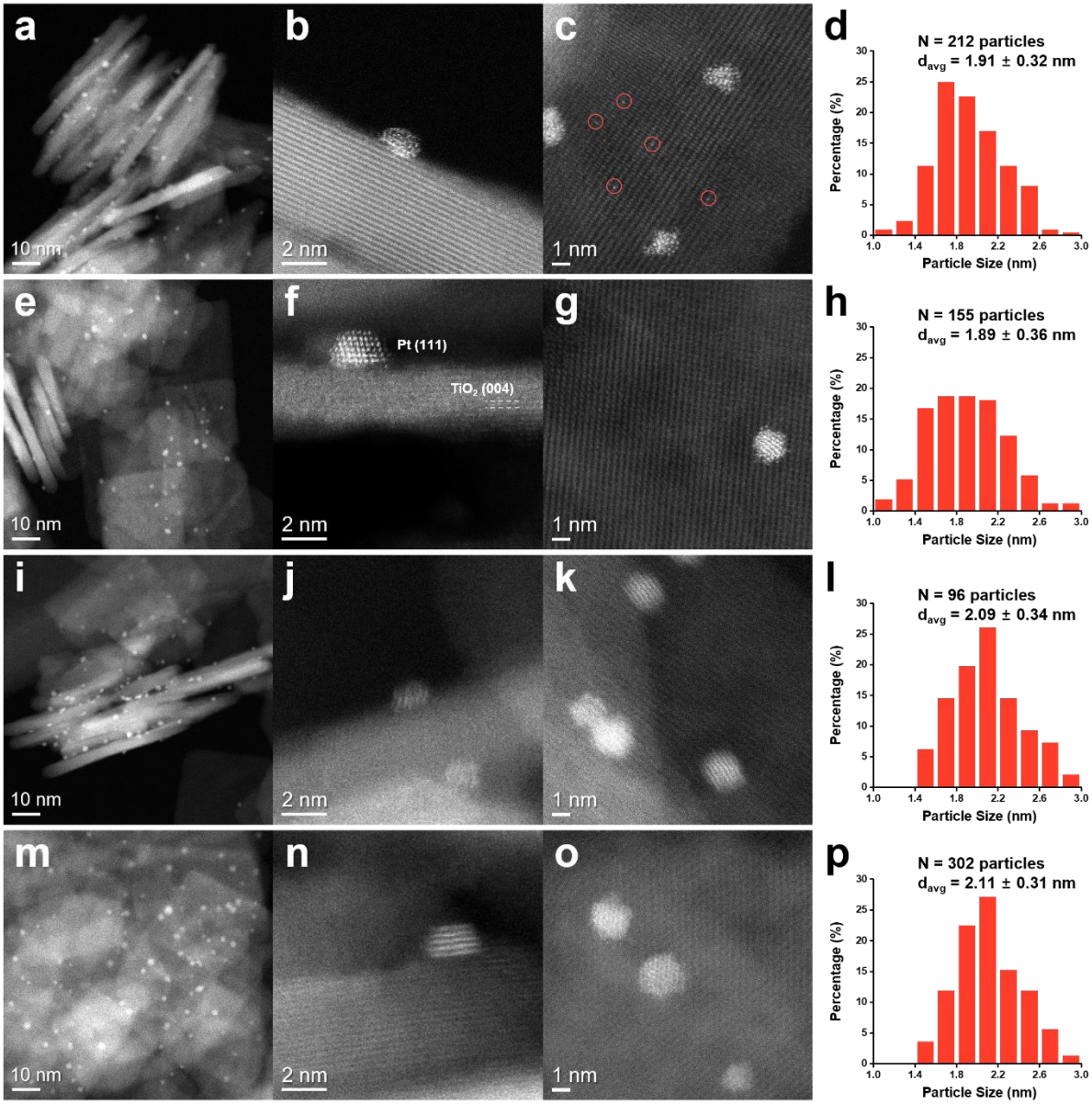

Supplementary Figure 14. HAADF−STEM images and corresponding Pt particle size distributions of the spent PTS catalyst after CO oxidation under varying CO/O_2 ratios: (a–d) CO/O_2 = 0.2, (e–h) CO/O_2 = 1, (i–l) CO/O_2 = 3, and (m–p) CO/O_2 = 5. Each set shows representative NP morphology and size histogram, indicating facet-dependent reconstruction behavior of Pt on TiO_2(001). Spent catalysts were prepared by treating the samples at 300 °C for 2 h (CO/O_2 = 0.2 and 1), 350 °C for 2 h (CO/O_2 = 3), and 400 °C for 2 h (CO/O_2 = 5). No significant sintering of the spent PTS catalyst was observed across all conditions. Further details regarding the temperature selection criteria are provided in Supplementary Note 2.

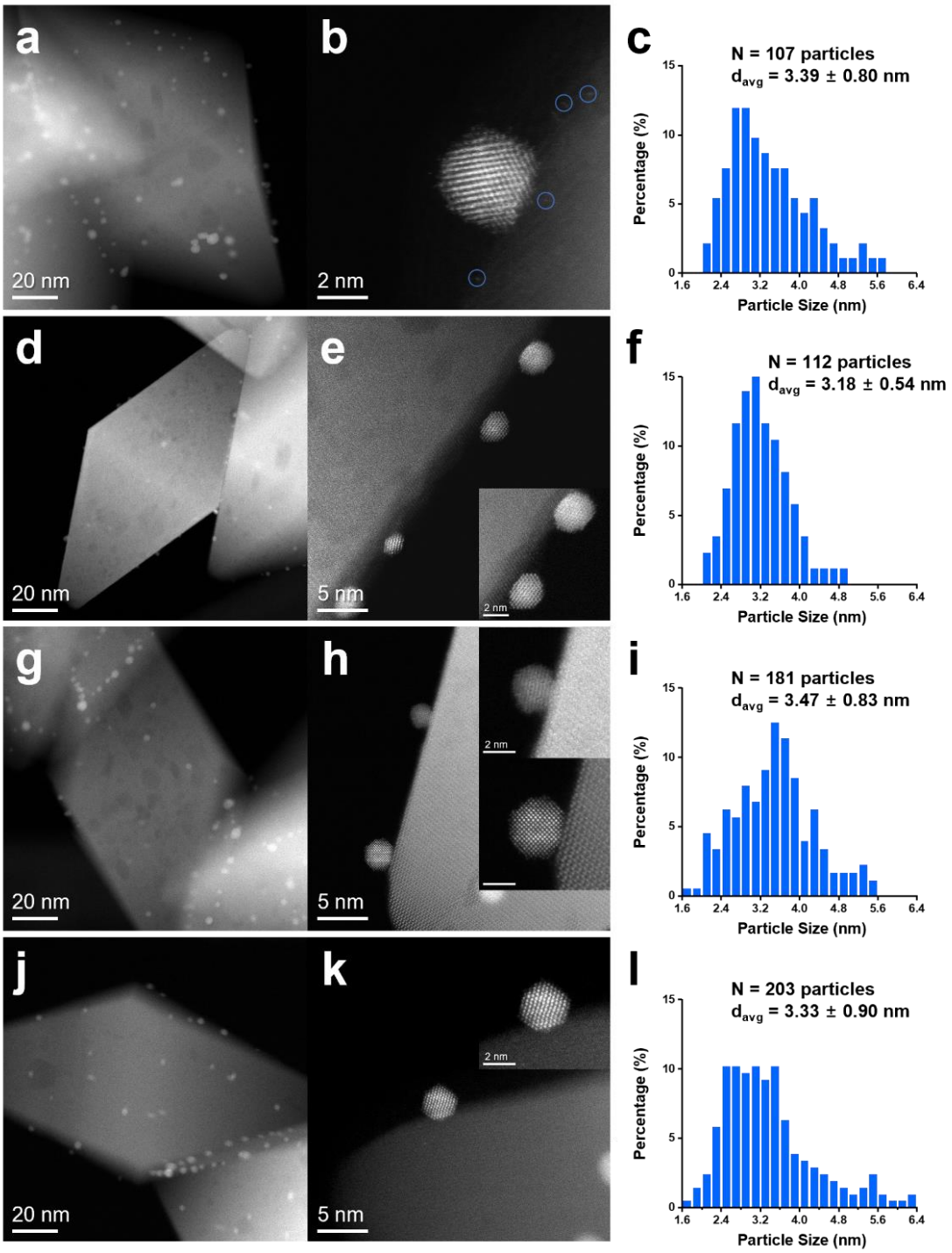

Supplementary Figure 15. HAADF−STEM images and corresponding Pt particle size distributions of the spent PTR catalyst after CO oxidation under various CO/O_2 ratios: (a–c) CO/O_2 = 0.2, (d–f) CO/O_2 = 1, (g–i) CO/O_2 = 3, and (j–l) CO/O_2 = 5. Each set shows representative NP morphology and size histogram, indicating facet-dependent reconstruction behavior of Pt on TiO_2(101). Spent catalysts were prepared by treating the samples at 300 °C for 2 h (CO/O_2 = 0.2 and 1), 350 °C for 2 h (CO/O_2 = 3), and 400 °C for 2 h (CO/O_2 = 5). Significant sintering of the spent PTR catalyst was observed across all conditions, indicating intrinsically weaker Pt–TiO_2 interactions compared with PTS. Further details regarding the temperature selection criteria are provided in Supplementary Note 2.

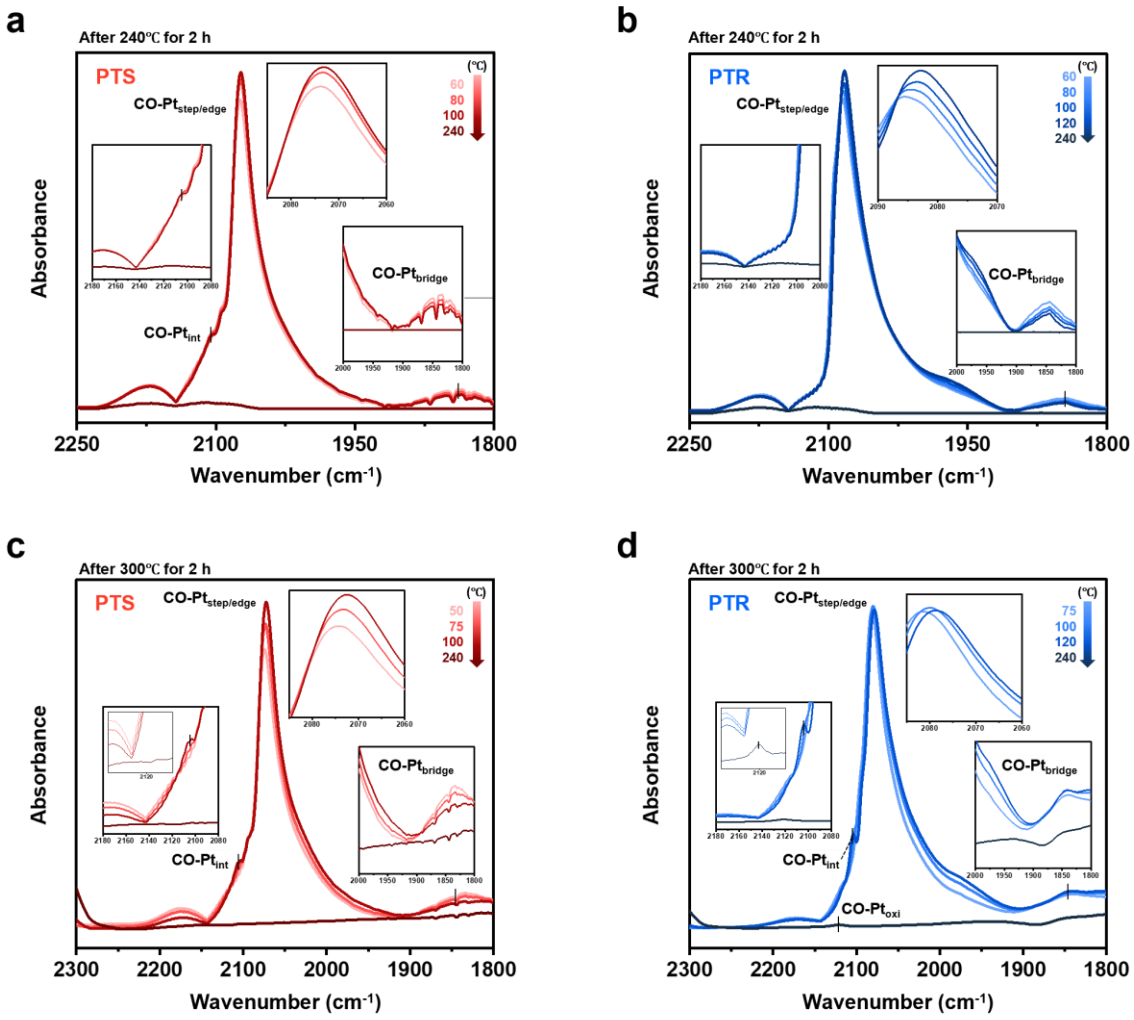

Supplementary Figure 30. *In situ* DRIFT spectra of (a, c) spent PTS and (b, d) spent PTR catalysts under CO oxidation condition ($CO/O_2 = 1$) at increasing temperatures. Spent catalysts were prepared by treating the samples at (a, b) 240 °C for 2 h and (c, d) 300 °C for 2 h. Characteristic bands corresponding to CO adsorbed on Pt_{int} sites, along with surface roughening features, highlight facet-dependent CO-induced Pt restructuring. Note that the spectrum in (d) was obtained using a spent PTR catalyst in which thermally induced sintering was observed (Supplementary Fig. 15). Additionally, a peak at ~2120 cm^{-1} observed in the inset of (d) appears after ignition and is assigned to CO adsorbed on oxidized Pt sites (Pt_{oxi}), which may hinder catalytic activity due to stronger CO binding.[1, 2]

Supplementary Table 2. Fitting results of the Pt L_3-edge EXAFS spectra for fresh and spent Pt/TiO_2 catalysts under different CO/O_2 ratios (0.2, 1, and 5), compared with Pt foil and PtO_2 references. Spent catalysts were prepared by treating the samples at 240 °C for 2 h (CO/O_2 = 0.2 and 1) and 350 °C for 2 h (CO/O_2 = 5). Further details regarding the temperature selection criteria are provided in Supplementary Note 2.

Catalysts	shell	CN	d (Å)	σ^2	E_0 shift	R factor
Pt foil	Pt−Pt	12.0	2.76 ± 0.01	0.004 ± 0.001	7.1 ± 0.7	0.0095
PtO_2	Pt−O	6.0	2.02 ± 0.01	0.003 ± 0.001	10.5 ± 1.5	0.0063
Fresh PTS	Pt−Pt	6.4 ± 1.2	2.71 ± 0.01	0.010 ± 0.002	5.5 ± 1.7	0.0113
	Pt−O	1.6 ± 0.4	1.97 ± 0.01	0.005 ± 0.003		
Spent PTS, O_2-rich (CO/O_2=0.2)	Pt−Pt	6.6 ± 2.2	2.74 ± 0.02	0.010 ± 0.003	8.2 ± 2.5	0.0063
	Pt−O	1.9 ± 0.7	2.00 ± 0.02	0.005 ± 0.004		
Spent PTS (CO/O_2=1)	Pt−Pt	6.8 ± 1.7	2.70 ± 0.02	0.011 ± 0.003	4.0 ± 1.9	0.0162
	Pt−O	1.7 ± 0.4	1.96 ± 0.02	0.004 ± 0.003		
Spent PTS, CO-rich (CO/O_2=5)	Pt−Pt	8.6 ± 1.6	2.73 ± 0.01	0.010 ± 0.002	5.3 ± 1.6	0.0096
	Pt−O	1.3 ± 0.6	1.97 ± 0.02	0.005 ± 0.004		
Fresh PTR	Pt−Pt	8.1 ± 1.2	2.74 ± 0.01	0.008 ± 0.001	6.7 ± 1.7	0.0077
	Pt−O	1.4 ± 0.8	2.00 ± 0.03	0.011 ± 0.009		
	Pt−Pt	8.2 ± 1.4	2.74 ± 0.01	0.007 ± 0.001	6.2 ± 1.3	0.0115

Spent PTR, O_2-rich (CO/O_2=0.2)	Pt–O	1.2 ± 0.5	1.97 ± 0.01	0.007 ± 0.005		
Spent PTR (CO/O_2=1)	Pt–Pt	8.2 ± 1.2	2.74 ± 0.01	0.007 ± 0.001	7.0 ± 1.3	0.0032
	Pt–O	1.2 ± 0.4	1.97 ± 0.02	0.005 ± 0.004		
Spent PTR, CO-rich (CO/O_2=5)	Pt–Pt	9.8 ± 0.8	2.75 ± 0.01	0.007 ± 0.001	6.3 ± 0.6	0.0033
	Pt–O	1.1 ± 0.4	1.99 ± 0.02	0.010 ± 0.006		

CN represents the average coordination number around the Pt absorber atom, σ^2 is the Debye–Waller factor, d is the bond distance, and R-factor indicates the quality of the fit. The amplitude reduction factor (S_0^2) was fixed at 0.77, as determined from Pt foil fitting. EXAFS fitting was performed using k^2-weighted spectra over the ranges: $2.8(3.0) < k < 10.8(11.2)$ Å^{-1} and $1(1.3) < r < 3.3(3.5)$ Å. Only single-scattering paths from the first coordination shell were included in the EXAFS fitting.

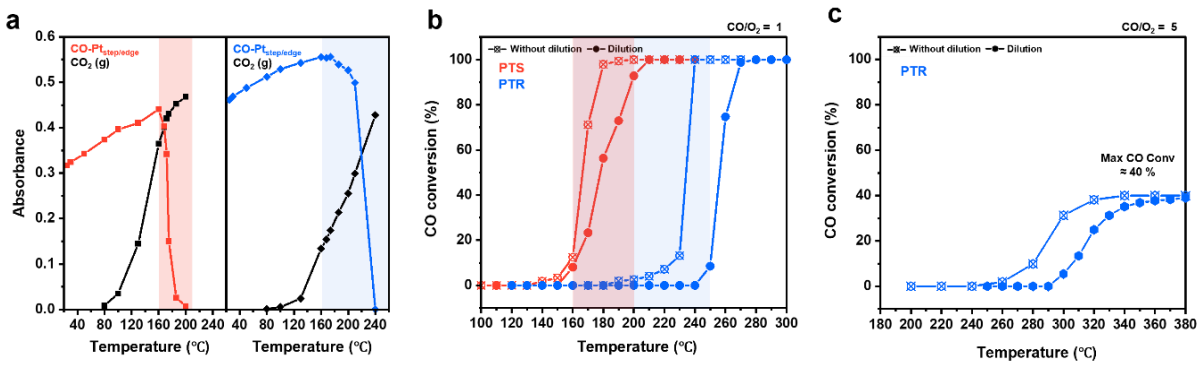

Supplementary Figure 44. (a) Intensity plots tracking CO adsorbed on $Pt_{step/edge}$ sites and gas-phase CO_2 evolution under the $CO/O_2 = 1$ condition, corresponding to the data shown in Fig. 3. (b–c). Temperature-dependent CO conversion profiles of PTS and PTR catalysts, comparing diluted and undiluted catalyst beds under (b) $CO/O_2 = 1$ and (c) $CO/O_2 = 5$ conditions. The colored region highlights the catalytic ignition temperature range that matches the ignition behavior observed in both the *in situ* DRIFTS measurements and the reactivity tests under the $CO/O_2 = 1$ condition.

Comment 1: The reshaping of the Pt NPs lacks sufficient/direct evidence. The STEM images of fresh samples exhibit insufficient resolution, which did not show their authentic shape and lattice structure. Notably, the high-resolution images of fresh Pt NPs in Figure S2d exhibit a cuboctahedral shape that is highly similar to that of the spent sample. This significantly undermining the validity of the authors' conclusions regarding Pt reshaping. Atomic-resolution STEM images of both Pt NPs before and after reaction should be provided with the same quality. *In situ* TEM experiment is also encouraged to show direct evidence of the reconstruction of Pt NPs.

Response: We sincerely appreciate the reviewer's thoughtful comment. As correctly noted, the STEM images of the fresh and spent samples in the original manuscript lacked sufficient resolution for a rigorous comparison of Pt shape and lattice structure. To address this, we performed additional STEM measurements aimed at obtaining atomic-resolution images that resolve the lattice fringes of both Pt and TiO_2. However, as discussed in Supplementary Note 4, there is an inherent experimental limitation when aligning the zone axis of the thin TiO_2 nanosheets in PTS, in contrast to the more symmetric rhombic TiO_2 crystals in PTR. As a result, in many PTS images—both fresh and spent—the Pt lattice fringes are only partially visible or appear along a single direction, and in most cases, only the TiO_2(004) lattice planes are clearly resolved. Nevertheless, the side-view images of Pt NPs on the TiO_2(001) facet (PTS) versus the TiO_2(101) facet (PTR) still reveal distinct differences in contact angles and surface faceting. Within these experimental constraints, we believe the new images provide sufficient resolution to assess facet-dependent morphological trends in Pt.

In the revised manuscript, we have replaced the STEM images of the fresh catalysts (Fig. 1) and spent catalysts (Fig. 2) with higher-resolution data. Additional representative STEM images of the fresh samples are now provided in Supplementary Fig. 1, and those of the spent samples in Supplementary Figs. 12 and 13. These are annotated with schematic indicators of Pt shape and contact angles to clarify the facet-specific morphology.

We also appreciate the reviewer's point regarding Supplementary Fig. 2d (now Supplementary Fig. 1c in the revised version). As clarified in the updated figure caption, the cuboctahedral Pt NPs in this image are not located on the TiO_2(001) facet but instead on the (101) termination of the nanosheet. Our intention was to demonstrate that Pt morphology on the (101) termination of PTS resembles that observed for PTR, supporting the idea of facet-dependent stabilization. However, this context was not clearly explained in the original manuscript, and we appreciate

the reviewer for pointing out the potential for confusion. In the revised version, we have explicitly marked the Pt NPs located on the (001) facet with red arrows and those on the nanosheet (101) termination with blue arrows in Supplementary Fig. 1, and we have revised the figure caption accordingly.

We also appreciate the reviewer's recommendation to perform *in situ* TEM experiments to directly observe Pt restructuring. Accordingly, we conducted in situ heating TEM measurements using a Climate GVB holder (DENS solutions, Netherlands). Given that Pt NPs are more readily observable in PTR, the *in situ* measurements were first performed using the PTR sample.

For sample preparation, the catalyst dispersion in ethanol was drop-cast onto the bottom SiN_x heating chip and dried overnight. The top chip, containing electron-transparent SiN_x windows (50 nm thickness), was then assembled, mounted onto the holder, and inserted into the TEM (Fig. R2a, b). All observations were carried out on a JEOL JEM-ARM300F microscope operated at 160 kV, the lowest available accelerating voltage, to minimize beam damage. TEM images were initially acquired at 25 °C under a gas flow of 0.04 $mL \cdot min^{-1}$ of 1% CO + 1% O_2 in Ar (500 mbar). However, during the experiment, rapid electron-beam-induced CO decomposition led to severe carbon contamination (>30 nm) across the catalyst surface (Fig. R2c–e), which prevented meaningful observation of Pt structural evolution under reaction conditions.

While direct *in situ* evidence of Pt reconstruction could not be obtained due to this limitation, the newly acquired atomic-resolution STEM images, together with the facet-dependent morphology trends that remain consistent regardless of Pt particle size (as discussed in our response to Comment 2), provide strong complementary support for our interpretation of facet-controlled Pt restructuring in this system.

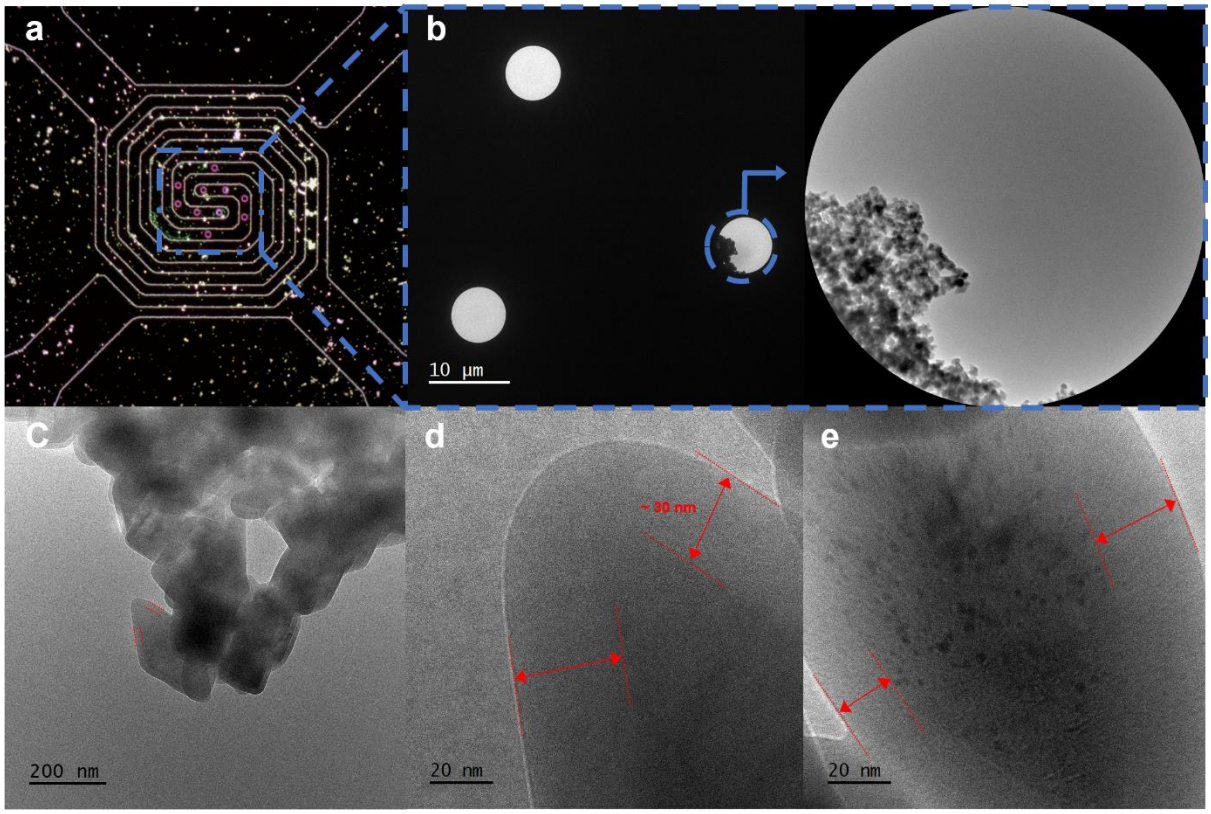

Figure R2. (a) Optical microscope image of the assembled SiN_x heating chip. (b) TEM overview of the electron-transparent SiN_x window region loaded with the PTR catalyst. (c–e) TEM images of the PTR sample acquired under 1% CO + 1% O_2/Ar flow (500 mbar) at 25 °C, showing severe carbon contamination (>30 nm) resulting from electron-beam-induced CO decomposition. This contamination prevented meaningful visualization of the Pt NP.

Action taken: In the revised manuscript, the STEM images of the fresh catalysts (Fig. 1) and spent catalysts (Fig. 2) have been replaced with higher-resolution images. Additional representative STEM images of the fresh samples are now provided in Supplementary Fig. 1, and those of the spent samples in Supplementary Figs. 12 and 13, with schematic indicators of Pt particle shapes and annotated contact angles to more clearly illustrate the facet-dependent morphological trends of Pt NPs on TiO_2.

Supplementary Fig. 1 has also been updated to explicitly distinguish Pt NPs on different TiO_2 facets. Particles on the TiO_2(001) facet are marked with red arrows, while those on the nanosheet (101) termination are indicated with blue arrows. The following clarifying caption has been added: *"For PTS, Pt NPs located on the TiO_2(001) facet are marked with red arrows, whereas those positioned on the nanosheet (101) termination are indicated with blue arrows. The Pt morphology observed on the nanosheet (101) termination resembles that on the TiO_2(101) facet in PTR, consistent with facet-dependent Pt morphology."*

Although direct atomic-scale tracking of Pt reconstruction under reaction conditions by in situ TEM remains experimentally challenging in this system, we hope that the revised structural evidence offers improved contextual clarity and adequately addresses the reviewer's concern regarding Pt reshaping.

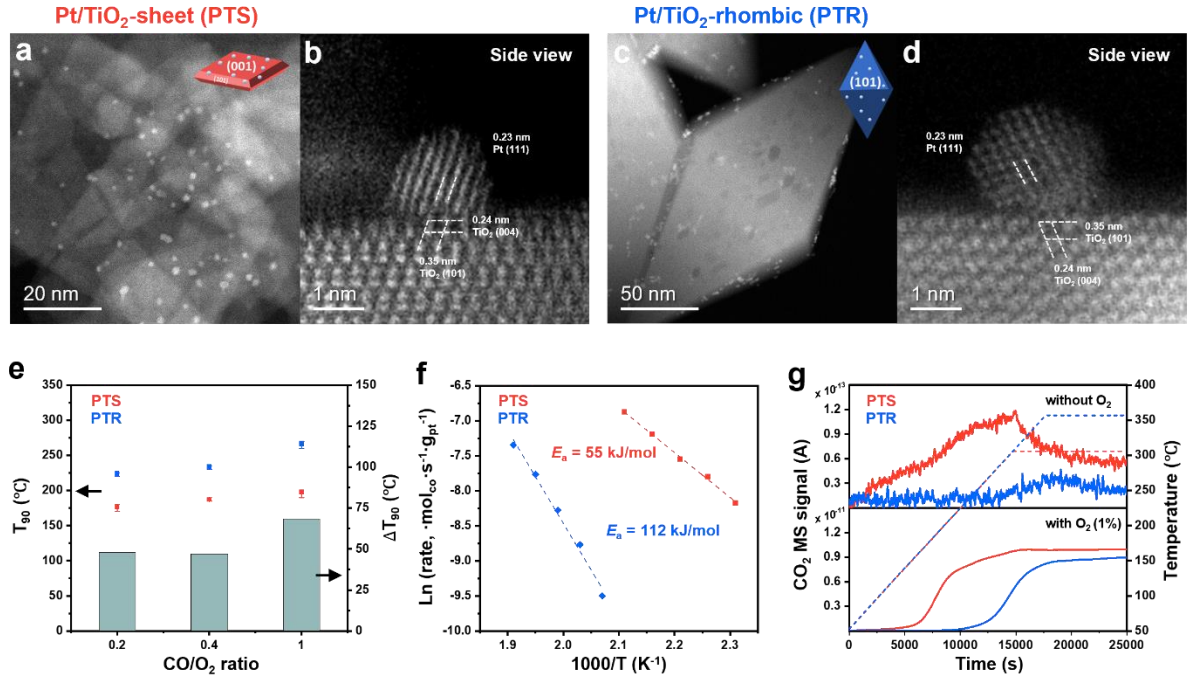

Figure 1. Structural characterisation and CO oxidation performance of Pt/TiO_2 catalysts. (a–d) HAADF–STEM images of the as-prepared catalysts: (a, c) low-magnification images of PTS and PTR, respectively, and (b, d) high-magnification side-view images showing Pt NPs on the TiO_2(004) plane (PTS) and TiO_2(101) plane (PTR). (e) T_{90} values representing the temperature at which 90% CO conversion is reached for PTS and PTR at various CO:O_2 ratios. (f) Apparent activation energies (E_a) for CO oxidation at $CO/O_2 = 1$. (g) CO_2 mass spectrometry signals during CO-TPR experiments under CO with and without O_2 (Bottom: 5% CO + 1% O_2/Ar, Top: 5% CO/Ar).

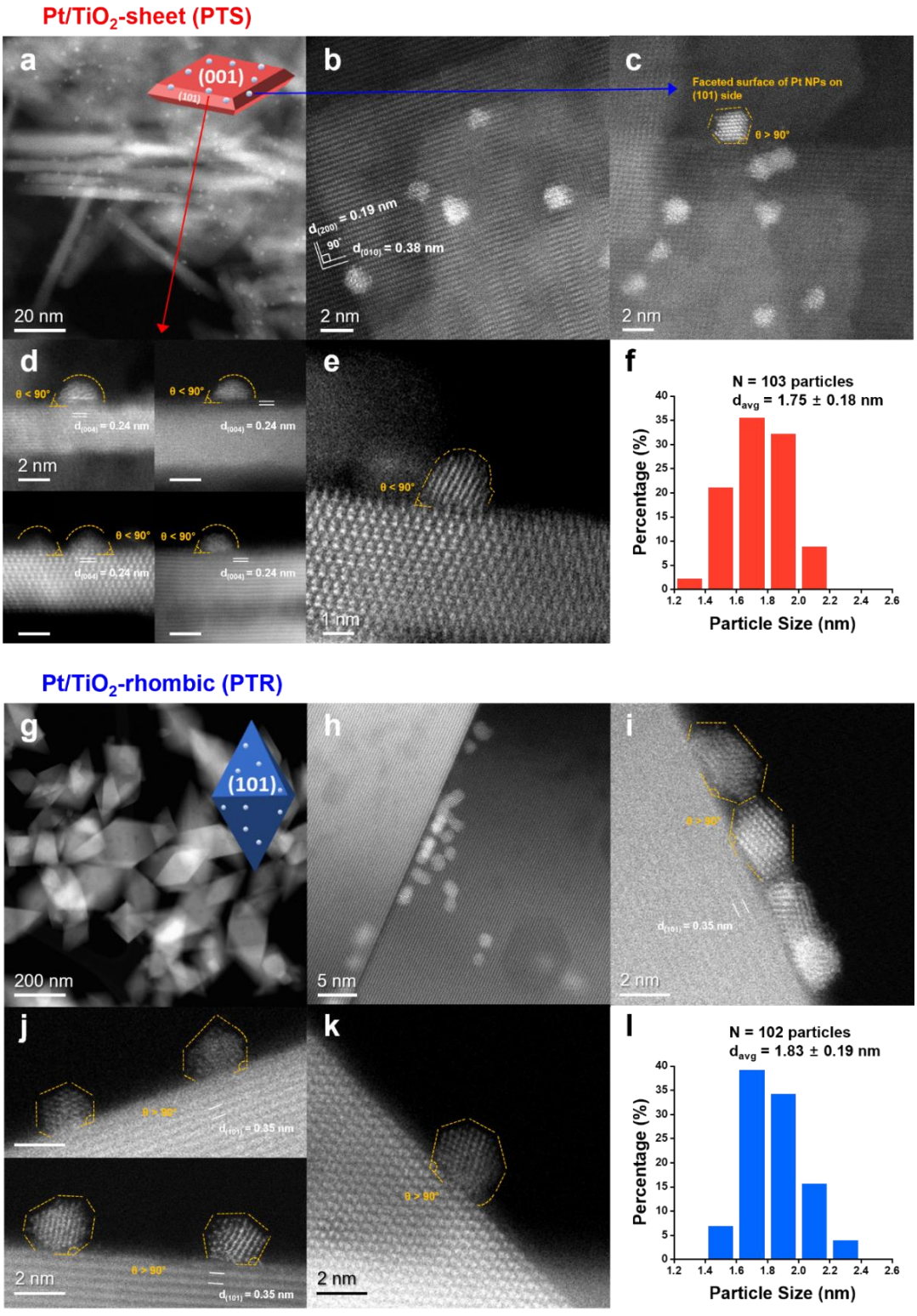

Supplementary Figure 1. (a–e, g–k) HAADF-STEM images of the as-prepared Pt/TiO_2 catalysts: (a–e) PTS with exposed (001) facets and (g–k) PTR with exposed (101) facets. (f, l) Corresponding histograms showing the Pt NP size distributions for (f) PTS and (l) PTR. For PTS, Pt NPs located on the TiO_2(001) facet are marked with red arrows, whereas those positioned on the nanosheet (101) termination are indicated with blue arrows. The Pt morphology observed on the nanosheet (101) termination resembles that on the TiO_2(101) facet in PTR, consistent with facet-dependent Pt morphology.

Fig. 2 and Supplementary Figs. 12 and 13 are presented in the response to General Comments.

Comment 2: In Figure S13, the size of Pt NPs on PTR shows a significant increase from 1.8nm to 3.2nm after reaction likely due to sintering. However, a critical inconsistency emerges when comparing this data to the spent Pt NPs presented in Figure 2. The Pt NP selected for analysis in Figure 2 are substantially smaller than the 3.2 nm average size reported in Figure S13. This seems to be arbitrary and raises concerns about the representativeness of the data used to support claims about post-reaction shape changes. The authors should show more individual Pt NPs of different sizes to validate the change of shape after reaction statistically.

Response: We appreciate the reviewer's important observation regarding the representativeness of the STEM images shown for the spent PTR catalyst in the original Fig. 2i. As discussed in our response to the General Comments, all post-reaction structural characterizations have now been repeated under revised conditions (240 °C for 2 h) to eliminate sintering effects (see Supplementary Note 2). The resulting STEM images (Figs. 2h, j and Supplementary Figs. 10–13) are fully consistent with the central conclusions of the original manuscript. Accordingly, the reviewer's concern regarding data representativeness has been carefully addressed in the revised version.

Building on this, we also appreciate the reviewer's thoughtful suggestion to examine the morphological evolution of Pt nanoparticles across a range of sizes. Although the revised dataset already reflects statistically representative populations, we agree that demonstrating size-independent Pt morphology trends would further reinforce our conclusions. To this end, we conducted additional experiments in which Pt nanoparticles with controlled diameters ranging from 1.5 to 5 nm were deposited on each TiO_2 facet, followed by post-reaction treatment under the same conditions (240 °C for 2 h, $CO/O_2 = 1$).

The STEM images of these size-controlled catalysts and the comparison of their pre- and post-reaction Pt size distributions (Supplementary Figs. 17 and 18) confirm that sintering remains negligible across all sizes. Moreover, high-magnification STEM images (Supplementary Fig. 19) reveal a consistent, size-independent trend in Pt morphology depending on the TiO_2 facet: Pt on TiO_2(001) forms hemispherical particles with a broad interfacial contact, whereas Pt on TiO_2(101) exhibits smaller contact areas together with faceted, cuboctahedral-like surface structures. As the particle size approaches ~4 nm, Pt on TiO_2(001) also exhibits a gradual

evolution toward more faceted geometries due to geometric size effects; however, even in this size regime, the interfacial contact area remains noticeably larger than that observed for Pt on TiO_2(101). Furthermore, for the size-controlled catalysts, the post-reaction CO–DRIFTS spectra (Supplementary Fig. 20) revealed systematic changes in CO adsorption features that correlate with the Pt surface structures. As the Pt particle size increased, both spent Pt/TiO_2(001) and Pt/TiO_2(101) catalysts exhibited an increased relative intensity of the CO–$Pt_{terrace}$ feature (2100–2080 cm^{-1}) compared to the CO–$Pt_{step/edge}$ feature (2080–2060 cm^{-1}). In our Pt/TiO_2 system, spent catalysts with an average post-reaction Pt size above ~ 3 nm exhibited sharper CO adsorption bands with reduced full width at half maximum (FWHM) compared with the sub-3-nm samples, consistent with geometric NP models showing that the fraction of exposed terrace sites increases with particle size and that dipoles couple more effectively on flatter surfaces (*ACS Catal*. 2018, 8, 7368-7387, *J. Am. Chem. Soc.* 2011, 133, 4498-4517).

Importantly, even within the sub-3-nm size regime, clear facet-dependent differences were observed. The spent Pt/TiO_2(001) catalyst with an average Pt size of 2.72 nm exhibited a peak at 2081 cm^{-1}, whereas the spent Pt/TiO_2(101) catalyst—despite its smaller average Pt size of 1.99 nm—exhibited a peak at 2083 cm^{-1}. Although CO adsorption peaks generally shift to higher wavenumbers with increasing Pt particle size due to effective dipole–dipole coupling, the larger Pt NPs on TiO_2(001) nonetheless showed lower-wavenumber peaks than the smaller Pt NPs on TiO_2(101). Moreover, even the smallest Pt/TiO_2(101) catalyst (1.59 nm) exhibited a distinct CO–$Pt_{terrace}$ feature. Across all catalysts with comparable Pt sizes, Pt/TiO_2(101) consistently showed a more pronounced CO–$Pt_{terrace}$ feature than Pt/TiO_2(001), indicating a higher proportion of faceted Pt surfaces on TiO_2(101), even when particles were smaller.

As discussed in the Introduction, the Wulff–Kaischew theorem states that the equilibrium morphology of supported metal NPs is governed by the balance between the metal–support interfacial free energy and the intrinsic surface free energy of the metal. Both STEM observations and CO-DRIFTS analyses reveal a size-independent trend in Pt morphology, consistently showing that the stronger Pt–TiO_2(001) interaction favors hemispherical particles with broader metal–support contact areas, whereas the weaker interaction on TiO_2(101) allows Pt to adopt more stable faceted geometries with smaller contact areas. These differences originate from facet-dependent metal–support interactions rather than particle-size effects. Accordingly, the additional experiments further reinforce the central conclusion of the manuscript, demonstrating that the facet-dependent reconstruction behavior indeed persists

even when the Pt particle size is systematically varied.

Action taken: We have expanded the *Characterization of TiO_2 facet-dependent structural dynamics of Pt NPs* section to include additional results obtained using size-controlled Pt/TiO_2 catalysts, in order to validate the facet-dependent Pt morphology trends across different particle sizes. The size-independent nature of Pt morphological evolution on each TiO_2 facet is now discussed in detail, and the corresponding experimental results are presented in Supplementary Figs. 17–20. The following paragraph has been added on Pages 8–9: *"To assess the generality of the facet-dependent Pt morphologies across different particle sizes, additional experiments were conducted using size-controlled Pt/TiO_2 catalysts with average Pt sizes ranging from 1.5 to 5 nm (Supplementary Figs. 17 and 18). Detailed discussion is provided in Supplementary Note 3. In summary, high-magnification STEM images (Supplementary Fig. 19) further reveal a consistent facet-dependent trend in Pt morphology that is largely independent of particle size. Post-reaction CO-DRIFTS spectra of the size-controlled catalysts (Supplementary Fig. 20) further corroborate these observations. For example, size-controlled $Pt/TiO_2(101)$ catalysts consistently exhibits a stronger CO–$Pt_{terrace}$ feature than that of (001) catalysts at comparable particle sizes. Notably, a distinct CO–$Pt_{terrace}$ feature is already evident for the smallest $Pt/TiO_2(101)$ catalyst (1.59 nm), indicating that the tendency toward faceted Pt surfaces on $TiO_2(101)$ is preserved even at small particle sizes. These results demonstrate that the differences in Pt morphology are predominantly governed by the TiO_2 facet, rather than by particle size. Separately, electron-beam-induced Pt reconstruction observed during STEM analysis of the fresh PTS and PTR catalysts provides additional qualitative evidence supporting the observed facet-dependent reconstruction behaviour (Supplementary Note 4)."*

An extended discussion of these results is also provided in Supplementary Note 3: *"**Supplementary Note 3. Facet-Dependent Pt NP Morphology Across Different Particle Sizes***

To further elucidate whether the facet-dependent Pt morphologies observed in this study persist across different particle sizes, additional experiments were conducted using size-controlled Pt/TiO_2 catalysts with average Pt diameters ranging from 1.5 to 5 nm. This size regime was intentionally selected because the dominant fractions of exposed Pt surface sites—particularly under-coordinated step/edge sites versus well-coordinated terrace sites—are known to vary substantially with NP size according to geometric NP models.[10] All size-controlled catalysts were subjected to identical post-reaction treatment at 240 °C for 2 h prior to structural and spectroscopic analyses. STEM images and corresponding Pt size distributions of the size-

controlled catalysts (Supplementary Figs. 17 and 18) confirm well-defined Pt NPs across the investigated size range. High-magnification STEM images (Supplementary Fig. 19) reveal a consistent facet-dependent trend in Pt morphology that is largely preserved across different particle sizes. Regardless of size, Pt NPs supported on TiO_2(001) preferentially adopt hemispherical geometries characterized by broad metal–support contact areas, whereas Pt NPs on TiO_2(101) exhibit more faceted morphologies with smaller interfacial contact regions. As the particle size increases toward approximately 4 nm, Pt NPs on TiO_2(001) gradually evolve toward more faceted shapes due to geometric size effects. Nevertheless, even in this size regime, the interfacial contact area between Pt and TiO_2(001) remains noticeably larger than that observed for Pt NPs on TiO_2(101), indicating that facet-dependent metal–support interactions continue to influence the equilibrium morphology beyond purely size-driven effects.

Post-reaction CO–DRIFTS spectra of the size-controlled catalysts (Supplementary Fig. 20) provide further insight into the relationship between particle size, surface coordination, and facet-dependent Pt morphology. As the Pt particle size increases, both Pt/TiO_2(001) and Pt/TiO_2(101) catalysts exhibit an increased relative intensity of the CO–$Pt_{terrace}$ feature (2100–2080 cm^{-1}) compared to the CO–$Pt_{step/edge}$ feature (2080–2060 cm^{-1}). This trend is consistent with geometric NP models, in which the fraction of exposed terrace sites increases with particle size. In addition, Pt NPs with average post-reaction sizes exceeding approximately 3 nm exhibit sharper CO adsorption bands with reduced full width at half maximum (FWHM) compared to sub-3-nm particles. This spectral sharpening is consistent with enhanced dipole–dipole coupling of adsorbed CO molecules on flatter, more extended terrace surfaces, as reported previously for supported Pt NPs.[10, 11] Importantly, clear facet-dependent differences are observed even within comparable Pt size regimes. For example, a Pt/TiO_2(001) catalyst with an average Pt size of 2.72 nm exhibits a CO adsorption peak at 2081 cm^{-1}, whereas a Pt/TiO_2(101) catalyst—despite its smaller average size of 1.99 nm—shows a higher-wavenumber peak at 2083 cm^{-1}. Although CO adsorption bands generally shift to higher wavenumbers with increasing particle size due to stronger dipole–dipole interactions, the larger Pt NPs on TiO_2(001) nonetheless display lower-wavenumber CO adsorption peaks than the smaller Pt NPs on TiO_2(101). Moreover, a distinct CO–$Pt_{terrace}$ feature is already evident for the smallest Pt/TiO_2(101) catalyst (1.59 nm). Across all catalysts with comparable Pt particle sizes, Pt/TiO_2(101) consistently exhibits more pronounced terrace-related spectral features than Pt/TiO_2(001), indicating a higher proportion of well-coordinated, faceted Pt surfaces on the TiO_2(101) facet—even when the particles are small.

These combined STEM and CO–DRIFTS results demonstrate that the observed differences in Pt morphology and surface coordination are predominantly governed by the TiO_2 facet rather than by particle size alone. As discussed in the Introduction, the Wulff–Kaischew theorem predicts that the equilibrium morphology of supported metal NPs is determined by the balance between the metal–support interfacial free energy and the intrinsic surface free energy of the metal. In line with this framework, the stronger Pt–TiO_2 interaction on the TiO_2(001) facet favors hemispherical particles with broader metal–support contact areas, whereas the weaker interaction on TiO_2(101) allows Pt to adopt more stable faceted geometries with higher terrace-site exposure. Importantly, these facet-dependent trends persist across a broad particle-size range, confirming that facet-dependent MSI play a dominant role in determining Pt NPs morphology and surface structure in this system, beyond purely geometric size effects."

Experimental procedures for the synthesis of size-controlled Pt/TiO_2 catalysts have been added to the Methods section: *"**Synthesis of size-controlled Pt/TiO_2 catalysts.** For the size-controlled Pt/TiO_2 catalysts, different amounts of NaOH/EG or HCl/EG solutions were added prior to the heating step to create basic or acidic environments that regulate Pt nucleation and growth. The resulting samples were denoted as xPTS (Pt/TiO_2 sheet) or xPTR (Pt/TiO_2 rhombic), where x corresponds to the fresh Pt particle size determined from TEM (Supplementary Figs. 17 and 18). Typically, for the synthesis of 1.45PTS, TiO_2 sheet (0.1 g) and ethylene glycol (25 mL) were sonicated for 20 min in a three-neck flask, followed by addition of a Pt/EG solution (5 $mg \cdot mL^{-1}$, 0.25 mL) and stirring under N_2 for 30 min. Then, 0.25 M NaOH/EG (5 mL) was injected, and the mixture was heated to 160 °C for 2 h (10 $°C \cdot min^{-1}$). After cooling to room temperature, 0.25 M HCl/EG (1 mL) was added and stirred for 2 h. The product was centrifuged and washed with ethanol and DI water until neutral pH was reached, followed by drying under vacuum at 60 °C overnight. For 1.59PTS, the same procedure was used as for 1.45PTS, except that 0.25 M NaOH/EG (2.5 mL) was employed. For 2.69PTS and 3.76PTS, the same protocol was used as for 1.45PTS, but 0.25 M HCl/EG (0.5 and 2 mL, respectively) was added instead of the NaOH/EG solution. For 1.33PTR, 1.60PTR, and 1.68PTR, the synthesis followed the same procedure as for 1.45PTS, except that TiO_2 rhombic was used as the support and 0.25 M NaOH/EG (5, 2.5, and 1.25 mL, respectively) was introduced. For 2.79PTR and 4.75PTR, the synthesis route was the same as for 1.33PTR, except that 0.25 M HCl/EG (0.5 and 2 mL, respectively) was added instead of the NaOH/EG solution."*

Accordingly, the following reference 10 was added to the revised Supplementary Information

files.

10. Ro, I. et al. Approaches for understanding and controlling interfacial effects in oxide-supported metal catalysts. *ACS Catal.* **8**, 7368-7387 (2018).

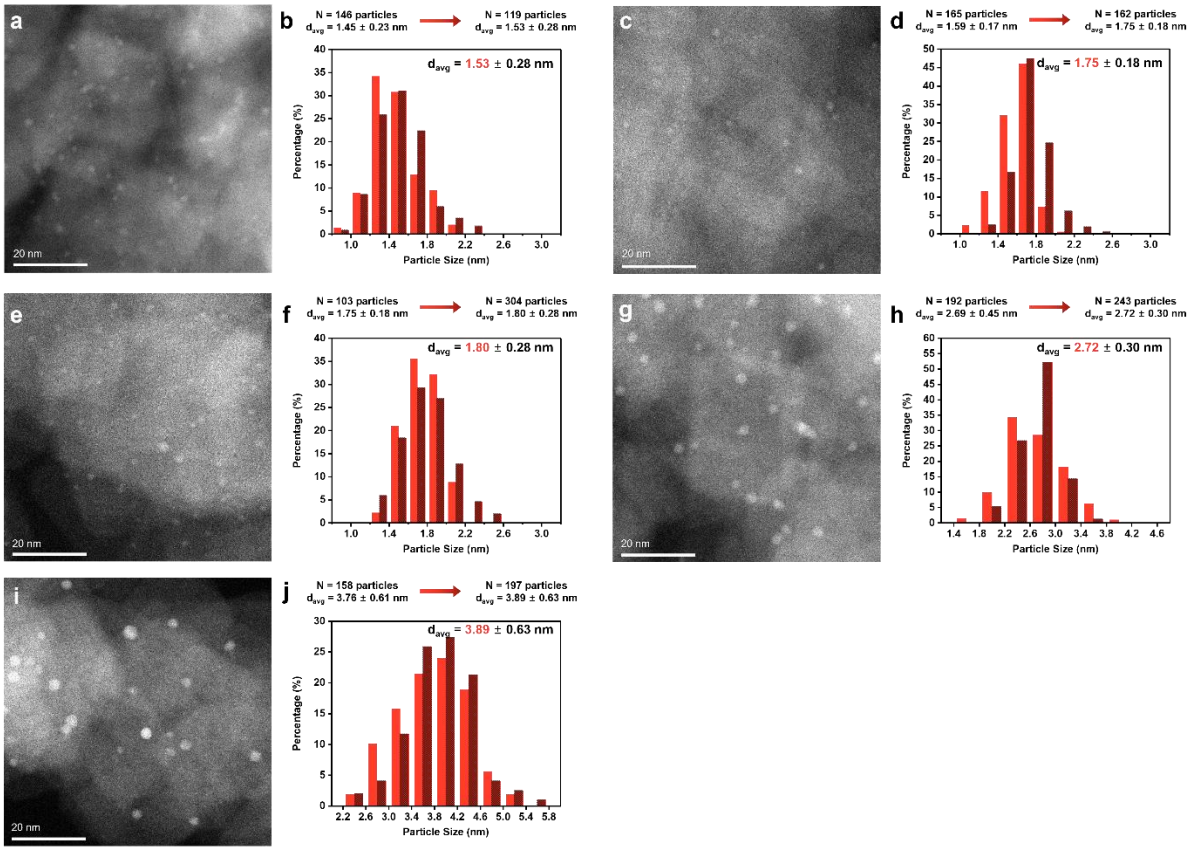

Supplementary Figure 17. HAADF–STEM images and corresponding Pt particle size distributions of the size-controlled Pt/TiO_2(001) catalysts after CO oxidation, with final Pt sizes of (a, b) 1.53 nm, (c, d) 1.75 nm, (e, f) 1.80 nm, (g, h) 2.72 nm, and (i, j) 3.89 nm. Each set shows the post-reaction STEM image together with the corresponding pre- and post-reaction size distributions. All samples were treated at 240 °C for 2 h under CO/O_2 = 1 to prevent thermal sintering while ensuring that CO-adsorbate-induced reconstruction is reflected.

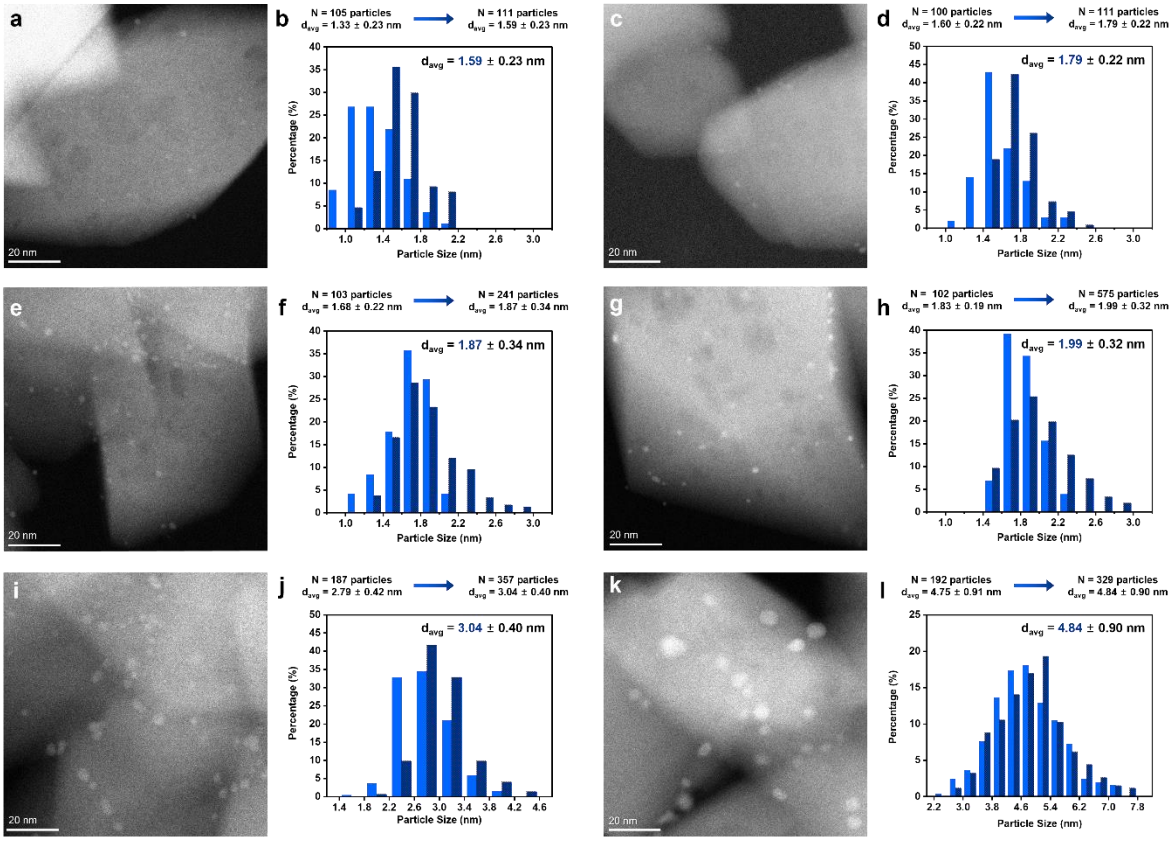

Supplementary Figure 18. HAADF–STEM images and corresponding Pt particle size distributions of the size-controlled Pt/TiO_2(101) catalysts after CO oxidation, with final Pt sizes of (a, b) 1.59 nm, (c, d) 1.79 nm, (e, f) 1.87 nm, (g, h) 1.99 nm, (i–j) 3.04 nm, and (k–l) 4.84 nm. Each set shows the post-reaction STEM image together with the corresponding pre- and post-reaction size distributions. All samples were treated at 240 °C for 2 h under CO/O_2 = 1 to prevent thermal sintering while ensuring that the CO-adsorbate-induced reconstruction process is reflected.

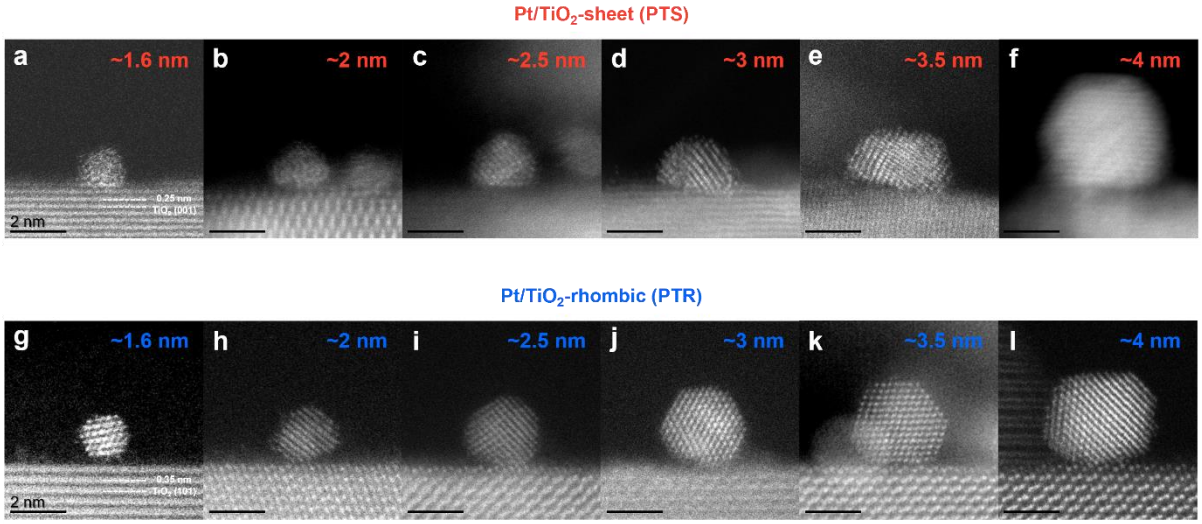

Supplementary Figure 19. High-magnification HAADF–STEM images of size-controlled Pt/TiO_2 catalysts after CO oxidation, with particle sizes ranging from ~1.6 to 4 nm. (a–f) Side-view images showing Pt NPs on the TiO_2(004) plane (PTS), and (g–l) side-view images showing Pt NPs on the TiO_2(101) plane (PTR). Each set demonstrates a size-independent trend in Pt morphology that depends on the exposed TiO_2 facet. All samples were treated at 240 °C for 2 h under CO/O_2 = 1 to prevent thermal sintering while ensuring that the CO-adsorbate-induced reconstruction process is reflected.

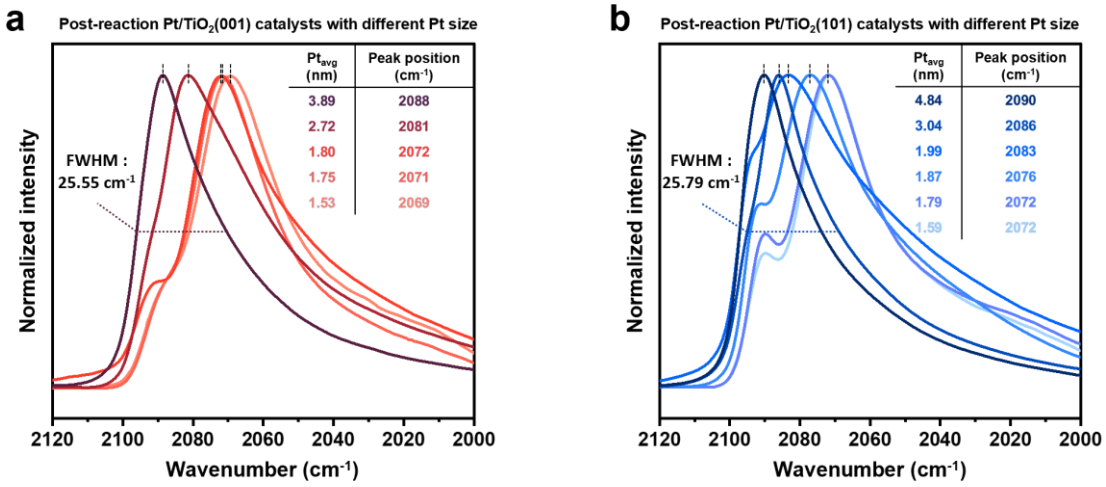

Supplementary Figure 20. Post-reaction CO-DRIFTS spectra of size-controlled (a) PTS and (b) PTR catalysts with final Pt particle sizes ranging from ~1.5 to ~5 nm. All samples were treated at 240 °C for 2 h under CO/O_2 = 1 to suppress thermal sintering and to ensure that the CO-adsorbate-induced reconstruction process is reflected in the resulting Pt surface structures. The insets indicate the average Pt particle size, corresponding CO adsorption peak positions, and the decrease in FWHM observed for samples with Pt sizes above ~3 nm.

Comment 3: A critical oversight in the current analysis is the failure to consider the size difference of PTS and PTR when interpreting their shape evolution and reactivity. The sintering of PTR can be a major reason for its low reactivity rather than the reshaping. A more careful investigation is needed before the authors draw their conclusion.

Response: We appreciate the reviewer's thoughtful comment regarding the potential influence of particle size and sintering on the interpretation of Pt reshaping and catalytic reactivity. As addressed in our response to Comment 2, we conducted additional experiments using size-controlled Pt NPs (1.5–5 nm) deposited on each TiO_2 facet. These measurements revealed that the facet-dependent Pt morphologies—namely the stepped geometry on TiO_2(101) and planar alignment on TiO_2(001)—are consistently maintained across the full size range. This confirms that the observed shape differences are intrinsic to the Pt–TiO_2 interfacial interaction and are not driven by particle size, thereby alleviating concerns regarding size-induced effects on structural evolution.

Regarding the reviewer's concern that the low CO oxidation reactivity of PTR may be attributed to sintering rather than reshaping, we clarify that this possibility was carefully considered and experimentally addressed. In the original manuscript, catalytic tests at $CO/O_2 = 2$ were conducted at 300 °C, under which post-reaction STEM analysis showed that PTR underwent significant sintering. To eliminate this confounding factor, all post-reaction analyses in the revised manuscript were performed under milder conditions (240 °C for 2 h), as described in Supplementary Note 2. Under these revised conditions, STEM analysis confirms the absence of significant particle growth for both PTS and PTR (Supplementary Figs. 12 and 13).

Furthermore, the reactivity comparison in the revised Fig. 1e and Supplementary Fig. 4 now exclusively reflects the intrinsic catalytic behavior under sintering-free conditions. Therefore, the lower reactivity of PTR is not due to sintering-induced deactivation but instead correlates with its weaker interfacial Pt–TiO_2 interaction and less favorable Pt morphology, as consistently supported by DRIFTS, EXAFS, and STEM analyses.

To complement the previously presented DRIFTS results obtained at 240 °C for 2 h, we additionally conducted post-reaction CO-DRIFTS measurements at 300 °C for 1 h and compared them with the original 300 °C for 2 h condition, under which sintering had occurred. The CO-DRIFTS results (Supplementary Fig. 45) confirmed that no sintering occurred under

either the 240 °C for 2 h or the 300 °C for 1 h conditions (a more detailed discussion is provided in our response to Comment 4). Based on these findings, we conclude that the catalysts used in the reactivity measurements—which all completed reaction below 300 °C—did not undergo sintering. Accordingly, only the reactivity data ($CO/O_2 = 2$) obtained under conditions harsher than 300 °C were excluded from the revised manuscript, while all other activity test results can be reliably interpreted without the influence of sintering.

To evaluate the intrinsic catalytic behaviour of the reshaped Pt structures, reaction-order analysis of CO oxidation was performed using post-reaction Pt/TiO_2 catalysts prepared at 240 °C for 2 h, ensuring that the reaction-induced Pt restructuring is preserved. Reaction rates were measured in the kinetically relevant regime (<5% CO conversion) at 80 °C for PTS and 160 °C for PTR, corresponding to their respective light-off temperatures.

As shown in Fig.6e, both catalysts exhibited near-zero reaction orders with respect to CO ($nCO = 0.07$ for PTS and 0.09 for PTR), whereas the reaction orders with respect to O_2 were substantially larger, particularly for PTR ($nO_2 = 0.20$ for PTS and 0.41 for PTR). The negligible CO dependence indicates that CO adsorption or activation does not control the overall rate under these conditions, consistent with a saturated CO coverage under the tested conditions. Meanwhile, the fractional dependence on O_2 suggests that lattice oxygen replenishment, rather than O_2 dissociation, governs the overall rate. (*J. Am. Chem. Soc.* 2017, 139, 40, 14150-14165)

Such rate behavior is consistent with a MvK–type mechanism in which lattice oxygen participates directly in CO oxidation. Within this framework, the higher O_2 reaction order of PTR points to slower reoxidation, implying less efficient transfer of oxygen species across the $Pt–TiO_2$ interface. PTS, in contrast, shows a weaker O_2 dependence, consistent with a more facile oxygen supply from TiO_2, potentially enabled by the reconstructed interfacial geometry. This interpretation is consistent with previous reports on reverse oxygen spillover, in which oxygen migrates from oxide supports to interfacial metal atoms, and aligns with the mechanism proposed for Pt/TiO_2 systems, where oxygen transfer from TiO_2 to interfacial Pt sites on Pt_{metal} clusters governs the reaction rate. (*ACS Catal.* 2017, 7, 10, 6493-6513 / *J. Am. Chem. Soc.* 2017, 139, 40, 14150-14165)

All kinetic measurements were performed after the reaction-induced restructuring of Pt and under conditions where no sintering was detected. The observed differences in activity therefore cannot be explained by particle size effects and instead reflect distinct interfacial

oxygen dynamics that arise from Pt restructuring on both TiO_2. These results support the conclusion that the enhanced reactivity of PTS is linked to a reconstructed interface that more effectively mediates lattice-oxygen transfer during the reaction.

We hope that these additional analyses and revisions help clarify and strengthen the correlation between Pt reshaping and catalytic reactivity, thereby addressing the reviewer's important concern.

Action taken: We have revised Fig. 1e and Supplementary Fig. 4a by excluding the CO/O_2 = 2 reactivity data, which were obtained under conditions where thermally induced sintering of PTR could not be excluded. The following paragraph has been revised on Page 5: *"PTS consistently outperformed PTR across all examined CO/O_2 ratios, exhibiting lower light-off temperatures (Supplementary Fig. 4). Comparison of T_{90} values (Fig. 1e) shows that under O_2-rich conditions (CO/O_2 = 0.2 and 0.4), the differences in the T_{90} values (ΔT_{90}) remains nearly constant (48 and 47 K), whereas under oxygen-limited conditions (CO/O_2 = 1), ΔT_{90} increases to ~68 K, reflecting a stronger contribution of the TiO_2 support when the reaction becomes MvK-dominated.[44, 45] Consistent with this trend, Arrhenius analysis in the kinetically controlled regime (Supplementary Fig. 5) reveals a significantly lower apparent activation energy (E_a) for PTS (55 kJ·mol^{-1}) compared to PTR (112 kJ·mol^{-1}) (Fig. 1f), indicating intrinsically enhanced activity of PTS under MvK conditions. "*

We have performed reaction-order analyses of CO oxidation using post-reaction Pt/TiO_2 catalysts prepared at 240 °C for 2 h under sintering-free conditions. These results have been added to the *Reaction mechanism and the origin of superior catalytic activity* section and are presented in Fig. 6e, with the corresponding discussion included on Page 13: *"To evaluate the intrinsic catalytic behaviour of the reshaped Pt structures, reaction-order analysis of CO oxidation was performed using post-reaction Pt/TiO_2 catalysts prepared at 240 °C for 2 h. (See Methods) As shown in Fig. 6e, both catalysts exhibit near-zero reaction orders with respect to CO (n_{CO} = 0.07 for PTS and 0.09 for PTR), indicating CO-saturated surfaces. In contrast, the reaction orders with respect to O_2 are substantially larger (n_{O2} = 0.20 for PTS and 0.41 for PTR), and this fractional O_2 dependence suggests that lattice oxygen replenishment governs the overall rate, in accordance with a MvK–type mechanism.[68] Within this framework, the higher O_2 dependence of PTR reflects slower reoxidation kinetics and less efficient oxygen transfer across the Pt–TiO_2(101) interface, whereas the weaker O_2 dependence of PTS indicates a more facile supply of lattice oxygen from TiO_2(001) to interfacial Pt sites enabled*

by the reconstructed interface geometry. This interpretation is consistent with reports of reverse oxygen spillover, in which lattice oxygen migrates from oxide supports to interfacial metal atoms,[14] and aligns with mechanistic studies identifying oxygen transfer to interfacial Pt sites as rate-limiting in Pt/TiO_2 systems.[68] These kinetic trends, together with structural observations and DFT-predicted energetics of O_v formation and oxygen replenishment, highlight the central role of facet-dependent interfacial restructuring in determining catalytic activity."

We have added the experimental procedure for the reaction-order measurements to the Methods section: *"Reaction-order analysis of CO oxidation was conducted using post-reaction Pt/TiO_2 catalysts treated at 240 °C for 2 h, ensuring the reaction-induced Pt restructuring was preserved. The catalyst (40 mg) was mixed with quartz sand (960 mg), and all measurements were performed at a total flow rate of 100 mL·min^{-1} with Ar as the balance gas. Reaction rates were measured in the kinetically relevant regime (<5% CO conversion) at 80 °C for post-reaction PTS and 160 °C for post-reaction PTR, corresponding to their respective light-off temperatures. For CO partial-pressure dependence measurements, the CO concentration was varied from 0.5 to 3% while keeping the O_2 concentration constant at 5%. For O_2 partial-pressure dependence measurements, the O_2 concentration was varied from 0.5 to 3% with the CO concentration fixed at 0.5 %. Reaction rates were determined under steady-state conditions, and the reaction orders with respect to CO and O_2 were obtained from linear fits of log–log plots of the reaction rate as a function of the corresponding reactant partial pressure."*

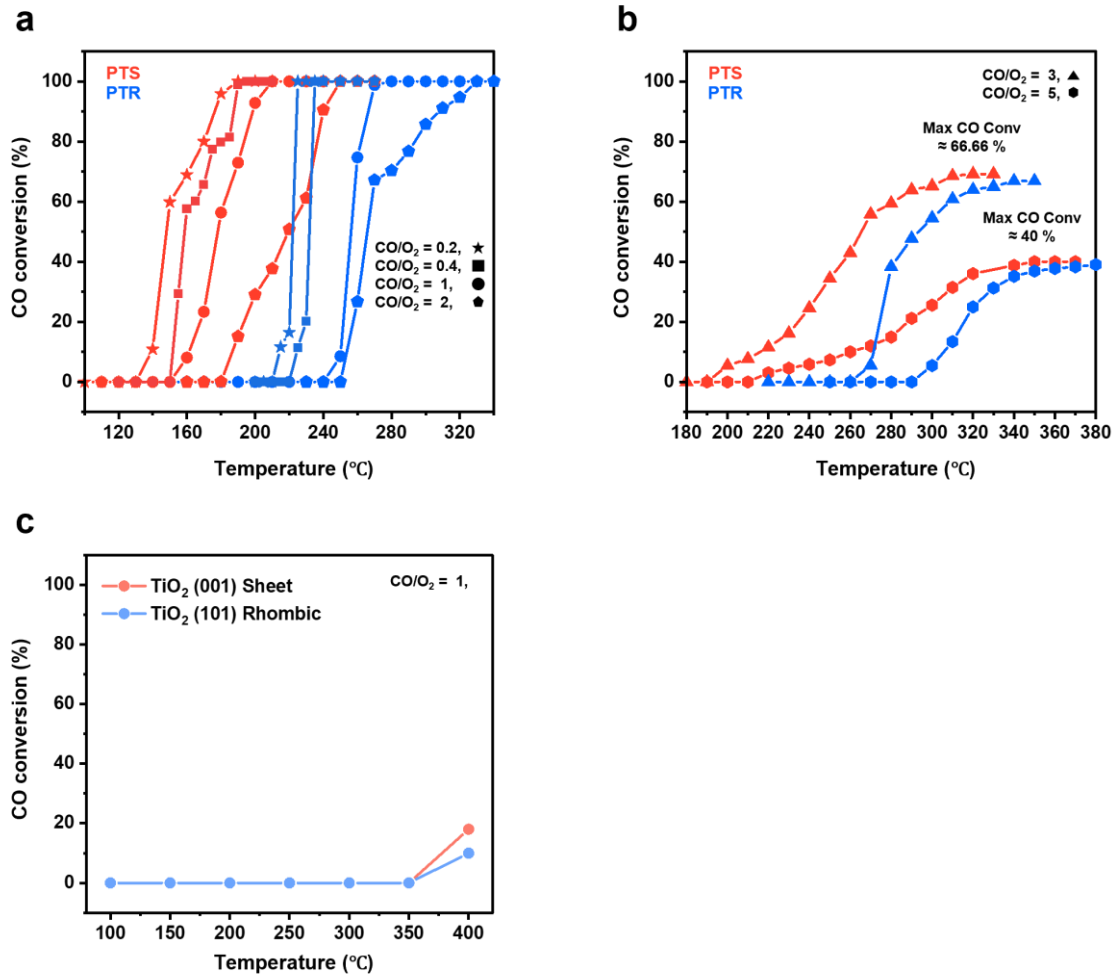

Supplementary Figure 4. Temperature-dependent CO conversion profiles of PTS and PTR catalysts under varying CO/O_2 ratios. (a) Conversion curves under O_2-rich to stoichiometric conditions: CO/O_2 = 0.2 (1% CO / 5% O_2, ★), 0.4 (1% CO / 2.5% O_2, ■), and 1 (1% CO / 1% O_2, ●). (b) Conversion curves under CO-rich conditions: CO/O_2 = 3 (3% CO / 1% O_2, ▲) and 5 (5% CO / 1% O_2, ⬢). (c) CO conversion curves of pristine TiO_2 under stoichiometric conditions (CO/O_2 = 1). The total gas flow rate was maintained at 50 $mL \cdot min^{-1}$ for all measurements.

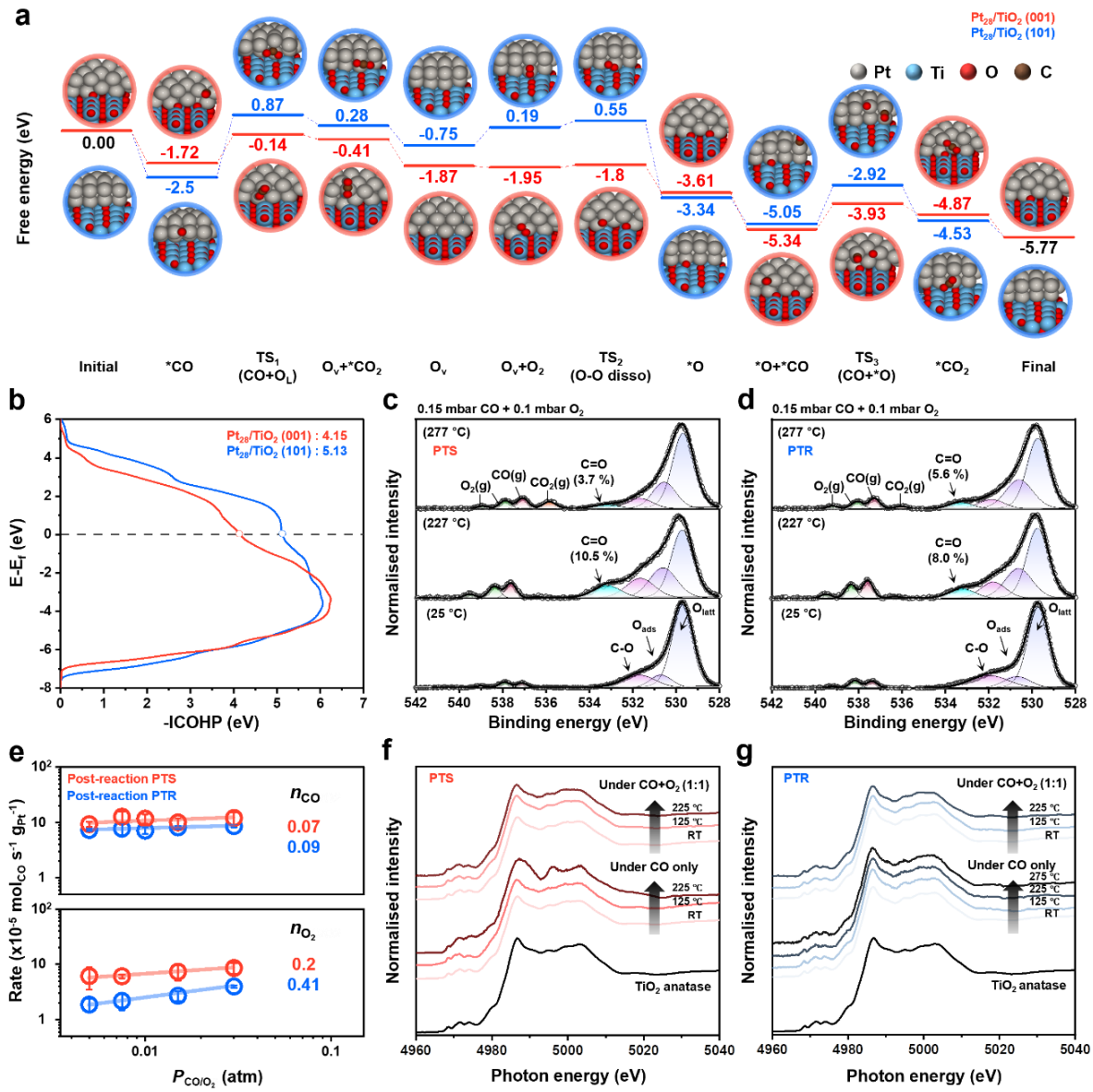

Figure 6. Synergistic effects of Pt morphology and TiO_2 facets on CO oxidation activity. (a) DFT-calculated reaction energy profiles for CO oxidation via the MvK mechanism on $Pt_{28}/TiO_2(001)$ and (101). (b) ICOHP analysis of oxygen vacancy formation on Pt_{28}/TiO_2 models. (c, d) Normalised *in situ* O 1*s* AP-XPS spectra ($h\nu$ = 650 eV) for (c) PTS and (d) PTR catalysts under CO oxidation conditions (0.15 mbar of CO, 0.1 mbar of O_2) at 25, 227, and 277 °C. (e) Reaction-order analysis of CO oxidation on post-reaction Pt/TiO_2 catalysts with respect to CO and O_2 partial pressures. Reaction rates were measured in the kinetically relevant regime (<5% CO conversion) at 80 °C for PTS and 160 °C for PTR, corresponding to their respective light-off temperatures. (f, g) Ti *K*-edge *in situ* XANES spectra of (f) PTS and (g) PTR under CO-reducing (middle panels: 5% CO/He) and CO + O_2 co-feed (upper panels: 5% CO + 5% O_2/He) conditions.

Fig. 1e is included in the response to Comment 1.

Comment 4: The DRIFTS data of PTS and PTR (Figure 3a–b) show very minor difference, which is not sufficient to substantiate the authors' claim of a significant disparity in Pt shape between the two samples. Additionally, the sintering of PTR could be another reason for the increase of terrace sites, which should be considered.

Response: We sincerely appreciate the reviewer's insightful comment regarding the interpretation of the CO-DRIFTS spectra and the possibility that the observed increase in terrace-site contributions for PTR may arise from sintering rather than structural reshaping. As this concern could relate to both the comparison between PTS and PTR and the structural changes occurring before and after reaction within each catalyst, we address both aspects below.

The CO-DRIFTS spectra presented in the original manuscript reflect coordination changes associated with the morphology of Pt NPs in the ~1.7–2.0 nm size range on both TiO_2 facets. Accordingly, the pre-reaction DRIFTS spectra of fresh PTS and PTR showed only minor differences, consistent with their similar initial Pt sizes and dispersions, with the CO band of fresh PTR appearing at a slightly higher wavenumber in line with the more faceted Pt morphology identified by STEM. Based on the post-reaction CO-DRIFTS results obtained for the size-controlled catalysts (Supplementary Fig. 20), we would expect that if substantial particle growth were induced by sintering relative to the fresh catalysts, pronounced spectral changes would emerge between the pre- and post-reaction states. Such changes would include narrower FWHM, reflecting the increased fraction of well-coordinated Pt surface sites associated with larger particles. In this context, we agree with the reviewer that the post-reaction PTR data included in the original manuscript were influenced by sintering. Specifically, the spent PTR treated at 300 °C for 2 h exhibited pronounced particle growth to an average Pt size of approximately 3.1 nm (Supplementary Fig. 15), accompanied by clear changes in the CO-DRIFTS spectra, including narrower CO adsorption bands in Fig. 3 (Supplementary Fig. 45b in the revised manuscripts).

As discussed in our response to General Comment (see also Supplementary Note 2), we have already confirmed that no sintering occurs under the newly established post-reaction conditions (240 °C for 2 h). Nevertheless, to directly address the reviewer's concern regarding the interpretation of the post-reaction CO-DRIFTS results in the revised manuscript, we additionally acquired DRIFTS spectra after a 300 °C for 1 h treatment and compared these data with the previously obtained post-reaction spectra collected at 240 °C for 2 h and 300 °C for 2 h, as well as with those of the size-controlled Pt/TiO_2 catalysts.

Comparing the DRIFTS spectra of the fresh catalysts with those collected after treatment at 240 °C for 2 h and 300 °C for 1 h (Supplementary Fig. 45), both PTS and PTR showed moderate increases in terrace-related features. Specifically, PTS maintains its main peak at ~2072 cm^{-1} while exhibiting an increased terrace contribution, whereas PTR shows a modest blueshift (2079 → 2083 cm^{-1}) together with enhanced terrace intensity. Notably, in both catalysts, the overall peak shape remains similar to that of their fresh counterparts. As previously discussed, PTS is more resistant to sintering, and the spent PTS (300 °C for 2 h) therefore shows only gradual increases in CO–Pt_{int} features without significant peak-shape alteration. In contrast, the spent PTR (300 °C for 2 h) exhibits a clearly different spectral profile, characterized by a narrowed FWHM, as highlighted by the blue arrow in Supplementary Fig. 45b, consistent with particle growth to ~3.1 nm confirmed by STEM (Supplementary Fig. 15).

From the post-reaction CO-DRIFTS spectra of the size-controlled Pt/TiO_2 catalysts (Supplementary Fig. 20), we observed that Pt NPs exceeding ~3 nm consistently display narrowed FWHM values and terrace-dominated spectral features. The strong similarity with minor FWHM difference between the post-reaction DRIFTS spectrum of the spent PTR (300 °C for 2 h) and those of the 3.04–4.81 nm size-controlled Pt/TiO_2(101) catalysts confirms that the 300 °C for 2 h treatment results in a substantial sintering contribution in addition to intrinsic reconstruction. In contrast, the DRIFTS spectra of spent PTR obtained at 240 °C for 2 h and 300 °C for 1 h retain peak shapes that closely resemble those of the fresh PTR catalyst. The preservation of the overall peak profile—without the FWHM narrowing characteristic of particle growth—indicates that these measurements were not influenced by sintering. Accordingly, the terrace-related increases observed under these conditions can be attributed to Pt NP reconstruction, reflecting facet-dependent behaviour rather than size-induced effects

Accordingly, the revised manuscript now incorporates a sintering-excluded STEM–DRIFTS analysis together with size-controlled comparisons, enabling a more rigorous distinction between sintering and intrinsic reconstruction. These additions substantially reinforce the central argument of the study—that the enhanced terrace-site contribution of PTR originates from facet-dependent Pt reshaping rather than sintering—while providing a clearer and more internally consistent interpretation of the structural evolution of Pt NPs on TiO_2. We sincerely appreciate the reviewer's comment, which significantly improved the rigor and clarity of our work.

Action taken: We have added comparative post-reaction CO-DRIFTS results to Supplementary Note 2 to distinguish facet-dependent Pt reshaping from sintering effects. These results are presented in Supplementary Fig. 45.

Corresponding discussion has been added to Supplementary Note 2:

"To further validate that sintering effects are excluded under the selected post-reaction conditions, additional CO-DRIFTS measurements were performed after a treatment at 300 °C for 1 h and compared with the post-reaction spectra obtained at 240 °C for 2 h and 300 °C for 2 h, as well as with those of the size-controlled Pt/TiO_2 catalysts.

Comparison of the DRIFTS spectra of the fresh catalysts with those collected after treatment at 240 °C for 2 h and 300 °C for 1 h (Supplementary Fig. 45) shows that both PTS and PTR exhibit moderate increases in terrace-related features. For PTS, the main CO adsorption band remains centered at ~2072 cm^{-1}, accompanied by a gradual increase in terrace contribution. For PTR, a modest shift of the CO band toward higher wavenumbers (2079 → 2083 cm^{-1}) is observed together with enhanced terrace-site intensity. Importantly, under both conditions, the overall peak shapes for PTS and PTR remain similar to those of their fresh counterparts, indicating that significant particle growth has not occurred.

As discussed above, PTS exhibits higher resistance to sintering. Accordingly, even after treatment at 300 °C for 2 h, the spent PTS catalyst shows only gradual increases in terrace-related and CO–Pt_{int} features without substantial changes in peak shape. In contrast, the spent PTR catalyst treated at 300 °C for 2 h displays a distinctly different spectral profile, characterized by a pronounced narrowing of the full width at half maximum (FWHM), as highlighted in Supplementary Fig. 45. This spectral narrowing is consistent with particle growth to approximately 3.1 nm, as independently confirmed by STEM analysis (Supplementary Fig. 18).

Consistent trends are observed from the post-reaction CO-DRIFTS spectra of the size-controlled Pt/TiO_2 catalysts (Supplementary Fig. 20), where Pt NPs larger than ~3 nm systematically exhibit narrowed FWHM values and terrace-dominated spectral features. The strong similarity—aside from minor FWHM differences—between the post-reaction DRIFTS spectrum of the spent PTR catalyst treated at 300 °C for 2 h and those of the 3.04–4.81 nm size-controlled Pt/TiO_2(101) catalysts confirms that the 300 °C for 2 h treatment introduces a substantial sintering contribution in addition to intrinsic reconstruction effects.

By contrast, the DRIFTS spectra of spent PTR catalysts obtained after treatment at 240 °C for 2 h and 300 °C for 1 h closely resemble those of the fresh PTR catalyst. The preservation of the

overall peak profiles—without the FWHM narrowing characteristic of particle growth—demonstrates that these conditions are not influenced by sintering. Accordingly, the terrace-related spectral changes observed under these conditions can be attributed to Pt NP reconstruction driven by facet-dependent metal–support interactions rather than by size-induced effects."

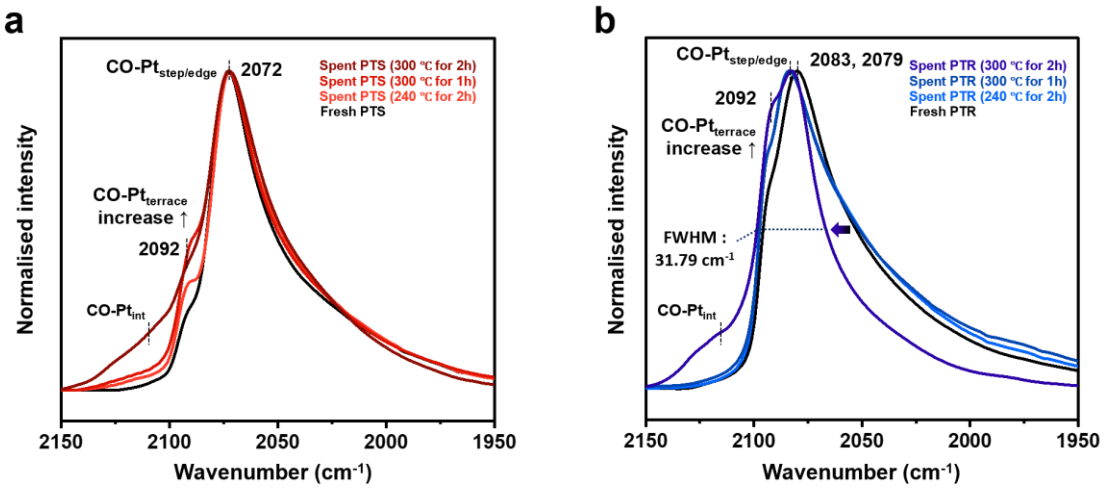

Supplementary Figure 45. Post-reaction CO-DRIFTS spectra of (a) PTS and (b) PTR catalysts. The spent catalysts were prepared by post-reaction treatments at 240 °C for 2 h, 300 °C for 1 h, and 300 °C for 2 h under CO/O_2 = 1 reaction conditions prior to DRIFTS measurements.

Comment 5: The EXAFS data of PTR before and after reaction in Figure 2a also shows very minor difference, whereas the TEM data in Figure S13 shows an obvious sintering of PTR after reaction. The authors should explain this discrepancy.

Response: We thank the reviewer for comments regarding the EXAFS results of the PTR catalyst before and after reaction. As noted, TEM analysis shows sintering of the PTR catalyst after reaction, with the average Pt particle size increasing to approximately 3.2 nm in Supplementary Fig. 13 (Supplementary Fig. 15 in the revised manuscripts).

It should be noted that, for supported Pt NPs in the 1–5 nm size range on TiO_2, the FT-EXAFS spectra are typically dominated by local Pt–Pt coordination in the 2–3 Å range, accompanied by a shoulder associated with Pt–O coordination in the 1–2 Å range (*J. Am. Chem. Soc.* 2014, 136, 26, 9320-9326, *J. Phys. Chem. C* 2019, 123, 16, 10666-10676, *Nat. Commun.* 2022, 13, 4379). Within the present Pt particle size range, even after sintering, these characteristic spectral features are expected to remain qualitatively similar. Consequently, only minor differences are observed upon visual inspection of the FT-EXAFS spectra before and after reaction. Importantly, changes in local structure associated with particle growth are more reliably identified through quantitative EXAFS fitting rather than direct comparison of FT-EXAFS spectra.

For example, in the spent PTR catalyst under CO-rich conditions ($CO/O_2 = 5$) in the original manuscripts, where more pronounced sintering up to ~6.4 nm ($Pt_{avg} \sim 3.33 \pm 0.90$ nm) was observed by TEM, the corresponding FT-EXAFS spectra still exhibit only subtle visual differences compared to other spent PTR samples. Nevertheless, EXAFS fitting reveals a significant increase in the Pt–Pt CN (up to ~10.7), providing clear quantitative evidence for particle growth. This interpretation is further supported by the WT-EXAFS results, which show a reduced Pt–O contribution and a more distinct Pt–Pt feature approaching that of Pt foil (Supplementary Figs. 8d, 9f, 13l and Supplementary Table 2 in the original manuscript).

In the revised manuscript, all EXAFS data for PTR have been newly acquired and reanalyzed under the revised post-reaction conditions (Figs. 2a–g and Supplementary Figs. 7–9, and Supplementary Table 2). The updated FT-EXAFS spectra for both fresh and spent PTR still exhibit only subtle visual differences, despite the presence of sintering observed by TEM under specific conditions ($CO/O_2 = 5$). Accordingly, the interpretation of particle growth and sintering effects in this study is based primarily on quantitative EXAFS fitting combined with STEM

analyses, rather than on visual comparison of FT-EXAFS spectra alone, as discussed in the General Comments.

We hope that this explanation satisfactorily addresses the reviewer's concern.

* Figs. 2a–g and Supplementary Figs. 7–9, and Supplementary Table 2 are presented in the response to General Comments.

Comment 6: The parameters of EXAFS fitting should be carefully checked. For example, the σ^2 for Pt−O bond in the Spent PTS, CO-rich (CO/O_2=5) is too high. And the uncertainty in curve fitting is also important to present.

Response: We thank the reviewer for the careful examination of the EXAFS fitting parameters and for pointing out the unusually large σ^2 value for the Pt–O bond in the spent PTS catalyst under CO-rich conditions (CO/O_2 = 5), as well as the importance of properly presenting the fitting uncertainties.

In response to this comment, all EXAFS data (Figs. 2a–g and Supplementary Figs. 7–9, and Supplementary Table 2) presented in the revised manuscript have been newly acquired and reanalyzed. During this process, all fitting parameters, including the Debye–Waller factors (σ^2), coordination numbers (CN), bond distances (d), and energy shifts (E_0), were carefully checked and reoptimized, and the corresponding fitting uncertainties are now explicitly reported (Supplementary Table 2). As a result, the previously noted large σ^2 value for the Pt–O bond has been corrected, and the revised fitting results now show physically reasonable σ^2 values with appropriate uncertainties. These improvements ensure that the EXAFS analysis more accurately reflects the local structural characteristics of the catalysts.

In general, for supported Pt NPs, the structural disorder quantified by σ^2 is approximately 2–3 times larger than that of bulk Pt references, reflecting the intrinsic static disorder associated with nanoscale systems (*Curr. Appl. Phys.* 2024, 59, 25-32, *J. Am. Chem. Soc.* 2014, 136, 26, 9320-9326). This enhanced disorder originates from the large fraction of surface and interfacial Pt atoms, whose local coordination environments deviate significantly from those of bulk Pt references. For Pt–O pairs, the σ^2 values additionally exhibit relatively large uncertainties due to their low coordination numbers, heterogeneous interfacial bonding environments, and the weak backscattering strength of oxygen compared to heavier scatterers, as commonly reported

in previous EXAFS studies on supported Pt catalysts (*J. Phys. Chem. C* 2019, 123, 16, 10666-10676).

Consistent with this understanding, both PTS and PTR catalysts exhibit substantial disorder due to their nanoscale nature, while the relative disorder trends differ between the two catalysts in a facet-dependent manner. In PTS, the disorder associated with Pt–Pt pairs is higher, whereas the disorder associated with Pt–O pairs is lower. This behavior is consistent with a more dispersed metallic Pt morphology dominated by under-coordinated Pt sites and a relatively uniform Pt–O interfacial interaction, which can be attributed to the predominance of O_{2c}–Ti_{5c}–O_{2c} configurations on the TiO_2(001) facet (Supplementary Fig. 3c). In contrast, PTR exhibits a more well-coordinated Pt framework accompanied by higher disorder in Pt–O pairs, reflecting more heterogeneous Pt–O interfacial interactions arising from mixed O_{5c}–Ti_{6c} and O_{2c}–Ti_{5c} configurations on the TiO_2(101) facet (Supplementary Fig. 3d).

When considered alongside STEM and DRIFTS analyses, these trends indicate that PTS is characterized by a more dispersed and under-coordinated metallic Pt morphology with relatively stronger and more uniform metal–support interfacial bonding, whereas PTR exhibits a well-coordinated, cuboctahedral-like Pt structure associated with a weaker and more heterogeneous metal–support interfacial interaction. These disorder characteristics are consistent with the facet-dependent Pt morphologies proposed in this study.

In summary, the reviewer's comment prompted a thorough remeasurement and refitting of the EXAFS data, enabling us to present more reliable and robust EXAFS results with properly evaluated fitting uncertainties. We believe that these revisions significantly improve the overall quality and clarity of the EXAFS analysis presented in the revised manuscript

Action taken: In the revised manuscript, all EXAFS fitting parameters were carefully reexamined, and Supplementary Table 2 was updated to include newly extracted fitting results with corresponding uncertainties.

The related EXAFS discussion in the main text has been revised accordingly to explicitly present the uncertainties of the coordination numbers. The following paragraph has been revised on Page 6: *"Least-squares fitting of the FT-EXAFS spectra (Supplementary Table 2) revealed the coordination numbers (CNs) of Pt–O and Pt–Pt, which were 1.6 ± 0.4 and 6.4 ± 1.2 for fresh PTS, and 1.4 ± 0.8 and 8.1 ± 1.2 for fresh PTR, respectively. For the spent catalysts,*

the Pt–Pt CN marginally increased to 6.8 ± 1.7 in the PTS and to 8.2 ± 1.4 in the PTR. Under O_2-rich conditions (CO/O_2 = 0.2), PTS still retained strong Pt–O features, with the Pt–O CN increasing to 1.9 ± 0.7, whereas that of PTR decreased to 1.2 ± 0.5. Under CO-rich conditions (CO/O_2 = 5), both spectral features became more metallic, with the Pt–Pt CNs in the PTS and PTR increasing to 8.6 ± 1.6 and 9.8 ± 0.8, respectively. Wavelet transform EXAFS (WT-EXAFS) results further corroborated these findings, with fresh PTS showing dominant Pt–O contributions (Figs. 2b, c) and fresh PTR showing pronounced Pt–Pt features (Figs. 2e, f). For all spent catalysts (Figs. 2d, g and Supplementary Fig. 9), similar trends were observed, with enhanced Pt–Pt contributions under CO-rich conditions for both catalysts, in agreement with the FT-EXAFS and CN results."

Figs. 2a–g and Supplementary Figs. 7–9, and Supplementary Table 2 are presented in the response to General Comments.

Comment 7: The size difference of PTR and PTS after reaction should be also considered for their DFT calculation.

Response: We thank the reviewer for highlighting the potential influence of post-reaction particle size differences between PTS and PTR on the DFT calculations. As clarified in our responses to Comments 2 and 4, all post-reaction structural characterizations in the revised manuscript were performed under carefully controlled conditions (240 °C for 2 h, CO/O_2 = 1), which eliminate thermally induced sintering while still capturing CO-adsorbate-induced reconstruction (see Supplementary Note 2). Under these revised conditions, both PTS and PTR maintain their initial particle sizes, and STEM analyses confirm that the observed facet-dependent Pt morphologies persist without interference from particle growth (Supplementary Figs. 12 and 13).

Accordingly, the DFT models were constructed based on experimentally validated Pt morphologies that reflect intrinsic facet effects, independent of post-reaction size differences. We believe this alignment between theory and experiment ensures the robustness and relevance of the DFT analysis.

To further strengthen this conclusion, we additionally investigated size-controlled Pt/TiO_2 catalysts within the investigated size range of 1.5–5 nm (Supplementary Note 3). Post-reaction STEM and CO-DRIFTS analyses show that, although general size-related trends such as

increased terrace-site contributions emerge with increasing particle size, the characteristic differences between PTS and PTR persist across comparable Pt sizes. In particular, Pt/TiO_2(101) consistently exhibits more faceted morphologies and stronger CO–$Pt_{terrace}$ features than Pt/TiO_2(001), indicating that the observed structural distinctions are governed primarily by facet-dependent MSI rather than particle size.

In parallel, reaction-order analyses and complementary O 1*s* XPS measurements (additional discussion is provided in the response to Comment 8) further demonstrate that the superior activity of PTS originates from the intrinsically O_v-rich TiO_2(001) facet and the distinct behavior of reactive oxygen species at the Pt–TiO_2(001) interface under reaction conditions. Together, these results establish that the enhanced catalytic performance arises from the synergistic interplay between the redox-active TiO_2(001) support and the reconstructed Pt interface, rather than from particle-size effects.

Accordingly, the DFT models employed in this work are designed to capture the essential features of the experimentally observed Pt–TiO_2 interfaces under sintering-free conditions and show good qualitative and mechanistic agreement with the experimental structural, spectroscopic, and kinetic results. On this basis, additional size-dependent DFT calculations were not pursued in the revised manuscript.

We hope that this explanation adequately addresses the reviewer's concern and clarifies the rationale for the DFT modeling strategy adopted in this study.

Comment 8: Many earlier studies have been documented regarding the TiO_2-facet dependency and MSI effect (*Chin. J. Catal*., 2019, 40, 1534-1539; *J. Catal*, 2021, 398, 109-122; *Chin. J. Catal*., 2025, 70,378-387), where TiO_2(001) support itself is also essential for the catalytic performance (*Prog. Nat. Sci.: Mater. Int.*, 2021, 31, 1-13). Therefore, the role of TiO_2(001) support, such as enriched oxygen vacancies, should be also considered for their high reactivity, other than the reshaping of Pt NPs.

Response: We thank the reviewer for emphasizing the important role of the intrinsic properties of TiO_2 facets in determining catalytic performance. We fully agree that, in addition to Pt NP reshaping, the facet-dependent characteristics of TiO_2—particularly the abundance of O_v—should be considered when interpreting the enhanced reactivity of TiO_2(001)-supported catalysts.

O_v are commonly evaluated via O 1*s* XPS analysis, where the relative contribution of adsorbed oxygen or surface hydroxyl–related components is often used as a descriptor for O_v concentration. (*ACS Catal*. 2011, 1, 4, 348-354, *ACS Catal*. 2023, 13, 20, 13691-13703) Following this approach, we carried out a comparative analysis of O 1*s* XPS spectra for both pristine TiO_2 supports and Pt/TiO_2 catalysts measured under UHV conditions, as well as for Pt/TiO_2 catalysts measured under CO oxidation conditions at 227 and 277 °C. Under reaction environments, the O 1*s* region is complicated by overlapping contributions from gas-phase intermediates (e.g., C–O and C=O species). Therefore, instead of comparing the total O 1*s* intensity (O_{total}), we compared the O_{ads}/O_{latt} area ratios to enable a consistent relative comparison of O_v-related oxygen with respect to bulk lattice oxygen. In addition, because reactive gas atmospheres inherently cause signal attenuation, peak broadening, and reduced surface sensitivity due to inelastic scattering of photoelectrons by gas molecules, our analysis was restricted to relative comparisons of O_{ads}/O_{latt} ratios between catalysts under identical environments, rather than absolute quantification across different conditions.

Within this framework, both pristine $TiO_2(001)$ sheets and $Pt/TiO_2(001)$ catalysts measured under UHV conditions exhibit significantly higher O_{ads}/O_{latt} ratios than their $TiO_2(101)$ counterparts, by factors of 1.76 and 1.95, respectively (Supplementary Fig. 35). This result demonstrates that the (001) facet intrinsically possesses a higher density of O_v sites, irrespective of Pt loading. Under CO oxidation conditions, distinct facet-dependent trends were observed for the Pt/TiO_2 catalysts. With increasing temperature, PTS shows a pronounced decrease in the O_{ads}/O_{latt} ratio from 0.56 to 0.38, whereas PTR exhibits only a marginal change (0.53 to 0.51). This contrast indicates that oxygen species associated with O_v sites on $TiO_2(001)$ are more readily consumed and subsequently replenished at the Pt–TiO_2 interface. Such behavior is consistent with more efficient oxygen transfer from the $TiO_2(001)$ support to interfacial Pt sites, ultimately leading to higher catalytic activity on the (001) facet.

In the original manuscript, we emphasized the facet-dependent redox characteristics of TiO_2—closely linked to the intrinsic abundance and accessibility of O_v sites—through multiple complementary analyses, including DFT-calculated O_v formation energies, O_2-TPD, EPR, *in situ* Ti *K*-edge XANES, and H_2-TPR, as discussed in the section *Reaction mechanism and the origin of superior catalytic activity*. To further clarify the role of O_v, in the revised manuscript, we have expanded the discussion by explicitly incorporating O 1*s* XPS–based comparisons to directly connect the intrinsically O_v-rich nature of $TiO_2(001)$ with its enhanced oxygen

activation capability and its synergistic interplay with the reconstructed Pt–TiO_2(001) interface.

Action Taken: We have added the results of O 1s XPS measurements acquired under UHV conditions to the *Reaction mechanism and the origin of superior catalytic activity* section to explicitly evaluate the intrinsic O_v characteristics of TiO_2 facets, while the existing O_2-TPD and EPR results are summarized. These data are now presented in Supplementary Fig. 35, and the following paragraph has been revised on Page 13: "*Beyond the theoretical and kinetic insights into facet-dependent Pt reconstruction and catalytic activity, the intrinsic redox properties of TiO_2 facets were examined, focusing on O_v abundance and reactive oxygen species relevant to interfacial redox behaviour (Supplementary Note 11). O 1s XPS analyses under UHV conditions (Supplementary Figs. 35a,b) show that pristine TiO_2(001) and PTS exhibit O_{ads}/O_{latt} ratios—as a descriptor of O_v abundance—that are 1.76 and 1.95 times higher, respectively, than those of their TiO_2(101) counterparts. Consistently, O_2-TPD and EPR analyses (Supplementary Figs. 36 and 37 and Supplementary Note 11) reveal a higher population of reactive oxygen species on the (001) facet, which is further enhanced at the Pt–TiO_2(001) interface, consistent with its intrinsically higher O_v abundance.*"

To further clarify the role of O_v and to emphasize the synergistic interplay between the redox-active TiO_2(001) support and the reconstructed Pt interface in determining the enhanced catalytic activity, we have expanded the corresponding discussion on Page 14: *"Overall, these spectroscopic results indicate that the TiO_2(001) facet provides more efficient oxygen reservoir at the Pt–TiO_2 interface under reaction conditions, owing to its higher intrinsic O_v abundance and more reactive oxygen species. Consistently, O 1s XPS analyses under reaction environments (Supplementary Figs. 35c, d and Supplementary Note 11) show that PTS exhibits a pronounced decrease in the O_{ads}/O_{lat} ratio with increasing temperature (from 0.56 to 0.38), whereas PTR shows only a marginal change. This behaviour suggests that oxygen species associated with O_v sites on TiO_2(001) are more efficiently consumed and replenished at the Pt–TiO_2(001) interface, facilitating oxygen transfer to interfacial Pt sites and thereby supporting the enhanced catalytic activity observed for PTS."*

In addition, further details regarding the role of O_v in oxide-supported catalysts, as well as the methodology and limitations associated with comparing O_v–related features under UHV and reaction environments, together with detailed O_2-TPD and EPR analyses, have been included in Supplementary Note 11:

*"**Supplementary Note 11. Facet-dependent Properties of Oxygen Species on TiO_2** In addition*

to carbonate-related species, we further considered the role of oxygen-vacancies (O_v), which are widely recognized as a critical factor governing the catalytic activity of oxide-supported catalysts.[16] O_v are commonly evaluated via O 1s XPS analysis, where the relative contribution of adsorbed oxygen or surface hydroxyl–related components is used as an indirect descriptor of O_v concentration.[17, 18] Following this established approach, we performed a comparative analysis of O 1s XPS spectra for both pristine TiO_2 supports and Pt/TiO_2 catalysts measured under UHV conditions, as well as for Pt/TiO_2 catalysts measured under CO oxidation conditions at 227 and 277 °C.

Under reactive gas environments, the O 1s region is further complicated by overlapping contributions from gas-phase intermediates (e.g., C–O and C=O species). Therefore, rather than comparing the total O 1s intensity (O_{total}), we evaluated the O_{ads}/O_{latt} area ratios to enable a consistent relative comparison of O_v-related oxygen species with respect to bulk lattice oxygen. In addition, because the presence of gas molecules induces significant inelastic scattering of photoelectrons—leading to signal attenuation, peak broadening, and reduced surface sensitivity—our analysis was restricted to relative comparisons of O_{ads}/O_{latt} ratios between catalysts measured under identical environments, rather than absolute quantification across different conditions.

O 1s XPS analyses under UHV conditions (Supplementary Figs. 35a, b) show that pristine TiO_2(001) and PTS exhibit O_{ads}/O_{latt} ratios—as a descriptor of O_v abundance—that are 1.76 and 1.95 times higher, respectively, than those of their TiO_2(101) counterparts, indicating that the (001) facet intrinsically possesses a higher abundance of O_v–related sites irrespective of Pt loading. O 1s XPS analyses under reaction environments (Supplementary Figs. 35c, d) further show that PTS exhibits a pronounced decrease in the O_{ads}/O_{lat} ratio with increasing temperature (from 0.56 to 0.38), whereas PTR shows only a marginal change (from 0.53 to 0.51), consistent with more efficient oxygen transfer from the TiO_2(001) support to interfacial Pt sites In line with this trend, O_2-temperature-programmed desorption (O_2-TPD) profiles of Pt/TiO_2 and pristine TiO_2 (Supplementary Fig. 36a) exhibit two broad peaks between 100 and 300 °C and between 300 and 600 °C attributed to the superoxide (O_2^-) and peroxide (O^-) species, respectively.[19] The calculated oxygen storage capacity (Supplementary Fig. 36b) increased substantially on the (001) facet from 9.65 to 18.17 μmol·m^{-2} upon Pt loading, whereas the (101) facet showed a smaller increase from 11.97 to 16.58 μmol·m^{-2}. The desorption peak temperatures for PTS were also lower than those for PTR and the pristine

supports, indicating the presence of more reactive oxygen species at the Pt–TiO_2 interface, driven by the stronger MSI on the (001) facet. Electron paramagnetic resonance (EPR) spectra (Supplementary Fig. 37) confirm the presence of superoxide radicals ($O_2^{\bullet-}$) with signals at g = 2.001–2.033 in PTS, while no such signals are observed for pristine TiO_2 rhombic and PTR samples.[20, 21, 22, 23] *Overall, these results demonstrate that the TiO_2(001) facet intrinsically possesses a higher abundance of O_v and more reactive oxygen species, which are further promoted at the Pt–TiO_2 interface by stronger MSI."*

Accordingly, the relevant references (17 and 18) have been added to the revised Supplementary information files.

17. Huang, H. et al. Complete oxidation of formaldehyde at room temperature using TiO_2 supported metallic Pd nanoparticles. *ACS Catal.* **1**, 348-354 (2011).
18. Lee, J. et al. Reversible Pd catalysts supported on hierarchical titanate nanosheets for an N-methylindole-based liquid organic hydrogen carrier. *ACS Catal.* **13**, 13691-13703 (2023).

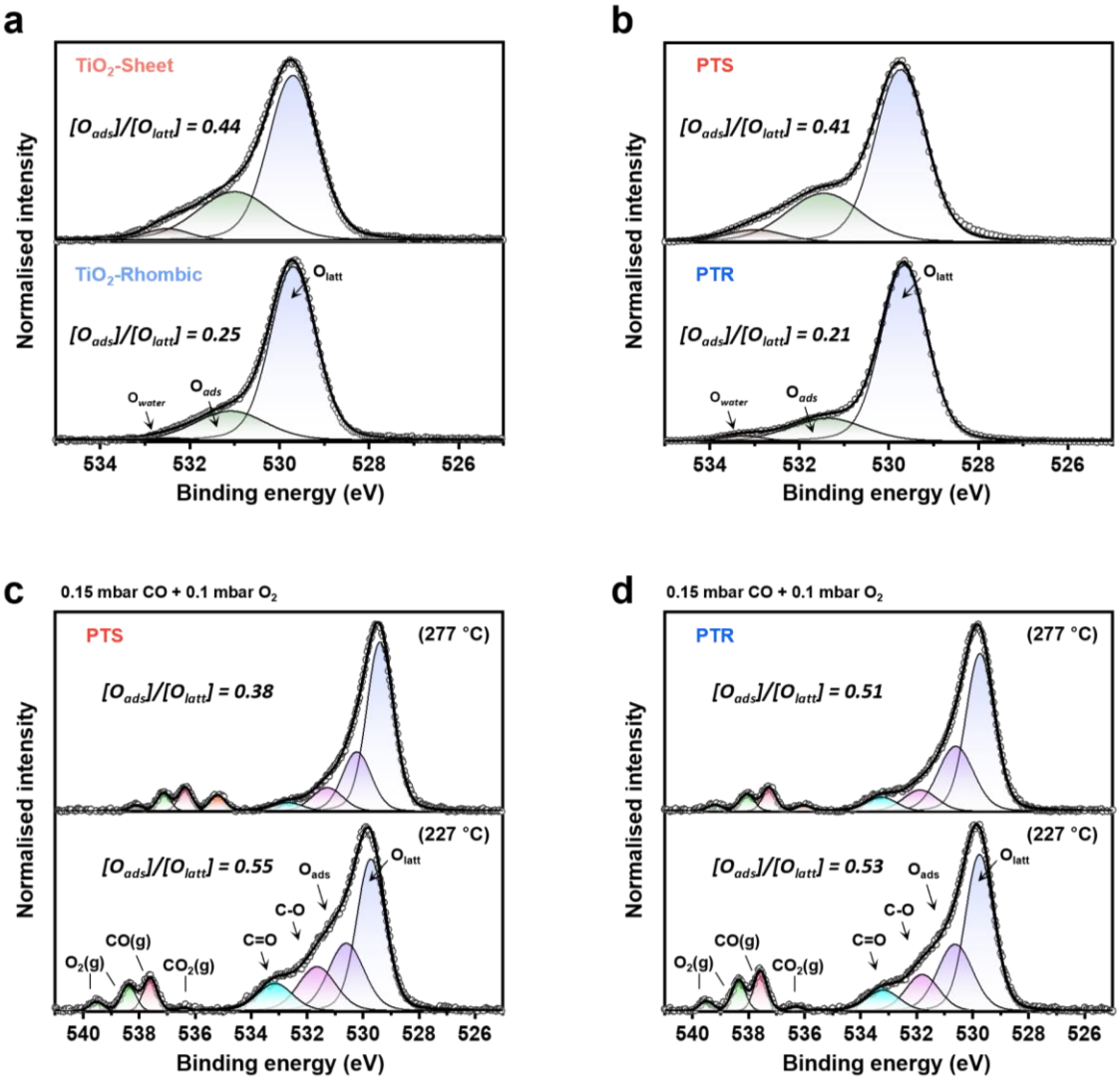

Supplementary Figure 35. Normalised O 1*s* XPS spectra of (a) pristine TiO_2 and (b) Pt/TiO_2 catalysts measured under UHV conditions, and of (c) PTS and (d) PTR catalysts measured under CO oxidation conditions (0.15 mbar CO and 0.1 mbar O_2) at 227 and 277 °C.

We sincerely appreciate the all reviewer's insightful and constructive comments, which have played a crucial role in significantly improving the quality and clarity of our manuscript.

Response to the reviewers' comments

The followings are the responses to the reviewers' comments for the manuscript *NCOMMS-25-68798A*

Reviewer #1

General comments: While the authors have addressed several of my previous concerns, several critical technical issues remain that require further clarification.

Response: We sincerely thank the reviewer for recognising our earlier revisions and for the incisive follow-up questions raised in this round. For clarity, we have organised the reviewer's general comments into several specific points. We address each of the remaining concerns in detail below with additional calculations, analyses, and clarifications, and believe that these revisions have substantially strengthened the manuscripts.

Comment 1: Specifically, the methodology used to determine CO coverage on the Pt surface needs to be clearly defined, as it is unclear if the "abundant" CO model utilized is physically accurate under realistic conditions. This high CO loading also raises questions regarding cluster stability; the authors should investigate whether such high adsorbate density causes cluster "lifting" or structural instability.

Response: We sincerely thank the reviewer for this incisive and scientifically rigorous critique. Upon careful reflection, we fully acknowledge that the initial approach, in which CO molecules were placed on all geometrically accessible surface Pt sites to approximate a CO-saturated regime, may constitute a thermodynamically unphysical upper-bound model that conflates geometric site accessibility with equilibrium site occupancy. The reviewer's identification of this fundamental inconsistency has prompted a substantive revision of our methodology, and we appreciate the reviewer for pointing out the oversight.

To rigorously determine the thermodynamically appropriate CO surface coverage, we implemented a grand-canonical surface thermodynamics framework in which the stable number of adsorbed CO molecules, N*, is identified by minimizing the surface grand potential:

$$\Omega(N) = E(N) - \mu_{CO}(T, p),$$

where E(N) is the total energy of the Pt_{201}/TiO_2 system with N CO molecules adsorbed in order of decreasing binding strength, evaluated using the Preferred Potential (PFP) machine learning

interatomic potential as implemented in the Matlantis platform, and $u_{CO}(T,p)$ is the chemical potential of gas-phase CO evaluated as:

$$u_{CO}(T,p) = E_{CO,elec} + \Delta H(T) - T\Delta S(T) + k_{BT} \ln\left({}^{p}/_{p^0}\right).$$

The thermal enthalpy and entropy contributions, $\Delta H(T)$ and $\Delta S(T)$, were obtained from JANAF thermochemical tables managed by NIST to ensure thermodynamic accuracy across the experimentally relevant temperature range. To construct the sequential adsorption energy landscape, *E*(N), CO adsorption energies were computed individually for all distinct surface Pt sites on the GA-optimized $Pt_{201}/TiO_2(001)$ and $Pt_{201}/TiO_2(101)$ structures and ranked in order of decreasing binding affinity, thereby capturing the energetic heterogeneity inherent to a realistic nanoparticle surface.

To account for the partial retention of entropy by adsorbed CO through constrained surface modes, an approximate adsorption entropy correction $\Delta\mu_{corr} = T \cdot (0.30 \cdot S_{\mathrm{gas}}^{\mathrm{JANAF}} + 3.3 \cdot k_{\mathrm{B}})$ was applied to the effective CO chemical potential $u_{eff} = \mu_{CO}^{JANAF} - \Delta\mu_{\mathrm{corr}}$. This correction accounts for the loss of translational and rotational entropy on adsorption, in line with the empirical scaling $S_{ads} \approx 0.70 \cdot S_{gas} - 3.3\mathrm{R}$ reported for chemisorbed molecules (*J. Am. Chem. Soc.* 2012, 134, 18109–18115). Using this chemical-potential construction, the thermodynamically stable CO coverage as a function of temperature and CO partial pressure was evaluated and presented as a two-dimensional contour phase diagram (Supplementary Figs. 28a, b).

Regarding the choice of representative conditions for the surface phase diagram, we note that the CO-covered MD simulations are intended to elucidate CO-induced structural reconstruction of Pt nanoparticles (NPs) under experimentally relevant environments. The appropriate reference conditions are therefore those under which the experimentally observed CO-induced Pt restructuring is directly probed, namely the *in situ* DRIFTS measurements. On this basis, the representative reaction point marked on the surface phase diagram is T = 240°C (513 K) and p_{CO} = 0.01 bar ($\log_{10}(p_{CO}/\mathrm{bar}) = -2$), matching the experimental characterisation protocol described above. At this condition, the thermodynamically stable CO coverages, N*, are 39 CO molecules on $Pt_{201}/TiO_2(001)$ (PTS) and 45 CO molecules on $Pt_{201}/TiO_2(101)$ (PTR), as detailed in Figs. 4e, f and Supplementary Figs. 28c, d. The revised CO adsorbed GNN-based MD simulations then used these N* values, replacing the earlier saturation-coverage model

with a physically grounded representation of experimentally relevant surface state.

To connect the MD trajectories to the *in situ* DRIFTS signal, which reports mainly on CO bound to under-coordinated Pt, we tracked the coordination-number (CN) distribution of the CO-adsorbable surface Pt atoms, those with CN ≤ 9, following the DRIFT-based criterion of Kappers and van der Maas for supported Pt catalysts, before and after the 100 ps CO-covered GNN-MD runs at 513 K. (*Catal. Lett.* 1991, 10, 365–373) The resulting CN values are summarised in Supplementary Table 6. For both models, the standard deviation of the surface-Pt CN distribution increases and the mean CN decreases after the MD run, indicating a growth of the under-coordinated Pt population and thereby supporting the surface roughening inferred from the CO-DRIFTS measurements. Although the thermodynamically appropriate CO-coverage condition is milder than the earlier saturation-coverage model, this roughening response still exhibits a discernible facet dependence, as reflected in Figs. 4e, f. Specifically, the mean CN of PTS decreases from 7.48 to 7.40 (ΔCN = 0.08), whereas that of PTR decreases from 7.54 to 7.42 (ΔCN = 0.12) in Supplementary Table 6, showing a larger coordination-environment broadening on PTR. The facet-dependent structural responses obtained from the revised simulations remain qualitatively consistent with the central conclusions of the original manuscript. Although the absolute magnitude of the CN change is reduced relative to the saturation-coverage model—a direct consequence of the thermodynamically more appropriate lower coverage—the final snapshots in Supplementary Figs. 28e, f confirm that the revised conditions do not induce the cluster lifting or structural instability flagged by the reviewer. This is further corroborated by the temperature and energy convergence profiles and the radial distribution function (RDF) in Supplementary Fig. 29, which evolves along the same qualitative trend as in the original analysis.

Therefore, under thermodynamically appropriate CO coverage, CO adsorption still induces more pronounced coordination-environment broadening and interfacial restructuring on TiO_2(101) than on TiO_2(001), in direct correspondence with the experimentally observed facet-dependent CO-induced Pt morphological evolution. We are grateful to the reviewer for prompting this essential methodological refinement, which substantially strengthens the physical rigour and internal consistency of the computational framework presented in this work.

Action taken: The corresponding figures and analyses (Supplementary Figs. 28, 29, and Supplementary Table 6) have been added and revised to the current manuscript, and the following paragraph has been added to the *Computational insights into facet-dependent Pt*

reconstructions on TiO_2 section on pages 10–11: *"To further elucidate experimentally observed CO-induced reconstruction behaviour, additional CO-covered GNN-based MD simulations were performed on $Pt_{201}/TiO_2(001)$ and $Pt_{201}/TiO_2(101)$ (Supplementary Note 7). A grand-canonical surface phase diagram constructed from an empirical chemical-potential framework identified the experimentally relevant CO coverage matching the in situ DRIFTS condition (T = 513 K, pCO = 0.01 bar) as 39 and 45 CO molecules on $Pt_{201}/TiO_2(001)$ and $Pt_{201}/TiO_2(101)$, respectively (Supplementary Fig. 28). Under these thermodynamically appropriate CO coverages and reaction-relevant thermal conditions (100 ps at 513 K), CO adsorption perturbed the coordination environment of surface Pt atoms in a facet-dependent manner, as evidenced by broadening of CN distributions (Figs. 4e, f) and Pt–Pt RDFs (Supplementary Figs. 29c, d), particularly on the (101) facet (Supplementary Table 6). Specifically, the mean CN of the CO-adsorbable (CN ≤ 9) surface Pt subpopulation decreased from 7.48 to 7.40 on $Pt_{201}/TiO_2(001)$ ($\Delta CN = 0.08$) and from 7.54 to 7.42 on $Pt_{201}/TiO_2(101)$ ($\Delta CN = 0.12$), supporting experimental observations of CO-induced Pt roughening."*

In addition, details of the GNN-based MD methodology employed to reproduce CO-induced reconstruction were added in Supplementary Note 7.

Supplementary Note 7. CO-induced Reconstruction Simulations *CO-induced structural reconstruction of Pt nanoparticles (NPs) was investigated using a grand-canonical determination of the experimentally relevant CO coverage, followed by structural relaxation and molecular dynamics (MD) simulations under the in situ DRIFTS reaction condition. For each optimized Pt_{201}/TiO_2 structure, surface Pt atoms were first identified based on a combined coordination and geometric criterion. Pt–Pt coordination numbers were evaluated using a cutoff distance of 3.0 Å, while interactions with the TiO_2 support (Ti and O atoms) were identified using a cutoff distance of 3.5 Å. Pt atoms with reduced Pt coordination were classified as surface atoms when they were either located at the metal–support interface, positioned far from the cluster center, or exhibited very low Pt coordination. In addition, Pt atoms located near the top of the NP were also considered surface atoms if their coordination number was below a threshold. This procedure enabled robust identification of catalytically accessible surface Pt sites across different NP morphologies.*

The thermodynamically stable CO coverage on each Pt_{201}/TiO_2 facet was then identified from a grand-canonical surface phase diagram. The stable number of adsorbed CO molecules, N, was obtained by minimizing the surface grand potential,*

$$\Omega(N) = E(N) - N \cdot \mu_{CO}(T, p_{CO}), \qquad (S7.1)$$

where E(N) is the total energy of the Pt_{201}/TiO_2 system with N CO molecules adsorbed in order of decreasing binding strength, evaluated using the Preferred Potential (PFP) machine learning interatomic potential implemented in the Matlantis platform, and $\mu_{CO}(T, p_{CO})$ is the chemical potential of gas-phase CO, evaluated as

$$\mu_{CO}(T, p_{CO}) = E_{CO}(DFT) + \Delta H(T) - T \cdot \Delta S(T) + k_B T \ln(p_{CO}/p^{\circ}), \qquad (S7.2)$$

where $\Delta H(T)$ and $\Delta S(T)$ were obtained JANAF thermochemical tables managed by NIST, and the reference pressure $p^{\circ} = 1$ bar. To account for the partial retention of entropy by adsorbed CO through contrained surface modes, an approximate adsorption entropy correction was applied to the effective CO chemical potential using the empirical scaling relation reported by Campbell and Sellers,[12]

$$S_{ads} \approx 0.70 \cdot S_{gas} - 3.3R. \qquad (S7.3)$$

CO adsorption energies were computed individually for every distinct surface Pt site identified above and ranked in order of decreasing binding affinity to construct E(N). The surface grand potential was minimized over N at each (T, p_{CO}) grid point, yielding the two-dimensional surface phase diagram shown in Supplementary Figs. 28a, b. At the reference condition, matching the in situ DRIFTS protocol (T = 513 K, p_{CO} = 0.01 bar), N corresponded to 39 CO molecules on $Pt_{201}/TiO_2(001)$ (PTS) and 45 CO molecules on $Pt_{201}/TiO_2(101)$ (PTR), as summarised by the adsorption-energy landscapes in Figs. 4e, f and Supplementary Figs. 28c, d.*

CO molecules were adsorbed on the N most strongly binding surface Pt sites using a site-by-site construction protocol. For each selected Pt atom, a CO molecule was placed along an outward direction defined relative to the NP geometry, with a fixed Pt–C distance of 1.85 Å and a C–O bond length of 1.15 Å. To avoid unphysical steric overlap, newly added CO molecules were excluded if the distance between any CO atom and existing atoms was smaller than 1.8 Å; when overlap was detected, the corresponding adsorption site was skipped.*

The CO-covered structures were subsequently relaxed using the limited-memory Broyden–Fletcher–Goldfarb–Shanno (LBFGS) algorithm to remove residual forces arising from the initial CO placement. Structural optimization was performed until the maximum atomic force fell below 0.05 $eV{\cdot}Å^{-1}$. The relaxed CO-covered configurations were then used as initial

structures for finite-temperature MD simulations.

MD simulations were carried out in the canonical (NVT) ensemble using a Langevin thermostat at the experimental reaction temperature of 513 K, matching the in situ DRIFTS measurement condition. A time step of 1.0 fs was employed, and a friction coefficient of 0.001 was used to ensure stable temperature control while allowing sufficient atomic mobility. Each simulation was propagated for 100,000 MD steps, corresponding to a total simulation time of 100 ps. Atomic trajectories and thermodynamic quantities were recorded at regular intervals throughout the simulation. These simulations enabled direct observation of CO-induced structural rearrangements of Pt NPs under experimentally representative CO coverages.

To connect the MD trajectories to the in situ DRIFTS signal, which reports mainly on CO bound to under-coordinated Pt, the coordination-number (CN) distribution of the CO-adsorbable surface Pt subpopulation, defined as Pt atoms with CN ≤ 9 following the DRIFT-based criterion of Kappers and van der Maas,[13] was extracted before and after each 100 ps trajectory. These simulations enabled direct observation of CO-induced structural rearrangements of Pt NPs under experimentally observed CO-induced Pt roughening."

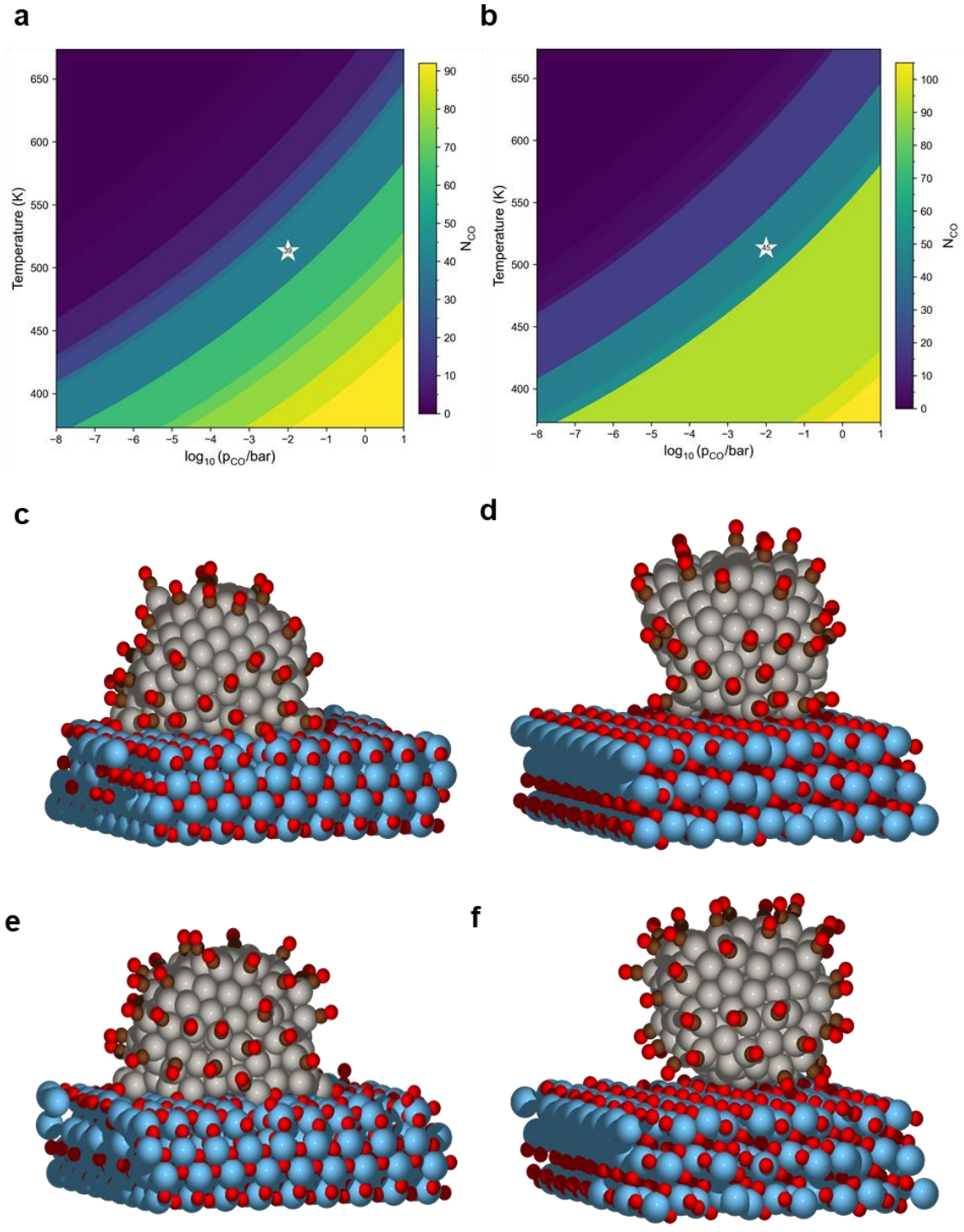

Supplementary Figure 28. Grand-canonical surface phase diagram of CO coverage and CO-induced reconstruction of Pt_{201} NPs on TiO_2 facets. (a, b) Stable CO coverage as a function of temperature and CO partial pressure on (a) TiO_2(001) and (b) TiO_2(101). (c, d) Initial configurations with CO adsorbed at available Pt top sites on (c) TiO_2(001) and (d) TiO_2 (101). (e, f) Corresponding structures after GNN–MD simulations at 513 K for 100 ps under CO-rich conditions on (e) TiO_2(001) and (f) TiO_2(101).

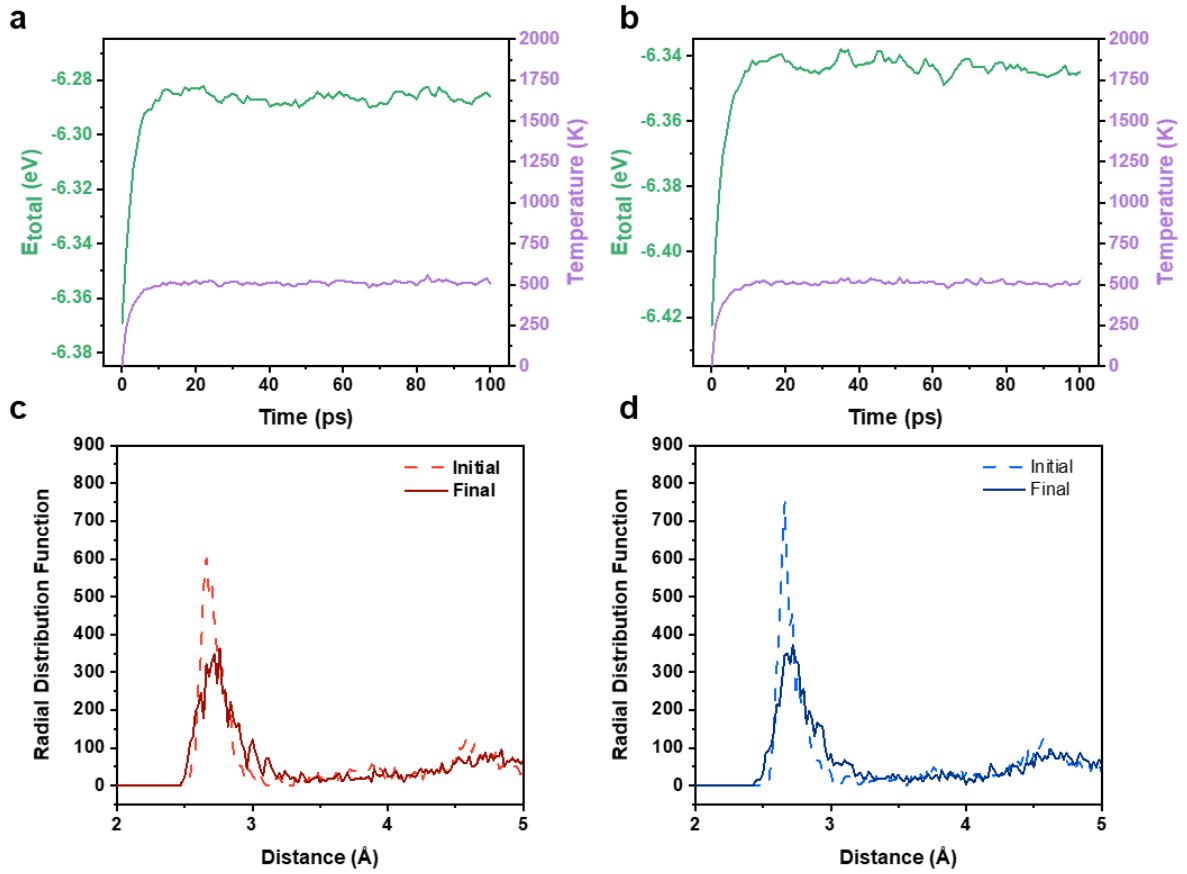

Supplementary Figure 29. Thermal convergence and CO-induced structural evolution of Pt_{201} NPs on TiO_2 facets revealed by GNN–MD simulations. Time evolution of total energy and temperature for (a) $Pt_{201}/TiO_2(001)$ and (b) $Pt_{201}/TiO_2(101)$ during GNN–MD simulations at 513 K, confirming thermal equilibration under CO-rich conditions. Radial distribution functions of Pt atoms before and after simulation are shown for (c) $Pt_{201}/TiO_2(001)$ and (d) $Pt_{201}/TiO_2(101)$.

Supplementary Table 6. Pt–Pt coordination number (CN) statistics for CO-covered Pt_{201} NPs before and after GNN-MD simulations at 513 K for 100 ps.

System	Mean CN	Std. dev.
Initial $Pt_{201}/TiO_2(001)$	7.48	0.97
Final $Pt_{201}/TiO_2(001)$	7.40	1.07
Initial $Pt_{201}/TiO_2(101)$	7.54	0.98
Final $Pt_{201}/TiO_2(101)$	7.42	1.17

Comment 2: Furthermore, the observed lack of full encapsulation on the anatase surfaces may be attributed to the absence of oxygen vacancies in the model, which are generally considered a fundamental driver of the SMSI.

Response and Action taken: We thank the reviewer for this follow-up comment. Before addressing the specific question regarding oxygen vacancies (O_v), we would like to briefly clarify the scope of the present work, as we believe this context is essential for interpreting the results appropriately.

The central focus of this study is the facet-dependent formation of Pt NPs on anatase TiO_2 and their resulting catalytic behaviour in CO oxidation, specifically how the (001) and (101) facets dictate the Pt NP morphology and modulate the ability to supply and activate lattice oxygen via the Mars–van Krevelen (MvK) mechanism under CO oxidation conditions. Strong metal–support interaction (SMSI) phenomena, including TiO_x encapsulation, are well established to occur predominantly under high-temperature reducing conditions (typically >700 K for Pt/TiO_2 systems, *Angew. Chem. Int. Ed.* 2020, 59, 11824–11829), which are fundamentally distinct from the conditions examined throughout the present study.

Nevertheless, to directly and rigorously address the reviewer's concern that the absence of O_v in our model may have precluded encapsulation, we performed additional GNN-MD simulations with 12.5% surface O_v on both $Pt_{201}/TiO_2(001)$ and $Pt_{201}/TiO_2(101)$ surfaces. These simulations were performed under reductive high-temperature conditions analogous to those employed by Wang et al. (*Science* 2024, 386, 915–920), specifically at 1500 K for 800 ps, which were shown in our previous response to produce pronounced SMSI encapsulation on rutile $TiO_2(011)$. The results are shown in the R1Fig. 1.

Under these reductive high-T conditions, the Pt NP undergoes full TiO_x encapsulation on both anatase facets, consistent with the classical O_v-driven SMSI mechanism; the corresponding changes in interfacial structural descriptors relative to the initial configuration are summarised in R1Table below. This result directly confirms the reviewer's physical insight that O_v can drive Pt encapsulation on anatase when thermodynamically and kinetically enabled, and validates our computational framework's ability to capture O_v-driven reconstruction. These high-T trajectories probe conditions distinct from those examined in the present study, under which full TiO_x encapsulation is not observed experimentally on either PTS or PTR. We therefore provide them here as a response to the reviewer's comment, while keeping the main manuscript

and Supplementary Information focused on the experimentally relevant regime.

Furthermore, comparing the two anatase facets under these reductive high temperature conditions, the structural signatures of encapsulation are more pronounced on $Pt_{201}/TiO_2(001)$ than on $Pt_{201}/TiO_2(101)$: Specifically, ΔPt–Ti bonds and the absolute value of ΔPt height are all larger in magnitude on the (001) facet (R1Table 1), indicating stronger TiO_x migration toward the Pt surface and deeper Pt burial on (001). This facet dependence is fully consistent with the baseline MSI trend observed in the O_v-free models of the present study, in which $Pt/TiO_2(001)$ exhibits a substantially lower effective contact angle (95.7°) than $Pt/TiO_2(101)$ (118.7°, Figs. 4a, b), reflecting a SMSI on the (001) facet. The 1500 K, 12.5% O_v benchmark therefore amplifies, under extreme reductive thermal conditions, the same facet-dependent MSI asymmetry that governs the Pt morphologies in the experimentally relevant regime.

Taken together, the GNN-MD simulation under 1500 K for 800 ps with 12.5% surface O_v reproduces classical TiO_x encapsulation on both anatase facets, directly confirming the reviewer's physical insight that O_v can drive Pt encapsulation on anatase once a reductive high temperature chemical potential is thermodynamically and kinetically activated. Nevertheless, since the present manuscript does not make claims regarding SMSI-type TiO_x encapsulation, a regime established to occur under reductive high temperature conditions that lie outside those examined here, no revision to the main manuscript was deemed necessary.

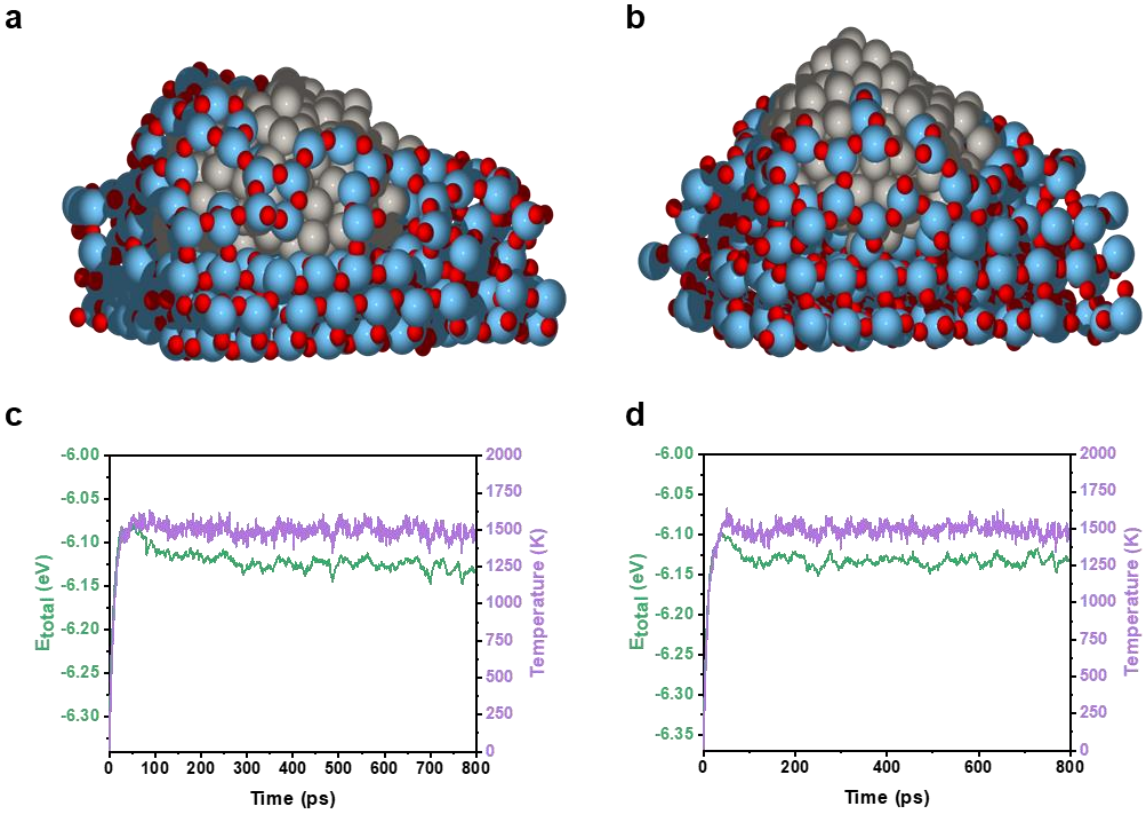

R1Figure 1. Thermal convergence and facet-dependent structural evolution of Pt_{201} NPs on TiO_2 with 12.5% O_v revealed by GNN-MD simulations under extreme conditions. Final snapshots after the simulations at 1500 K for 800 ps for (a) $Pt_{201}/TiO_2(001)$ and (b) $Pt_{201}/TiO_2(101)$ with 12.5% O_v, along with time evolution of total energy and temperature confirming stable thermal equilibration during simulations for O_v added (c) $Pt_{201}/TiO_2(001)$ and (d) $Pt_{201}/TiO_2(101)$ with 12.5% O_v.

R1Table 1. Quantitative structural descriptors extracted from GNN-MD simulations after 800 ps at 1500 K for Pt_{201} NPs supported on different TiO_2 facets with 12.5% O_v.

	ΔPt–Ti bonds	ΔO average z (Å)	ΔPt–O separation (Å)	ΔPt height (Å)
Pt/anatase $TiO_2(001)$ with 12.5% O_v	+300	+0.69	+0.14	−6.06
Pt/anatase $TiO_2(101)$ with 12.5% O_v	+266	+0.69	+0.14	−4.43

Reported values correspond to changes (Δ) relative to the corresponding initial configurations prior to MD simulations. Specifically, changes in number of Pt–Ti bonds (ΔPt–Ti bonds), the changes in the average vertical displacement of surface oxygen atoms (ΔO average z (Å)), the changes in the mean Pt–O separation (ΔPt–O separation (Å)), and the changes in the overall height of the Pt NP with respect to the initial structure (ΔPt height (Å))

Comment 3: Regarding the kinetic results, the reported activation barrier of 3.37 eV for Pt_{28}/TiO_2 is exceptionally high and deviates significantly from values typically found in the literature; therefore, this result must be carefully re-verified.

Response: We sincerely thank the reviewer for this critical observation. Upon re-examination, the 3.37 eV value reported on $Pt_{28}/TiO_2(101)$ is a physically meaningful transition-state (TS) energy rather than a numerical artefact; however, it corresponds to a specific reference state: the MvK barrier computed with CO initialised at the thermodynamically most-stable terrace site ($\Delta E_{ads} = -2.50$ eV). The apparent activation barrier of CO oxidation is intrinsically CO-coverage dependent, and its numerical value depends on the kinetic reference state chosen for the rate-determining step. Under the saturated-coverage limit relevant to the original calculation, the adsorbed CO* at the most-stable site is the operative reference and the corresponding barrier is 3.37 eV; under the CO-coverage and CO/O_2 conditions at which the experimental kinetics are actually measured, however, strongly-bound terrace CO is kinetically inert and the MvK step proceeds at more weakly-bound CO at the Pt–TiO_2 interfacial perimeter. We therefore re-evaluated the MvK barrier with CO initialised at the perimeter-adjacent Pt sites on both facets and supplemented the reinterpretation with direct experimental evidence from CO/O_2 dependent light-off measurements.

The appropriate reference state follows the standard coverage-dependent picture of CO oxidation on supported metal catalysts. Following Iglesia et al. (*J. Am. Chem. Soc.* 2011, 133, 12, 4498–4517), two limiting regimes can be distinguished. In the low-coverage regime (low CO/O_2), the Pt surface is predominantly *O-covered and adsorbed CO* is nearly absent at steady state, so the operative kinetic reference is CO(g) + *O; the apparent barrier is measured from CO(g) + *O to the [O···C···O]‡ TS, and the strong CO adsorption energy no longer acts as an energetic penalty but as a driving force that is released during CO–O coupling. In the high-coverage regime (high CO/O_2, the zero-order regime of Iglesia et al.), the Pt surface is nearly saturated with CO* and adsorbed CO* itself is the operative reference. Crucially, within this regime strongly-bound terrace CO* species are kinetically inert spectators and turnover proceeds preferentially at the more weakly bound Pt–TiO_2 interfacial perimeter sites that have been identified as the catalytically relevant centers on supported group-VIII metals on reducible oxides (Cargnello et al., *Science* 2013, 341, 771).

Applying this framework to our Pt_{28}/TiO_2 system, the CO adsorption energies at the perimeter-adjacent Pt sites are −1.05 eV on $Pt_{28}/TiO_2(001)$ (PTS) and −0.80 eV on $Pt_{28}/TiO_2(101)$ (PTR),

substantially weaker than the terrace-site values (−1.72 eV and −2.50 eV) that were used as the NEB initial state in the original calculations; a comparison between the two configurations is shown in R1Fig. 2. Recomputing the MvK barrier with CO initialised at these perimeter sites, under otherwise identical computational settings (same functional, *k*-point sampling, and Pt_{28}/TiO_2 models), yields effective activation barriers of 0.91 eV on PTS and 1.67 eV on PTR. Both values lie well within the range of DFT barriers reported for supported Pt CO oxidation (*Catal Lett,* 2019, 149, 390–398 / *J. Phys. Chem. C* 2023, 127, 43, 21132–21149), and they preserve the facet ordering (PTS < PTR), consistent with the experimentally measured apparent activation energies of 55 and 112 $kJ \cdot mol^{-1}$, for PTS and PTR, respectively (Fig. 1f). The magnitude of this reference-state sensitivity has been quantified recently for Pt/anatase-TiO_2(101) by Tesvara et al. (*ACS Catal.* 2024, 14, 7562), where the apparent activation energy of the same MvK cycle is shown to vary from 0.29 to 1.15 eV depending on which rate-controlling intermediate is chosen as the reference, directly corroborating the reference-state logic invoked here.

The coverage-dependent reinterpretation is directly supported by the measured CO/O_2 dependence of the catalyst light-off behaviour (Supplementary Fig. 4). Increasing the CO/O_2 ratio from 0.2 to 5 systematically shifts the light-off temperature to higher values on both PTS and PTR, precisely the trend expected for an apparent activation barrier that rises with CO coverage as the kinetic reference state shifts from CO(g) toward a CO*-saturated surface. The consistent facet ordering of this shift across the full CO/O_2 range, together with its persistence even in the O_2-rich regime where stoichiometric oxygen limitation cannot dominate, confirms that the coverage-dependent reference state, not simple O_2 scarcity, governs the apparent activation energy of CO oxidation on Pt/TiO_2.

Taken together, these two values are complementary rather than contradictory: 3.37 eV remains the correct MvK barrier on Pt_{28}/TiO_2(101) under the terrace-CO reference used in the original calculation, and is preserved here as the thermodynamic limit, while 1.67 eV is the barrier under the perimeter-CO reference that actually governs the experimentally measured kinetics. The perimeter-CO barriers (0.91 eV on PTS; 1.67 eV on PTR) are therefore the appropriate DFT quantities for direct comparison with the Arrhenius data, and are adopted throughout the revised reaction-energy analysis below.

Upon re-evaluating the MvK cycle with the perimeter-CO reference described above, we were further able to refine the mechanistic picture: the overall rate-determining step is not the initial

lattice-oxygen activation step ($CO + O_L \rightarrow CO_2 + O_v$; 0.91 eV on $Pt_{28}/TiO_2(001)$ and 1.67 eV on $Pt_{28}/TiO_2(101)$), but the subsequent coupling of a second CO with the refilled surface oxygen ($CO + *O \rightarrow CO_2$; 1.41 eV on $Pt_{28}/TiO_2(001)$ and 2.13 eV on $Pt_{28}/TiO_2(101)$). Importantly, these results nevertheless show that $Pt_{28}/TiO_2(001)$ remains more reactive than $Pt_{28}/TiO_2(101)$ throughout the MvK pathway, exhibiting consistently lower barriers for both the initial lattice-oxygen activation step and the subsequent second-CO coupling step, in line with the overall facet-dependent reactivity trend observed in the AP-XPS results. This revised rate-determining-step assignment is also consistent with previous reports (*J. Phys. Chem. C* 2023, 127, 43, 21132–21149), in which the second CO_2 formation was identified as the most energy-demanding step in MvK-type CO oxidation over supported Pt catalysts.

We are grateful to the reviewer for raising this point, as it led us to re-examine our calculations in depth and arrive at a mechanistic picture that is both internally consistent and in line with the established literature. The main text has been updated accordingly, as detailed below.

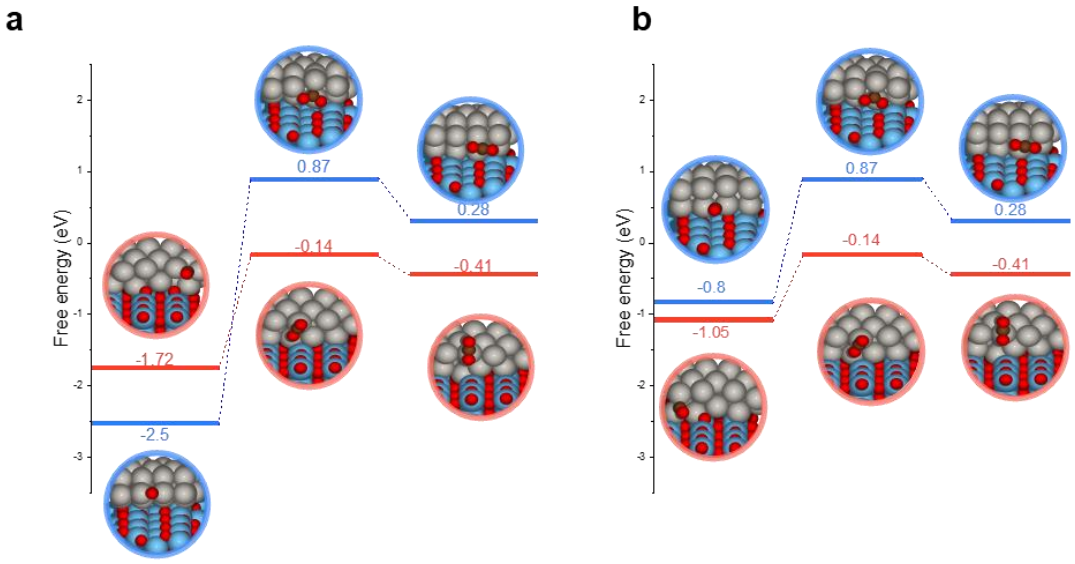

R1Figure 2. Reaction energy diagrams illustrating the effect of the initial CO adsorption site on CO oxidation. (a) Pathway initiated from the thermodynamically most stable CO adsorption configuration. (b) Pathway initiated from CO adsorbed at the Pt–TiO_2 perimeter site.

Action taken: In the main text (on pages 11–12, section on the *Reaction mechanism and the origin of superior catalytic activity*), the paragraphs have been revised as follows, and the reaction energy diagram in Fig. 6a has been updated: *"DFT calculations were employed to*

elucidate the influence of reconstructed Pt structures at the Pt–TiO_2 interfaces on the catalytic activity. A complete reaction energy diagram was derived for the optimised Pt_{28}/TiO_2(001) and (101) models following the MvK pathway (Fig. 6a). The lattice-oxygen activation step exhibits strong facet dependence, with activation barriers of 0.91 eV on Pt_{28}/TiO_2(001) and 1.67 eV on Pt_{28}/TiO_2(101). The overall rate-determining step, however, is the subsequent coupling of a second CO with the refilled surface oxygen, for which the barriers are 1.41 eV on Pt_{28}/TiO_2(001) and 2.13 eV on Pt_{28}/TiO_2(101), in agreement with previous reports that the second CO_2 formation is the most energy-demanding step in MvK-type CO oxidation over supported Pt catalysts.[42] *These values mirror the experimentally observed facet-dependent E_a with Pt_{28}/TiO_2(001) achieving higher CO oxidation rates due to more facile lattice-oxygen activation; the trend is further supported by microkinetic modeling results, which qualitatively reproduce the facet-dependent reactivity trends (Supplementary Fig. 31 and Supplementary Note 8). Calculated O_v formation energies across multiple surface sites (Supplementary Fig. 32) further support this facet-intrinsic difference in reducibility, revealing the greater intrinsic reactivity of lattice oxygen on the (001) facet.*

In addition, a minor corresponding revision has been made in the AP-XPS-related discussion (on page 13, section on the *Reaction mechanism and the origin of superior catalytic activity*) to align the discussion with the revised DFT interpretation and the consistently higher MvK reactivity of Pt_{28}/TiO_2(001) relative to Pt_{28}/TiO_2(101): *"This behaviour reflects the consistently lower DFT barriers calculated for Pt_{28}/TiO_2(001) than for Pt_{28}/TiO_2(101) across the MvK pathway, indicating that the reaction proceeds more readily on PTS during CO oxidation."*

Also, in line with the revised mechanistic assignment described above, the phrase "lattice oxygen activation" has been replaced with "oxygen activation" in the *Abstract*, the final paragraph of the *Introduction* and the *Discussion* section: Specifically, the *Abstract* now reads *"...DFT calculations support facile oxygen activation on the (001) facet throughout the MvK pathway, ...the final paragraph of the Introduction now reads "...Finally, DFT calculations using Pt_{28} cluster models evaluated facet-dependent energetics and oxygen activation during CO oxidation..", and the Discussion section now reads "...Supported by reaction-order analysis and DFT-predicted energetics, this kinetic evolution confirms that the superior performance cannot be attributed solely to the intrinsic support properties of the fresh catalyst, but instead arises from facile oxygen replenishment at the reaction-evolved Pt–TiO_2(001) interface via a MvK-type mechanism..."*.

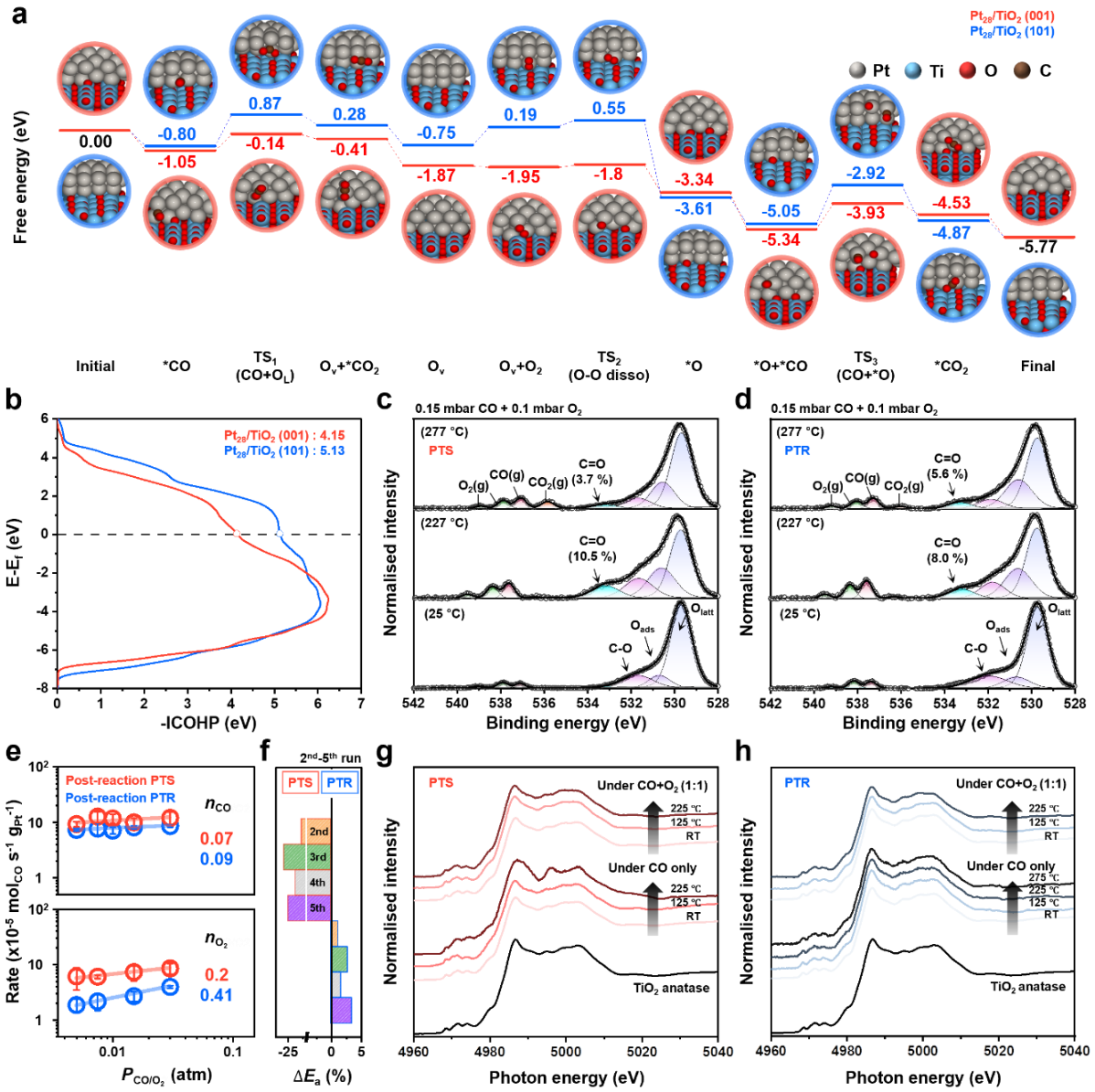

Figure 6. Synergistic effects of Pt morphology and TiO_2 facets on CO oxidation activity. (a) DFT-calculated reaction energy profiles for CO oxidation via the MvK mechanism on $Pt_{28}/TiO_2(001)$ and (101). (b) ICOHP analysis of oxygen vacancy formation on Pt_{28}/TiO_2 models. (c, d) Normalised *in situ* O 1*s* AP-XPS spectra ($h\nu$ = 650 eV) for (c) PTS and (d) PTR catalysts under CO oxidation conditions (0.15 mbar of CO, 0.1 mbar of O_2) at 25, 227, and 277 °C. (e) Reaction-order analysis of CO oxidation on post-reaction Pt/TiO_2 catalysts with respect to CO and O_2 partial pressures. Reaction rates were measured in the kinetically relevant regime (<5% CO conversion) at 80 °C for PTS and 160 °C for PTR, corresponding to their respective light-off temperatures. (f) Relative changes in apparent activation energy (ΔE_a) for PTS and PTR over five consecutive catalytic runs, with respect to the 1st run. (g, h) Ti *K*-edge *in situ* XANES spectra of (f) PTS and (g) PTR under CO-reducing (middle panels: 5% CO/He) and CO + O_2 co-feed (upper panels: 5% CO + 5% O_2/He) conditions.

Comment 4: Finally, to ensure the validity of the theoretical framework, a formal comparison

between the calculated reaction rates and measured experimental rates should be provided.

Response: We sincerely thank the reviewer for this important suggestion. In response, and in conjunction with the activation-energy revision introduced in Comment 3 above, we re-solved the DFT-parameterised microkinetic model (MKM) using the updated Mars–van Krevelen (MvK) barriers and compared the resulting per-site turnover frequencies (TOF) against the CO oxidation rates measured at the main experimental condition (WHSV = 1.5×10^5 mL·g_{cat}^{-1}·h^{-1}, 1% CO, 1% O_2/Ar, 1 atm) on both facets. Experimental per-site TOFs were obtained by dividing the measured rate (≤15% conversion, Supplementary Fig. 5) by the CO-chemisorption-derived surface Pt site density ($N_{surf} = 2.80 \times 10^{-3}$ and 2.31×10^{-3} mol·g_{Pt}^{-1} for PTS and PTR, respectively; Supplementary Table 1). The updated MKM (Supplementary Fig. 31) was evaluated under the matching feed composition, and the revised values are compared in Supplementary Table 7.

The updated MKM reproduces the experimentally observed facet ordering ($TOF_{PTS} \gg TOF_{PTR}$) under the matched flow condition, confirming the ordering and interfacial-MvK predictions on which the theoretical framework rests; the full per-site comparison is provided in Supplementary Table 7. The calculated per-site TOFs lie below the measured rates by less than an order of magnitude on PTS and by approximately one order of magnitude on PTR, an offset that falls within the typical accuracy range of DFT-based microkinetic modelling for heterogeneous oxidation (*Acc. Chem. Res*. 2022, 55, 9, 1237–1248). Because the present model treats only the MvK mechanism and does not include the parallel Langmuir–Hinshelwood channel on metallic Pt that contributes additively to the measured rate, this direction of the residual is the expected one. We have correspondingly adjusted the relevant main-text wording on the microkinetic comparison to more faithfully reflect this level of agreement. We thank the reviewer for prompting this comparison.

Action taken: In the revised manuscript, the microkinetic analysis has been updated using the revised energetics discussed in our response to Comment 3, and the corresponding results are presented in Supplementary Fig. 31. Accordingly, the main-text wording has been revised to reflect qualitative, rather than quantitative, agreement with the experimental rates. The sentence (on page 12) *"This trend is further supported by microkinetic modeling results, which qualitatively reproduce the facet-dependent reactivity trends (Supplementary Fig. 31 and Supplementary Note 8)."* has replaced the previous statement in the main text.

In addition, to provide a direct comparison between the calculated and experimentally measured rates, Supplementary Table 7 has been added, and the following paragraph has been included in Supplementary Note 8: *"A direct comparison between the calculated per-site MvK turnover frequencies and the experimentally measured CO oxidation rates is summarised in Supplementary Table 7. The model reproduces the experimentally observed facet ordering ($TOF_{PTS} \gg TOF_{PTR}$); the calculated per-site TOFs lie below the measured rates by less than an order of magnitude on PTS and by approximately one order of magnitude on PTR, an offset that falls within the typical accuracy range of DFT-based microkinetic modelling for heterogeneous oxidation.[16]"*

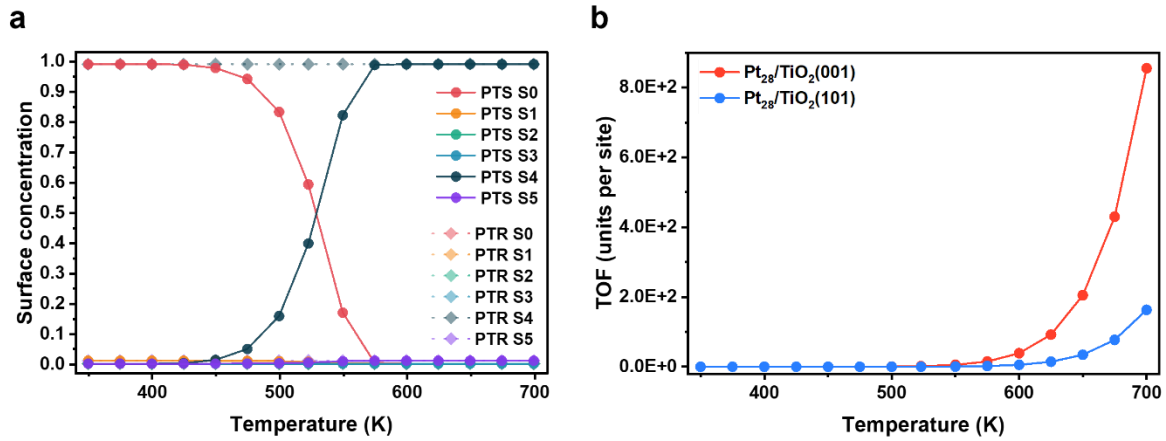

Supplementary Figure 31. Microkinetic modeling results for CO oxidation on Pt_{28}/TiO_2 catalysts. (a) Temperature-dependent surface coverages of reaction intermediates predicted for $Pt_{28}/TiO_2(001)$ (PTS) and $Pt_{28}/TiO_2(101)$ (PTR). (b) Corresponding CO_2 turnover frequencies (TOFs), highlighting the markedly enhanced activity of $Pt_{28}/TiO_2(001)$ at elevated temperatures.

Supplementary Table 7. Comparison of per-site CO oxidation TOF ($s^{-1}\cdot site^{-1}$) at WHSV = 1.5×10^5 $mL\cdot g_{cat}^{-1}\cdot h^{-1}$, 1% CO, 1% O_2/Ar, 1 atm from the MvK microkinetic model and the experimentally measured rates, for PTS and PTR.

T (°C)	TOF_{exp}, PTS	TOF_{calc},PTS (MvK)	TOF_{exp}, PTR	TOF_{calc},PTR (MvK)
170	0.024	0.018	–	9.1×10^{-6}
180	0.075	0.034	–	4.0×10^{-5}
190	0.111	0.062	–	1.3×10^{-4}
200	0.148	0.115	–	4.4×10^{-4}

210	0.220	0.201	–	1.3×10^{-3}
220	0.372	0.347	0.036	3.8×10^{-3}
230	–	0.591	0.066	0.011
240	–	0.972	0.135	0.027
250	–	1.60	0.275	0.070

Reviewer #2

General comments: The authors have thoroughly addressed my technical questions. However, I remain somewhat concerned about the novelty of the work in the context of a high-profile journal such as *Nature Communications*. It is well established that the Pt–TiO_2(001) interface exhibits stronger metal–support interactions compared to Pt–TiO_2(101), and the lower oxygen vacancy (V_O) formation energy and correspondingly higher catalytic activity on the (001) facet are therefore somewhat expected. I would encourage the authors to more clearly articulate the distinctive scientific advance or conceptual novelty of their findings to better align with the high standards of *Nature Communications*.

Response: We thank the reviewer for this important and insightful comment. We agree that the stronger MSI, higher reducibility, and enhanced O_v-related reactivity of TiO_2(001), when considered on their own, may appear broadly consistent with prior expectations. We therefore appreciate the reviewer's point that the distinctive scientific advance of the present work should be articulated more explicitly.

Previous interpretations of facet-dependent activity often focused primarily on differences in intrinsic support properties, particularly O_v abundance and reducibility. By contrast, our central finding is that TiO_2 facets govern not only the intrinsic redox properties of the support, but also the initial Pt morphology, the subsequent restructuring behaviour under CO oxidation conditions, and the reaction-evolved Pt–TiO_2 interfacial state that ultimately determines catalytic performance. In this sense, the present work goes beyond those earlier interpretations by systematically examining, in a well-defined catalyst system, how facet-dependent support properties couple with Pt morphology and its dynamic structural evolution under reaction conditions, using complementary experimental characterisation and computational simulations.

To make this point more explicit, we revised *the Abstract* and *the final paragraph of the*

Introduction to emphasise that facet dependence extends beyond intrinsic support properties to govern the initial morphology, restructuring behaviour, and catalytic interface of supported Pt NPs. We also revised *the discussion associated with Fig. 5* to clarify that facet-dependent MSI defines not only the equilibrium Pt morphology, but also distinct restructuring behaviour under reaction conditions. In *the Discussion section*, we further clarified that the facet-dependent catalytic behaviour of Pt/TiO_2 cannot be understood solely in terms of intrinsic support properties, but must also account for the interplay between support redox properties and the reaction-evolved Pt–TiO_2 interface. We also emphasised that this framework may be relevant more broadly when interpreting facet-driven MSI in reducible oxide-supported catalysts.

Importantly, this central interpretation is further strengthened by the additional results incorporated during revision. The catalytic cycle tests (Supplementary Fig. 35 and Fig. 6f) show that PTS undergoes a further 22.7–25.6% decrease in E_a after the 1st run, demonstrating that its superior activity cannot be explained solely by intrinsic facet-dependent redox properties, but instead arises from formation of a more active reaction-evolved Pt state. In addition, the corresponding structural analyses of the spent catalysts after the 5th cycle (Supplementary Fig. 36) support the stability of this evolved state under repeated reaction conditions. Furthermore, the comparative Pt/Al_2O_3 experiments and further GA-optimised simulations using O_v-modulated TiO_2 models (Supplementary Figs. 42–47 and Supplementary Note 12) clarify that, although O_v contribute to both catalytic reactivity and Pt structural evolution, they do not solely determine the superiority of PTS. Rather, the enhanced performance of PTS arises from the coupling between the redox-active TiO_2(001) surface and the facet-directed evolution of the Pt–TiO_2 interface.

Action taken: In the revised manuscript, we have clarified the distinctive scientific advance of this work, emphasising that the key contribution is not simply the identification of TiO_2(001) as the more active facet, but the demonstration that TiO_2 facets govern the initial Pt morphology, the restructuring behaviour under CO oxidation conditions, and the resulting reaction-evolved Pt–TiO_2 interfacial state. To reflect this more clearly, *the Abstract*, *the final paragraph of the Introduction*, *the discussion associated with Fig. 5* (on page 11), and *the Final Discussion section* (on page 16) have been revised. We respectfully refer the reviewer to the revised manuscript for these integrated changes to the overall interpretation and emphasis of the study.

In addition, to further support and strengthen this central interpretation, we incorporated the catalytic cycle results together with the corresponding structural analyses of the spent catalysts

after the 5th cycle. These additions clarify that the superior activity of PTS cannot be explained solely by intrinsic facet-dependent redox properties, but instead arises from the formation of a more active reaction-evolved Pt state after the 1st run that remains stable under repeated reaction conditions. The corresponding results are presented in Supplementary Fig. 35, Fig. 6f, and Supplementary Fig. 36, and the following sentence has been added to the section on the *Reaction mechanism and the origin of the superior catalytic activity* on page 13: *"Catalytic cycle tests provide direct kinetic evidence of how this facet-directed restructuring dictates catalytic reactivity. As shown in Fig. 6f and Supplementary Fig. 35, relative to the 1st run, PTS exhibits a further 22.7–25.6% decrease in E_a over the 2nd to 5th runs, accompanied by enhanced low-temperature activity, whereas PTR shows almost no change in E_a or light-off behaviour. Consistently, Pt particle-size distributions and high-magnification STEM images after the 5th cycle (Supplementary Fig. 36) show no significant change in Pt size, while facet-dependent Pt morphology is maintained without clear evidence of TiO_2 surface reconstruction near the Pt–TiO_2 interface. These results indicate that reaction-induced restructuring in PTS leads to a more active catalytic state that remains stable over repeated runs."*

We have also expanded the section on the *Reaction mechanism and the origin of the superior catalytic activity* by incorporating additional comparative experiments using a Pt/Al_2O_3 (PtA) catalyst and additional GA-optimised simulations using O_v-modulated TiO_2 models. These additions clarify that O_v contribute to both catalytic reactivity and Pt structural evolution, but do not solely determine the observed superiority of PTS. The corresponding results are presented in Supplementary Figs. 42–47 and Supplementary Note 12, and the following paragraph has been added on page 15: *"To further assess the respective roles of O_v in catalytic reactivity and Pt structural evolution, we conducted comparative experiments using Pt/Al_2O_3 (PtA) catalyst, a representative non-reducible oxide support, together with GA-optimised simulations using O_v-modulated TiO_2 models. Detailed discussions are provided in Supplementary Note 12. In summary, compared with PtA, which shows negligible support-oxygen participation and much less pronounced reaction-induced Pt restructuring (Supplementary Figs. 42–45),[55] PTR exhibited a lower E_a and faster CO_2 light-off, indicating the catalytic contribution of the redox-active TiO_2 support and O_v-related oxygen participation. PTS showed an even lower E_a than PTR in the 1st run, consistent with the combined effects of enriched O_v and the more favourable initial Pt structure on TiO_2(001), while the catalytic cycle test further revealed an additional activity enhancement arising from reaction-induced Pt restructuring. GA-optimised simulations using 5–10% O_v TiO_2 models (Supplementary Figs.*

46 and 47) further showed O_v can modulate the local Pt–TiO_2 interaction and influence Pt morphology, while the overall facet-dependent structural trend remains preserved within the experimentally relevant range. These results indicate that, while O_v contribute to both catalytic reactivity and Pt structural evolution, they do not solely determine the observed superiority of PTS. Instead, the enhanced reactivity arises from the dynamic interplay between the intrinsically higher O_v-related redox reactivity, the initial facet-dependent Pt structure, and the continued evolution of the Pt–TiO_2(001) interface under reaction conditions."

Accordingly, an extended discussion of these results is now provided in Supplementary Note 12: ***"Supplementary Note 12. Indirect Assessment of O_v-related Catalytic Effects and O_v Influences on Facet-dependent Pt Structural Evolution*** *To further assess the respective roles of O_v in catalytic reactivity and Pt structural evolution, we additionally conducted comparative experiments using a Pt/Al_2O_3 (PtA) catalysts, together with GA-optimised simulations using O_v-modulated TiO_2 models. Because direct separation of Pt morphology and O_v effects within the Pt/TiO_2 system is difficult, as the catalytic activity of each catalyst reflects the combined contributions of the initial Pt structure, facet-dependent O_v abundance, and reaction-induced Pt restructuring, PtA was introduced as a non-reducible reference catalyst in which support oxygen does not directly participate in CO oxidation and the reaction proceeds predominantly via a Langmuir–Hinshelwood (L–H) mechanism. As shown in Supplementary Figs. 42a–c and Supplementary Table 1, we synthesised a Pt/Al_2O_3 (PtA) catalyst with a Pt size and dispersion comparable to those of the Pt/TiO_2 catalysts. Accordingly, catalytic activity tests over two consecutive runs and CO-DRIFTS analyses under pre-, in situ, and post-reaction conditions were additionally performed for PtA.*

The PtA catalyst exhibited the highest E_a among the three catalysts, with a value of 130.7 ± 1.1 kJ·mol^{-1}, and showed only a minor change in E_a during the 2nd run (Supplementary Fig. 43). Unlike the catalytic behaviour of the Pt/TiO_2 catalysts during CO-DRIFTS experiments (Fig. 3), the normalized pre- and post-reaction CO-DRIFTS spectra of PtA (Supplementary Fig. 44a) were nearly unchanged, while the in situ DRIFTS contour map (Supplementary Fig. 44b) showed an even more pronounced redshift of the CO–$Pt_{step/edge}$ feature during reaction. In addition, the temperature-resolved CO_2 (g) and CO–$Pt_{step/edge}$ intensity profiles (Supplementary Fig. 44c) showed stronger CO adsorption and a much weaker CO_2 (g) signal than those of Pt/TiO_2. These observations indicate that, although PtA also undergoes CO-induced spectral changes under reaction conditions, its surface remains more strongly CO-

covered and less effective in promoting CO oxidation, consistent with L–H-type reaction behaviour without direct participation of support oxygen.[27]

Compared with PtA, which shows negligible support-oxygen participation and much less pronounced reaction-induced Pt restructuring, PTR showed a substantially lower E_a in the 1st run together with faster CO_2 light-off at low temperature, indicating an additional O_v-related redox contribution from the TiO_2 support. This enhancement became more pronounced in PTS, which exhibited a much lower E_a than PTR in the 1st run, reflecting the combined effects of the more O_v-rich TiO_2(001) surface and the more favourable initial Pt structure on that facet. In addition, the catalytic cycle test showed that only PTS undergoes a further decrease in E_a together with enhanced low-temperature activity after the 1st run, indicating an additional contribution from reaction-induced Pt restructuring beyond the O_v-related support contribution alone.

To further examine how O_v influence the facet-dependent Pt morphology, we performed additional GA-optimised simulations using O_v-modulated TiO_2 models. The original GA optimisation for the Pt_{201}/TiO_2 models (Figs. 4a, b) was carried out on stoichiometric anatase TiO_2 facets without introducing O_v, to isolate the role of TiO_2 surface geometry itself in determining facet-specific equilibrium Pt morphologies. Even in the absence of O_v, these calculations already revealed a pronounced facet dependence in Pt wetting, with the effective contact angle on TiO_2(001) (95.7°) substantially lower than that on TiO_2(101) (118.7°). This ~23° difference indicates that the intrinsic geometric characteristics of the TiO_2 facet alone are sufficient to generate the distinct Pt morphologies observed experimentally, without invoking O_v as a prerequisite.

At the same time, the real catalyst system is expected to contain facet- and condition-dependent O_v populations, which may additionally influence Pt morphology through local changes in MSI. To examine this effect directly, we performed additional GA optimisations using O_v-modulated TiO_2 models containing 10% surface O_v in the relaxed top two layers, corresponding to 5% of the total lattice oxygen in the slab. O_v were placed within the top two layers with a minimum inter-vacancy separation of 5 Å to preserve the dilute-limit interpretation of isolated defects. This concentration falls within the 5–10% range commonly used in DFT studies of anatase oxygen vacancies.[28, 29] *Three independent GA optimisations were carried out for each facet using distinct randomly generated O_v distributions to account for configurational variability in vacancy placement. The corresponding GA energy*

convergence profiles are shown in Supplementary Fig. 46.

The additional GA-optimised simulations reveal a clear facet dependence in the structural response to O_v (Supplementary Fig. 47). On TiO_2(001), introducing O_v leaves the Pt contact angle nearly unchanged, from 95.7° for the stoichiometric surface to 94.3–99.9° (mean 96.5°) across the three O_v-containing realizations, indicating that Pt wetting on this facet is governed primarily by intrinsic surface geometry rather than by O_v. By contrast, on TiO_2(101), introducing 10% surface O_v decreases the Pt contact angle from 118.7° to 102.4–108.2° (mean 104.6°), showing that O_v can partially promote Pt wetting on this facet. However, even at 10% surface O_v, Pt/TiO_2(101) still retains a contact angle on average approximately 8° higher than that of Pt/TiO_2(001).

Notably, the O 1s XPS results show that the O_v-related oxygen ratio on TiO_2(101) is only about one-half of that on TiO_2(001). To reflect this experimentally observed asymmetry, we additionally performed GA optimisation for Pt/TiO_2(101) at 5% surface O_v, corresponding to 2.5% of the total lattice oxygen. The resulting contact angles from three independent realizations were 108.2°, 122.0°, and 116.1° (mean 115.4°), remaining close to the value for stoichiometric TiO_2(101). These results indicate that, although O_v can modulate local Pt wetting, they do not override the dominant role of facet-dependent TiO_2 surface geometry and its resulting MSI in determining the experimentally observed Pt morphology. Together with the comparative Pt/Al_2O_3 analysis discussed above, these results support the conclusion that O_v contribute to both catalytic reactivity and Pt structural evolution, but do not solely determine the observed superiority of PTS."

"

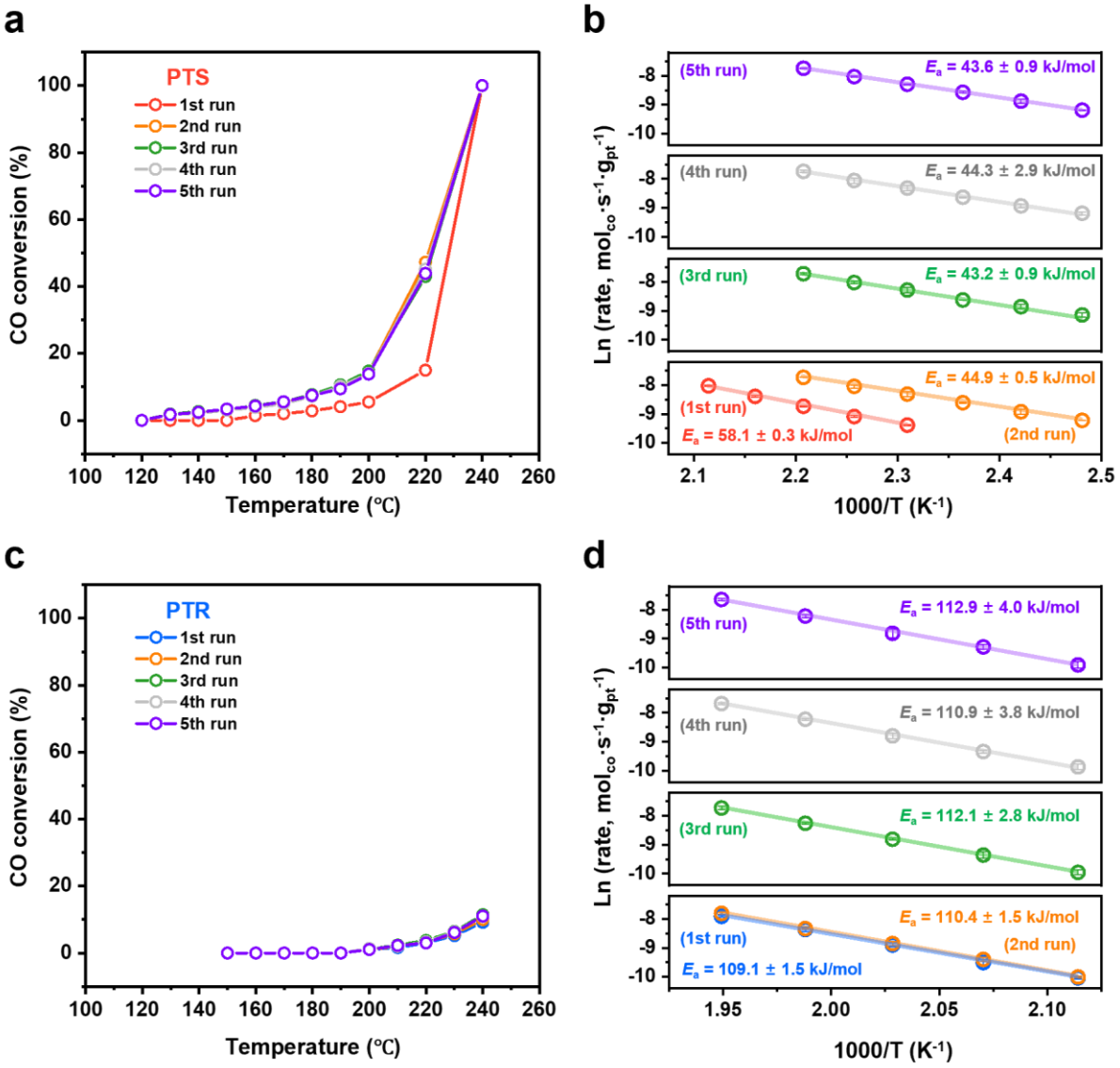

Supplementary Figure 35. Temperature-dependent catalytic cycle tests and corresponding apparent activation energies (E_a) for (a, b) PTS and (c, d) PTR. Five consecutive catalytic runs were performed for each catalyst in a single experiment over the temperature range up to 240 °C, where complete catalytic ignition was observed in the DRIFTS results. After the 1st run, the catalyst was held at 240 °C for 2 h before the 2nd run. All E_a values were obtained at a total flow rate of 100 mL·min^{-1} with a CO/O_2 ratio of 1 under the kinetically relevant regime (<10% CO conversion), and were averaged over three independent experiments using newly loaded catalysts to ensure reproducibility, with error bars representing the standard deviation.

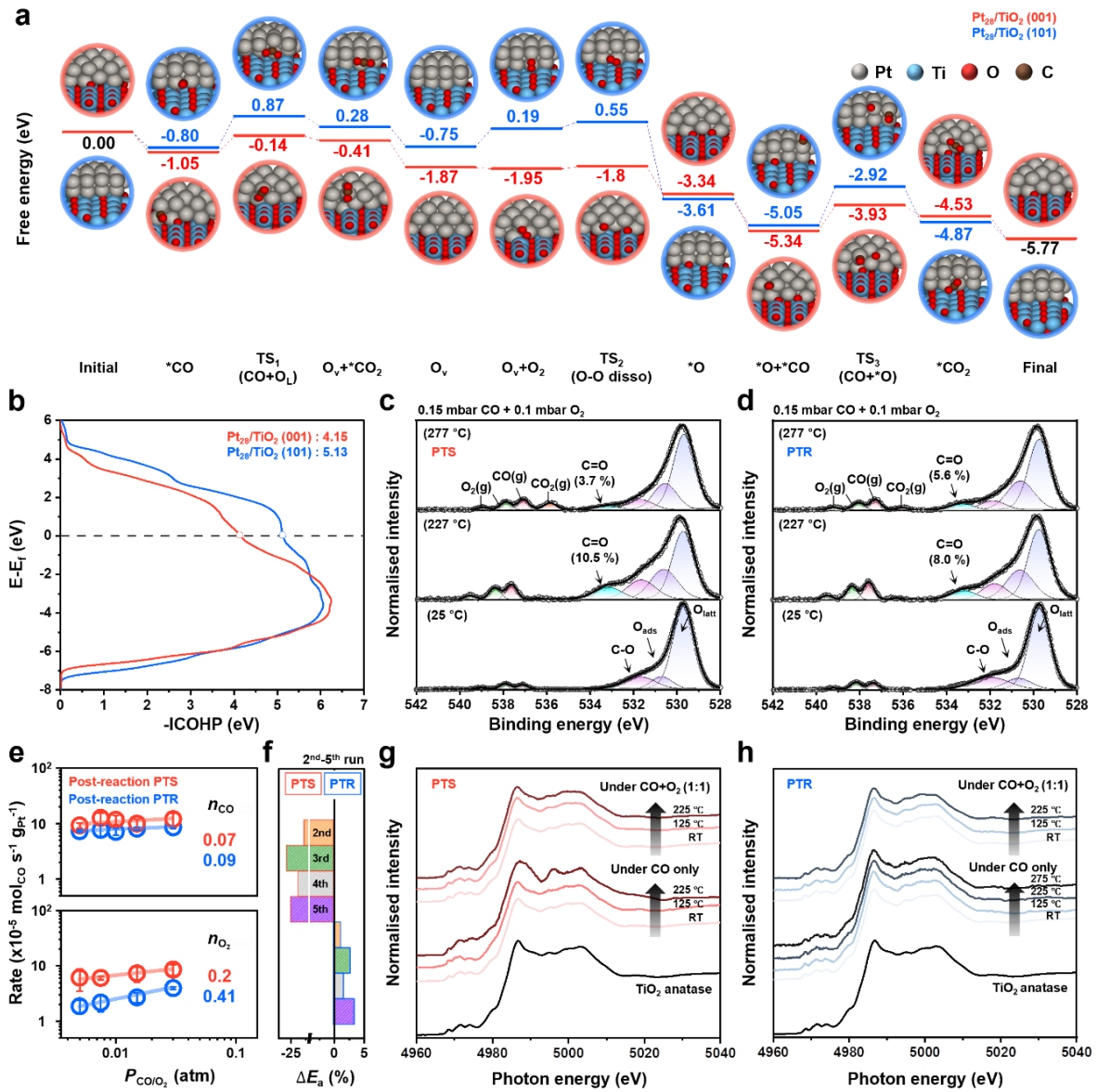

Figure 6. Synergistic effects of Pt morphology and TiO_2 facets on CO oxidation activity. (a) DFT-calculated reaction energy profiles for CO oxidation via the MvK mechanism on $Pt_{28}/TiO_2(001)$ and (101). (b) ICOHP analysis of oxygen vacancy formation on Pt_{28}/TiO_2 models. (c, d) Normalised *in situ* O 1*s* AP-XPS spectra ($h\nu$ = 650 eV) for (c) PTS and (d) PTR catalysts under CO oxidation conditions (0.15 mbar of CO, 0.1 mbar of O_2) at 25, 227, and 277 °C. (e) Reaction-order analysis of CO oxidation on post-reaction Pt/TiO_2 catalysts with respect to CO and O_2 partial pressures. Reaction rates were measured in the kinetically relevant regime (<5% CO conversion) at 80 °C for PTS and 160 °C for PTR, corresponding to their respective light-off temperatures. (f) Relative changes in apparent activation energy (ΔE_a) for PTS and PTR over five consecutive catalytic runs, with respect to the 1st run. (g, h) Ti *K*-edge *in situ* XANES spectra of (f) PTS and (g) PTR under CO-reducing (middle panels: 5% CO/He) and CO + O_2 co-feed (upper panels: 5% CO + 5% O_2/He) conditions.

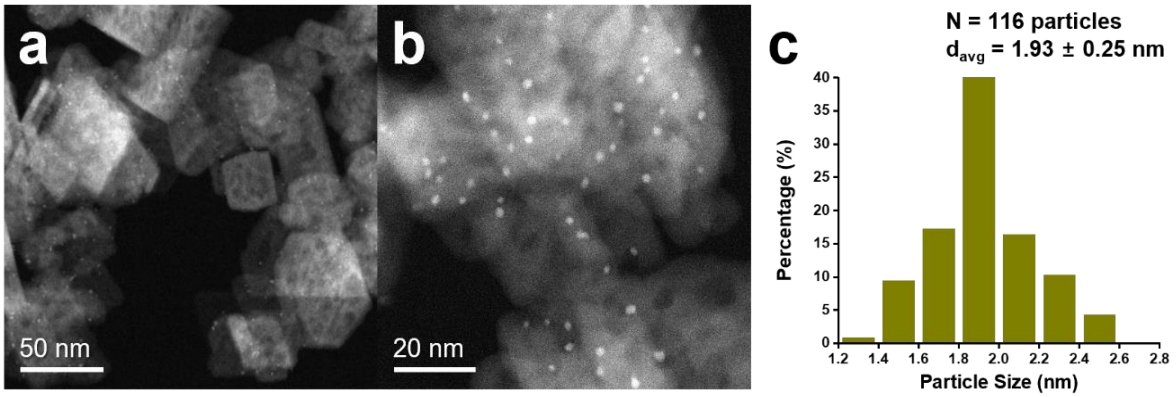

Supplementary Figure 42. (a, b) HAADF–STEM images of the as-prepared Pt/Al_2O_3 (PtA) catalyst. (c) The corresponding histogram showing the Pt NP size distribution for PtA.

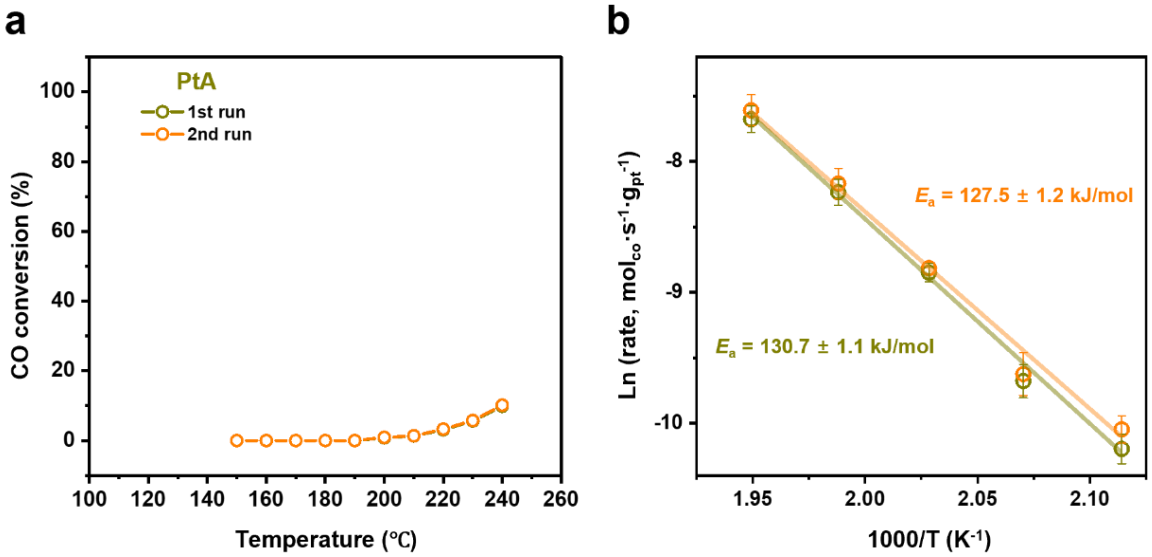

Supplementary Figure 43. (a) Temperature-dependent catalytic cycle tests and (b) corresponding apparent activation energies (E_a) for PtA. Two consecutive catalytic runs were performed for each catalyst in a single experiment over the temperature range up to 240 °C, where complete catalytic ignition was observed in the DRIFTS results. After the 1st run, the catalyst was held at 240 °C for 2 h before the 2nd run. All E_a values were obtained at a total flow rate of 100 mL·min^{-1} with a CO/O_2 ratio of 1 under the kinetically relevant regime (<10% CO conversion), and were averaged over three independent experiments using newly loaded catalysts to ensure reproducibility, with error bars representing the standard deviation.

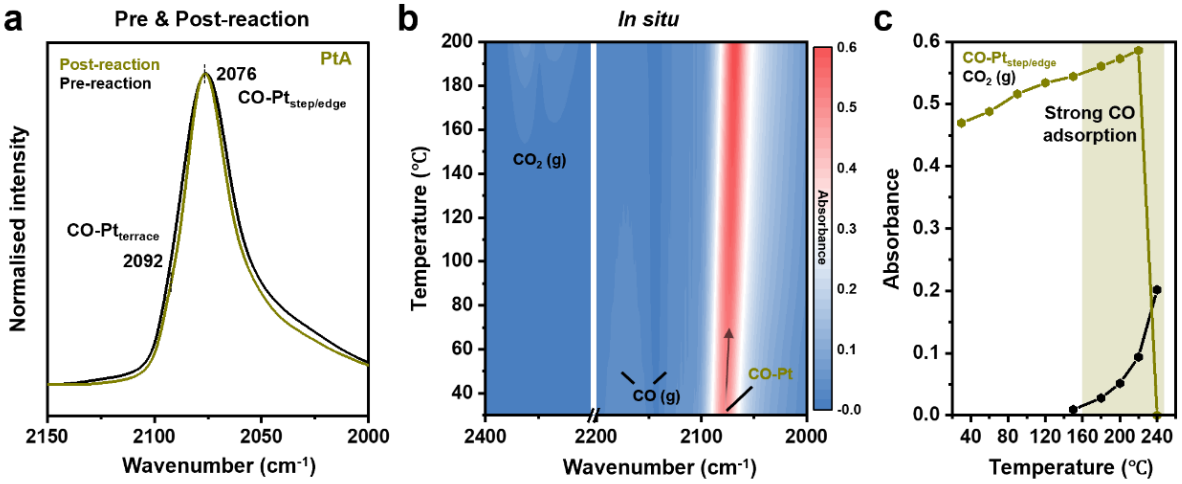

Supplementary Figure 44. *In situ* DRIFTS spectra of PtA catalyst during CO oxidation. (a) Normalised CO-DRIFTS spectra recorded pre- and post-CO oxidation at 25 °C. (b) Contour maps of *in situ* DRIFTS spectra acquired under CO oxidation. (c) Intensity plots tracking CO adsorbed on $Pt_{step/edge}$ sites and gas-phase CO_2 evolution.

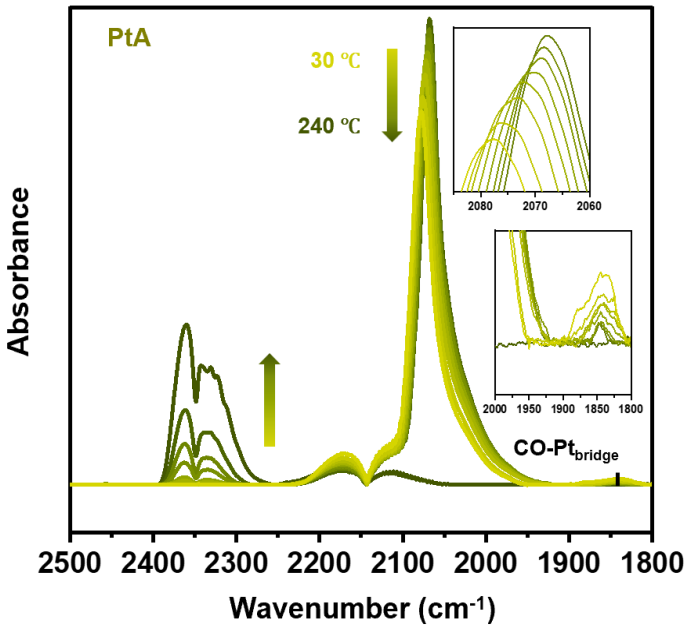

Supplementary Figure 45. Full *in situ* DRIFTS spectra of PtA catalyst recorded under CO oxidation conditions ($CO/O_2 = 1$) at various temperatures. The spectra capture the temperature-dependent evolution of surface species, including CO adsorption and CO_2 formation.

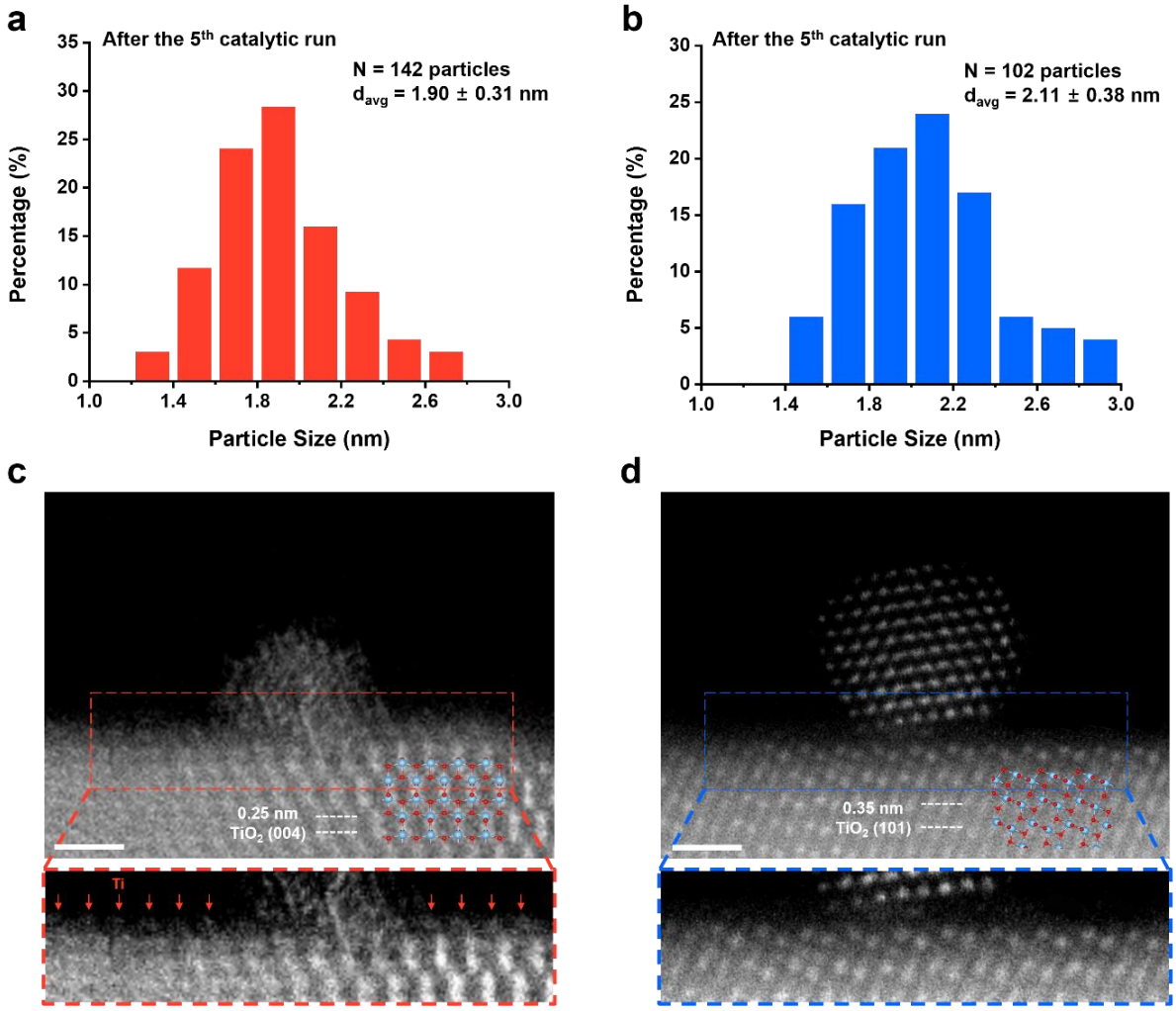

Supplementary Figure 36. (a, b) Histograms showing the Pt NP size distributions and (c, d) HAADF-STEM images of the spent catalysts after the 5th catalytic run for (a, c) PTS and (b, d) PTR. The HAADF-STEM images and corresponding atomic models show that both supports retain anatase TiO_2 lattice structures with predominantly exposed (001) and (101) facets, respectively (Scale bars, 1 nm). The dashed rectangular regions further indicate that no clear TiO_2 surface reconstruction is observed near the Pt–TiO_2 interface under the present conditions.

Reviewer #3

General comments: I truly appreciate the authors' efforts in providing supplementary experimental results. Nevertheless, upon reviewing the additional data, I still consider it insufficient to support their claim regarding "TiO_2-facet-dependent reconstruction of Pt nanoparticles during CO oxidation". The morphology of Pt nanoparticles (NPs) is predominantly dictated by the TiO_2 support, attributed to wetting/dewetting effects that are well-documented in the literature. During CO oxidation reactions, only surface roughening of Pt NPs is observed and similar CO-induced surface roughening phenomena have been extensively reported by *in situ* TEM/STM. Critically, no evidence is provided in the manuscript to illustrate how these subtle structural changes modulate catalytic reactivity. Alternatively, it is more plausible that the enhanced CO oxidation reactivity stems from the initial structure of Pt NPs on different TiO_2 support, rather than their reconstruction during the reaction. Notably, the enriched oxygen vacancies (O_v) on TiO_2(001) may play a more pivotal role than Pt NP morphology that is inadequately addressed in the current manuscript. Overall, this work lacks significant scientific advances and may not meet the rigorous standards of *Nature Communications*. Therefore, I regret that I cannot recommend the publication of this manuscript in its present form. Some specific comments for the authors to consider:

Response: We sincerely thank the reviewer for the careful evaluation of our manuscript and for the constructive comments. We appreciate the reviewer's concern regarding whether the current evidence sufficiently supports our claim of TiO_2-facet-dependent reconstruction of Pt NPs during CO oxidation and its relationship to catalytic reactivity.

We acknowledge that the reconstruction of Pt NPs during the reaction can appear subtle and that the respective roles of the initial Pt structure and support properties, such as oxygen vacancies (O_v), require further clarification. To address these important points, we have performed additional experimental analyses and computational simulations to better disentangle the contributions of the initial Pt structure, reaction-induced structural evolution, and support redox properties.

In particular, to compare catalytic behaviour associated with the initial and reconstructed Pt states, we conducted catalytic cycle tests to evaluate the catalytic consequence of reaction-induced Pt restructuring. To further assess the catalytic contribution of O_v, we additionally examined a Pt/Al_2O_3 reference catalyst with a comparable Pt size as a non-reducible support.

Furthermore, to investigate O_v influences on facet-dependent Pt structural evolution, we performed additional GA-optimised simulations using O_v-modulated TiO_2 models.

Detailed responses to each of the reviewer's specific comments and the corresponding additions to the revised manuscript are provided below. We believe that these additional analyses clarify the respective roles of Pt NP structure, reaction-induced reconstruction, and TiO_2 surface properties, and thereby strengthen the mechanistic interpretation of the facet-dependent MSIs discussed in this study.

Comment 1: The initial structure of Pt NPs is determined by the TiO_2 facet due to wetting/dewetting, but the reconstruction during reaction is quite subtle. The author should provide more compelling evidence to clarify how such subtle surface roughening modulates catalytic reactivity, other than their initial structure.

Response: We thank the reviewer for this important comment. We agree that the initial structure of Pt NPs is strongly influenced by the TiO_2 facet (Fig. 1) and that this facet-dependent difference is an important factor governing catalytic behaviour. At the same time, our study indicates that the Pt structure evolves under CO oxidation conditions, making it necessary to clarify how this reaction-induced structural evolution affects catalytic reactivity depending on the TiO_2 facets. To address this point more directly, we performed catalytic cycle tests that allow comparison between the initial and reconstructed catalyst states.

For each catalyst, five consecutive catalytic runs were performed in a single experiment over the temperature range up to 240 °C, at which complete catalytic ignition was observed in the DRIFTS results. After completion of the 1st run, the catalyst was held at 240 °C for 2 h before starting the 2nd run. The apparent activation energy (E_a) was obtained by averaging the results of three independent experiments using newly loaded catalysts to ensure reproducibility and consistency, and the error bars represent the standard deviation.

In Supplementary Figs. 35a–d, the 1st run represents the catalytic behaviour of the fresh catalysts, where the activity is governed by the initial facet-dependent Pt structure and also influenced by O_v on the TiO_2 facets. By contrast, the 2nd to 5th runs represent the catalytic behaviour after the Pt NPs have undergone reaction-induced structural evolution during the 1st run. In the 1st run, PTS already showed higher activity and a lower E_a than PTR, indicating that the initial catalyst state of PTS is more favourable for CO oxidation, consistent with the

comprehensive analyses presented throughout the manuscript. Importantly, after the 1st run, PTS exhibited a further decrease in E_a from 58.1 ± 0.3 to 43.2–44.9 ± 0.5–0.9 kJ·mol^{-1} (Supplementary Figs. 35a, b), together with enhanced low-temperature activity, and this improved reactivity was maintained throughout the subsequent runs. In contrast, PTR showed almost no change in E_a over repeated runs, remaining within 109.1 ± 1.5 to 112.9 ± 4.0 kJ·mol^{-1} (Supplementary Figs. 35c, d). This trend is also consistent with our previous reaction-order analysis for post-reaction catalysts, which showed more favourable oxygen-transfer behaviour for reconstructed PTS than for PTR.

These results provide direct catalytic evidence that PTS undergoes enhanced reactivity after the 1st run. This behaviour indicates that the superior performance of PTS cannot be explained solely by differences in the initial catalyst state. Rather, the 1st run leads to the formation of a more active Pt state in PTS, which remains stable throughout the subsequent runs. By contrast, although PTR also undergoes structural evolution during reaction, this change does not lead to a comparable enhancement in activity, suggesting that its restructuring does not promote a more catalytically favourable Pt–TiO_2 interfacial state under the same conditions. Thus, these cycle-test results directly show that the subtle reaction-induced reconstruction observed for PTS is accompanied by a measurable enhancement in catalytic reactivity beyond that determined by the initial catalyst state alone. The stable catalytic behaviour observed from the 2nd to the 5th runs further suggests that the restructured Pt state remains stable under repeated reaction conditions.

Action taken: In the revised manuscript, we have further strengthened the section on the *Reaction mechanism and the origin of the superior catalytic activity* by incorporating the catalytic cycle test results and the corresponding E_a variation behaviour. These additions provide direct catalytic evidence that the restructured PTS undergoes further activity enhancement relative to its initial state. The corresponding experimental results are added in Supplementary Fig. 35 and Fig. 6f, and the following paragraph has been incorporated on page 13: *"Catalytic cycle tests provide direct kinetic evidence of how this facet-directed restructuring dictates catalytic reactivity. As shown in Fig. 6f and Supplementary Fig. 35, relative to the 1st run, PTS exhibits a further 22.7–25.6% decrease in E_a over the 2nd to 5th runs, accompanied by enhanced low-temperature activity, whereas PTR shows almost no change in E_a or light-off behaviour."*

Additionally, as more reliable E_a values were obtained, the 1st run E_a values and the

corresponding Fig. 1f have been revised accordingly.

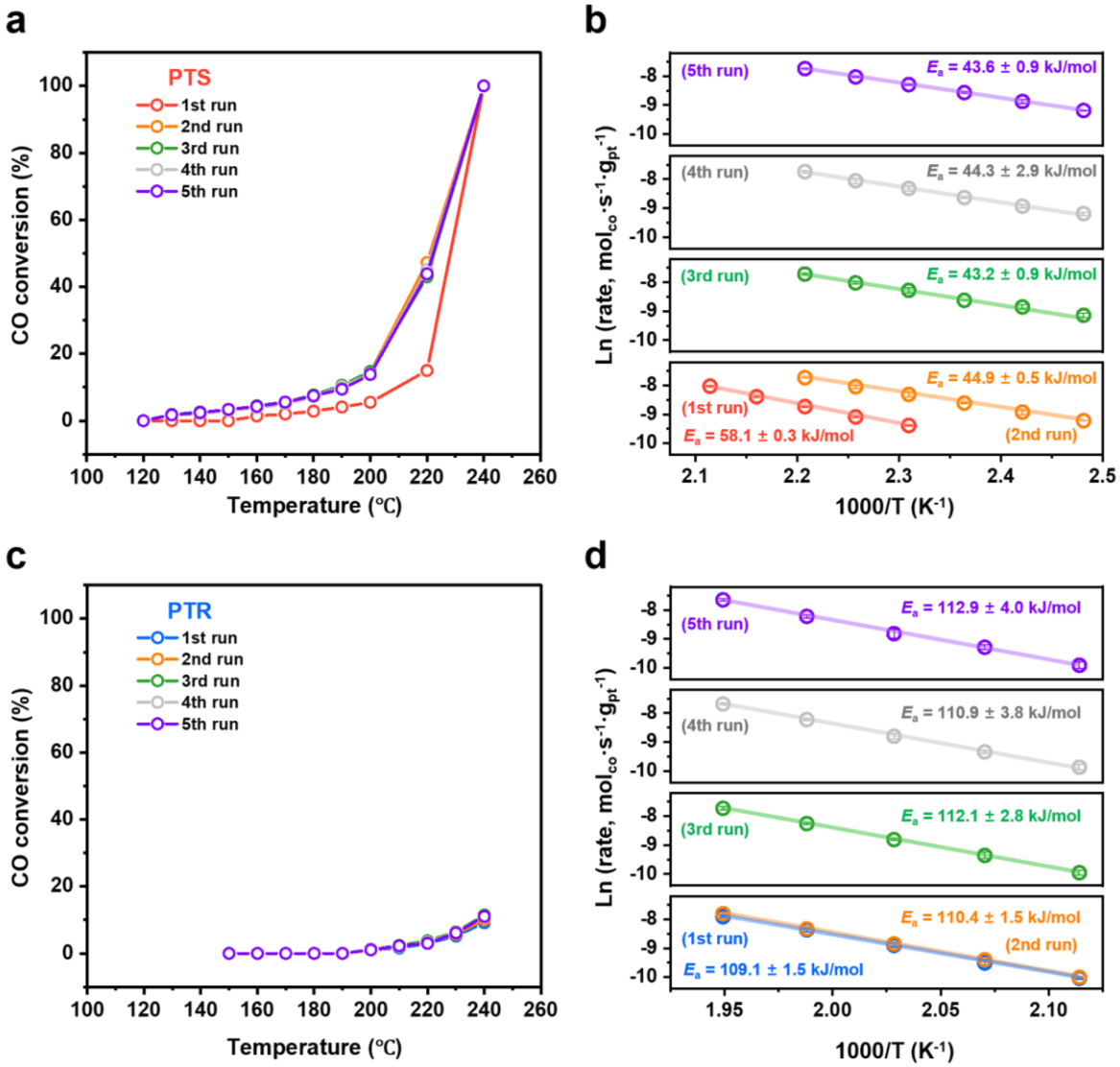

Supplementary Figure 35. Temperature-dependent catalytic cycle tests and corresponding apparent activation energies (E_a) for (a, b) PTS and (c, d) PTR. Five consecutive catalytic runs were performed for each catalyst in a single experiment over the temperature range up to 240 °C, where complete catalytic ignition was observed in the DRIFTS results. After the 1st run, the catalyst was held at 240 °C for 2 h before the 2nd run. All E_a values were obtained at a total flow rate of 100 mL·min^{-1} with a CO/O_2 ratio of 1 under the kinetically relevant regime (<10% CO conversion), and were averaged over three independent experiments using newly loaded catalysts to ensure reproducibility, with error bars representing the standard deviation.

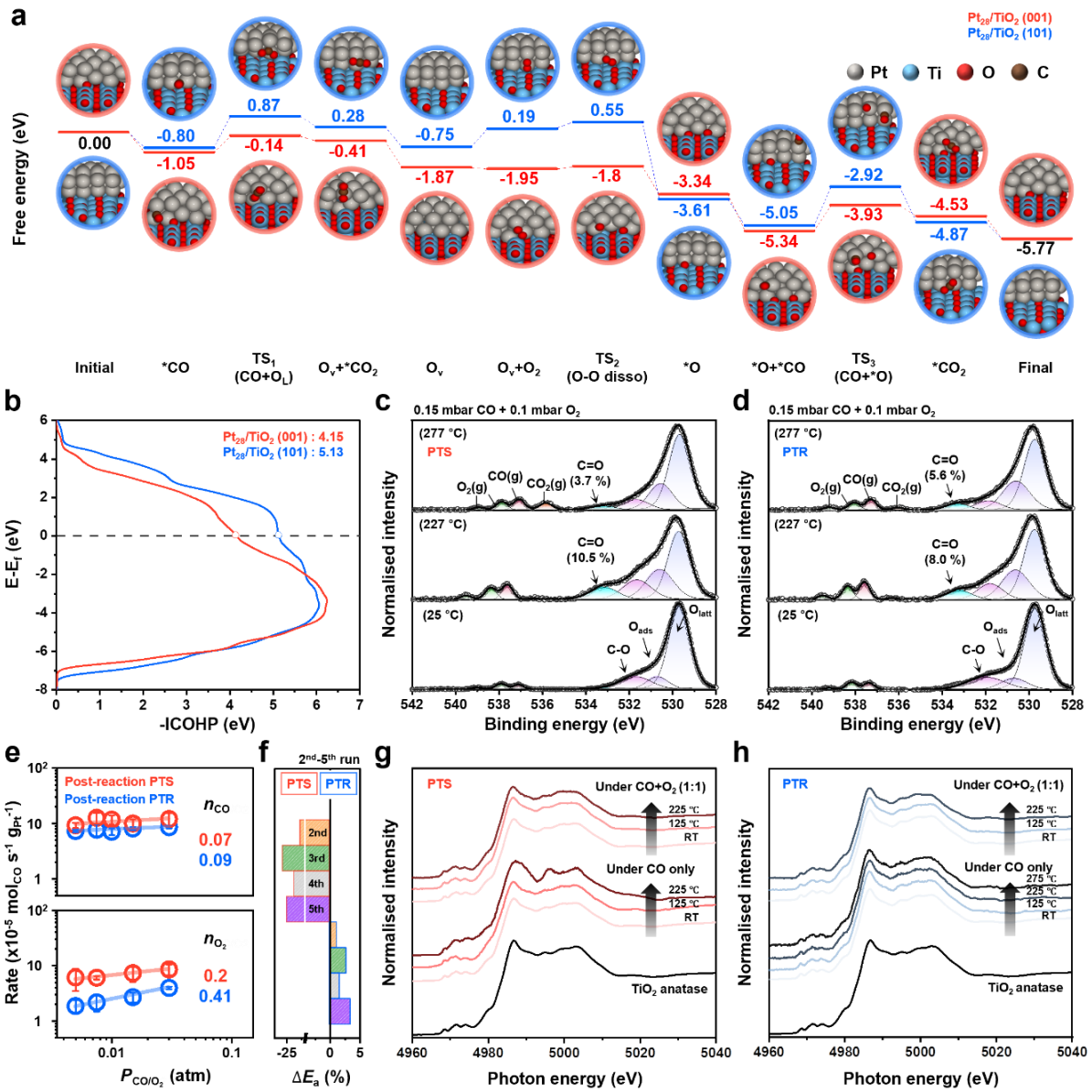

Figure 6. Synergistic effects of Pt morphology and TiO_2 facets on CO oxidation activity. (a) DFT-calculated reaction energy profiles for CO oxidation via the MvK mechanism on Pt_{28}/TiO_2(001) and (101). (b) ICOHP analysis of oxygen vacancy formation on Pt_{28}/TiO_2 models. (c, d) Normalised *in situ* O 1*s* AP-XPS spectra ($h\nu$ = 650 eV) for (c) PTS and (d) PTR catalysts under CO oxidation conditions (0.15 mbar of CO, 0.1 mbar of O_2) at 25, 227, and 277 °C. (e) Reaction-order analysis of CO oxidation on post-reaction Pt/TiO_2 catalysts with respect to CO and O_2 partial pressures. Reaction rates were measured in the kinetically relevant regime (<5% CO conversion) at 80 °C for PTS and 160 °C for PTR, corresponding to their respective light-off temperatures. (f) Relative changes in apparent activation energy (ΔE_a) for PTS and PTR over five consecutive catalytic runs, with respect to the 1st run. (g, h) Ti *K*-edge *in situ* XANES spectra of (f) PTS and (g) PTR under CO-reducing (middle panels: 5% CO/He) and CO + O_2 co-feed (upper panels: 5% CO + 5% O_2/He) conditions.

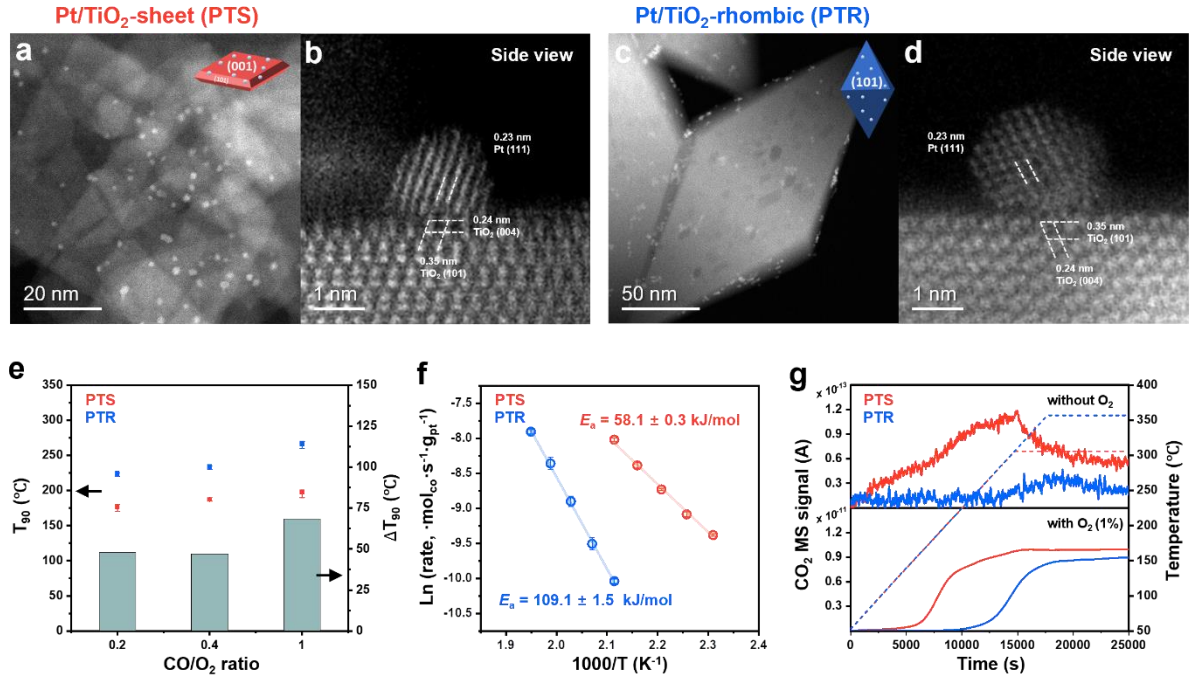

Figure 1. Structural characterisation and CO oxidation performance of Pt/TiO_2 catalysts. (a–d) HAADF–STEM images of the as-prepared catalysts: (a, c) low-magnification images of PTS and PTR, respectively, and (b, d) high-magnification side-view images showing Pt NPs on the TiO_2 (004) plane (PTS) and TiO_2 (101) plane (PTR). (e) T_{90} values representing the temperature at which 90% CO conversion is reached for PTS and PTR at various CO:O_2 ratios. (f) Apparent activation energies (E_a) for CO oxidation at $CO/O_2 = 1$. (g) CO_2 mass spectrometry signals during CO-TPR experiments under CO with and without O_2 (Bottom: 5% CO + 1% O_2/Ar, Top: 5% CO/Ar).

Comment 2: I strongly suspect that the enriched O_v on TiO_2(001) may play a more crucial role than the morphology of Pt NPs. These O_v species can facilitate O_2 activation through the MVK mechanism and thus enhance the CO oxidation reactivity. To distinguish the respective contributions of Pt NP shape and O_v on TiO_2 support, the authors are advised to compare the reactivity of Pt clusters deposited on different TiO_2 facets.

Response: We thank the reviewer for this insightful comment. We agree that O_v on TiO_2(001) can play an important role in CO oxidation by facilitating oxygen activation and lattice oxygen participation, consistent with the MvK-type mechanism. We also agree that it is important to distinguish the contribution of O_v from that of Pt NP morphology when interpreting the origin of the enhanced reactivity.

To address this point, we first note that the contribution of Pt morphology to the activity enhancement was already examined in our response to Comment 1, where the catalytic cycle

test directly showed that reaction-induced Pt restructuring in PTS leads to additional activity enhancement after the 1st run. In the present comment, we therefore focus on the role of O_v. Specifically, we considered O_v from two aspects: (i) their direct contribution to catalytic reactivity through oxygen activation and transfer at the Pt–TiO_2 interface, and (ii) their possible influence on Pt morphology through changes in the local MSI. The latter aspect was further examined through additional GA-based simulations and is discussed in detail in our response to Comment 3.

At the same time, it should be noted that the activity difference between PTS and PTR in the 1st run reflects the combined effects of the initial Pt structure and the O_v abundance associated with each TiO_2 facet. Although the catalytic cycle test demonstrates that Pt restructuring in PTS leads to additional activity enhancement after the 1st run, the absolute activity observed for each catalyst still contains contributions from both Pt morphology and O_v, making a strict experimental separation of the two factors difficult. For the same reason, comparison using additional TiO_2 facets would introduce simultaneous changes in both Pt morphology and O_v characteristics, which would make their individual effects difficult to disentangle.

Therefore, to indirectly assess the catalytic contribution of O_v, we additionally performed a comparative analysis using Pt/Al_2O_3 catalysts. As shown in Supplementary Figs. 42a–c and Supplementary Table 1, we synthesized a Pt/Al_2O_3 (PtA) catalyst with a Pt size and dispersion comparable to those of the Pt/TiO_2 catalysts. Because Al_2O_3 is a representative non-reducible metal oxide support, for which support oxygen does not directly participate in CO oxidation and the reaction proceeds predominantly via a Langmuir–Hinshelwood (L–H) mechanism, PtA provides a useful reference system in which O_v-related support effects are not expected to be significant. Therefore, catalytic activity tests over two consecutive runs and CO-DRIFTS analyses under pre-, *in situ*, and post-reaction conditions were additionally performed for PtA.

The PtA catalyst exhibited the highest E_a among the three catalysts, with a value of 130.7 ± 1.1 kJ·mol^{-1}, and showed only a minor change in E_a during the 2nd run (Supplementary Fig. 43). Unlike the catalytic behaviour of the Pt/TiO_2 catalysts during CO-DRIFTS experiments (R3Figs. 1a-f), the normalized pre- and post-reaction CO-DRIFTS spectra of PtA (R3Fig. 1g) were nearly unchanged, while the *in situ* DRIFTS contour map (R3Fig. 1h) showed an even more pronounced redshift of the CO–$Pt_{tstep/edge}$ feature during reaction. In addition, the temperature-resolved CO_2 (g) and CO–$Pt_{step/edge}$ intensity profiles (R3Fig. 1i) showed stronger CO adsorption and a much weaker CO_2 (g) signal than those of Pt/TiO_2. These observations

indicate that, although PtA also undergoes CO-induced spectral changes under reaction conditions, its surface remains more strongly CO-covered and less effective in promoting CO oxidation, consistent with L–H-type reaction behaviour without direct participation of support oxygen.

In summary, compared with PtA, PTR showed a substantially lower E_a in the 1st run (109.1 vs. 130.7 kJ·mol^{-1}) together with a faster CO_2 light-off at low temperature, indicating that the TiO_2 support provides an additional O_v-related redox contribution, consistent with MvK-type oxygen participation during CO oxidation. This O_v-related enhancement is further strengthened in PTS, which exhibits a much lower E_a than PTR in the 1st run (58.1 vs. 109.1 kJ·mol^{-1}), reflecting the combined effects of enriched O_v and the more favourable initial Pt structure on TiO_2(001). Furthermore, although PtA and PTR also show slight changes over repeated runs, neither exhibits the substantial activity enhancement and E_a decrease observed for PTS. In contrast, PTS exhibits a further decrease in E_a together with enhanced low-temperature activity after the 1st run, indicating that reaction-induced Pt restructuring on TiO_2(001) provides an additional activity enhancement beyond the O_v-related support effect alone.

Although the respective contributions of Pt morphology and O_v cannot be quantitatively separated within a single catalyst system, these comparative results allow their enhancement effects to be distinguished more clearly. Overall, these results strengthen our central conclusion that the superior catalytic performance of PTS originates from the synergistic interplay between the intrinsic redox-active properties of the TiO_2(001) facet and the reconstructed Pt–TiO_2 interface under reaction conditions, rather than from O_v abundance alone. We sincerely appreciate the reviewer's insightful comment, and hope that these additional analyses and discussions provide a clearer basis for interpreting the respective roles of O_v and Pt morphology.

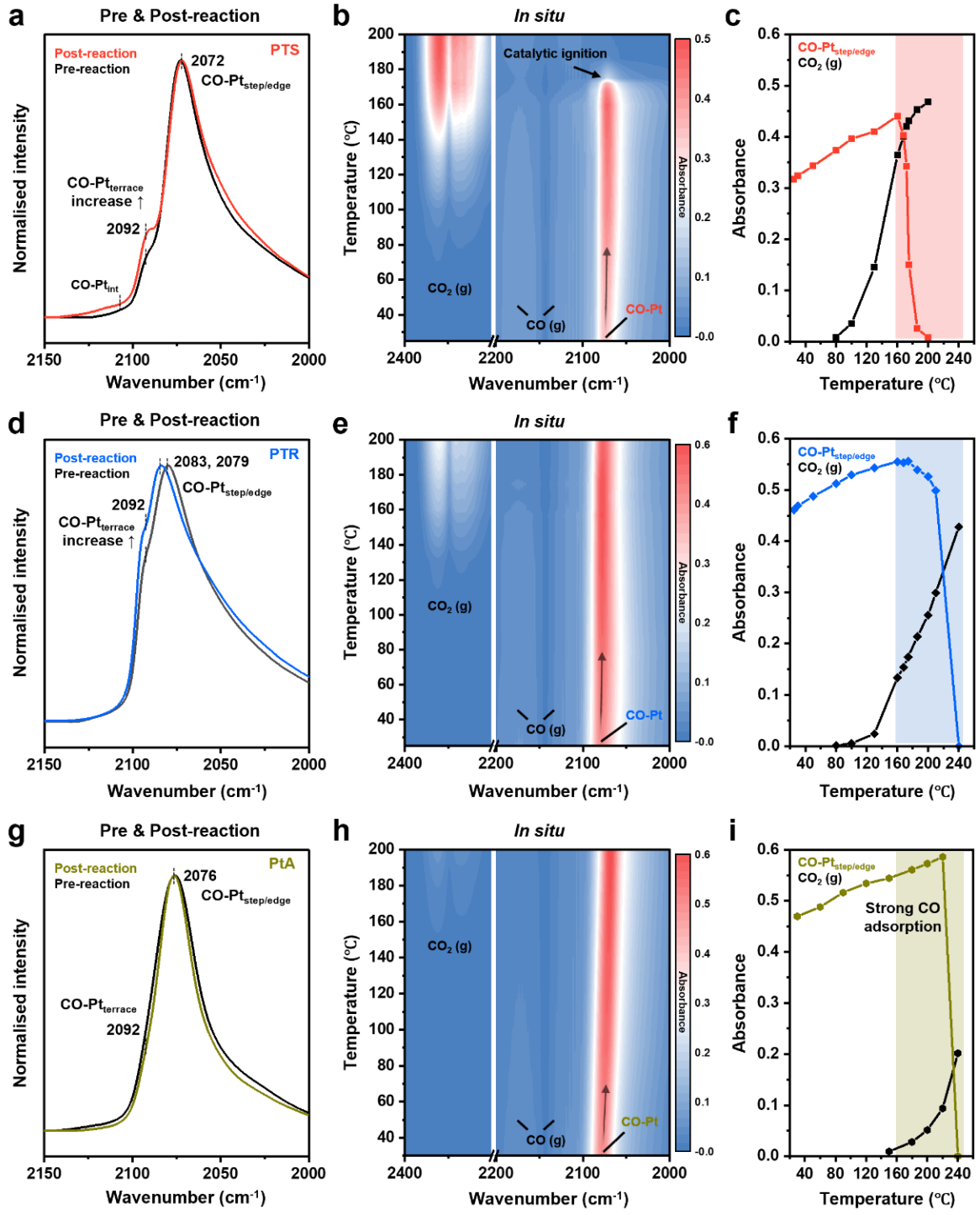

R3 Figur

Action taken: In the revised manuscript, we have expanded the section on the *Reaction*

1. *In*

PAGE

mechanism and the origin of the superior catalytic activity by incorporating additional comparative experiments using a PtA catalyst and additional GA-optimised simulations using O_v-modulated TiO_2 models (The simulation results are discussed in detail in our response to Comment 3.). These additions clarify that O_v contributes to both catalytic reactivity and Pt structural evolution, but do not solely determine the observed superiority of PTS. The corresponding results are presented in Supplementary Note 12, Supplementary Figs. 42–45, and the following paragraph has been added on page 15: *"To further assess the respective roles of O_v in catalytic reactivity and Pt structural evolution, we conducted comparative experiments using Pt/Al_2O_3 (PtA) catalyst, a representative non-reducible oxide support, together with GA-optimised simulations using O_v-modulated TiO_2 models. Detailed discussions are provided in Supplementary Note 12. In summary, compared with PtA, which shows negligible support-oxygen participation and much less pronounced reaction-induced Pt restructuring (Supplementary Figs. 42–45),[55] PTR exhibited a lower E_a and faster CO_2 light-off, indicating the catalytic contribution of the redox-active TiO_2 support and O_v-related oxygen participation. PTS showed an even lower E_a than PTR in the 1st run, consistent with the combined effects of enriched O_v and the more favourable initial Pt structure on TiO_2(001), while the catalytic cycle test further revealed an additional activity enhancement arising from reaction-induced Pt restructuring."*

Accordingly, an extended discussion of these results is now provided in Supplementary Note 12: ***"Supplementary Note 12. Indirect Assessment of O_v-related Catalytic Effects and O_v Influences on Facet-dependent Pt Structural Evolution*** *To further assess the respective roles of O_v in catalytic reactivity and Pt structural evolution, we additionally conducted comparative experiments using a Pt/Al_2O_3 (PtA) catalysts, together with GA-optimised simulations using O_v-modulated TiO_2 models. Because direct separation of Pt morphology and O_v effects within the Pt/TiO_2 system is difficult, as the catalytic activity of each catalyst reflects the combined contributions of the initial Pt structure, facet-dependent O_v abundance, and reaction-induced Pt restructuring, PtA was introduced as a non-reducible reference catalyst in which support oxygen does not directly participate in CO oxidation and the reaction proceeds predominantly via a Langmuir–Hinshelwood (L–H) mechanism. As shown in Supplementary Figs. 42a–c and Supplementary Table 1, we synthesised a Pt/Al_2O_3 (PtA) catalyst with a Pt size and dispersion comparable to those of the Pt/TiO_2 catalysts. Accordingly, catalytic activity tests over two consecutive runs and CO-DRIFTS analyses*

under pre-, in situ, and post-reaction conditions were additionally performed for PtA.

The PtA catalyst exhibited the highest E_a among the three catalysts, with a value of 130.7 ± 1.1 kJ·mol^{-1}, and showed only a minor change in E_a during the 2nd run (Supplementary Fig. 43). Unlike the catalytic behaviour of the Pt/TiO_2 catalysts during CO-DRIFTS experiments (Fig. 3), the normalized pre- and post-reaction CO-DRIFTS spectra of PtA (Supplementary Fig. 44a) were nearly unchanged, while the in situ DRIFTS contour map (Supplementary Fig. 44b) showed an even more pronounced redshift of the CO–$Pt_{step/edge}$ feature during reaction. In addition, the temperature-resolved CO_2 (g) and CO–$Pt_{step/edge}$ intensity profiles (Supplementary Fig. 44c) showed stronger CO adsorption and a much weaker CO_2 (g) signal than those of Pt/TiO_2. These observations indicate that, although PtA also undergoes CO-induced spectral changes under reaction conditions, its surface remains more strongly CO-covered and less effective in promoting CO oxidation, consistent with L–H-type reaction behaviour without direct participation of support oxygen.[27]

Compared with PtA, which shows negligible support-oxygen participation and much less pronounced reaction-induced Pt restructuring, PTR showed a substantially lower E_a in the 1st run together with faster CO_2 light-off at low temperature, indicating an additional O_v-related redox contribution from the TiO_2 support. This enhancement became more pronounced in PTS, which exhibited a much lower E_a than PTR in the 1st run, reflecting the combined effects of the more O_v-rich TiO_2(001) surface and the more favourable initial Pt structure on that facet. In addition, the catalytic cycle test showed that only PTS undergoes a further decrease in E_a together with enhanced low-temperature activity after the 1st run, indicating an additional contribution from reaction-induced Pt restructuring beyond the O_v-related support contribution alone."

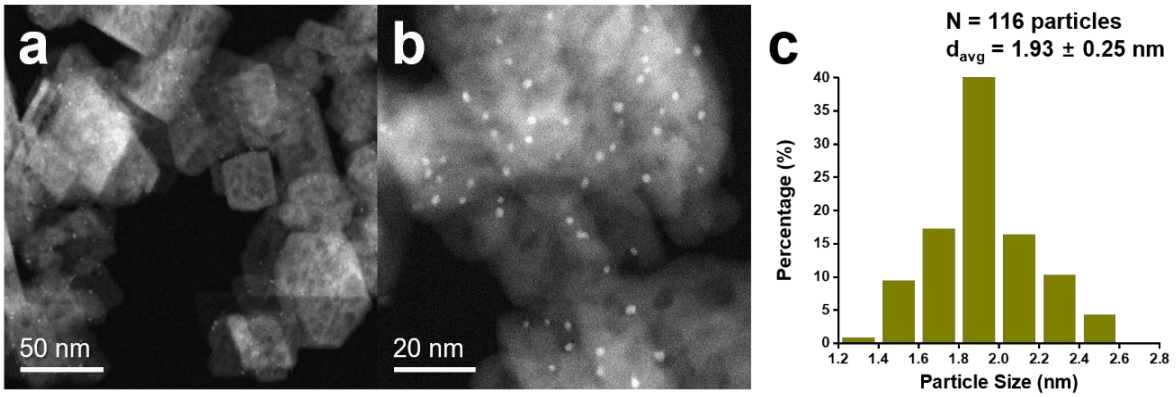

Supplementary Figure 42. (a, b) HAADF–STEM images of the as-prepared Pt/Al_2O_3 (PtA) catalyst. (c) The corresponding histograms showing the Pt NP size distribution for PtA.

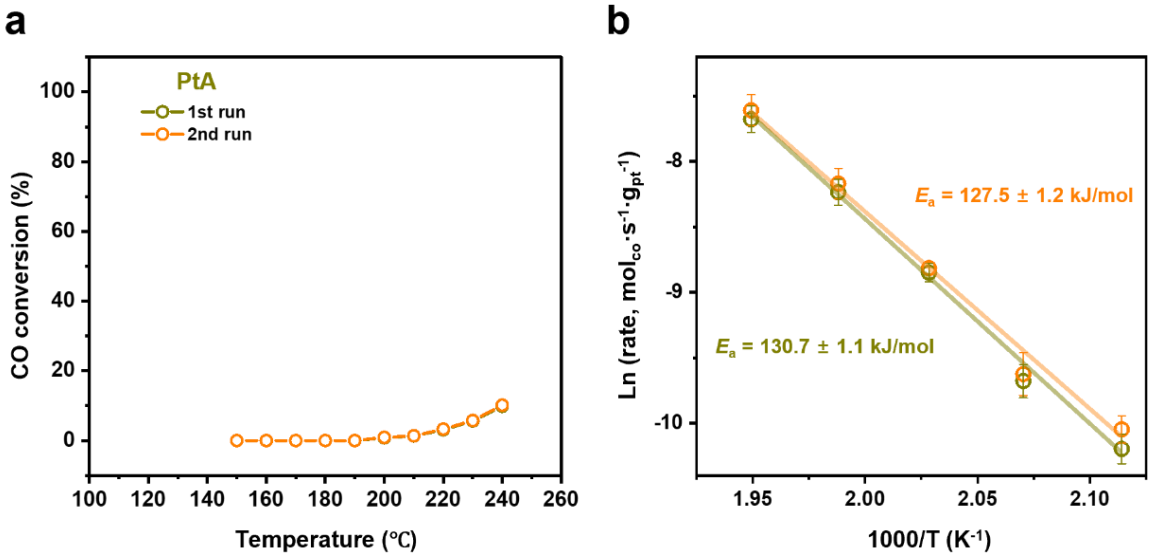

Supplementary Figure 43. (a) Temperature-dependent catalytic cycle tests and (b) corresponding apparent activation energies (E_a) for PtA. Two consecutive catalytic runs were performed for each catalyst in a single experiment over the temperature range up to 240 °C, where complete catalytic ignition was observed in the DRIFTS results. After the 1st run, the catalyst was held at 240 °C for 2 h before the 2nd run. All E_a values were obtained at a total flow rate of 100 mL·min^{-1} with a CO/O_2 ratio of 1 under the kinetically relevant regime (<10% CO conversion), and were averaged over three independent experiments using newly loaded catalysts to ensure reproducibility, with error bars representing the standard deviation.

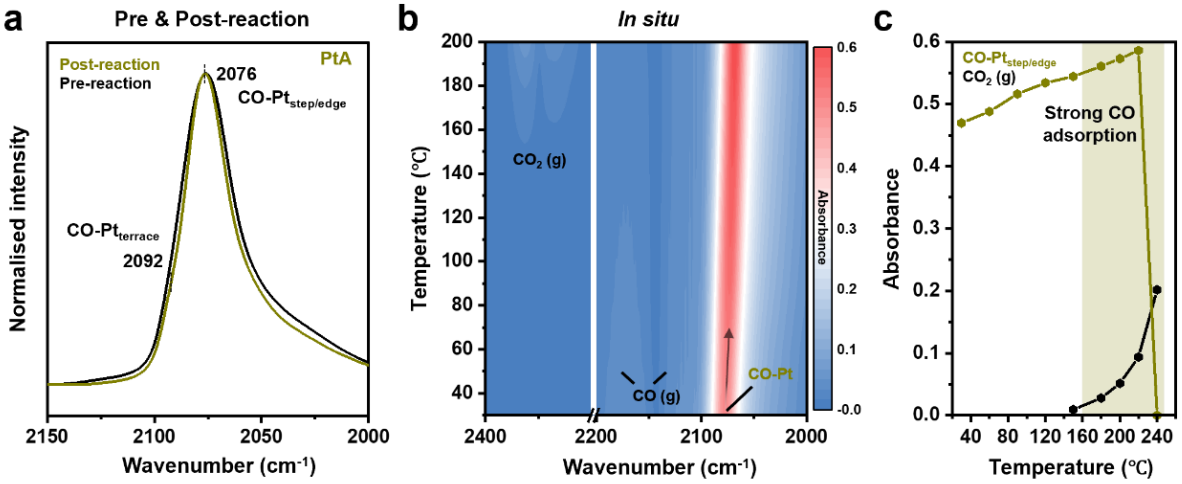

Supplementary Figure 44. *In situ* DRIFTS spectra of PtA catalyst during CO oxidation. (a) Normalised CO-DRIFTS spectra recorded pre- and post-CO oxidation at 25 °C. (b) Contour maps of *in situ* DRIFTS spectra acquired under CO oxidation. (c) Intensity plots tracking CO adsorbed on $Pt_{step/edge}$ sites and gas-phase CO_2 evolution.

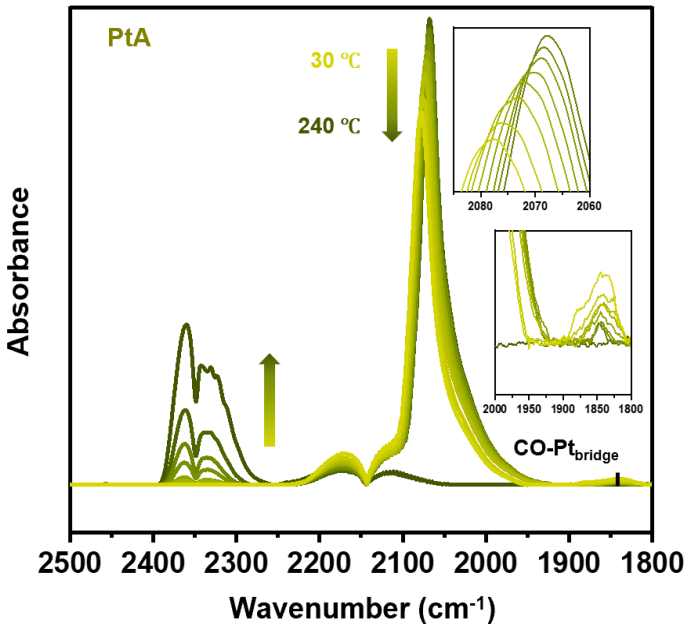

Supplementary Figure 45. Full *in situ* DRIFTS spectra of PtA catalyst recorded under CO oxidation conditions ($CO/O_2 = 1$) at various temperatures. The spectra capture the temperature-dependent evolution of surface species, including CO adsorption and CO_2 formation.

Comment 3: The authors should note that the enriched O_v on TiO_2(001) (reducibility of the support) results in stronger MSI interaction and consequently the shape of Pt NPs, rather than vice versa. Earlier studies have shown the electron transfer from the defects of support can influence the shape of support metal particles.

Response: We thank the reviewer for this constructive comment. We agree with the reviewer that defect sites on the support, such as O_v, can influence the shape of supported metal particles through changes in the local MSI. To examine whether such O_v-related effects contribute to the facet-dependent Pt morphologies observed in our catalyst system, we performed additional GA-optimised simulations using O_v-modulated TiO_2 models.

We first note that the original GA optimisation for the Pt_{201}/TiO_2 models (Figs. 4a, b), performed during the first revision, was carried out on stoichiometric anatase TiO_2 facets without introducing O_v. This was intended to isolate the role of the TiO_2 surface geometry itself in determining the facet-specific equilibrium Pt morphologies. Despite the absence of O_v, these results already revealed a pronounced facet-dependent difference in Pt wetting: the effective contact angle on TiO_2(001) (95.7°) is substantially lower than that on TiO_2(101) (118.7°). This ~23° difference indicates that the intrinsic geometric characteristics of the TiO_2 facet alone are sufficient to generate the distinct Pt morphologies observed experimentally, without invoking O_v as a prerequisite.

At the same time, in the real catalyst system, the presence and concentration of O_v can vary depending on the TiO_2 facet and reaction environment, and such defect sites may additionally influence Pt morphology through stronger local electronic MSI. To directly examine this effect, we performed additional GA optimisations using O_v-modulated TiO_2 models containing 10% surface O_v in the relaxed top 2 layers (corresponding to 5% of the total lattice oxygen in the slab), and compared the resulting structures with the original stoichiometric models. Oxygen vacancies were placed on of the top 2 layers of the slab, with a minimum inter-vacancy separation of 5 Å to preserve the dilute-limit interpretation of isolated defects. This concentration of 10% surface O_v falls within the 5–10% range commonly adopted in DFT studies of anatase oxygen vacancies. (*J. Chem. Phys.* 2009, 131, 054703 / *Catalysts* 2020, 10, 4, 397) In addition, three independent GA optimisations were carried out for each facet with distinct randomly generated O_v distributions to account for the stochastic nature of random O_v placement, with GA energy convergence shown in Supplementary Fig. 46.

The additional GA-optimised simulations reveal a clear facet dependence in the structural response to O_v (Supplementary Fig. 47). On TiO_2(001), introducing O_v leaves the Pt contact angle nearly unchanged, from 95.7° without O_v to 94.3–99.9° (mean 96.5°) across the three independent realizations, indicating that Pt wetting on this facet is governed primarily by the intrinsic surface geometry rather than by O_v. By contrast, on TiO_2(101), the introduction of O_v decreases the Pt contact angle from 118.7° to 102.4–108.2° (mean 104.6°), showing that O_v can partially promote Pt wetting on this facet. However, even at 10% surface O_v, Pt/TiO_2(101) still retains a contact angle on average approximately 8° higher than that of Pt/TiO_2(001). Notably, the O 1*s* XPS results show that the O_v-related oxygen ratio on TiO_2(101) is only about one-half of that on TiO_2(001). To reflect this experimentally observed asymmetry, we additionally performed GA optimization for Pt/TiO_2(101) at 5% surface O_v (corresponding to 2.5% of total lattice oxygen). The resulting contact angles from three independent realizations were 108.2°, 122.0°, and 116.1° (mean 115.4°), remaining close to the value for stoichiometric TiO_2(101). These results indicate that, although O_v can modulate local Pt wetting, they do not override the dominant role of facet-dependent TiO_2 surface geometry and its resulting MSI in determining the experimentally observed Pt morphology. In this sense, O_v act as an additional modifying factor rather than the sole origin of the Pt shape difference.

Action taken: In the revised manuscript, as we already mentioned in response to Comment 2, the corresponding results and discussions about additional GA-optimised simulations using O_v-modulated TiO_2 models are presented in Supplementary Note 12, Supplementary Figs. 46 and 47, and the following paragraph has been added on page 15: "*GA-optimised simulations using 5–10% O_v TiO_2 models (Supplementary Figs. 46 and 47) further showed O_v can modulate the local Pt–TiO_2 interaction and influence Pt morphology, while the overall facet-dependent structural trend remains preserved within the experimentally relevant range. These results indicate that, while O_v contribute to both catalytic reactivity and Pt structural evolution, they do not solely determine the observed superiority of PTS. Instead, the enhanced reactivity arises from the dynamic interplay between the intrinsically higher O_v-related redox reactivity, the initial facet-dependent Pt structure, and the continued evolution of the Pt–TiO_2(001) interface under reaction conditions.*"

Accordingly, corresponding discussion has been added to Supplementary Note 12: *"To further examine how O_v influence the facet-dependent Pt morphology, we performed additional GA-optimised simulations using O_v-modulated TiO_2 models. The original GA optimisation for the*

Pt_{201}/TiO_2 models (Figs. 4a, b) was carried out on stoichiometric anatase TiO_2 facets without introducing O_v, to isolate the role of TiO_2 surface geometry itself in determining facet-specific equilibrium Pt morphologies. Even in the absence of O_v, these calculations already revealed a pronounced facet dependence in Pt wetting, with the effective contact angle on $TiO_2(001)$ (95.7°) substantially lower than that on $TiO_2(101)$ (118.7°). This ~23° difference indicates that the intrinsic geometric characteristics of the TiO_2 facet alone are sufficient to generate the distinct Pt morphologies observed experimentally, without invoking O_v as a prerequisite.

At the same time, the real catalyst system is expected to contain facet- and condition-dependent O_v populations, which may additionally influence Pt morphology through local changes in metal–support interaction. To examine this effect directly, we performed additional GA optimisations using O_v-modulated TiO_2 models containing 10% surface O_v in the relaxed top two layers, corresponding to 5% of the total lattice oxygen in the slab. O_v were placed within the top two layers with a minimum inter-vacancy separation of 5 Å to preserve the dilute-limit interpretation of isolated defects. This concentration falls within the 5–10% range commonly used in DFT studies of anatase oxygen vacancies.[28, 29] Three independent GA optimisations were carried out for each facet using distinct randomly generated O_v distributions to account for configurational variability in vacancy placement. The corresponding GA energy convergence profiles are shown in Supplementary Fig. 46.

The additional GA-optimised simulations reveal a clear facet dependence in the structural response to O_v (Supplementary Fig. 47). On $TiO_2(001)$, introducing O_v leaves the Pt contact angle nearly unchanged, from 95.7° for the stoichiometric surface to 94.3–99.9° (mean 96.5°) across the three O_v-containing realizations, indicating that Pt wetting on this facet is governed primarily by intrinsic surface geometry rather than by O_v. By contrast, on $TiO_2(101)$, introducing 10% surface O_v decreases the Pt contact angle from 118.7° to 102.4–108.2° (mean 104.6°), showing that O_v can partially promote Pt wetting on this facet. However, even at 10% surface O_v, $Pt/TiO_2(101)$ still retains a contact angle on average approximately 8° higher than that of $Pt/TiO_2(001)$.

Notably, the O 1s XPS results show that the O_v-related oxygen ratio on $TiO_2(101)$ is only about one-half of that on $TiO_2(001)$. To reflect this experimentally observed asymmetry, we additionally performed GA optimisation for $Pt/TiO_2(101)$ at 5% surface O_v, corresponding to 2.5% of the total lattice oxygen. The resulting contact angles from three independent realizations were 108.2°, 122.0°, and 116.1° (mean 115.4°), remaining close to the value for

stoichiometric TiO_2(101). These results indicate that, although O_v can modulate local Pt wetting, they do not override the dominant role of facet-dependent TiO_2 surface geometry and its resulting MSI in determining the experimentally observed Pt morphology. Together with the comparative Pt/Al_2O_3 analysis discussed above, these results support the conclusion that O_v contribute to both catalytic reactivity and Pt structural evolution, but do not solely determine the observed superiority of PTS."

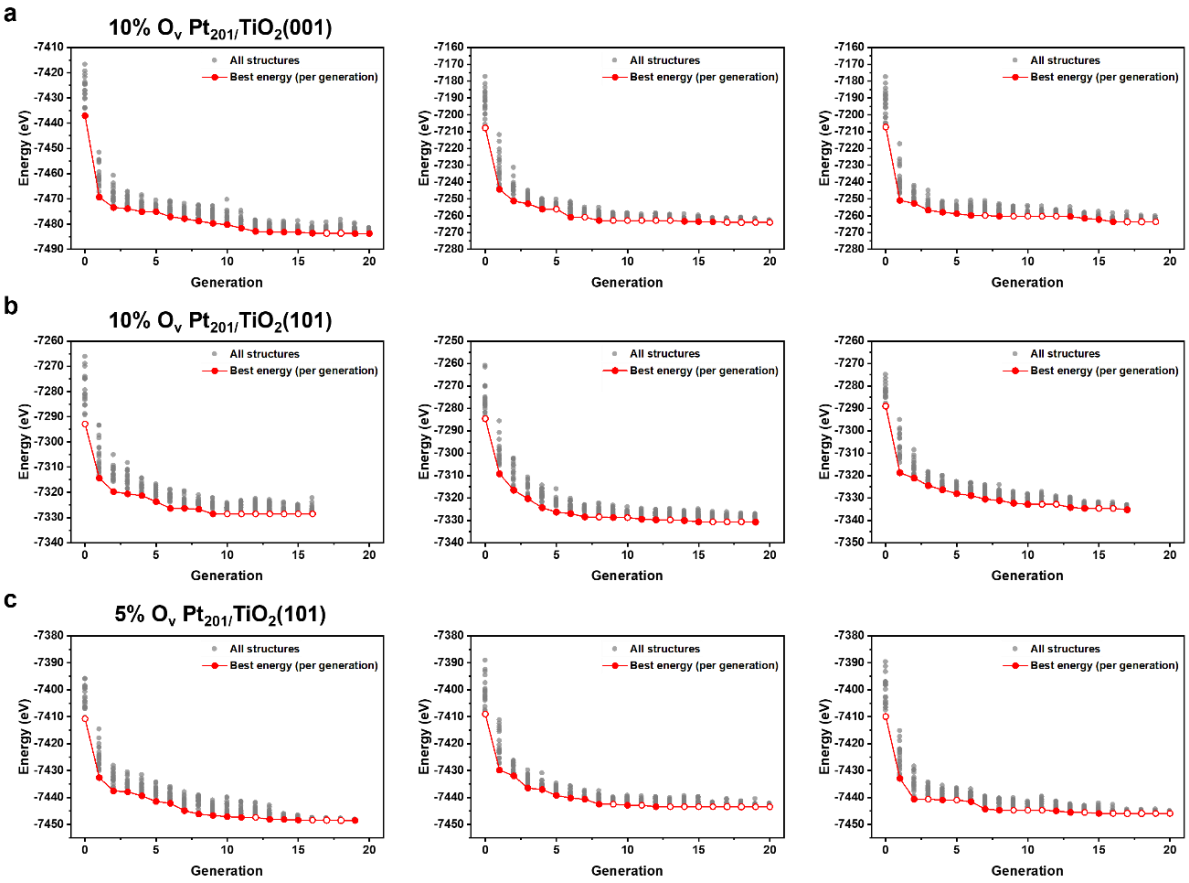

Supplementary Figure 46. The evolution of total energies during the GA optimization of Pt_{201} NPs on TiO_2 with surface O_v, shown for three independent random O_v configurations per facet: (a) 10% O_v Pt_{201}/TiO_2(001), (b) 10% O_v Pt_{201}/TiO_2(101), and (c) 5% O_v Pt_{201}/TiO_2(101). Grey dots represent the energies of all candidate structures sampled in each generation, while the red line denotes the lowest-energy structure per generation. Filled red circles indicate generations where a new global minimum energy was identified, whereas open red circles indicate generations in which the global minimum remained unchanged.

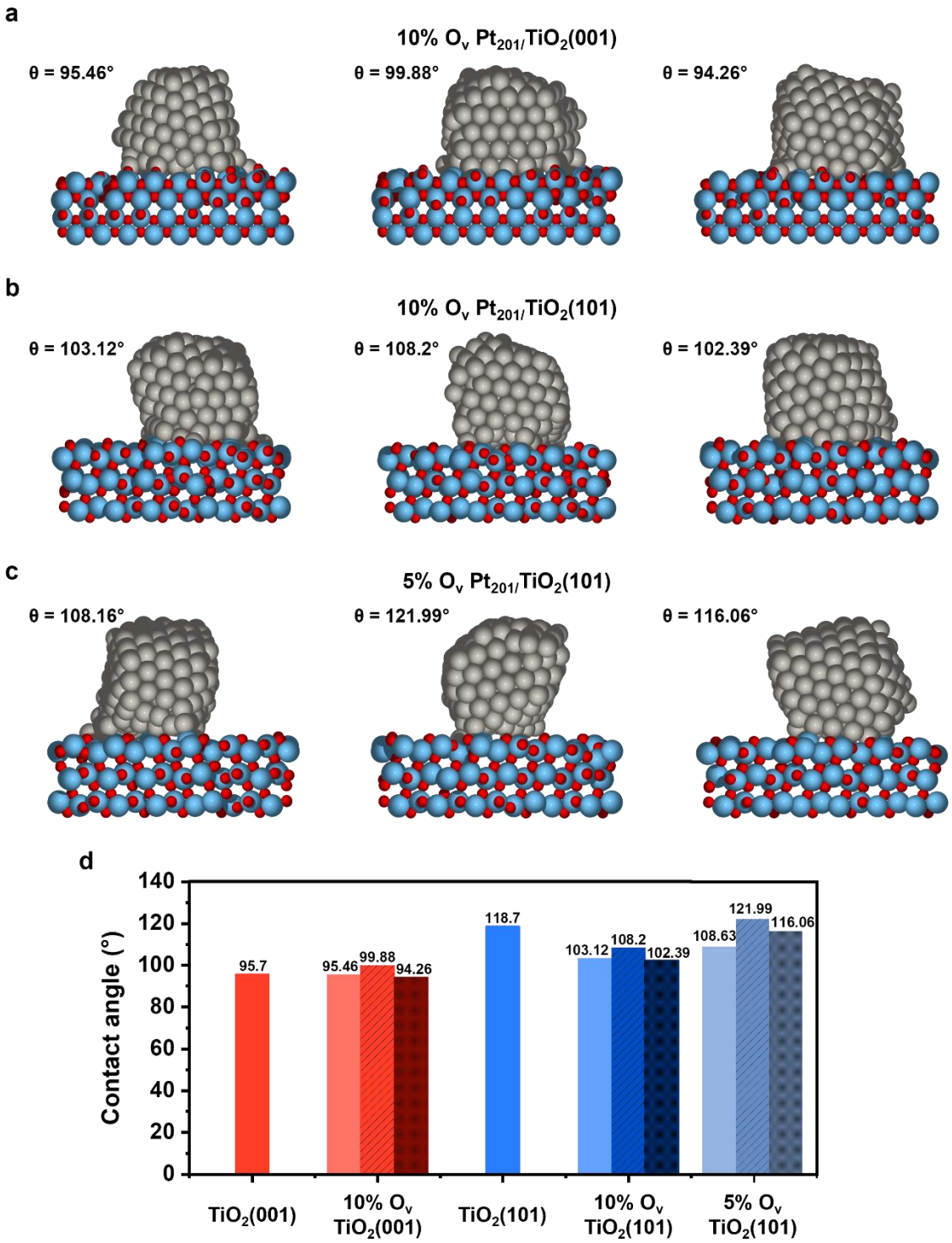

Supplementary Figure 47. Side-view images of the lowest-energy Pt_{201} NPs configurations on (a) 10% O_v TiO_2(001), (b) 10% O_v TiO_2(101), and (c) 5% O_v TiO_2(101), obtained by GA-based optimisation. Three independent O_v configurations were generated per facet by random placement to account for configurational variability of vacancy sites. The values indicated in side-view panels correspond to the effective contact angles (θ) of the Pt NPs on each O_v-modulated TiO_2 surfaces, extracted from the optimised geometries. (d) Summary of the contact angles obtained from the GA-optimised Pt_{201}/TiO_2 configurations on both stoichiometric and O_v-modulated TiO_2 surfaces.

Comment 4: Other than the reshaping of Pt NPs, the reconstruction of TiO_2 at Pt–TiO_2 interface and the stability of Pt NPs should be also considered.

Response: We thank the reviewer for this important comment. We agree that, in addition to Pt reshaping, possible structural changes of the TiO_2 support at the Pt–TiO_2 interface and the stability of Pt NPs under reaction conditions should also be considered.

The stability of Pt NPs was assessed using the catalytic cycle test results presented in our response to Comment 1. As shown in Supplementary Fig. 35, after the initial structural evolution during the 1st run, both PTS and PTR maintain stable catalytic behaviour from the 2nd to the 5th runs, with no significant changes in activity or E_a. In addition, the Pt particle-size distributions after the 5th cycle (Supplementary Figs. 36a, b) showed no significant difference from those of the corresponding spent catalysts after the initial run, indicating that no major sintering or additional structural degradation occurs during subsequent cycles. Furthermore, the corresponding HAADF-STEM images after the 5th cycle (Supplementary Figs. 36c, d) still show distinct Pt morphologies depending on the TiO_2 facet. We note that the PTR image shown in Supplementary Fig. 36d was selected because it provides clear lattice visibility for both Pt and TiO_2 at the interface, although the imaged particle is not exactly at the mean size of the overall PTR distribution. Nevertheless, as discussed in Supplementary Note 3, the facet-dependent trend in Pt morphology remains consistent over the investigated particle-size range, and the selected image is therefore representative of the structural trend relevant to the present discussion.

With respect to possible TiO_2 surface reconstruction, previous studies have reported that the anatase TiO_2(001) surface can reconstruct because of its high surface energy, and several reconstructed models have been proposed and supported by STM and ETEM analyses. (*Prog. Nat. Sci. Mater. Int.* 2021, 31, 1–13 / *Nano Lett*. 2016, 16, 132−137) Among these, the ad-molecule (ADM) model is one of the most widely accepted. To examine whether such reconstruction occurs in our system, we analysed the STEM images of the 5th-cycle spent catalysts and compared the observed TiO_2 atomic arrangements with the corresponding theoretical anatase lattice models. As shown in Supplementary Figs. 36c, d, both catalysts exhibit TiO_2 atomic structures consistent with the expected anatase lattice models. In particular, magnified STEM images of the dashed rectangular regions at and near the Pt–TiO_2 interface do not show detectable TiO_2 surface reconstruction. For PTS, the TiO_2(001) surface shows only the expected Ti termination, indicated by the red arrows, without detectable reconstructed

features such as ADM-like structures. More generally, the TiO_2 lattice fringes and facet framework remain preserved, and no obvious interfacial distortion or restructuring is identified within the resolution of the present measurements.

At the same time, we note that the present STEM images do not directly resolve the local Pt–TiO_2 interfacial geometry. Therefore, subtle and highly localized rearrangements cannot be fully excluded. In this context, the relatively flexible nature of the TiO_2(001) surface may be consistent with the observed stronger Pt wetting, for example through local atomic relaxation or stress accommodation near the interface, as suggested in previous studies of Pt single-atom diffusion preferentially occurring on TiO_2(001) (*Nat. Commun*. 2024, 15, 998). Such highly localized effects, if present, may be related to the observed difference in reconstructed Pt morphology, together with the different O_v abundance on the two facets. However, within the resolution of the present measurements, our results do not indicate significant TiO_2 surface reconstruction in this system.

These observations suggest that, under the present reaction conditions, the dominant measurable structural evolution occurs on the Pt side, while the TiO_2 framework remains largely preserved and the restructured Pt state remains stable over repeated catalytic runs.

Action Taken: In the revised manuscript, we have expanded the discussion of Pt stability and possible TiO_2 surface reconstruction by incorporating additional post-reaction structural analysis after the 5th catalytic cycle. The corresponding Pt particle-size distributions and high-magnification HAADF-STEM images are presented in Supplementary Fig. 36, and the following sentence has been added on page 13: "*Consistently, Pt particle-size distributions and high-magnification STEM images after the 5th cycle (Supplementary Fig. 36) show no significant change in Pt size, while facet-dependent Pt morphology is maintained without clear evidence of TiO_2 surface reconstruction near the Pt–TiO_2 interface. These results indicate that reaction-induced restructuring in PTS leads to a more active catalytic state that remains stable over repeated runs.*"

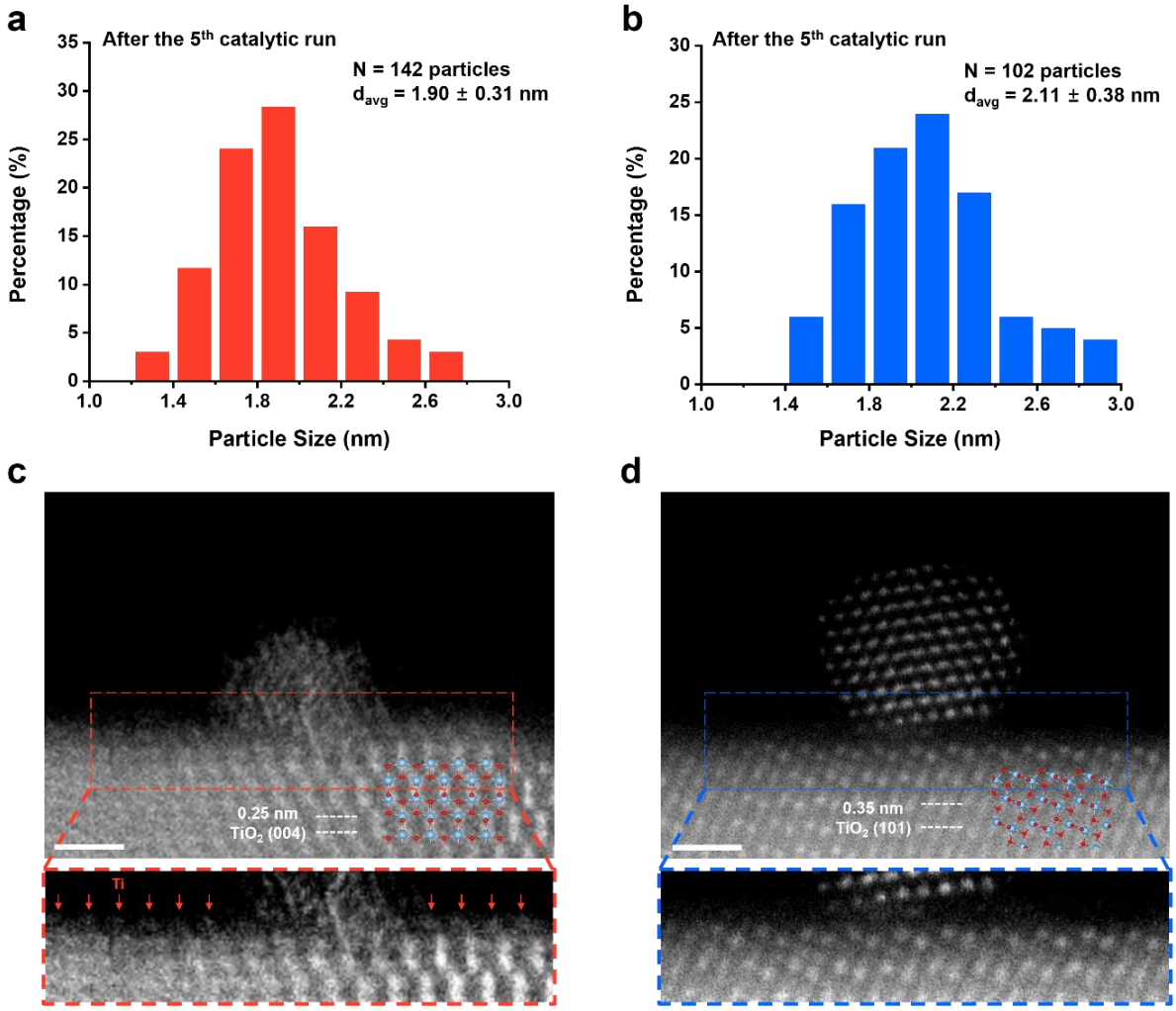

Supplementary Figure 36. (a, b) Histograms showing the Pt NP size distributions and (c, d) HAADF-STEM images of the spent catalysts after the 5th catalytic run for (a, c) PTS and (b, d) PTR. The HAADF-STEM images and corresponding atomic models show that both supports retain anatase TiO_2 lattice structures with predominantly exposed (001) and (101) facets, respectively (Scale bars, 1 nm). The dashed rectangular regions further indicate that no clear TiO_2 surface reconstruction is observed near the Pt–TiO_2 interface under the present conditions.

We sincerely thank the reviewer for these thoughtful and constructive comments. We particularly appreciate the reviewer's critical questions regarding the respective roles of Pt restructuring, support effects, and interfacial stability, which helped us clarify several key aspects of the manuscript and further strengthen the central conclusions of this work.

We sincerely appreciate the all reviewer's insightful and constructive comments, which have played a crucial role in significantly improving the quality and clarity of our manuscript.

Response to the reviewers' comments

The followings are the responses to the reviewers' comments for the manuscript *NCOMMS-25-68798B*

Reviewer #1

General comments: The authors have revised the paper accordingly and the paper looks more convincing. I recommend the paper for publication.

Response: We sincerely thank the reviewer for the positive evaluation of our revised manuscript. We greatly appreciate the reviewer's constructive comments, which helped us refine and strengthen the manuscript.

Reviewer #2

General comments: The authors have substantially improved the manuscript. Current version meets the criteria of *Nature Communications*.

Response: We sincerely thank the reviewer for the positive evaluation of our revised manuscript. We greatly appreciate the reviewer's constructive comments, which helped us improve the quality and clarity of the manuscript.

Reviewer #3

General comments: I appreciate the authors' efforts in providing a detailed response to my previous comments. But upon careful review of the revised manuscript, I still have substantial concerns regarding the novelty of this work, particularly for the high-profile journal like *Nature Communications*. The current results can only support a TiO_2-facet dependent reactivity derived from either the initial morphology of Pt NPs or metal-support interaction. Such effects have already been widely reported in the existing literature. Direct experimental evidence is still missing to explicitly identify the structural reconstruction of Pt/TiO_2 during CO oxidation, which represents the core claim of this work. Given limited novelty and the lack of sufficient in situ structural characterization, I cannot support the publication of this manuscript. Some specific comments for the authors to consider.

Response: We sincerely thank the reviewer for the careful evaluation of our revised manuscript and for clearly identifying the specific concerns regarding the novelty and the experimental evidence for Pt/TiO_2 reconstruction during CO oxidation. We appreciate this important point and agree that the meaning of Pt reconstruction and its relation to catalytic behaviour should be clarified more explicitly.

As reported in our first revision response, we attempted in situ TEM measurements under CO-containing atmospheres to directly observe the structural evolution of Pt/TiO_2 catalysts. However, reliable atomic-scale imaging could not be obtained because of severe CO-related contamination and limited imaging stability under the required gas environment. In addition, the Pt nanoparticles in our catalysts can be meaningfully distinguished only in STEM mode, but the current instrumental configuration does not provide sufficient spatial and temporal resolution in STEM mode to track subtle changes in Pt particle shape and $Pt–TiO_2$ interfacial geometry under CO oxidation conditions. This limitation is also reflected in our previous *in situ* heating study using the same instrumental platform (*Adv. Funct. Mater*. 2024, 34, 2400341), where structural evolution could be followed under pure air conditions only at relatively low magnification; this level of observation is insufficient for resolving the atomic-scale Pt morphology changes required in the present Pt/TiO_2 system. Therefore, although direct real-time visualization of atomic-scale Pt dynamics remains experimentally challenging in the present system, our interpretation is not based on a single indirect observation. Instead, it is supported by mutually consistent evidence from in situ and post-reaction spectroscopic analyses, post-reaction STEM observations, catalytic cycling tests, size-controlled Pt/TiO_2 experiments, and computational modelling. Together, these results provide a consistent experimental and theoretical basis for discussing the reaction-evolved $Pt–TiO_2$ structure and its catalytic relevance.

Regarding novelty, we agree that several individual elements of this work, such as facet-dependent TiO_2 reducibility, O_v-related reactivity, metal–support interactions, and CO-induced Pt surface roughening, have been discussed in previous studies of oxide-supported Pt catalysts. However, these prior studies have generally focused on the intrinsic redox properties of the oxide support, charge transfer or SMSI-type phenomena, or sintering/redistribution behaviour. In comparison, the specific connection between TiO_2 facet-controlled Pt nanoparticle morphology, reaction-evolved $Pt–TiO_2$ interfacial configuration during CO oxidation, and the resulting catalytic behaviour has not been clearly established. Moreover, to the best of our

knowledge, such relationships have not been systematically investigated in a well-defined model catalyst system using a comprehensive combination of experimental and theoretical approaches that link support facet, Pt morphology, interfacial structure, and catalytic performance.

The central point of our study is therefore not simply that TiO_2(001) is more reducible or that Pt/TiO_2 exhibits stronger MSI. Rather, our results indicate that the TiO_2 facet acts as a structural descriptor that regulates the supported Pt nanoparticles themselves. Specifically, the exposed TiO_2 facet determines the preferred Pt wetting/dewetting morphology and Pt–TiO_2 interfacial contact, which subsequently influences how the Pt surface and interface evolve under CO oxidation conditions. Although both PTS and PTR exhibit CO-induced Pt surface roughening during reaction, as evidenced by *in situ* DRIFTS and consistent with previous reports, the post-reaction STEM and CO-DRIFTS results show that the final Pt state remains facet-dependent rather than converging to a common structure. This distinction suggests that the catalytic role of TiO_2 facets extends beyond providing a more reducible support surface; the facet also influences the initial Pt morphology and the reaction-evolved Pt–TiO_2 interfacial configuration associated with support-oxygen participation during CO oxidation.

We also acknowledge that facet-dependent wetting/dewetting of supported metals has been reported previously, including systems where support facets induce clearly different metal configurations or influence metal redistribution, diffusion, aggregation, dissolution, or atom trapping. However, in many of these cases, the discussion has centered on large morphological transitions, sintering resistance, or stabilization of isolated metal species. In contrast, our study focuses on Pt nanoparticles that remain in the nanoparticle regime, but whose apparent morphology, interfacial contact, and post-reaction structural state are regulated by the TiO_2 facet. This provides a distinct perspective on facet-dependent MSI, where the support facet governs not only the support redox properties but also the structure and evolution of the supported Pt–TiO_2 interface.

In the present revision, we have made several targeted revisions and additions to address the reviewer's specific concerns. First, to clarify what we mean by Pt reconstruction, we have revised the manuscript to distinguish the initial Pt morphology, CO-induced surface roughening under reaction conditions, and the reaction-evolved Pt morphology and Pt–TiO_2 interfacial configuration retained after CO oxidation, as discussed in our response to *Comment 1*. Second, to examine whether the enhanced reactivity after the first catalytic cycle can be explained

simply by reductive activation or additional O_v generation, we have added post-reaction O 1*s* analyses and H_2 pretreatment controls, as described in our response to *Comment 2*. Third, we have revised the discussion of Pt/Al_2O_3 to clarify that it is used only as a qualitative irreducible-support reference, not as a direct structural analogue of Pt/TiO_2, as explained in our response to *Comment 3*. Together, we believe that these revisions provide a clearer and more carefully qualified basis for discussing the reaction-evolved $Pt–TiO_2$ structure and its catalytic relevance in the revised manuscript.

Comment 1: It is unclear what the reconstruction of Pt NPs refers to, beyond their initial morphology and surface roughening. Noted that both catalysts undergo surface roughening but display different reactivity, the authors should explicitly clarify the structural changes of Pt NPs during CO oxidation and their respective contributions to catalytic performance.

Response: We thank the reviewer for this important comment. We agree that the term "Pt reconstruction" should be more explicitly defined, particularly because both PTS and PTR exhibit CO-induced surface roughening features during reaction. In the revised manuscript, we therefore clarify that the reconstruction discussed in this work does not refer simply to the occurrence of CO-induced surface roughening. In our *in situ* DRIFTS results (Fig. 3), such roughening features are observed for both catalysts prior to catalytic ignition, where CO adsorption modifies the Pt surface coordination. Under these CO-saturated Pt/TiO_2 surface conditions, the lower-temperature reactivity is governed by the ability of perimeter CO species to react with support oxygen, which depends on the $Pt–TiO_2$ interfacial structure and the reducibility of support oxygen. This interpretation is consistent with the earlier CO_2 evolution on PTS and the delayed catalytic ignition of PTR.

This distinction is important because CO-induced roughening provides a dynamic surface state in which interfacial oxygen activation and Pt fluxional behaviour can be coupled, rather than representing the final reconstructed state itself. As described in the manuscript, previous microscopy and spectroscopy studies have reported CO-induced restructuring behaviours of supported Pt catalysts, including terrace-to-step transitions, facet rounding, and interfacial reconfiguration. Vincent et al. (*Nat. Commun*. **2021**, 12, 5789) further showed that CO adsorption can modify Pt surface energetics and weaken interfacial bonding at Pt/CeO_2 interfaces, while dynamic formation and annihilation of O_v at the Pt perimeter accompanies particle reshaping under CO oxidation. Similarly, in Pt/TiO_2 catalysts (*J. Chem. Phys.* **2019,**

151, 234716), the emergence of a DRIFTS feature at 2107 cm^{-1}, assigned to CO adsorbed at interfacial Pt sites ($CO–Pt_{int}$), has been associated with dynamic O_2 activation at the Pt perimeter. In our second *in situ* DRIFTS measurements (Supplementary Figs. 30a, b), $CO–Pt_{int}$ was observed for spent PTS but not for spent PTR under the same reaction history, although both catalysts exhibited CO-induced surface roughening features. In contrast, PTR showed comparable $CO–Pt_{int}$ features only after harsher treatment conditions (300 °C for 2 h). These results indicate that CO-induced roughening occurs on both catalysts, but the coupling between Pt surface fluxionality, $Pt–TiO_2$ interfacial reconfiguration, and perimeter oxygen activation is more facile on PTS than on PTR. Therefore, the facet-dependent Pt restructuring discussed in the manuscript arises not from the presence or absence of roughening, but from the different interfacial response of Pt/TiO_2 under CO oxidation conditions.

To make this distinction clearer in the revised manuscript, we have added a new section entitled "*Facet-dependent Pt structural evolution during CO oxidation*". In this section, the previously described literature background, second *in situ* DRIFTS results, post-reaction structural observations, and Fig. 5 schematic have been reorganized to explicitly describe the structural evolution of Pt/TiO_2 catalysts before, during, and after CO oxidation. Specifically, we now distinguish (i) the initial facet-dependent Pt morphology before reaction, (ii) CO-induced surface roughening during reaction, and (iii) the reaction-evolved Pt morphology and $Pt–TiO_2$ interfacial configuration retained after CO oxidation. Fig. 5 has also been revised to label these three structural states as "Initial Pt morphology", "CO-induced surface roughening", and "Reaction-evolved state". These revisions clarify that the Pt reconstruction discussed in the manuscript refers to the facet-dependent reaction-evolved Pt morphology and $Pt–TiO_2$ interfacial configuration, rather than to CO-induced surface roughening alone.

We acknowledge that the atomic-scale pathway leading to this reaction-evolved state could not be directly visualized in real time under CO oxidation conditions, as noted in the *General Response*. However, our structural interpretation focuses on the reaction-evolved Pt state retained after CO oxidation and its catalytic relevance, rather than on the transient atomic pathway alone. Literature precedents support that CO-induced roughening can be coupled with Pt fluxionality and perimeter oxygen activation, while our post-reaction STEM/CO-DRIFTS analyses and size-controlled Pt/TiO_2 experiments support that the retained Pt morphology and $Pt–TiO_2$ interfacial configuration remain facet-dependent after reaction.

The catalytic relevance of this reaction-evolved interfacial structure is further supported by the

catalytic cycling results and by the additional analyses described in our response to *Comment 2*. As shown in Supplementary Fig. 35, PTS shows an additional decrease in E_a from the 2nd run onward and maintains this lower-E_a state over repeated runs, whereas PTR remains nearly unchanged. The newly added post-reaction O 1*s* analyses and H_2 pretreatment controls further show that this activity enhancement cannot be explained solely by additional O_v generation or reductive activation, as discussed in detail in our response to *Comment 2*. These results are consistent with our interpretation that the reaction-evolved Pt–TiO_2(001) interfacial configuration provides a more favourable environment for support-oxygen participation during CO oxidation and contributes to the enhanced catalytic behaviour of PTS.

Action taken: In the revised manuscript, we have clarified the structural meaning of Pt reconstruction and its relationship to catalytic behaviour by distinguishing the initial facet-dependent Pt morphology, CO-induced surface roughening during reaction, and the reaction-evolved Pt morphology and Pt–TiO_2 interfacial configuration retained after CO oxidation. We have also revised Fig. 5 to explicitly label these three structural states as "Initial Pt morphology," "CO-induced surface roughening," and "Reaction-evolved state." To incorporate these revisions, a new section entitled *Facet-dependent Pt structural evolution during CO oxidation* has been added on Pages 11–12.

*"**Facet-dependent Pt structural evolution during CO oxidation***

The experimental observations and computational results described above consistently indicate that TiO_2 facets regulate the structural evolution of supported Pt NPs under CO oxidation conditions. This behaviour can be understood by considering how the initial facet-dependent Pt morphology responds to CO-induced surface roughening and interfacial reconfiguration.

CO-induced surface roughening and interfacial reconfiguration of supported Pt catalysts, including terrace-to-step transitions and facet rounding, have been reported by microscopy and spectroscopy.[52, 54, 66] Vincent et al. reported atomic-scale fluxional behaviour at Pt/CeO_2 interfaces driven by CO adsorption, where CO-modified Pt surface energetics and interfacial bonding were coupled with dynamic O_v formation and annihilation at the Pt perimeter, leading to particle reshaping under CO oxidation.[52] Similarly, CO-induced interfacial reconfiguration has been reported for Pt/TiO_2, where the emergence of a DRIFTS feature at 2107 cm^{-1}, assigned to CO adsorbed at interfacial Pt sites (CO–Pt_{int}), was associated with dynamic O_2 activation at the Pt perimeter.[67]

In the second in situ DRIFTS measurements (Supplementary Figs. 30a, b), the CO–Pt_{int} feature was observed exclusively for spent PTS and was absent for spent PTR, although CO-induced surface roughening features were present for both catalysts. By contrast, when the spent catalysts were prepared under harsher conditions (300 °C for 2 h), CO–Pt_{int} features also emerged for PTR (Supplementary Figs. 30c, d). These results indicate that PTR intrinsically exhibits weaker Pt–TiO_2 interactions, requiring higher energy for CO adsorbed at perimeter Pt sites to activate interfacial oxygen species. Consequently, Pt fluxional behaviour at the Pt/TiO_2 interface differs between the two facets, leading to facet-dependent Pt restructuring.

As illustrated in Fig. 5, facet-dependent MSIs establish distinct initial Pt–TiO_2 wetting geometries on TiO_2(001) and TiO_2(101). On TiO_2(001), the larger Pt–TiO_2 interfacial contact favours a more wetted Pt configuration, whereas TiO_2(101) stabilizes a more compact Pt configuration with a confined Pt–TiO_2 interface. During reaction, both catalysts undergo CO-induced surface roughening and catalytic ignition, but their reaction-evolved Pt morphologies and Pt–TiO_2 interfacial configurations remain distinct. For PTS, the post-reaction STEM and CO-DRIFTS results indicate a more extended Pt–TiO_2(001) interfacial configuration with pronounced interfacial and under-coordinated Pt features. By contrast, PTR retains a more faceted Pt morphology and a more confined Pt–TiO_2(101) interface after reaction, consistent with less facile interfacial oxygen activation and weaker Pt–TiO_2 interfacial reconfiguration. Accordingly, Pt reconstruction is described here not simply as CO-induced surface roughening, but as the facet-dependent reaction-evolved Pt morphology and Pt–TiO_2 interfacial configuration retained after CO oxidation. This structural framework suggests that facet-dependent Pt/TiO_2 catalysis cannot be understood solely from the intrinsic redox properties of TiO_2 facets, but also depends on the reaction-evolved Pt–TiO_2 interfacial geometry involved in support-oxygen participation."

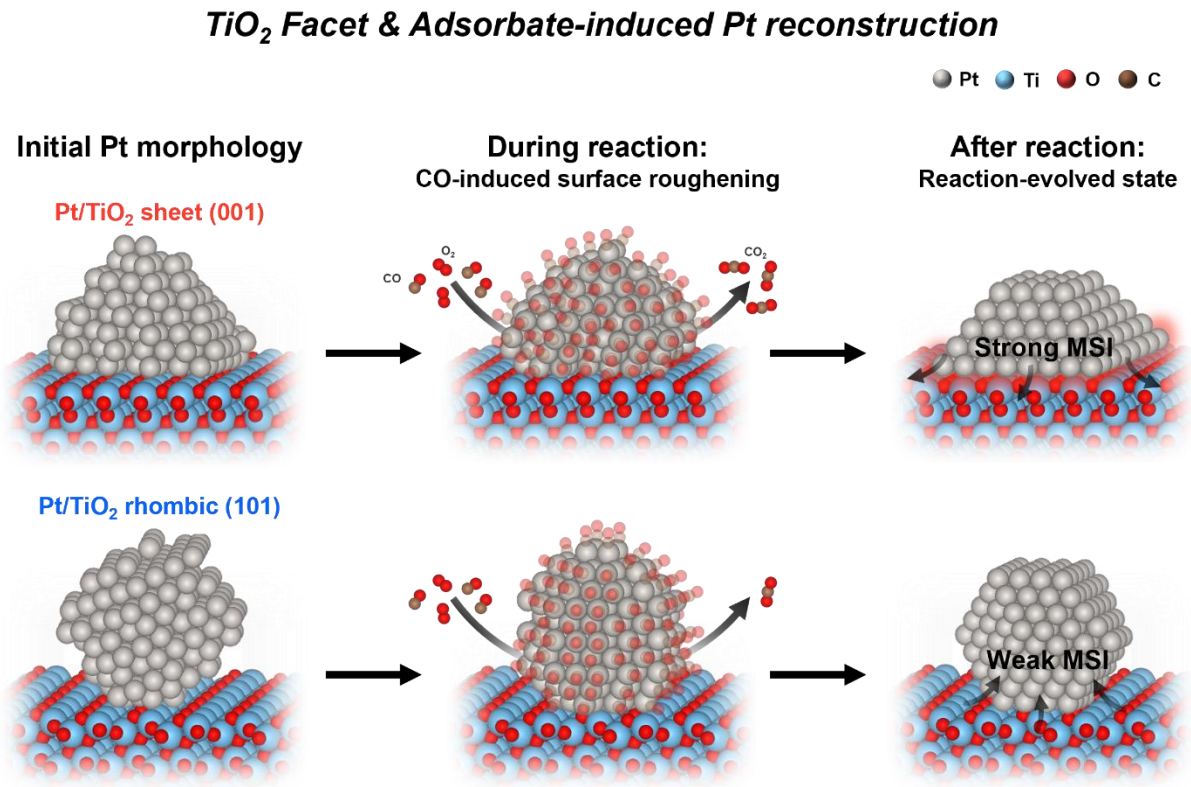

Figure 5. TiO_2 facet-dependent Pt structural evolution during CO oxidation. Schematic illustration highlighting the initial Pt morphology, CO-induced surface roughening, and reaction-evolved state. Strong and weak MSI schematically denote the relative extent of Pt–TiO_2 interfacial contact.

Comment 2: The enhanced reactivity after the first catalytic cycle may stem from the initial reduction of Pt NPs or the Pt–TiO_2 interface, which could generate abundant O_v. Direct experimental evidence is required to verify the intrinsic structural evolution of Pt NPs after the first run, to exclude simple surface reduction.

Response: We thank the reviewer for this important comment. We agree that the first catalytic cycle may induce partial reduction of Pt NPs or the Pt–TiO_2 interface, which could generate O_v-related sites that contribute to CO oxidation. Therefore, to examine whether the enhanced activity after the first run originates simply from surface reduction or the generation of additional O_v, we performed additional post-reaction surface analyses and H_2 pretreatment control experiments.

First, we analysed two sets of O 1*s* spectra to examine the surface oxygen state after reaction: (i) the spent catalysts obtained after the *in situ* AP-XPS measurements under CO oxidation conditions (Figs. 6c, d), and (ii) the spent catalysts obtained after the first run of the catalytic

cycling test (Supplementary Fig. 35). In both analyses (Supplementary Fig. 42), the O_v-related oxygen ratio of post-reaction PTS was not higher than that of PTR; instead, the two catalysts showed comparable O_v-related oxygen ratios after reaction. Thus, although fresh PTS initially contains more O_v-related oxygen species (Supplementary Fig. 37), the post-first-run state does not support the selective generation of abundant O_v on PTS. These results directly address the catalyst state before the subsequent catalytic run and indicate that the enhanced activity of PTS in the following run is not simply caused by additional O_v generation after the first run. Rather, the results suggest that the higher activity of PTS is more closely associated with the reaction-evolved Pt–TiO_2(001) interfacial structure and favourable support-oxygen participation during CO oxidation.

Second, to further test whether reductive activation alone can account for the enhanced activity after the first catalytic run, we performed H_2 pretreatment controls prior to CO oxidation. The pretreatment temperature was selected based on the H_2-TPR behaviour of Pt/TiO_2 catalysts. In our H_2-TPR profiles, Pt-related reduction occurs below ~250 °C, whereas the broader higher-temperature feature centred around ~350 °C is associated with H_2-spillover-assisted partial reduction of surface TiO_2 species adjacent to Pt. We therefore employed a 400 °C H_2 pretreatment as a reductive control condition that promotes Pt reduction and reductive modification of the Pt-adjacent TiO_2 surface.

As shown in Supplementary Figs. 43a, b and d, e, the 400 °C H_2 pretreatment enhanced the activity of both PTS and PTR, giving lower 1st-run E_a values and improved light-off behaviour compared with the corresponding fresh catalysts. This result indicates that reductive treatment can contribute to catalytic activation, likely by modifying Pt species and/or Pt-adjacent TiO_2 surface sites, consistent with the reviewer's suggestion that reduction-derived O_v-related sites may influence the reactivity.

Nevertheless, the subsequent catalytic behaviour after 400 °C H_2 pretreatment differed between PTS and PTR (Supplementary Figs. 43c, f). For PTS, the E_a decreased from 53.8 kJ·mol^{-1} after the 1st run to 47.5 and 43.6 kJ·mol^{-1} in the 2nd and 3rd runs, respectively, reaching values comparable to those observed from the 2nd run onward in the catalytic cycling experiment without H_2 pretreatment (Supplementary Fig. 35). By contrast, PTR maintained nearly similar E_a values over repeated runs after the 400 °C H_2 pretreatment, from 87.6 to 89.2 and 89.3 kJ·mol^{-1}, without showing the additional activity enhancement observed for PTS. This comparison suggests that reductive activation contributes to the activity enhancement, but is

not sufficient to explain the facet-dependent low-E_a state observed for PTS after CO oxidation. Pt size distributions and STEM analyses after the 3rd run over the H_2-pretreated catalysts showed no significant Pt particle growth or TiO_2 morphology degradation, indicating that the observed catalytic evolution is not associated with Pt sintering or apparent support morphological degradation (Supplementary Fig. 44).

To further support this interpretation, we analysed the O 1*s* spectra of the 400 °C H_2-pretreated catalysts and the corresponding post-reaction samples. As described in our previous revision, the higher-binding-energy O 1*s* components, including adsorbed oxygen, hydroxyl species, water-related species, and defect-associated surface oxygen, are commonly used as indirect descriptors of O_v-related surface states. As shown in Supplementary Fig. 45, the 400 °C H_2 pretreatment increased the relative contribution of these high-binding-energy O 1*s* components, indicating that the reductive treatment altered the surface oxygen environment in a manner consistent with increased O_v-/hydroxyl-related surface species. However, after the 3rd catalytic run following the 400 °C H_2 pretreatment, the O 1*s* spectra of PTS and PTR evolved toward comparable post-reaction states, without retaining a selectively higher contribution of these high-binding-energy O 1*s* components on PTS. This trend is consistent with the post-reaction O 1*s* results obtained after the *in situ* AP-XPS reaction sequence and after the first catalytic run (Supplementary Fig. 42), where PTS did not retain a selectively higher O_v-related oxygen contribution than PTR after reaction.

These O 1*s* analyses, together with the H_2 pretreatment activity tests, support that reductive surface modification and O_v-/hydroxyl-related surface oxygen species can contribute to the catalytic behaviour of Pt/TiO_2. However, the enhanced activity of PTS after the first run cannot be explained solely by the generation or retention of abundant O_v-/hydroxyl-related surface species. Rather, the results support that the higher activity of PTS is associated with the reaction-evolved $Pt–TiO_2(001)$ interfacial structure, which provides a more favourable environment for support-oxygen participation during CO oxidation.

Action taken: In the revised manuscript, we have added post-reaction O 1*s* analyses and H_2 pretreatment control experiments to examine whether the enhanced activity after the first catalytic run can be explained simply by surface reduction or additional O_v generation. The post-reaction O 1*s* analyses compare the surface oxygen states of PTS and PTR after CO oxidation, while the H_2 pretreatment experiments provide a reductive control for comparing catalytic evolution under an intentionally modified surface-reduction state. These additional

results clarify that reduction/O_v-related effects contribute to Pt/TiO_2 catalysis, but do not solely account for the enhanced activity of PTS after the first run. The corresponding figures and analyses (Supplementary Figs. 42–45) have been added to the revised manuscript, and the following paragraph has been added to the *Reaction mechanism and the origin of superior catalytic activity* section on Page 15: *"Post-reaction O 1s analyses further show that the initially higher O_{ads}/O_{lat} ratio of PTS relative to PTR becomes comparable after CO oxidation (Supplementary Fig. 42). When considered together with the catalytic cycle results, in which PTS shows an additional E_a decrease from the 2nd run onward whereas PTR remains nearly unchanged, this result indicates that the enhanced activity of PTS after the first run cannot be described simply by the initial O_v abundance. Instead, it is more closely associated with the reaction-evolved Pt–TiO_2(001) interfacial structure, which promotes favourable support-oxygen participation during CO oxidation. This interpretation is further supported by reductive pretreatment controls (Supplementary Figs. 43–45 and Supplementary Note 12). H_2 pretreatment increases the O_v-related O 1s contribution and enhances the initial activity of both catalysts, but only PTS shows an additional E_a decrease during subsequent CO oxidation runs, reaching the low-E_a state observed in the original catalytic cycling test, while the post-reaction O 1s spectral features of PTS and PTR again become comparable."*

In addition, detailed experimental results and discussion are provided in Supplementary Note 12. *"**Supplementary Note 12. Evaluating Reduction/O_v-related Contributions to Catalytic Activation** To examine the possible influence of surface reduction and changes in O_v-related oxygen species on the activity enhancement after the first catalytic run, post-reaction O 1s analyses and H_2 pretreatment experiments were performed. The post-reaction O 1s analyses compared the surface oxygen states of PTS and PTR after CO oxidation, while the H_2 pretreatment experiments provided a reductively modified Pt/TiO_2 state for comparison with the catalyst state evolved during CO oxidation. As shown in Supplementary Fig. 42, the initially higher O_{ads}/O_{lat} ratio of PTS relative to PTR became comparable after CO oxidation, both after the in situ AP-XPS reaction sequence and after the first catalytic run. Together with the catalytic cycle results, where PTS shows an additional E_a decrease from the 2nd run onward whereas PTR remains nearly unchanged, this result indicates that the enhanced activity of PTS after the first run cannot be described simply by the initial O_v abundance.*

H_2 pretreatment was performed in 10% H_2/Ar at 400 °C for 1 h with a total flow rate of 50 $mL \cdot min^{-1}$. This condition was selected based on the H_2-TPR profile, where Pt-related reduction

occurs below ~250 °C and the broader feature around ~350 °C is associated with H_2-spillover-assisted partial reduction of surface TiO_2 species adjacent to Pt. After H_2 pretreatment, both PTS and PTR showed enhanced initial CO oxidation activity, with lower 1st-run E_a values and improved light-off behaviour compared with the corresponding fresh catalysts (Supplementary Fig. 43). However, different trends were observed during subsequent catalytic runs. For PTS, the E_a decreased from 53.8 kJ mol^{-1} in the 1st run to 47.5 and 43.6 kJ mol^{-1} in the 2nd and 3rd runs, respectively, reaching the low-E_a state observed in the original catalytic cycling test. In contrast, PTR maintained similar E_a values over repeated runs after H_2 pretreatment, changing from 87.6 to 89.2 and 89.3 kJ mol^{-1} from the 1st to 3rd runs. These results show that reductive pretreatment enhances the initial activity of both catalysts, but the additional E_a decrease during subsequent CO oxidation occurs only for PTS. Pt size distributions and STEM analyses after the 3rd run over the H_2-pretreated catalysts showed no significant Pt particle growth or apparent degradation of the TiO_2 support morphology, indicating that the observed catalytic evolution is not associated with Pt sintering or support morphological degradation (Supplementary Fig. 44).

The O 1s spectra of the H_2-pretreated catalysts further show that the relative contribution of high-binding-energy O 1s components increased after H_2 pretreatment for both catalysts (Supplementary Fig. 45). These components include adsorbed oxygen, hydroxyl species, water-related species, and defect-associated surface oxygen, which are used as indirect descriptors of O_v-related surface states. After the 3rd catalytic run following H_2 pretreatment, the O 1s spectral features of PTS and PTR again became comparable, consistent with the post-reaction O 1s results described above.

Taken together, these results show that reductive surface modification and O_v-/hydroxyl-related surface oxygen species contribute to the catalytic behaviour of Pt/TiO_2 catalysts. However, the enhanced activity of PTS after the first catalytic run cannot be described solely by the initial O_v abundance or by reductive surface modification. Rather, the kinetic and O 1s results support that the low-E_a state of PTS is associated with the reaction-evolved Pt–TiO_2(001) interfacial structure, which provides a favourable environment for support-oxygen participation during CO oxidation."

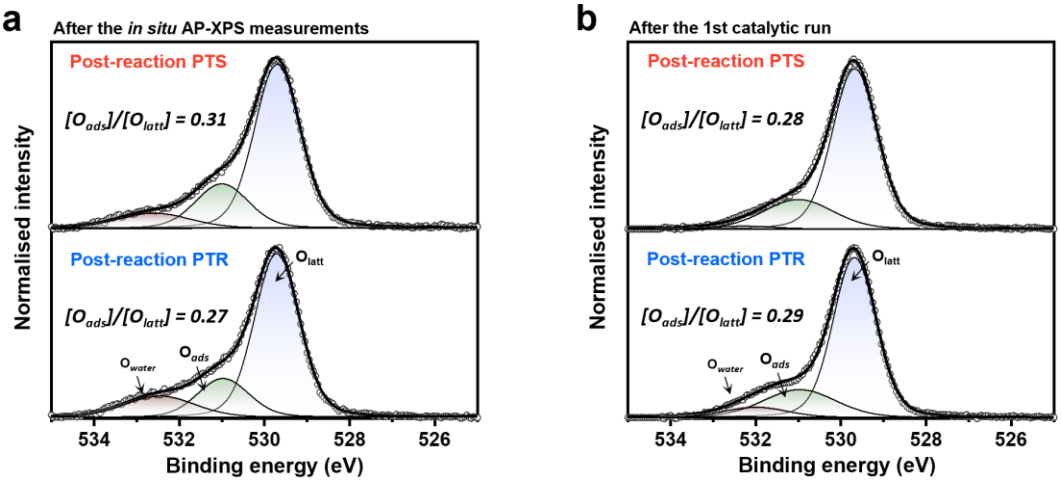

Supplementary Figure 42. Post-reaction O 1*s* XPS spectra of Pt/TiO_2 catalysts. (a) UHV O 1*s* spectra of PTS and PTR measured after the *in situ* AP-XPS measurements sequence. (b) *Ex situ* UHV O 1*s* spectra of spent PTS and PTR obtained after the first catalytic run.

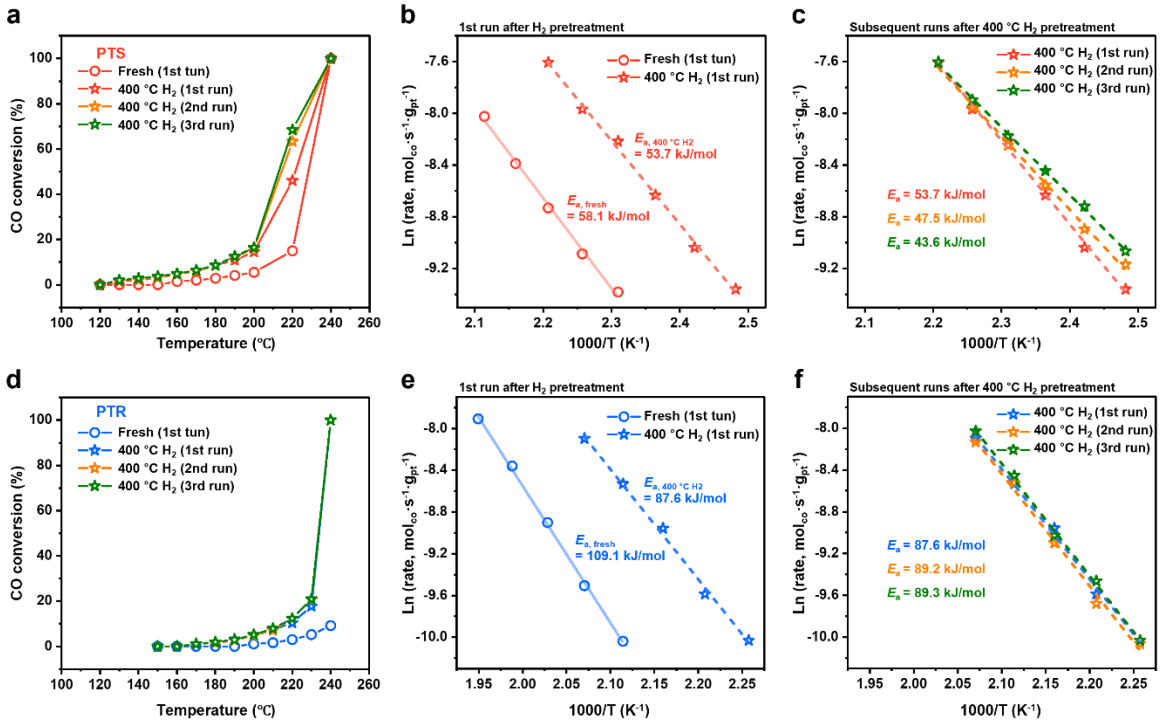

Supplementary Figure 43. Temperature-dependent CO conversion curves and Arrhenius plots for (a–c) PTS and (d–f) PTR after H_2 pretreatment at 400 °C. (a, d) Temperature-dependent CO conversion curves. (b, e) Arrhenius plots comparing the 1st-run activities of the fresh and 400 °C H_2-pretreated catalysts. (c, f) Arrhenius plots showing the subsequent catalytic runs after 400 °C H_2 pretreatment. For the 400 °C H_2-pretreated samples, the catalysts were held at 240 °C for 2 h under reaction conditions before the 2nd run. E_a values were calculated in the kinetically relevant regime (<10% CO conversion) at a total flow rate of 100 mL min^{-1} and a CO/O_2 ratio of 1.

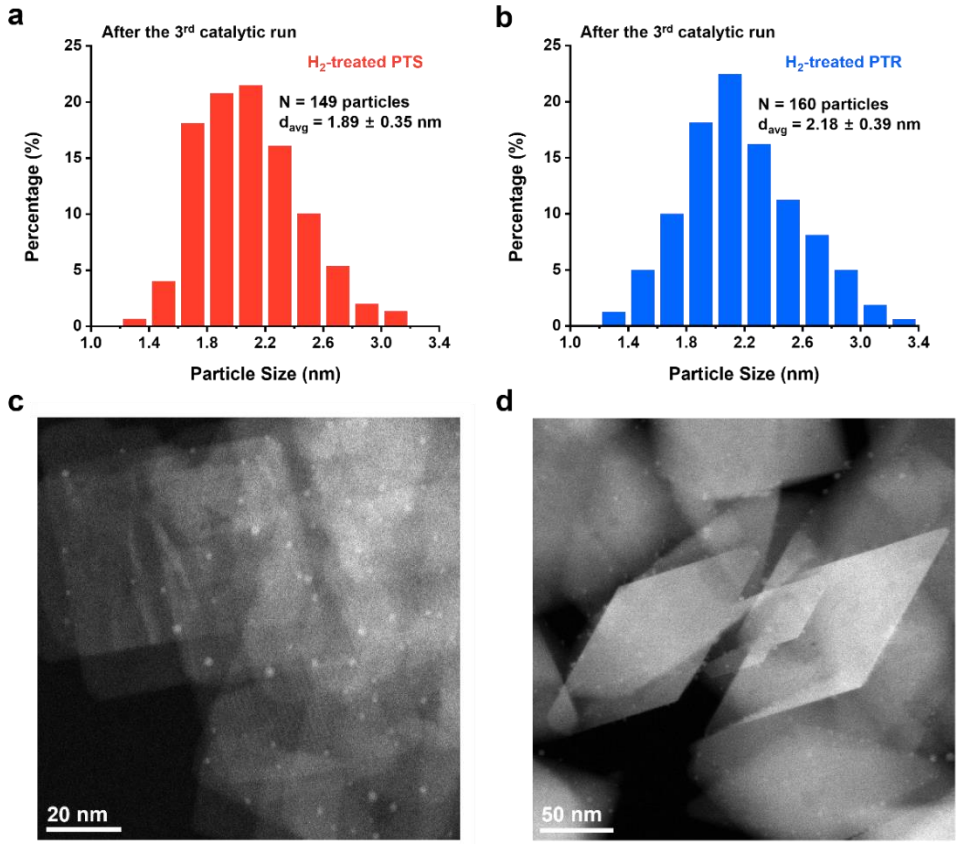

Supplementary Figure 44. (a, b) Histograms showing the Pt NP size distributions and (c, d) HAADF-STEM images of spent catalysts after the 3rd catalytic run following 400 °C H_2 pretreatment: (a, c) PTS and (b, d) PTR. Both catalysts show no significant sintering of Pt NPs or morphological degradation of the TiO_2 supports after H_2 pretreatment and subsequent CO oxidation cycles.

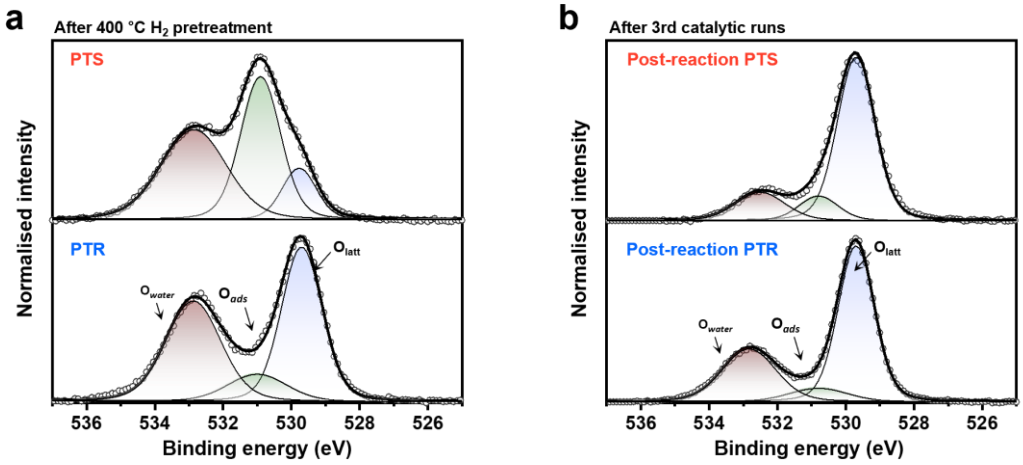

Supplementary Figure 45. O 1*s* XPS spectra of PTS and PTR after (a) H_2 pretreatment at 400 °C and (b) the 3rd CO oxidation run following the 400 °C H_2 pretreatment. The higher-binding-energy components include O_{ads} from adsorbed/hydroxyl- or defect-associated surface oxygen species and O_{water} from molecular or weakly bound water-related species.

Comment 3: The additional data on Pt/Al_2O_3 are not comparable or supportive, due to marked differences in particle size, morphology and metal–support interactions.

Response: We thank the reviewer for this important comment. We agree that Pt/Al_2O_3 (PtA) cannot be regarded as a direct structural analogue of the Pt/TiO_2 catalysts because Al_2O_3 is an irreducible support that does not provide a well-defined facet-controlled surface and exhibits different metal–support interactions from TiO_2. Therefore, we agree that PtA should not be used for quantitative comparison of catalytic activity with PTS and PTR, or as a direct structural basis for the facet-dependent structural evolution of Pt/TiO_2.

Accordingly, we have revised the manuscript and Supplementary Note 13 to clarify the limited role of the PtA data. In the previous manuscript, the PtA results were discussed together with the Pt/TiO_2 catalysts in a way that could imply a stepwise activity comparison among PtA, PTR, PTS, and cycled PTS. This discussion has been removed from the revised manuscript. The relationship between O_v-related surface states and the activity enhancement after the first catalytic run is now addressed using the newly added post-reaction O 1*s* analyses and H_2 pretreatment controls, as described in our response to *Comment 2*.

In the revised manuscript, PtA is retained only as a qualitative irreducible-support reference for comparing the reversibility of CO-induced Pt surface roughening. Specifically, although PtA also shows CO-induced spectral changes during reaction, the normalized pre- and post-reaction CO-DRIFTS spectra of PtA are nearly unchanged (Supplementary Fig. 48), indicating reversible Pt surface roughening (*ACS Catal*. **2016**, 6, 8, 5599–5609) without persistent Pt–support interfacial restructuring. This behaviour is contrasted qualitatively with the more persistent reaction-evolved Pt–TiO_2 interfacial structures observed on reducible TiO_2. We have explicitly stated this limitation in Supplementary Note 13 and revised the main-text discussion accordingly.

Action taken: In the revised manuscript, we have revised the discussion of Pt/Al_2O_3 (PtA) to address the reviewer's concern regarding its comparability with the Pt/TiO_2 catalysts. We now explicitly state that PtA is not considered a direct analogue of Pt/TiO_2 because Al_2O_3 is an irreducible support that lacks a well-defined facet-controlled surface and exhibits different metal–support interactions from TiO_2. Accordingly, we have removed the previous discussion that could imply a quantitative, stepwise activity comparison among PtA, PTR, PTS, and PTS after catalytic cycling. In the revised manuscript, PtA is used only as a qualitative irreducible-

support reference to distinguish reversible CO-induced Pt surface roughening on Al_2O_3 from the more persistent reaction-evolved Pt–TiO_2 interfacial restructuring observed on reducible TiO_2. The following paragraph has been revised in the *Reaction mechanism and the origin of superior catalytic activity* section on Pages 15–16: *"To further evaluate whether the facet-dependent Pt structural evolution can be attributed solely to O_v-related effects, we conducted qualitative Pt/Al_2O_3 (PtA) reference experiments and GA-optimised simulations using Ov-modulated TiO_2 models (Supplementary Note 13). PtA was used only as a qualitative irreducible-support reference, not as a direct analogue of Pt/TiO_2, because Al_2O_3 lacks a well-defined facet-controlled surface and exhibits different metal–support interactions from TiO_2. The PtA results show reversible CO-induced Pt surface roughening on irreducible Al_2O_3 without persistent Pt–support interfacial restructuring (Supplementary Figs. 46–49), unlike the reaction-evolved Pt–TiO_2 interfacial structures observed on reducible TiO_2. In parallel, GA-optimised simulations using Ov-modulated TiO_2 models show that O_v can modulate local Pt–TiO_2 interactions and Pt wetting, while the overall facet-dependent morphology trend remains preserved within the examined O_v range (Supplementary Figs. 50 and 51). These results indicate that O_v-related effects can influence Pt structural evolution, but do not solely determine the facet-dependent Pt morphology. Together with the experimental and computational evidence discussed above, the enhanced reactivity of PTS is consistent with the combined contribution of higher O_v-related redox reactivity and a reaction-evolved Pt–TiO_2(001) interfacial configuration derived from the initially wetted Pt morphology."*

The corresponding Supplementary Note 13 has also been revised to explicitly state the limitation of PtA as a qualitative irreducible-support reference and to clarify that the PtA results are not used for quantitative comparison of catalytic activity or Pt structural evolution with the Pt/TiO_2 catalysts. In the revised Supplementary Note 13, PtA is discussed only in terms of the reversibility of CO-induced Pt surface roughening on an irreducible support, whereas the O_v-modulated GA simulations are retained as a Pt/TiO_2-specific analysis showing that O_v can locally modulate Pt wetting but does not override the facet-dependent morphology trend.

We sincerely thank the reviewer for these thoughtful and constructive comments. We particularly appreciate the reviewer's critical suggestions regarding the possible contributions of surface reduction, O_v-related species, and the comparability of the Pt/Al_2O_3 reference catalyst. These comments helped us refine the interpretation of the activity enhancement after the first catalytic run, clarify the limited role of PtA as a qualitative irreducible-support reference, and more carefully distinguish the contributions of O_v-related redox properties from facet-dependent $Pt–TiO_2$ interfacial restructuring. These revisions have helped us further clarify the central message of the manuscript and strengthen the key conclusions of this work.

We sincerely appreciate the all reviewer's insightful and constructive comments, which have played a crucial role in significantly improving the quality and clarity of our manuscript.

Response to the reviewers' comments

The followings are the responses to the reviewers' comments for the manuscript *NCOMMS-25-68798D*

Reviewer #3

General comments: After careful evaluation, I still find insufficient evidence to support their core claim of "TiO_2-facet-dependent reconstruction of Pt nanoparticles during CO oxidation" in the title. The authors only demonstrate facet-dependent initial morphological features of the catalyst before reaction, arising from wetting/dewetting effects that have been well documented in existing literature. The authors also claim "a dynamic structural evolution of Pt-TiO_2 during reaction", but they only provided indirect evidence, inferring CO-induced surface roughening by DRIFTS and Pt facilitated reduction of TiO_2 support by TPR, which are also well known in literature. Simply combining these known observations cannot establish sufficient novelty for this work. Given the absence of direct evidence (e.g., in situ ETEM characterization) demonstrating how Pt reconstructs during the CO reaction and how such structural changes correlate with CO catalytic reactivity (rather than simple surface reduction), I remain skeptical about the novelty of this work.

Response: We sincerely thank Reviewer #3 for the continued critical evaluation of our manuscript. We understand the reviewer's concern that direct *in situ* structural characterization, such as ETEM, would provide the most definitive evidence for tracking the real-time restructuring pathway of Pt nanoparticles during CO oxidation.

As clarified in the previous revision, we do not intend to claim that the full reconstruction pathway of Pt nanoparticles was directly visualized under reaction conditions. We agree that facet-dependent wetting/dewetting of metal nanoparticles on oxide supports has been discussed in previous studies. However, the novelty of this work is not the initial wetting/dewetting behavior itself. Rather, to the best of our knowledge, systematic studies correlating facet-dependent Pt morphological evolution with CO oxidation behavior in a well-defined Pt/TiO_2 facet system remain limited. By combining similarly sized Pt nanoparticles, well-defined anatase TiO_2 facets, catalytic cycling, post-reaction STEM, in situ DRIFTS, NAP-XPS, XAFS, reduction pretreatment controls, and theoretical calculations, this study shows that the TiO_2 facet affects not only the initial Pt morphology but also the reaction-evolved Pt–TiO_2 interfacial structure after CO oxidation.

Regarding the reviewer's concern about simple surface reduction, we agree that support reduction and oxygen-vacancy-related effects are involved in the reaction-induced evolution of Pt/TiO_2 catalysts. However, the reduction pretreatment controls and post-reaction O 1*s* analyses indicate that the enhanced activity after catalytic cycling cannot be explained solely by additional TiO_2 reduction or oxygen-vacancy generation.

Reviewer #4

General comments: In the submission the authors show that the support facet governs the initial morphology, reaction-induced restructuring behaviour of supported Pt nanoparticles on TiO2 during CO oxidation, which are not unexpected. But a paper with solid experimental results to demonstrate them is of importance and interest in the community. and deserves the publication in Nature Communications. Below are two minor issues needed to be clarified before the publication:

Response: We sincerely thank Reviewer #4 for the positive evaluation of our manuscript and for recognizing its importance and interest to the catalysis community. We also thank the reviewer for the constructive comments, which helped us further clarify the terminology and explain why and how the spectra were normalized.

Comment 1: Based on the adopted reaction pressures, the "AP-XPS" should be "NAP-XPS".

Response and Action taken: We thank the reviewer for pointing this out. We agree that, based on the reaction pressures used in this study, "NAP-XPS" is the more appropriate term. Accordingly, we have replaced "AP-XPS" with "NAP-XPS" throughout the manuscript and Supplementary Information.

Comment 2: Figure 3 a and d: The y axis unit is normalized intensity. Why and how are the signals normalized? These are important for reproducibility.

Response and Action taken: We thank the reviewer for this helpful comment. The CO-DRIFTS spectra in Figs. 3a and d were normalized because our analysis focuses on the relative distribution of CO adsorption bands associated with different Pt surface sites rather than on the absolute adsorption intensity. In particular, the spectra are used to compare the relative contributions of Pt step/edge, terrace, and interfacial sites before and after CO oxidation. Normalization to the maximum intensity of the linearly adsorbed CO band enables a direct

comparison of these spectral features.

o clarify this procedure, we have revised the *Methods* section. The pre- and post-reaction CO-DRIFTS spectra were baseline-corrected and normalized to the maximum intensity of the linearly adsorbed CO band over the 2250–1900 cm^{-1} region. Figs. 3a and d show the enlarged 2150–2000 cm^{-1} region to highlight the main CO adsorption features discussed in the manuscript.

We sincerely appreciate the all reviewer's insightful and constructive comments, which have played a crucial role in significantly improving the quality and clarity of our manuscript.